UNIVERSITY OF LONDON THESIS

Degree PhD Year 2007 Name of Author WILLATS, Lisa

IMPROVED QUANTIFICATION OF PERFUSION IN PATIENTS WITH CEREBROVASCULAR DISEASE

Lisa Willats

RADIOLOGY AND PHYSICS UNIT
INSTITUTE OF CHILD HEALTH
UNIVERSITY COLLEGE LONDON

Submitted for the Degree of Doctor of Philosophy
University College London

April 2007

ProQuest LLC
789 East Eisenhower Parkway
P.O. Box 1346
Ann Arbor, MI 48106-1346

ABSTRACT

In recent years measurements of cerebral perfusion using bolus-tracking MRI have become common clinical practice in the diagnosis and management of patients with stroke and cerebrovascular disease. An active area of research is the development of methods to identify brain tissue that is at risk of irreversible damage, but amenable to salvage using reperfusion treatments, such as thrombolysis. However, the specificity and sensitivity of these methods are limited by the inaccuracies in the perfusion data.

Accurate measurements of perfusion are difficult to obtain, especially in patients with cerebrovascular diseases. In particular, if the bolus of MR contrast is delayed and/or dispersed due to cerebral arterial abnormalities, perfusion is likely to be underestimated using the standard analysis techniques. The potential for such underestimation is often overlooked when using the perfusion maps to assess stroke patients. Since thrombolysis can increase the risk of haemorrhage, a misidentification of 'at-risk' tissue has potentially dangerous clinical implications.

This thesis presents several methodologies which aim to improve the accuracy and interpretation of the analysed bolus-tracking data. Two novel data analysis techniques are proposed, which enable the identification of brain regions where delay and dispersion of the bolus are likely to bias the perfusion measurements. In this way true hypoperfusion can be distinguished from erroneously low perfusion estimates.

The size of the perfusion measurement errors are investigated *in vivo*, and a parameterised characterisation of the bolus delay and dispersion is obtained. Such information is valuable for the interpretation of *in vivo* data, and for further investigation into the effects of abnormal vasculature on perfusion estimates.

Finally, methodology is presented to minimise the perfusion measurement errors prevalent in patients with cerebrovascular diseases. The *in vivo* application of this method highlights the dangers of interpreting perfusion values independently of the bolus delay and dispersion.

TABLE OF CONTENTS

LIST OF FIGURES

LIST OF TABLES

ACKNOWLEDGEMENTS

I am hugely indebted to my supervisors, Fernando Calamante and Alan Connelly, for their continuous support, advice, and friendly guidance throughout my PhD. They have been brilliant colleagues and supervisors. I am very fortunate to have had the opportunity to work with them and to learn from their exceptional expertise in MRI. I would also like to express my gratitude to David Gadian, for welcoming me into his lab, and for his help and encouragement during my PhD.

Throughout my PhD I have been fortunate to have worked with some great people. I am very appreciative of many dynamic discussions and debates that have taught me a great deal, ranging from MRI research to football. I owe special thanks to Donald for all his help and humour.

I would also like to thank Professor Geoffrey Donnan, Henry Ma and Rudiger Seitz for their contribution and clinical insight to Chapter 9.

I am grateful to the Child Health Research Appeal Trust (CHRAT), for providing the financial support for this work.

I would like to thank my friends and family, who have made my life outside from work most enjoyable, and who have encouraged and supported me. Special thanks go to my many loyal long-distance friends, who, through emails and phone calls have remained close and supportive. To my housemates, thank you for your kindness and care, especially in the final stages of writing this thesis. And to Darrell, thank you so much for your patience, understanding and love. Finally, I am hugely thankful to my family, for the loving support and encouragement they have always given me.

PUBLICATIONS

Publications in peer-reviewed journals and international meetings during PhD thesis.

[1] Willats L, Connelly A, and Calamante F (2006) Improved deconvolution of perfusion MRI data in the presence of bolus delay and dispersion *Magn.Reson.Med.* 56:146-156

[2] Calamante F, Willats L, Gadian DG, and Connelly A (2006) Bolus delay and dispersion in perfusion MRI: implications for tissue predictor-models in stroke *Magn.Reson.Med.* 55:1180-1185

[3] Willats L, Connelly A, and Calamante F (2005) Improved characterisation of delayed and dispersed residue functions in bolus tracking MRI *In: Proceedings of the 13th Annual Meeting of ISMRM, Miami, USA*

[4] Willats L, Connelly A, and Calamante F (2006) Improved deconvolution of bolus tracking data using wavelet thresholding. *In: Proceedings of the 14th Annual Meeting of ISMRM, Seattle, USA*

[5] Willats L, Connelly A, and Calamante F (2007) Modelling bolus dispersion from DSC-MRI data. *In: Proceedings of the 15th Annual Meeting of ISMRM, Berlin, Germany*

"True freedom is not freedom from responsibility to God and others in order to live life for myself but freedom from myself in order to live for God and others"
John Stott

1 INTRODUCTION

Stroke is one of the most frequent causes of morbidity and disability in the developed world. Therapeutic treatments that are targeted at compromised brain tissue emphasise the importance of early and accurate diagnosis (Baird *et al.* 1998). However, routine clinical evaluations often provide unreliable information, potentially resulting in poor patient management. In recent years, Magnetic Resonance Imaging (MRI) has proved a powerful technique for evaluating patients with stroke and cerebral arterial diseases. As well as being non-invasive, the key strength of MRI is its ability to probe not only the tissue structure (using T_1- and T_2-weighted imaging), but also the bioenergetic tissue status (using diffusion MRI), the vascular anatomy (using MR angiography), and the haemodynamic tissue status (using perfusion MRI, which measures the rate of delivery of blood to the tissue), all within a single examination.

In combination the different MRI techniques are a valuable selection tool for acute stroke therapies. The concept of the diffusion-perfusion mismatch (an area observed to be abnormal on perfusion MRI but with normal diffusion properties) has received great interest in the last decade, and has shown great promise in distinguishing tissue that is not yet infarcted but is at risk of progressing to irreversible infarction (Sobesky *et al.* 2005; Gonzalez 2006; Kidwell *et al.* 2004). Abnormal regions on structural and diffusion MR images are thought to indicate tissue regions that are the 'core' of the infarct (Sobesky *et al.* 2005; Gonzalez 2006). Although it may be possible to reverse these abnormalities (Bardutzky *et al.* 2007), such tissue is usually irreversibly

destined for infarction. Perfusion measurements are thought to be main indicator of the 'at-risk' brain tissue. Depending on the severity and duration of the perfusion abnormality, it may be possible to salvage such tissue using reperfusion treatments such as thrombolysis (Schellinger *et al.* 2000). Therefore, in combination, these MRI techniques can be used to predict the final patient outcome, thus raising the possibility of identifying acute stroke patients most likely to benefit from intervention.

Within this context, the ultimate goal has been the development of algorithms to predict the fate of the affected tissue in a patient with stroke. These so-called predictor-models combine all the imaging information available to infer the most probable clinical and radiological outcome for the brain tissue from the acute imaging data in a patient-specific way (Wu *et al.* 2001; Wu *et al.* 2007; Rose *et al.* 2001; Rose *et al.* 2004; Gottrup *et al.* 2005). Because reperfusion treatments can increase the risk of haemorrhage (Trouillas *et al.* 2006), it is important to balance the risk of treatment against the potential benefits. These models aim at improving patient management in this way. Furthermore, such patient-specific predictions would allow the current rigid and short therapeutic time-window to be replaced with a patient-specific time-window for therapeutic intervention, potentially increasing the number of patients receiving treatment.

Since the haemodynamic information provided by perfusion MRI is the most sensitive MRI indicator of 'at-risk' brain tissue, it is also the main determinant of the outcome of predictor-models. Consequently, it is also the main source error. Inaccuracies in the perfusion MRI data limit the prediction capabilities of these models, and could lead to patients being treated inappropriately, with potentially serious clinical consequences.

The most widely employed clinical MRI method used for measuring cerebral perfusion is dynamic susceptibility-contrast (DSC-) MRI or bolus-tracking MRI (Calamante *et al.* 1999b). The technique involves the fast injection of a bolus of magnetic resonance (MR) contrast agent and the rapid measurement of the resulting

image signal changes. Over the last decade there has been a great deal of research into the development of both the acquisition and analysis of DSC-MRI data. In addition, the technique has been very popular for clinical studies. However, several studies have revealed that in current implementations of DSC-MRI, large errors may be present in the perfusion measurements. In particular, in patients with cerebral arterial diseases, abnormal blood flow patterns result in delay and dispersion of the bolus, which can introduce severe underestimations (up to 60-70%) in perfusion measurements (Calamante *et al.* 2000).

The work performed for this thesis focuses on the use of DSC-MRI in the patients with cerebrovascular disease, with a view to identify and minimise the errors associated with these perfusion measurements. The necessary background to the work is given in Chapters 2 to 5, Chapters 6 to 9 present the original work conducted for this thesis, concluding with a general discussion in Chapter 10.

Chapter 2 presents an overview of some of the fundamental principles of MRI. In particular, attention is given to those aspects that are employed in imaging ischaemic stroke.

In Chapter 3 a summary of the current thinking concerning the pathogenesis of tissue in stroke is given. This provides the necessary background to understanding the changes in structure, diffusion and perfusion that can be observed using MRI. There are also many non-MRI clinical imaging techniques currently being used to assess perfusion. The strengths and weaknesses of these techniques are discussed in context of their utility to manage stroke patients. In addition, an overview of the alternative perfusion MRI method of Arterial Spin Labelling is presented. Although this technique is not currently robust enough for routine clinical use, it has promising potential to obtain absolute perfusion measurements. It is consequently an active field of research, and may eventually prove to be a robust alternative clinical perfusion MR methodology. Further background is also given concerning the prediction of 'at-risk' tissue and therapeutic treatments, providing the clinical context

to the largely methodological and theoretical work presented in the remainder of the thesis.

Chapter 4 of this thesis describes the core theory of perfusion quantification using DSC-MRI, and the commonly used analysis methods. The caveats, limitations, and sources of error in the acquisition and analysis of these data are discussed. In particular, errors that are prevalent in data from patients with vascular abnormalities are highlighted, together with the errors endemic in the analysis of DSC-MRI data. This discussion provides the necessary background to understand the motivation for the methods and analysis presented in the proceeding chapters, which seek to improve the quantification of perfusion in patients with cerebrovascular diseases.

In Chapter 5, the framework for the development and testing of the novel analysis methods is described. Although this chapter is short, it is of primary importance in understanding the assessment of perfusion measurement errors that can adversely influence the prognosis of stroke patients.

Chapter 6 presents a new DSC-MRI analysis method (modified maximum-likelihood expectation-maximisation or mML-EM analysis), which seeks to overcome some of these limitations to provide an improved quantification of perfusion and an indication of the reliability of the perfusion measurements. If brain regions of unreliable perfusion (due to delay and/or dispersion of the bolus) can be identified on the perfusions maps, then the results of predictor-models using these input data can be interpreted in light of the possible errors. Identifying regions where perfusion is likely to be underestimated could avoid the potential misclassification of 'at-risk' tissue.

In Chapter 7, the methodology introduced in Chapter 6 is developed further with a view to make the analysis less sensitive to the MR imaging parameters and the quality of the data. It is important that analysis techniques are robust, automated, and suitable for equipment from any of the MRI manufacturers. This would enable the

widespread use of these more accurate methods. In this chapter, accurate perfusion quantification is sought by implementing wavelet analysis of the data.

Chapter 8 presents an *in vivo* investigation into vascular transport (i.e. delay and dispersion) of the bolus and the size of the associated perfusion measurement errors in DSC-MRI, using the methodology developed in Chapter 6. A parameterised model for the vascular transport is proposed, which has potentially important applications for the investigation of perfusion errors and development of analysis techniques (and consequently a better awareness of the reliability of predictions of tissue infarction).

In Chapter 9, two methods are presented, which seek to minimise perfusion measurement errors resulting from vascular transport. The first method seeks to relate delay and dispersion *in vivo*, with a view to correct for dispersion by means of the more easily estimated delay. The dispersion parameter is measured using the parameterised vascular transport model presented in Chapter 8. The second method utilises the analysis technique presented in Chapter 7 to identify regions on perfusion maps, which are subject to bolus delay and dispersion. A methodology is presented to correct for delay and dispersion within these regions, and as a result minimise the associated errors. The ability to correct for perfusion measurement errors would be a significant advancement for the accuracy of predictor-models.

Therefore this thesis investigates several aspects of perfusion quantification, which aim to improve the accuracy and robustness of perfusion MRI in stroke and cerebrovascular disease, and ultimately improve the identification of patients likely to benefit from reperfusion treatment. Furthermore, these improvements should help to further our understanding of the pathophysiology of brain tissue in stroke patients.

2 BACKGROUND TO MR IMAGING

2.1 INTRODUCTION

Magnetic Resonance Imaging (MRI) is very well suited to imaging soft tissue, such as the brain, due to the mechanisms governing image contrast. Using a carefully designed MR image acquisition, the image contrast can be made sensitive to specific properties of the tissue (e.g. T_1, T_2, BOLD and diffusion), which are indicative of its physiological condition. The purpose of this chapter is to introduce the MR imaging theory that is necessary to understand MRI in acute stoke. Particular attention is given to the MRI concepts that are most relevant to cerebral-perfusion imaging. The chapter outlines some of the important mechanisms governing image contrast, some of the methods used to create and sample the MR signal, and current methodology for reconstructing the MR image.

2.1.1 MAGNETIC RESONANCE

Only nuclei with intrinsic nuclear spin angular momentum exhibit the property of magnetic resonance. In most medical applications, the proton (^{1}H) is the nucleus of most interest because of its high natural abundance in biological tissue (e.g. in fat, water and other organic molecules). In particular, in the MR imaging of stroke, the blood and tissue-water protons are manipulated. The proton has charge +1, and an intrinsic spin angular momentum J=1/2, resulting in a magnetic *dipole* moment $\vec{\mu} = \gamma\vec{J}$, (where γ is the gyromagnetic ratio). Consequently, on application of an external magnetic field $\vec{B}_0$, the magnetic moment of the proton, or spin $\vec{\mu}$, is subject to a torque:

$$\frac{d\vec{\mu}}{dt} = \gamma\vec{\mu} \times \vec{B}_0 \qquad [2.1]$$

As a result $\vec{\mu}$ precesses about the $\vec{B}_0$ direction (or z-direction) at an angular frequency ω_0, known as the Larmor (resonant) frequency:

$$\omega_0 = \gamma B_0 \qquad [2.2]$$

The resonant frequency of protons in a 1.5T magnetic field is 63.9 MHz.

From a quantum mechanical perspective, there are two available quantum states for the spins. In the lower energy state the magnetic moment is aligned parallel to the field, and in the higher energy state, the alignment is antiparallel. The quantum energy difference between these two states is $\hbar\omega_0$ (where $\hbar$ is the Planck constant). In the human body, the temperature T is such that the average thermal energy of the protons, k_bT (where k_b is the Boltzmann constant) is millions of times larger than the quantum energy difference. Consequently, according to the Boltzmann probability distribution, the spin population difference between the two quantum states, the 'spin excess', is small.

$$spin \quad excess \approx N\left(\frac{\hbar\omega_0}{2k_bT}\right) \qquad [2.3]$$

where N is the number of spins in the sample. Even though the spin excess is small compared with the number of spins in the sample, the ensemble average of all the spins, gives rise to a measurable macroscopic longitudinal equilibrium magnetisation, M_0:

$$M_0 \approx \rho_0\left(\frac{\gamma\hbar}{2}\right)\left(\frac{\hbar\gamma B_0}{2k_bT}\right) \qquad [2.4]$$

where ρ_0 is number of spins per unit volume (proton density), $\left(\frac{\gamma\hbar}{2}\right)$ is the proton magnetic moment component along the direction of the field, and $\left(\frac{\hbar\gamma B_0}{2k_bT}\right)$ is the fractional spin excess. This equilibrium magnetisation, which scales linearly with field strength, provides a measurable MR signal.

2.2 MR RELAXATION THEORY

In equilibrium, the macroscopic magnetisation vector $\vec{M} = \sum_i \vec{\mu}_i$ precesses around the main static longitudinal external field $\vec{B}_0$ at angular frequency ω_0. When an additional external magnetic field $\vec{B}_1$ is applied, $\vec{M}$ is made to precess around the vector-sum of the two fields. In MR imaging, the externally applied field $\vec{B}_1$ is a radiofrequency (RF) pulse, orientated perpendicular to $\vec{B}_0$. As a result $\vec{M}$ precesses simultaneously about $\vec{B}_0$ at ω_0 and about $\vec{B}_1$ at $\omega_1 = \gamma B_1$. The effect becomes easier to visualise from the perspective of a reference frame that rotates around the $\vec{B}_0$-direction at the frequency of the applied field ω_{RF}. In this frame the direction of the $\vec{B}_1$ field is stationary during the pulse. In the simplest case where ω_{RF} is equal to the Larmor frequency ω_0, $\vec{M}$ appears to precess only about $\vec{B}_1$ at a rate ω_1 during the pulse. At the end of a pulse of duration τ_p, $\vec{M}$ will have rotated away from the $\vec{B}_0$ by $\omega_1 \tau_p$ radians. Short, high-amplitude RF pulses with a rectangular $\vec{B}_1(t)$ profile are typically referred to as 'hard pulses'. In contrast, 'soft pulses' have modulated $\vec{B}_1(t)$ profiles often designed to give a rectangular frequency-response for accurate slice-selection (Section 2.4.1). The application of an RF pulse or 'excitation' pulse is essential to all modern MR imaging experiments (see Section 2.3). Once the RF field has been removed, various processes take place on the microscopic level, which cause $\vec{M}$ to relax back to its equilibrium value (see Section 2.2.2).

2.2.1 T_1 AND T_2 RELAXATION TIMES

The contrast seen in a conventional MR image is determined by both the spin density ρ_0, and the rate of spin relaxation. The relaxation of the aggregated collection of spins, or $\vec{M}$, is characterised by two time-constants, T_1 and T_2:

1.) *Spin-lattice* relaxation time T_1: the T_1 time-constant characterises the recovery of the magnetisation along the direction of $\vec{B}_0$. Longitudinal equilibrium magnetisation is restored via the exchange of energy between the spins and the lattice (local environment).

2.) *Spin-spin* relaxation time T_2: the T_2 time-constant characterises the decay of the magnetisation perpendicular to the main field. Transverse magnetisation is lost via the exchange of energy between the spins (i.e. there is no net loss of energy from the spin system), which causes a loss in phase coherence of the precessing spins.

In the same way as an applied RF field affects the macroscopic magnetisation by changing its precessional path, various other field perturbations that are intrinsic to the spin ensemble, act to restore thermal equilibrium. The following sections describe some of the possible field perturbations and mechanisms by which equilibrium is restored. These concepts are key to understanding the MR image contrast that arises from the relaxation of the spins.

2.2.2 CORRELATION TIME AND SPECTRAL ENERGY DENSITY

After the applied RF field has been removed, a spin will relax back to its equilibrium state by exchanging energy with either its surroundings or another spin. Energy transfer is mediated by fluctuations in the local magnetic field vector $\Delta\vec{B}_0$, experienced by the spin, and is most effective when the frequency of fluctuation is close to the Larmor frequency of the spin. The effect of $\Delta\vec{B}_0$ on the T_1 and T_2 relaxation processes is most easily understood in the rotating reference frame (x', y', z), which rotates around the z-direction ($\vec{B}_0$-direction) at the Larmor frequency, ω_0.

In this frame the torque experienced by an individual spin $\vec{\mu}$, due to the field perturbation $\Delta\vec{B}_0$ is:

$$\begin{pmatrix} d\mu_{x'}/dt \\ d\mu_{y'}/dt \\ d\mu_z/dt \end{pmatrix} = \gamma \begin{pmatrix} \Delta B_z \mu_{y'} - \Delta B_{y'} \mu_z \\ \Delta B_{x'} \mu_z - \Delta B_z \mu_{x'} \\ \Delta B_{y'} \mu_{x'} - \Delta B_{x'} \mu_{y'} \end{pmatrix} \qquad [2.5]$$

Changes in μ_z, which are synonymous with the longitudinal or T_1 relaxation process, are only associated with changes in $\Delta B_{y'}$ and $\Delta B_{x'}$. In the laboratory (stationary) frame these fluctuations appear as frequencies close to the Larmor frequency. Changes in $\mu_{x'}$ and $\mu_{y'}$, which are synonymous with the transverse or T_2 relaxation process, are associated with field fluctuations in all three directions. In the laboratory frame, the ΔB_z fluctuations appear as frequencies close to zero frequency.

Therefore, both T_1 and T_2 relaxation processes are mediated by fluctuations in frequency close to ω_0 (the 'dynamic contribution'). T_2 relaxation processes are also mediated by field fluctuations that are close to $\omega = 0$ (the 'static contribution'). Consequently, because of the additional sensitivity of the transverse relaxation to low frequencies, T_2 is often considerably shorter than T_1. Furthermore, since the frequency of the 'dynamic contribution' is dependent on the external field strength B_0, T_1 relaxation has a much greater dependence on field strength than T_2.

The above analysis reveals that the spin relaxation processes are frequency-dependent. Consequently, the *spectral density* $J(\omega)$ of the field fluctuations is an important factor in determining the efficiency of energy transfer. Furthermore, since field fluctuations originate from the motion of other magnetic sources (e.g. molecules) in the local environment, $J(\omega)$ is governed by the time constant associated with molecular motion: the *correlation time* τ_c. This time depends on the molecule weight and size. For example, in a non-viscous fluid, such as free water, $\tau_c \sim 10^{-11}$s, whereas for a bound water molecule the correlation time is longer,

$\tau_c \sim 10^{-8}$ s, because the surrounding molecules are less mobile. The spectral density $J(\omega)$ is related to the correlation time τ_c via (Farrar *et al.* 1971):

$$J(\omega) = \frac{\tau_c}{1+(\omega\tau_c)^2} \qquad [2.6]$$

The relaxation rate of the spins within a substance therefore depends on the correlation times of molecules within that substance. Figure 2.1 shows a schematic diagram of $J(\omega)$ for solids, viscous and non-viscous liquids. For the solid, there is a very small spectral component at ω_0, and a large low-frequency component. Consequently, the spin-lattice relaxation process is inefficient (long T_1), whilst the spin-spin relaxation process is very efficient (short T_2), owing to the large static component. As the spins become more mobile, the breadth of the spectrum increases, causing T_1 to shorten, and T_2 to lengthen. For the viscous liquid there is a large spectral component around the Larmor frequency ω_0, leading to short T_1 and T_2 values. As the spins become increasingly dispersed, the spectrum flattens further, and T_1 will lengthen.

This qualitative understanding has been quantified by Bloembergen, Purcell and Pound (BPP theory) (Bloembergen *et al.* 1948), who expressed T_1 and T_2 relaxation time in terms of the spectral density, $J(\omega)$ and the correlation time τ_c:

$$\frac{1}{T_1} = K[J(\omega_0)+4J(2\omega_0)] \qquad [2.7]$$

$$\frac{1}{T_2} = \frac{K}{2}[3\tau_c+5J(\omega_0)+2J(2\omega_0)] \qquad [2.8]$$

where K is a constant. These expressions describe the situation for simple dipole-dipole interactions between spins (e.g. two protons of water). The term in Equation [2.8] that is independent of ω_0 represents the static component of T_2.

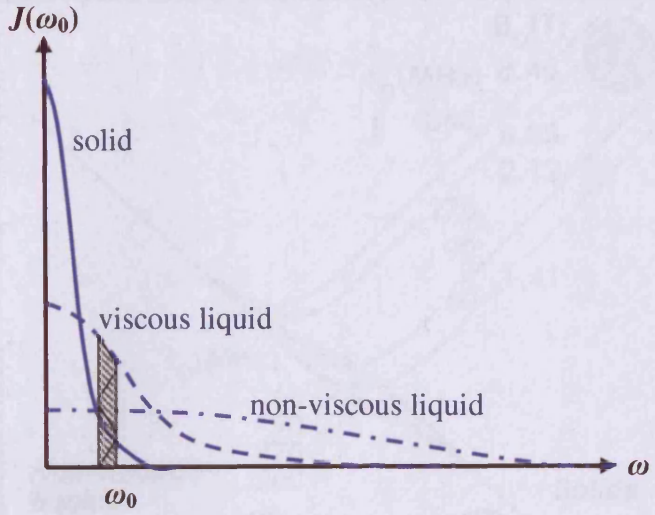

Figure 2.1: Schematic plot showing the spectral densities $J(\omega)$ as a function of frequency ω, for a solid (solid line), viscous liquid (dashed line), and non-viscous liquid (dash-dot line). The shaded area indicates that the viscous liquid contains the highest proportion of protons with correlation time that match the resonant frequency ω_0.

The terms in $2\omega_0$ account for the relaxation occurring as a result of field fluctuations at twice the Larmor frequency, which in quantum-mechanical terms corresponds to the exchange of two energy quanta.

Figure 2.2 illustrates the BPP dependency of T_1 and T_2 on τ_c. When $\omega_0\tau_c << 1$ (liquids), T_1 and T_2 relaxation times are predicted to be equal, $\frac{1}{T_1} = \frac{1}{T_2} = 5K\tau_c$, and independent of field strength. When $\omega_0\tau_c >> 1$ (solids), T_1 is predicted to be long and dependent on the field strength (owing to the small dynamic contribution), and T_2 is predicted to be short (owing to the large static component). Since ω_0 is dependent on field strength, and τ_c is dependent on temperature, the relaxation properties of a system are also field- and temperature- dependent. It should also be noted BPP theory is only valid for $\tau_c < T_2$, which corresponds to spins in the liquid sate, where dipole-dipole interactions dominate the relaxation (see Section 2.2.3).

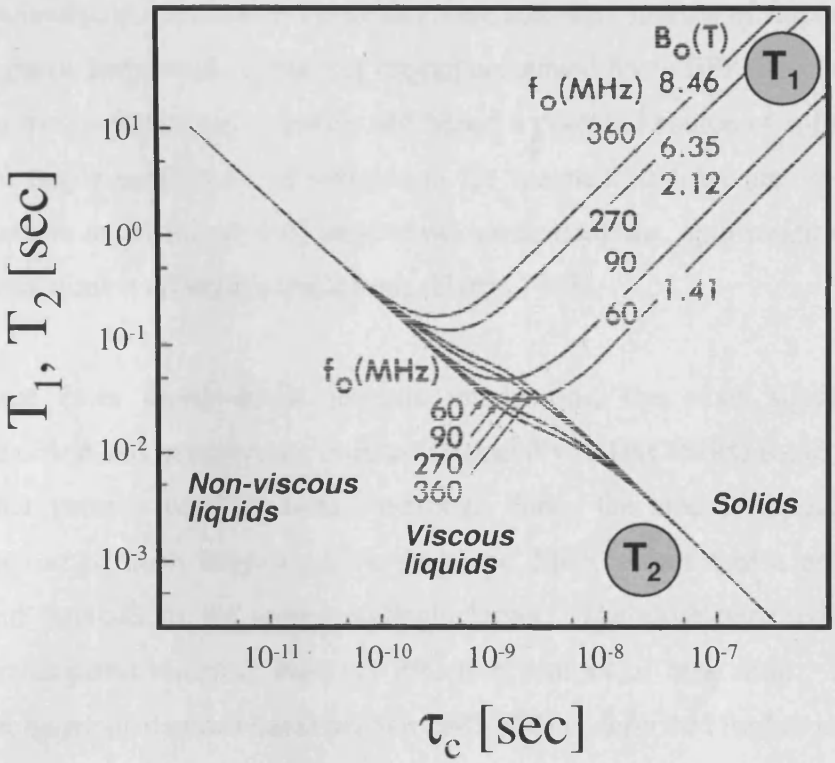

Figure 2.2: The dependence of T_1 and T_2 on the correlation time τ_c given by the relationships in Equations [2.7] and [2.8]. The effect of varying the field strength is also shown. The magnetic field strength is in Tesla, T, and the proton resonant frequency f_0, is in MHz. Reproduced from (Fullerton 1992).

In complex biological systems such as brain tissue, the situation is far more complex owing to multiple compartments, macromolecules, and chemical species present.

2.2.3 RELAXATION MECHANISMS

In standard MR imaging, the principle source of relaxation for water protons arises from the rotational motion of the water molecules. These generate an additional magnetic field $\Delta\vec{B}_0$, such that the magnetic dipole on a neighbouring water proton experiences a field $\vec{B}_0 + \Delta\vec{B}_0$. This coupling of magnetic dipoles is known as the

dipole-dipole interaction. However, there are other sources of fluctuation in the local magnetic and electric fields that are not accounted for in BPP theory. Any fluctuation is a means for energy transfer, and hence a potential source of spin relaxation. The five major mechanism of interaction for magnetic dipoles are: electric-quadrupole interactions, chemical-shift anisotropy, scalar-coupling, spin-rotation interaction, and interactions with unpaired elections (Harris 1983).

Aside from dipole-dipole protons interactions, the other significant source of relaxation and hence image contrast (especially in DSC-MRI) is the interaction of the water protons with unpaired electrons. Since the electric dipole moment of the electron is much larger than the magnetic dipole moment of a proton, the induced field fluctuations are correspondingly larger. Therefore unpaired electrons (e.g. a paramagnetic material) are very effective sources of relaxation. The effect of the paramagnetic contrast agent used in DSC-MRI is described further in Chapter 4.

2.2.4 BLOCH EQUATIONS

The evolution of the macroscopic magnetisation of a system of spins can be described in terms of the torque exerted on the macroscopic magnetisation vector $\vec{M} = (M_x, M_y, M_z)^T$, by the external field $\vec{B} = (B_x, B_y, B_z)^T$. Including terms accounting for the longitudinal T_1, and transverse T_2, relaxation, the equation of motion is:

$$\frac{d\vec{M}}{dt} = \gamma(\vec{M} \times \vec{B}) - \frac{(M_x \cdot \vec{i} + M_y \cdot \vec{j})}{T_2} - \frac{(M_z - M_0) \cdot \vec{k}}{T_1} \qquad [2.9]$$

where M_0 is the equilibrium longitudinal (z-direction) value of $\vec{M}$, and $\vec{i}, \vec{j}, \vec{k}$ are unit vectors along the $\vec{x}, \vec{y}, \vec{z}$ axes. This equation is known as the Bloch equation (Bloch 1948). The external field $\vec{B}$ may include contributions from an applied RF

field $\vec{B}_1$, or a gradient field. In their absence, when $\vec{B} = B_0 \cdot \vec{k}$, (the static magnetic field), the Bloch equation can be simplified to:

$$\frac{dM_x}{dt} = \gamma M_y B_0 - \frac{M_x}{T_2} \qquad [2.10]$$

$$\frac{dM_y}{dt} = -\gamma M_x B_0 - \frac{M_y}{T_2} \qquad [2.11]$$

$$\frac{dM_z}{dt} = \frac{M_0 - M_z}{T_1} \qquad [2.12]$$

These equations describe the exponential decay of the transverse magnetisation towards zero and exponential recovery of the longitudinal relaxation towards M_0.

2.3 IMAGE CONTRAST

A measurable MR signal is obtained by perturbing the main magnetic field experienced by the spins using an 'excitation' RF pulse, such that the macroscopic magnetisation vector is tipped away from the B_0 axis (longitudinal direction) and is set into precession. The contrast in an MR image can be manipulated by changing the nature and timing of perturbations to the magnetisation, and the time at which the signal is acquired.

2.3.1 FREE INDUCTION DECAY

The simplest MRI experiment involves detecting the MR signal after rotating the magnetisation into the transverse plane (using for example a 90° RF pulse), where the spins freely precess and relax. The time-varying field of this Free Induction Decay (FID) induces an *emf* in an RF coil tuned and orientated to detect the field changes.

As well as T_1 and T_2 relaxation, field inhomogeneities cause additional dephasing of the transverse magnetisation, leading to further signal loss. The decay time, T_2^* for the transverse magnetisation represents a combination of the external field-induced relaxation T_2' and the thermodynamic T_2 effects:

$$\frac{1}{T_2^*} = \frac{1}{T_2} + \frac{1}{T_2'} \qquad [2.13]$$

The time-constant T_2' is dependent on the homogeneity of the external field and the field distortions caused by the sample. T_2' signal loss is recoverable (see Section 2.3.2), whereas the T_2 relaxation is an intrinsic thermodynamic property of the spin ensemble and cannot be reversed.

2.3.2 SPIN-ECHO

In a Spin-Echo (SE) experiment, the sampled MR signal is the 'echo' formed at time TE (the echo time) using a 180° RF pulse applied at time TE/2 after the application of an excitation pulse. In the time TE/2 following the excitation pulse and preceding the 180° pulse, the magnetisation in the transverse plane dephases due both external field inhomogeneities (T_2' decay) and spin-spin energy exchange (T_2 decay). The effect of the 180° RF pulse at time TE/2 is to invert the phases of the precessing spins. Consequently, the phases accumulated due to static field inhomogeneities in the first TE/2 time period (prior to the 180° pulse) are rephased during the proceeding TE/2 time period (after the 180° pulse), to produce an 'echo' at time TE. Therefore, the T_2' signal loss is recovered and the signal strength at echo time TE is determined by the T_2 relaxation time.

In order to acquire an image with T_2-weighted contrast, the echo should be acquired when there is near maximum difference in the T_2 signal suppression of the two tissue types (e.g. grey-matter (GM) and white-matter (WM)). Furthermore, to produce an image, the SE experiment usually needs to be repeated in a repetition time TR, where TR is long enough to allow the longitudinal magnetisation to recover (ideally) to its

steady-state. In a 1.5T main field, typical T_1 values for nonpathological GM and WM are 1300ms and 660ms respectively (Vymazal *et al.* 1999). Typical T_2 values for nonpathological GM and WM are 93ms and 76ms respectively (Vymazal *et al.* 1999). Therefore, a T_2-weighted SE sequence with TE~80ms and TR~2s results in an image where the GM is brighter than the WM (Vymazal *et al.* 1999).

2.3.3 GRADIENT-ECHO

In a Gradient-Echo (GE) experiment, the sampled MR signal is the 'echo' typically formed by applying a constant magnetic field gradient for a time interval $\tau/2$ immediately following the excitation pulse, and then reversing this gradient for a time,τ. The phase accumulated by the spins during the first gradient lobe is reversed by the second gradient lobe, and an echo is formed halfway through the second gradient. The signal is suppressed according to the T_2^* relaxation time, since only the dephasing caused by the gradient is rephased in the echo. Dephasing due to field inhomogeneities remains.

A common application of GE imaging is to measure the blood-oxygenation-level-dependent (BOLD) MR signal. The magnetic properties of blood are dependent on the oxygenation state of the haemoglobin (Ogawa *et al.* 1990). Because deoxyhaemoglobin is paramagnetic (whereas oxyhaemogloblin is diamagnetic), it promotes both T_2 and T_2* signal loss (see Section 2.2.3). The BOLD phenomenon is widely used in functional MRI (fMRI). This involves the rapid and repeated acquisition of T_2^*-weighted (or GE) images, so that any changes between activation (where the subject is given a task to perform) and rest can be observed. In this way, the areas of the brain involved in that particular task can be mapped, e.g. (Gore 2003).

GE imaging can also be used to generate a T_1-weighted image of the brain by acquiring the echo at a very short TE (~10ms), so that there is minimum T_2/T_2^* decay, and repeating the experiment at a short TR, i.e. TR~1s, so that there is maximum difference in the T_1 signal suppression of GM and WM.

2.3.4 INVERSION RECOVERY

An alternative way to generate T_1-weighted images is by the so called Inversion-Recovery (IR) experiment, in which a 180° RF pulse is used to invert the longitudinal magnetisation so that it is aligned antiparallel to the main field. The inversion is followed by a delay, or inversion time TI, during which the magnetisation relaxes back towards equilibrium with time-constant T_1. The application of a 90° pulse flips the remaining longitudinal magnetisation into the transverse plane enabling the signal to be measured using either a GE or SE readout. If TI is varied over an appropriate range, T_1 can be measured by fitting the recovery curve to:

$$M_z(TI) = M_0\left(1 - 2\alpha\exp\left(-\frac{TI}{T_1}\right)\right) \qquad [2.14]$$

where α is the inversion efficiency that is determined by the longitudinal magnetisation immediately following the RF pulse.

It should be noted that any *in vivo* T_1 measurement is contaminated by blood-water protons flowing into the region of interest (ROI) and exchanging with the tissue water during the period between the inversion and the excitation pulses. The measurement is further complicated by the fact that blood and tissue have different T_1 values. Although the effect on the measured T_1 is small, it is these small changes that are exploited to provide the desired perfusion contrast in the Arterial Spin Labelling (ASL) technique (see Section 3.5.2).

An image of the brain with T_1 contrast can be obtained from an inversion recovery sequence by applying the excitation pulse at time TI when the T_1 generated signal difference between GM and WM is greatest, i.e. TI~1s. The echo should then be measured as soon as possible after to minimise T_2/T_2^* contrast.

An alternative application of the IR experiment is to null the signal from one component. For example, in the fluid-attenuated IR (FLAIR), the TI is chosen such that the signal from the cerebral spinal fluid (CSF) is nulled (White *et al.* 1992).

2.3.5 STIMULATED ECHOES

In addition to images with predominantly T_1, T_2, and T_2^* weighting, a mixed weighting can be achieved by making use of stimulated echoes.[1] Stimulated echoes arise when three or more RF pulses are present in the experiment. For example, five echoes can be observed with three RF pulses: four spin-echoes with T_2-weighting and one stimulated-echo with mixed T_1- and T_2-weighting. This is illustrated in Figure 2.3. The concept of stimulated echoes can be understood by recognising that for any RF pulse (other than a perfect 180°) there is a 0°, 90°, and 180° component, regardless of their rotation angle. The four spin-echoes are formed from the rephasing of the transverse magnetisation by the 180° component of the RF pulses. The stimulated-echo is formed from magnetisation rotated into the transverse plane with the 90° component of the first pulse, then into the longitudinal plane by the 90° component of the second pulse. Here, it retains the phase information from the transverse plane, but decays with time constant T_1. The longitudinal magnetisation is rotated back into the transverse plane by the 90° component of the third pulse, where it rephases to produce a stimulated echo.

2.3.6 DIFFUSION-WEIGHTED IMAGING

The MR image can also be given another contrast weighting indicative of the diffusion properties of the tissue. Diffusion is the thermally driven random motion of particles, or Brownian motion. The effect of diffusion on the MR signal can be understood from the simple pulse sequence illustrated in Figure 2.4. There are two

[1] A mixed weighting can of-course also be achieved by manipulating TE and TR of GE and SE sequences

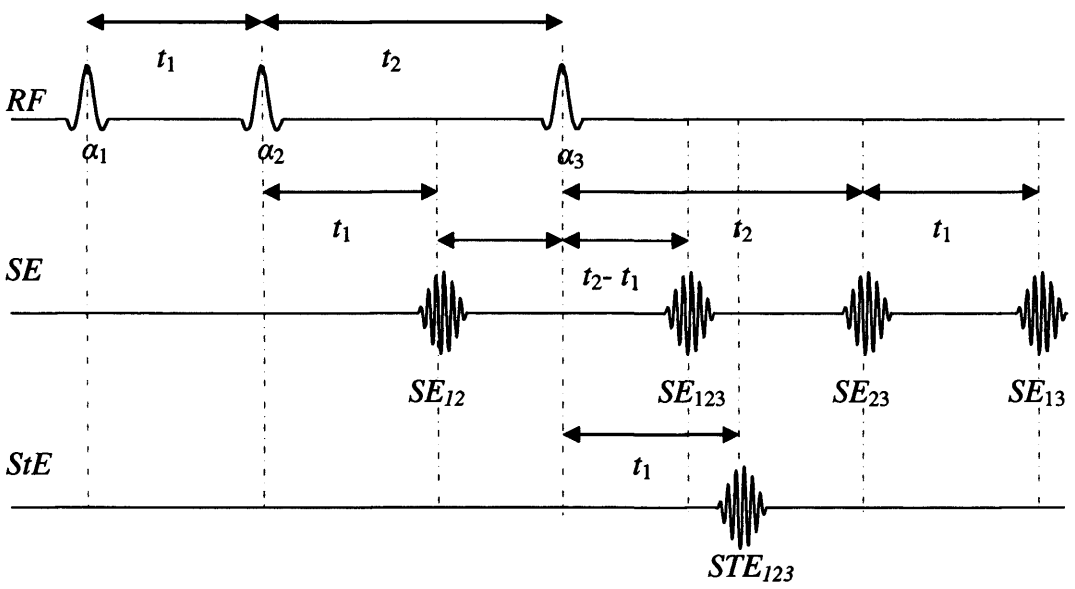

Figure 2.3: Schematic diagram illustrating the formation of four spin-echoes (SE) and one stimulated-echo (StE) from three RF pulses, α_1, α_2, and α_3. The echoes are labelled according to which RF pulses contributed to their formation. The intensity of the stimulated echo is T_1- and T_2- weighted, whilst the spin-echoes have pure T_2-weighting. The time t_1 =TE/2, and the time t_2 is usually known as the mixing-time (TM).

'diffusion' gradients with strength G, duration δ, and separation Δ, either side of the refocusing 180° RF pulse. The first diffusion gradient induces a position dependent phase shift, which for static spins is undone by the second gradient pulse. However, for spins that have moved along the direction of the diffusion-encoding gradient *between* the application of the two gradient pulses, the phase shift induced by the first gradient pulse will not be completely cancelled by the second. The dephasing and hence signal loss resulting from diffusion is increased by increasing the amplitude of the diffusion gradients G, increasing the gradient duration δ, increasing the time interval between the gradients Δ, (i.e. allowing more diffusion-time), or increasing the molecular diffusivity. This final parameter enables useful image contrast between different types of soft tissue, especially in the pathogenesis of cerebrovascular disease (see Section 3.7).

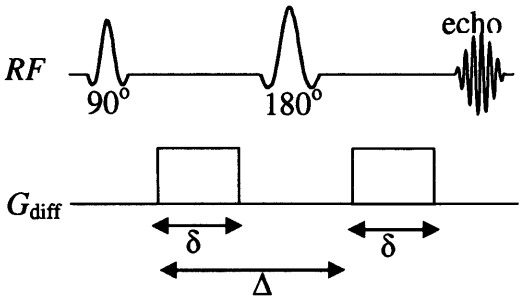

Figure 2.4: The Stejeskal-Tanner or pulse-field gradient spin-echo sequence. The spin-echo sequence is made sensitive to diffusion by additional diffusion gradients, G_{diff}, of duration δ and separation Δ. The magnitude of the echo depends on the degree of diffusion in the direction of the additional gradient during Δ.

Einstein showed that the diffusion coefficient D, relates the variance of the spin displacement $\langle z^2 \rangle$, to the diffusion-time t. For one-dimensional free diffusion:

$$\langle z^2 \rangle = 2Dt \qquad [2.15]$$

This linear relationship between diffusion-distance and time is not applicable when the diffusion is restricted. In this situation an 'apparent' diffusion coefficient (ADC) is measured, which is actually dependent on the diffusion-time (Norris *et al.* 1994). For diffusion within a closed space, the measured diffusion-distance eventually saturates as a function of diffusion-time as more molecules reach the boundaries, and therefore the ADC progressively decreases to zero. In tissue, the measured diffusion will not only depend on the diffusion properties of the molecule (i.e. 'free' diffusion coefficient D), but also on the presence and permeability of boundaries within the tissue structure, and the diffusion-time. Therefore the measured coefficient in MRI is often referred to as the ADC.

Stejeskal and Tanner (Stejskal *et al.* 1965) related the signal attenuation in the diffusion-weighted sequence (Figure 2.4) to the diffusion coefficient:

$$S(G) = S(0)\exp\left(-\gamma^2 G^2 \delta^2 \left(\Delta - \frac{1}{3}\delta\right) D\right) \qquad [2.16]$$

where $S(0)$ is the signal strength in the absence of G. For a general imaging sequence, Equation [2.16] can be written:

$$S(G) = S(0)\exp(-bD) \qquad [2.17]$$

where the b-value indicates the sensitivity of the sequence to (diffusion) motion.

An anisotropic (directionally dependent) medium cannot be characterised with a single ADC measurement, which is only sensitive to the diffusion properties in the direction of the diffusion gradient. A full characterisation requires the diffusion tensor **D** (Basser *et al.* 1994). At least seven measurements are required to characterise the tensor (compared with two for the ADC).

Alternatively, the directionality of ADC maps can be circumvented by measuring the trace of the diffusion tensor $\mathbf{Tr(D)} = (D_{11} + D_{22} + D_{33})$, which indicates the mean diffusivity, averaged uniformly over all directions. To measure the trace, it is not necessary to characterise the full tensor. By suitably applying multiple gradients with different directions within the same sequence, the off-diagonal elements of the diffusion tensor can be cancelled (Mori *et al.* 1995). The resulting trace-weighted image can be calculated with just two images.[2]

2.4 IMAGE ACQUISITION

In order to obtain an MR image, there must be spatial encoding of the MR signal. By superimposing onto the main longitudinal magnetic field B_0, a field gradient

[2] Acquiring images in 3 orthogonal directions also allows you to compute the trace without calculating the full tensor

$\vec{G} = (G_x, G_y, G_z)^T = \left(\frac{\partial B_z}{\partial x}, \frac{\partial B_z}{\partial y}, \frac{\partial B_z}{\partial z} \right)^T$, the MR signal from the sample will have a spatially varying frequency according to:

$$\omega(\vec{r}) = \gamma(B_0 + \vec{G} \cdot \vec{r}) \qquad [2.18]$$

where $\vec{r} = (x, y, z)$. The resonant frequency of the spins is now position dependent. For example, frequency analysis of the FID in the presence of a gradient field in the x-direction, $G_x = \frac{\partial B_z}{\partial x}$, shows a distribution of frequencies representing the spin-density profile of the sample along the x-axis (ignoring relaxation effects). By applying field gradients along a range of angles, a number of spin-density profiles can be acquired and the internal distribution of spins within the sample can be deduced by means of the 'back-projection' algorithm. Image reconstruction using back-projection formed the basis of the original MRI methods (Callaghan 1991). There are many drawbacks associated with the back-projection method, including inefficient data sampling and smearing of off-resonance signals. Consequently, most of the modern techniques encode the object co-ordinates by applying the gradient fields along just three perpendicular axes. 2 or 3D image reconstruction is achieved by performing the 2D/3D Fourier transform of the 'reciprocal space', which is defined from the integral of the encoding gradients over their corresponding durations. This reciprocal space is termed *k*-space, and will be described in detail in Section 2.4.2.

2.4.1 SLICE SELECTION

MR images are often acquired in the form of a series of two-dimensional slices. This is achieved by only exciting spins within a specified section of the sample. For example, to select an axial slice, a field gradient is applied in the z-direction, such that the resonant frequency of the spins in the sample is a linear function of the z coordinate:

$$\omega(z) = \gamma(B_0 + G_z \cdot z) \qquad [2.19]$$

A slice of thickness Δz at location z can then be excited by applying a frequency selective RF pulse with a central frequency $\omega(z)$ and bandwidth $\Delta\omega$:

$$\Delta z = \frac{\Delta\omega}{\gamma G_z} \qquad [2.20]$$

The thickness of the slice is therefore determined by the magnitude of the field gradient and the RF pulse bandwidth.[3] The excitation of a slice of spins leaves two spatial dimensions unresolved. 2D spatial encoding is described in the following section using *k*-space and the 2D Fourier Transform.

2.4.2 CONCEPT OF K-SPACE

Ignoring the effects of relaxation, the MR signal from location $\vec{r}$ as a function of time is:

$$S(t) = \int_V \rho(\vec{r}) e^{-i\phi(\vec{r},t)} d^3\vec{r} \qquad [2.21]$$

where $\rho(\vec{r})$ is the spin density, $\phi(\vec{r},t)$ is the phase of spins at location $\vec{r}$, and V is the sample volume. The phase increases according to the spin's resonant frequency:

$$\phi(\vec{r},t) = \int_0^t \omega(\vec{r},t')dt' \qquad [2.22]$$

The spatial dependence of the resonant frequency is governed by the applied field gradients according to Equation [2.18]. The B_0 contribution to the Larmor frequency is much larger than the gradient induced field, and is identical for all spins in the sample. Since only the phase-differences are important for spatial encoding, the B_0 term can be ignored. The relative phase is given by:

[3] It should be noted that the finite duration of the RF pulse and field imperfections result in imperfect slice-profiles.

$$\phi(\vec{r},t) = \gamma\left[\int_0^t \vec{G}(t')dt'\right]\cdot\vec{r} \qquad [2.23]$$

Accordingly, the *k*-space vector is defined as:

$$\vec{k}(t) = \gamma\int_0^t \vec{G}(t')dt' \qquad [2.24]$$

By combining Equations [2.21] to [2.24], the MR signal can be expressed as:

$$S(\vec{k}) = \int_V \rho(\vec{r})e^{-\vec{k}\cdot\vec{r}}d^3\vec{r} \qquad [2.25]$$

Equation [2.25] states that the MR signal $S(\vec{k})$ is the Fourier Transform of the spin density distribution $\rho(\vec{r})$.

Many imaging sequences are based on the 2D Fourier Transform. If a single slice is excited (as described in Section 2.4.1), the MR signal $S(\vec{k})$ becomes:

$$S(\vec{k}) = \Delta z\int_A \rho(\vec{r})e^{-\vec{k}\cdot\vec{r}}d^2\vec{r} \qquad [2.26]$$

where Δz is the slice thickness, *A* is the sample area, and $\vec{r}$ is a two dimensional vector in the image plane. The application of gradients in the *x* and *y* dimensions will change the position within *k*-space, in order to sample all spatial frequencies.

A typical 2D-FT gradient-echo imaging sequence and its corresponding *k*-space sampling scheme are illustrated in Figure 2.5. The simultaneous application of the excitation pulse (labelled α) and a gradient in the *z*-direction (*slice*-direction) G_{slice}, results in the excitation of only a slice of spins. Following the α pulse, G_{slice}, is reversed, which rephases the gradient induced phase-variation across the slice during the application of the RF pulse. This ensures the spins are in-phase across the slice, thereby minimising signal loss. A gradient is then applied along the negative *x*-direction, G_{read}, shifting the position of the *k*-space vector along the k_x-axis, or

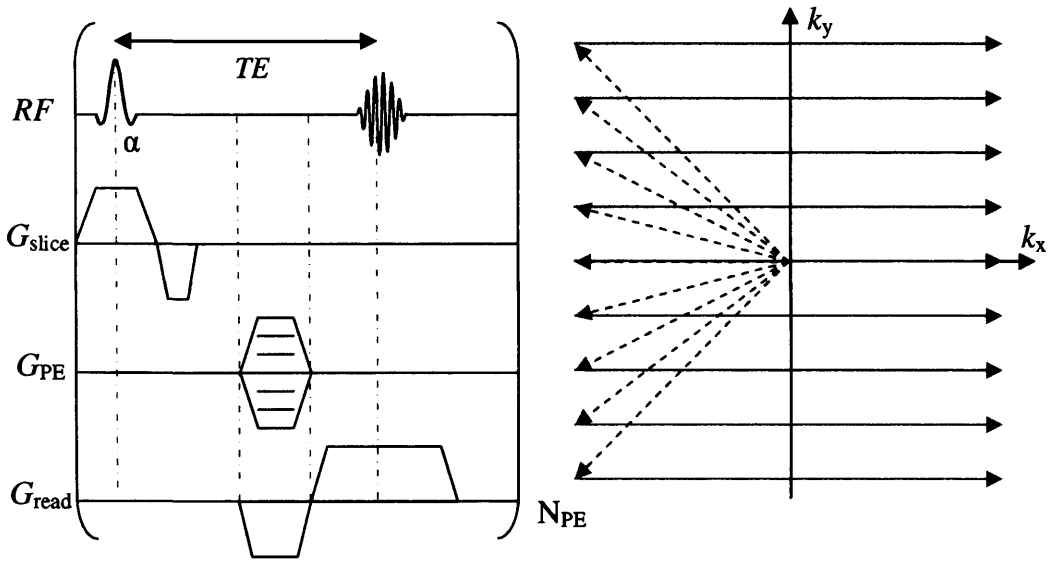

Figure 2.5: A basic gradient-echo (GE) pulse sequence (left) and the corresponding *k*-space trajectory (right). In the left diagram, G_{slice}, G_{PE} and G_{read}, are the gradients applied in the slice, phase-encoding, and read (frequency-encoding) directions respectively. *TE* is the echo time, and N_{PE} is the number of phase-encoding steps. In the right diagram, k_x corresponds the read direction of *k*-space, and k_y corresponds to the phase-encoding direction. One line of *k*-space (solid grey arrow) is acquired per excitation pulse. The dashed grey arrows indicate the effect of the phase-encoding and read-dephase gradients in moving the *k*-space vector along the k_x and k_y axes.

frequency-encoding direction. The positive lobe of G_{read} moves the *k*-space vector to positive k_x passing through the central k_x=0 axis (corresponding to zero phase), where the gradient-echo occurs. One line of *k*-space is sampled in the period following the excitation pulse. The k_y-axis or *phase-encoding* (PE) axis is traversed by applying a gradient in the *y*-direction, G_{PE}. The PE gradient is incremented at each TR in order to sample a new line of *k*-space. Multiple excitation pulses are required to achieve full *k*-space coverage. The sequence is repeated N_{PE} times before Fourier Transformation.

The signal intensity in the image resulting from the Fourier Transform of the *k*-space data depends on the relaxation properties of the sample. For the gradient-echo

sequence illustrated in Figure 2.5, the sampled echo has a peak amplitude along the central line of *k*-space proportional to e^{-TE/T_2^*}.

A spin-echo imaging sequence and corresponding *k*-space trajectory are shown in Figure 2.6. As discussed in Section 2.3.2, the effect of the 180° pulse is to invert the phase of the transverse magnetisation. Since *k*-space has conjugate symmetry, this corresponds to reversing the position in *k*-space: $\vec{k} \rightarrow -\vec{k}$. The sampled echo has a peak amplitude along the central line of *k*-space proportional to e^{-TE/T_2}.

2.4.3 PROPERTIES OF K-SPACE

During an MR imaging experiment, the MR signal will be sampled at discrete time points. The Nyquist criterion states that in order to accurately represent the original signal, the sampling rate must be higher than twice the maximum frequency represented in the sample:

$$\frac{1}{\Delta t} \geq 2\left(\frac{\omega_{max}}{2\pi}\right) \qquad [2.27]$$

where Δt is the time between successive samples. If this sampling criterion is not satisfied, frequencies higher than the sampling rate will be *aliased*, such that their original angular frequency ω will be interpreted as $\omega - \frac{\omega_{max}}{2\pi}$.

When G_{read} and G_{PE} are applied to the sample, the relative frequency of the MR signal from the spins is higher at the edges of the sample where the effect of the gradients is greatest. On one side the frequency is negative with respect to the other, and the centre of the sample has zero frequency off-set. In MRI, differentiation between positive and negative frequency is achieved using quadrature detection

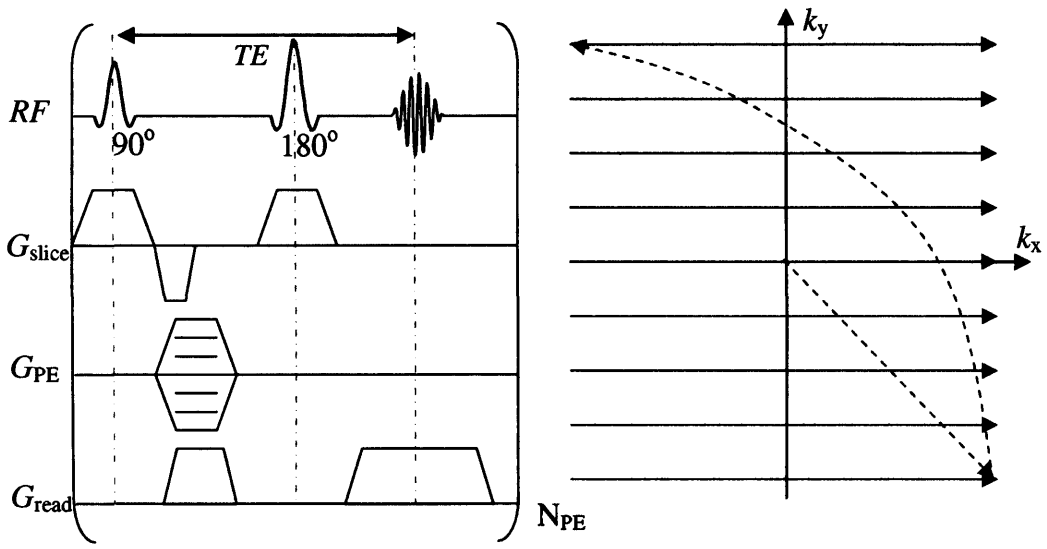

Figure 2.6: Basic spin-echo (SE) sequence (left) and corresponding *k*-space trajectory (right). The labelling is the same as in Figure 2.5. The application of the 180° pulse reverses the position in *k*-space, as indicated by the dashed curved arrow. The dashed lines are only shown for one of the phase-encoding steps.

(Gadian 1995). The Nyquist criterion can be used to determine the *k*-space sampling rate $\frac{1}{\Delta k}$, required to image a particular spatial extent (field of view, FOV). Considering the *x*-dimension, since $\omega_{max} = \gamma G_{read} \cdot x_{max}$ and $\Delta t = \frac{\Delta k_x}{\gamma G_{read}}$, it follows from Equation [2.27] that:

$$FOV = \frac{2\pi}{\Delta k} \qquad [2.28]$$

where the FOV extends $-x_{max}$ to $+x_{max}$, such that the factor of 2 is dropped. If the sample is larger than the FOV, the signal emanating from the outlying regions will be aliased, such that they appear to originate from a region displaced by one FOV.

The extent of the sampled *k*-space, k_{max} determines the maximum spatial frequency that can be correctly represented in the image, and is related to the image resolution:

$$k_{max} = \frac{\pi}{\Delta x} \qquad [2.29]$$

Data acquired in the centre of *k*-space contain information about the low spatial frequency components of the spin density distribution, and therefore give the image its gross contrast. Whereas regions further away from the centre of *k*-space contain information about the higher spatial frequency components, and therefore provide the fine detail and edge information. If the edge of *k*-space is discarded the resulting image will have very low spatial resolution (see Equation [2.29]). If the centre of *k*-space is discarded, the image will primarily contain edge information.

2.4.4 ECHO-PLANAR IMAGING

In the 2D-FT technique described in Section 2.4.2, one line of *k*-space is acquired per excitation and so image acquisition is slow (~2mins). Many applications, including perfusion imaging, require much faster imaging methods. In Echo-Planar-Imaging (EPI), a complete image can be formed from a single excitation pulse in a few tens of milliseconds (Mansfield *et al.* 1977). Figure 2.7 shows a schematic GE-EPI pulse sequence, with 'blipped' phase-encoding gradient, and the corresponding *k*-space trajectory. In order to acquire all of the *k*-space data from a single excitation, during the sampling of a spin- or gradient-echo, the polarity of G_{read} is rapidly switched, and at the reversal of G_{read}, G_{PE} is 'blipped'. The 'effective' echo time TE_{eff}, is defined as the time to the maximum echo amplitude, which coincides with the acquisition along the central line of *k*-space. Providing that the signal is only sampled when G_{read} is constant, a Cartesian grid of sample points in *k*-space is achieved with the 'blipped' G_{PE} scheme. In practice, since such a scheme would incur a large time penalty from the gradient ramp-up time, data are also acquired during the gradient ramps. Consequently, to preserve a Cartesian grid, and hence use the 2D Fourier Transform, the echoes must be sampled non-linearly in time.

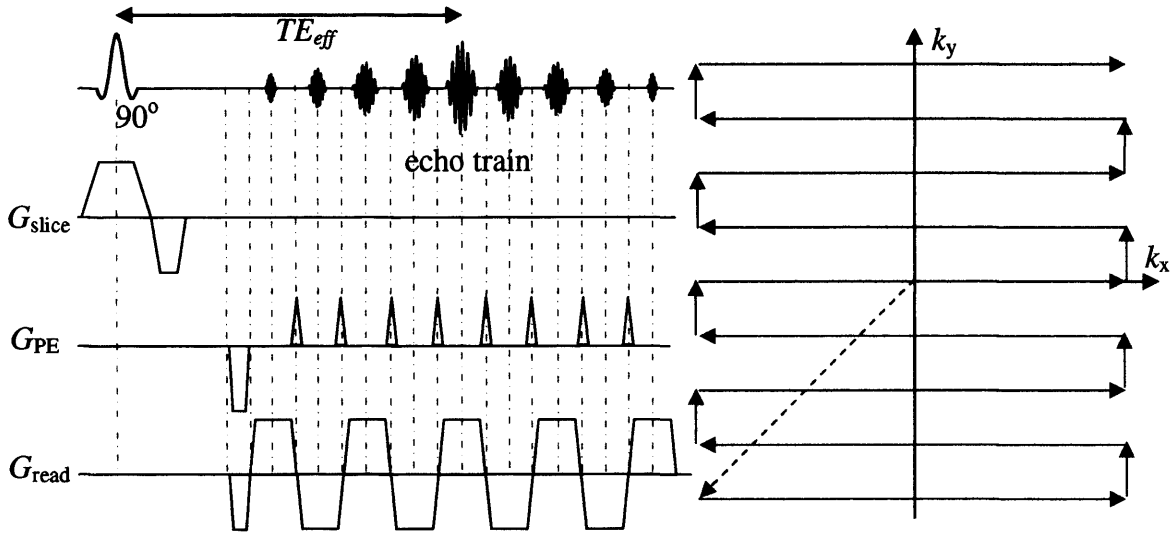

Figure 2.7: Schematic GE-EPI sequence diagram (left) and corresponding *k*-space trajectory (right). The labelling is the same as Figure 2.5. TE_{eff} is the effective echo-time. The whole of *k*-space is acquired following a single excitation pulse. The horizontal solid grey arrows on the *k*-space trajectory change direction at each line according to the polarity G_{read}. The short vertical grey arrows move the *k*-space vector along the phase-encoding direction at each G_{PE} 'blip'.

2.4.4.1 Artefacts in EPI

Despite the obvious advantage of high temporal resolution images, EPI is more prone to artefacts than conventional MRI (Morgan *et al.* 2004; Jezzard *et al.* 1999). Many of the artefacts in EPI are related to the fact that the frequency difference between adjacent voxels (or bandwidth per pixel) in the phase-encoding direction is much smaller than in the frequency-encoding direction. The bandwidth per pixel is inversely proportional to the dwell time (the time between adjacent samples). Along the frequency-encoding axis the dwell time Δt is very short, whereas along the phase-encoding it is approximately $N\Delta t$, where N is the number of samples along the frequency-encoding axis. Consequently, the bandwidth per pixel is much smaller along the phase-encoding direction. Typically, for an EPI *k*-space matrix size of 128×128, there is a $5\,\mu$s dwell time, corresponding to a 12Hz bandwidth per pixel

along the phase-encoding direction. This small bandwidth per pixel is the cause of the image distortion that is common along the phase-encoding direction, due to for example, the frequency offset resulting from field inhomogeneities or chemical shifts. Artefacts along the frequency-encoding direction are insignificant in comparison.

Because of the long dwell time along the phase-encoding direction, the *k*-space data along the phase-encoding direction is also modulated by the T_2^* decay envelope, which for typical sampling schemes attenuates the high frequencies. The image resolution is determined by the point-spread-function (PSF), which determines the smallest resolvable structure, and therefore blurs the ideal representation of an object in the observed image. Ignoring the effects of relaxation, the width of the PSF width is inversely proportional to the finite extent of sampled *k*-space. In EPI there is additional blurring along the phase-encoding direction, because the PSF along the phase-encoding direction is the convolution of the original PSF with the Fourier Transform of the T_2^* envelope (Jesmanowicz *et al.* 1998). Relaxation effects along the frequency-encoding direction can be ignored.

Another common artefact in EPI is the Nyquist ghost image, which is often seen displaced half a FOV from the main image in the phase-encoding direction. In EPI, alternate lines of *k*-space along the frequency-encoding axis are acquired in opposite directions. Inconsistencies between alternate lines introduce an additional frequency component at exactly half the sampling frequency, resulting in the ghost image. Inconsistencies can arise from timing errors in the synchronisation of the RF receiver with the *k*-space trajectory, or delays caused by eddy currents induced by the rapidly switching gradients (Schmithorst *et al.* 2001). Several techniques are available to minimise the Nyquist ghost, e.g.(Chen *et al.* 2004; Grieve *et al.* 2002; Yang *et al.* 1996; Schmithorst *et al.* 2001). Receiver timing errors can be minimised by repeatedly acquiring the central line of *k*-space in opposite directions to estimate the delay, and the effects of eddy-currents can be alleviated using 'gradient pre-emphasis' (Jehenson *et al.* 1990).

It should also be noted that because of the rapid traversal of *k*-space, and consequent high sampling rate, the bandwidth of the receiver must be correspondingly large. Since the SNR scales as $\frac{1}{\sqrt{BW}}$, where BW is the receiver bandwidth, EPI images have a reduced SNR compared with conventional imaging. However, the SNR *per unit time* is much higher than conventional imaging.

2.4.5 PARALLEL IMAGING

The artefacts mentioned in Section 2.4.4.1 are particularly problematic for high-field imaging. In addition, scanning the whole of *k*-space following a single excitation pulse imposes considerable demands on the scanner hardware, for example, high gradient slew-rates and high currents for the gradient amplifier. Parallel imaging is one of the most promising recent advances in scanner technology, which attempts to circumvent hardware limitations and accelerate MRI.

In parallel imaging, fewer phase-encoding steps are necessary for a desired spatial resolution, and image acquisition time can be accelerated compared with standard imaging. A correct image reconstruction is achieve from the sparsely sample phase-encoding direction by using multiple independent receiver coils. The spatial variation of the coils' sensitivity is used in conjunction with gradient-based image-encoding to determine the missing data. The reduction in phase-encoding time can be utilised to either achieve a higher temporal resolution or to increase the spatial resolution. In EPI, the echo train length will be shortened, therefore reducing image distortion and blurring. However, one disadvantage of parallel imaging is a lower SNR. Some of the popular parallel imaging techniques are SMASH (Sodickson *et al.* 1997), SENSE (Pruessmann *et al.* 1999), and GRAPPA (Griswold *et al.* 2002). A review of clinical parallel imaging can be found in (Bammer *et al.* 2004).

3 PERFUSION IMAGING IN STROKE

3.1 INTRODUCTION

The vitality of cerebral tissue depends upon the sufficient delivery of oxygen and nutrients; this is controlled by the microvascular blood flow, or perfusion. When perfusion is significantly reduced, due to for example vascular stenosis or occlusion, the physiology and biochemistry of the brain tissue is altered. The interruption of blood flow to a region of brain, which results in neurological injury, is known as ischaemic stroke. Without prompt diagnosis and appropriate treatment, the tissue damage may be permanent. The size and severity of the ischaemic region depends on collateral flow and the sufficiency of regulatory mechanisms which seek to meet the metabolic needs. This chapter aims to provide an overview of the cerebral haemodynamics and autoregulation in healthy tissue, and in the pathogenesis of cerebrovascular disease.

Haemodynamic and pathological changes can be identified using MR and non-MR imaging methodologies. Some commonly used non-MR imaging techniques are reviewed, and their usefulness in the assessment and management of stroke patients is discussed. In addition, the MR perfusion techniques used in humans are described. Complementary to these MR perfusion measurements, information about the pathophysiological tissue status can be obtained using other MR techniques such as diffusion-weighted (DWI) and blood-oxygenation-level-dependent (BOLD) measurement. The utility of combining these techniques to assess patients with cerebrovascular disease is described, in particular their application in identifying patients likely to benefit from reperfusion treatments.

The sensitivity and specificity of these techniques to identifying tissue that is likely to become irreversible damaged, is dependent on the imaging (delay) time following stroke, and is limited by accuracy of the imaging methods. Understanding the limitations is an important first step towards improving patient outcome in stroke, and is one of the primary objectives of this thesis.

3.2 CEREBRAL HAEMODYNAMICS AND AUTOREGULATION

Cerebral perfusion refers to the rate of flow of blood through the capillaries, where the exchange of oxygen and nutrients between the blood and tissue occurs. Cerebral perfusion, also known as the cerebral blood flow (*CBF*), is determined by the ratio of cerebral perfusion pressure (*CPP*) and cerebrovascular resistance (*CR*) (Powers 1991). *CPP* is the difference in pressure between the forward arterial pressure into the cerebral circulation and backward venous pressure. In healthy vasculature, the venous pressure is small, and the arterial pressure is constant. In this situation, the *CBF* is primarily determined by the *CR*, which is itself controlled by the diameter of the small arteries (vasodilation and contraction). The volume occupied by the small capillaries indicates the microvascular blood volume, or cerebral blood volume (*CBV*). *CBV* is therefore determined by the capillary density within a voxel and the diameter of these capillaries. For a given capillary density, an increase in *CBV* (vasodilation) causes a decrease in *CR*. Both *CBV* and *CBF* will increase as vessels dilate and both decrease as vessels contract, such that the ratio *CBV/CBF* remains relatively constant. This ratio, known as the mean transit time (*MTT*), represents the average time taken for the blood to flow from the arterial input to the venous output of the tissue capillary bed. A larger *MTT* corresponds to slower cerebral circulation. Under normal physiological conditions, changes in *CPP* have little effect on *CBF* due to the autoregulatory mechanisms of vasodilation (in response to a decrease in *CPP*) and contraction (in response to an increase in *CPP*), which ensure the adequate delivery of metabolites to the functioning neurons.

3.3 PERFUSION IN CEREBROVASCULAR DISEASE

CPP is reduced in cerebrovascular diseases due to impediment of arterial flow. Autoregulatory vasodilation (increasing *CBV* and reducing *CR*) in response to reductions in *CPP* endeavours to maintain *CBF*. However, this autoregulatory vasodilation impairs the ability of the blood vessels to react to other vasoactive

stimuli. When the capacity for vasodilation is exceeded, autoregulation fails and any further reduction in *CPP* will result in a decrease in *CBF*, and consequently an increase in *MTT* (a slower cerebral circulation).

When the oxygen supply to the tissue is reduced because of a decreasing *CBF*, the brain responds by becoming more efficient in extracting oxygen from the limited blood flow. An increased Oxygen Extraction Fraction (*OEF*) helps to maintain cerebral oxygen metabolism ($CMRO_2$). Hudetz *et al.* (Hudetz *et al.* 1996) demonstrated that a graded decrease in *CPP* causes progressive loss of the high flow components of the blood flow. A slower and more homogeneous flow distribution was shown to improve the effectiveness of oxygen transport (increased *OEF*). The haemodynamic parameter of flow heterogeneity (*FH*) indicates the heterogeneity (or conversely the homogeneity) of the velocity distribution in the tissue element. A decreased *FH* therefore appears to assist in maintaining sufficient gradients to drive the diffusion of oxygen and nutrients from the blood to the cells (Kuschinsky *et al.* 1992).

This phase of ischaemia, where *CBF* is low, *OEF* is raised, and $CMRO_2$ is normal, is termed oligemia, and is clinically silent. However, if *CPP* continues to fall, the reduction in *CBF* will eventually be too great to be compensated by the *OEF*, and so insufficient oxygen and nutrients are exchanged with the brain tissue to drive normal neuronal function. As a result $CMRO_2$ will fall. This phase, when *CBF* is very low, *OEF* has reached a plateau, and $CMRO_2$ has fallen, is termed cerebral ischaemia. If the circulation is not rapidly restored, permanent tissue damage will occur. Once tissue damage has occurred, the normal autoregulatory mechanisms may no longer work even if the *CPP* returns to normal. When the impairment of neuronal function becomes irreversible the tissue is infarct, and any relationship between *CBF*, *CBV* and *OEF* is lost.

In summary, regional haemodynamics in cerebrovascular disease can be separated into five stages: (1) (Normal) *CPP* is normal, *FH*, *CBF*, *MTT*, *OEF* and $CMRO_2$ are also normal, (2) (Autoregulation) *CPP* is reduced and so *FH* decreases. Vessels

dilate causing *CBV* and *MTT* to increase, but *CBF*, *OEF* and $CMRO_2$ remain normal. (Recent work has suggested that *CBF* may actually decrease slightly in this stage (Dohmen *et al.* 2007)) (3) (Oligemia) *CPP* is reduced further and the compensatory vasodilation capacity is exceeded: *CBF* begins to fall; *MTT* continues to increase. *OEF* starts to increase, maintaining normal $CMRO_2$. (4) (Ischaemia) *CPP* is decreased still further, and since the capacity for vasodilation has already been exceeded, the continual fall in *CPP* causes *MTT* increases further and *CBF* to fall further. Consequently, the compensatory mechanism of increased *OEF* is exhausted and $CMRO_2$ begins to fall. (5) (Infarction) The relationship between the haemodynamic and metabolic parameters is lost. Figure 3.1 shows schematic graphs representing the dynamic change of the various haemodynamic and metabolic parameters in cerebrovascular disease.

With the aim of identifying suitable patients for treatment, there is much current research into the accurate identification of ischaemic tissue at risk of infarction e.g. (Wu *et al.* 2001; Wu *et al.* 2007; Shen *et al.* 2004; Shen *et al.* 2005; Sorensen *et al.* 1996; Rose *et al.* 2001) (see Section 3.12). Such tissue is marked by prolonged *MTT*, reduced *CBF*, and decreased *FH*. An accurate quantification of these haemodynamic parameters is the first stage towards a more accurate diagnosis and prognosis in cerebrovascular diseases. For this reason, numerous neuroimaging techniques have been developed and applied to evaluate brain haemodynamics. A selection of these techniques is summarised the proceeding sections.

3.4 MEASURING PERFUSION USING NON MR TECHNIQUES

Amongst the techniques in clinical use for the evaluation of brain haemodynamics are Positron Emission Tomography (PET), Single Photon Emission Computer Tomography (SPECT), Xenon-enhanced Computer Tomography (XeCT), and dynamic Computer Tomography (dynamic CT). All these techniques give similar

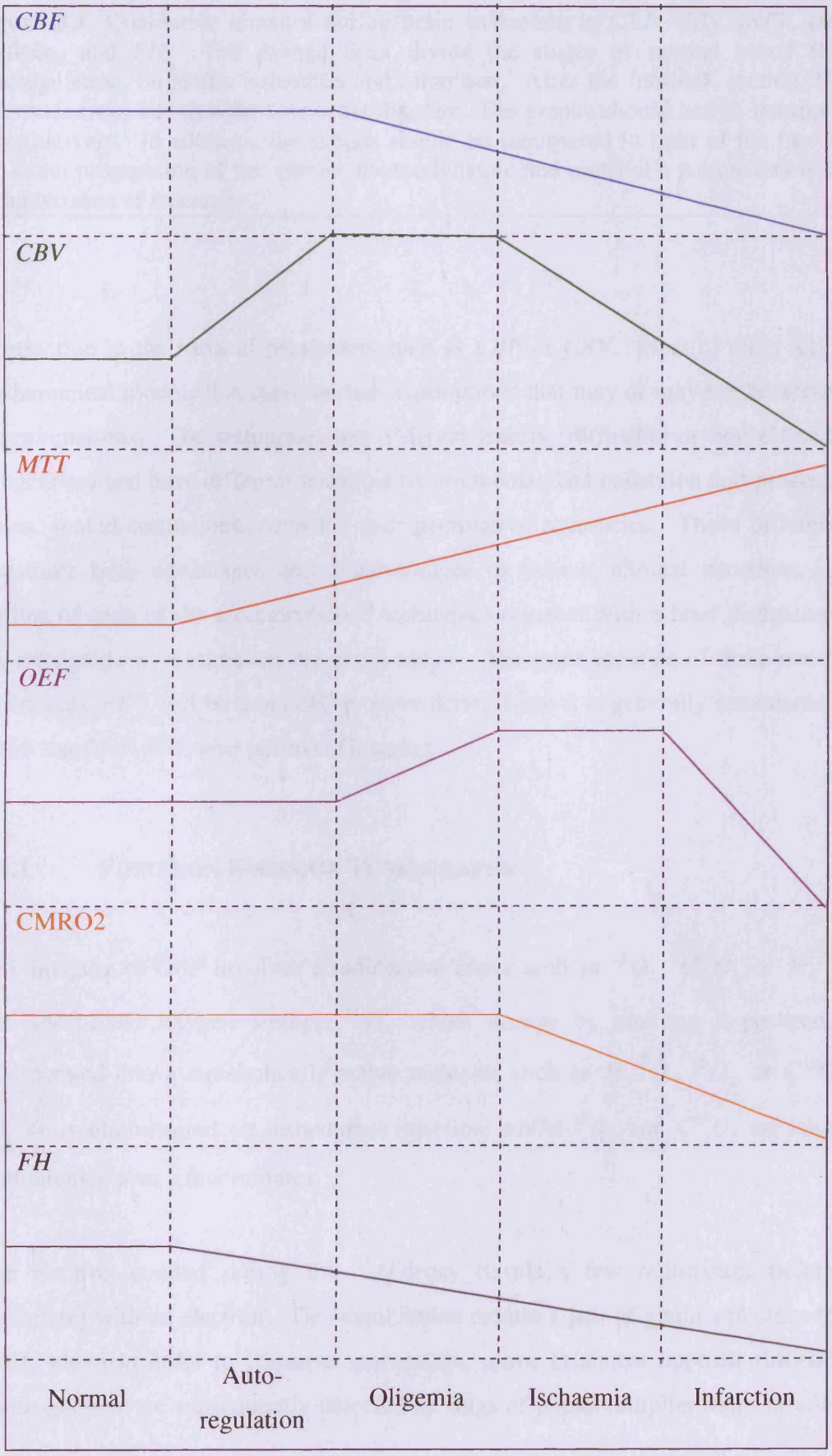
CBF
CBV
MTT
OEF
CMRO2
FH
Normal
Auto-regulation
Oligemia
Ischaemia
Infarction

Figure 3.1: Qualitative changes during brain ischaemia in *CBF*, *CBV*, *MTT*, *OEF*, $CMRO_2$, and *FH*. The dashed lines divide the stages of normal blood flow, autoregulation, oligemia, ischaemia and infarction. After the 'normal' section, *CPP* decreases from left to right across the diagram. The graphs should not be interpreted quantitatively. In addition, the graphs should be interpreted in light of the fact that the exact progression of the various haemodynamic and metabolic parameters is still an active area of research.

information in the form of parameters such as *CBF* or *CBV*. Most of them rely on mathematical models that make certain assumptions that may or may not be accurate approximations. The techniques use different tracers (diffusible or non diffusible, exogenous) and have different technical requirements, data collection and processing times, spatial resolutions, coverage and quantitative accuracies. These differences constitute both advantages and disadvantages in various clinical situations. An outline of each of the aforementioned techniques together with a brief discussion of the strengths and weaknesses are given below. The most accurate of these non-MR techniques, PET will be described in more detail, since it is generally considered the 'gold-standard' of *in vivo* perfusion imaging.

3.4.1 POSITRON EMISSION TOMOGRAPHY

PET imaging of *CBF* involves a radioactive tracer such as $^{15}O_2$, $C^{15}O_2$ or $H_2{}^{15}O$. The short-lived oxygen isotope ^{15}O, which decays by emitting a positron, is incorporated into a metabolically active molecule such as $H_2{}^{15}O$, $^{15}O_2$ or $C^{15}O_2$. $H_2{}^{15}O$ is administered via intravenous injection, whilst $^{15}O_2$ and $C^{15}O_2$ are inhaled continuously over a few minutes.

The positron emitted during the ^{15}O decay travels a few millimetres before it annihilates with an electron. This annihilation creates a pair of gamma photons (511 keV), which in order to conserve momentum, move in almost opposite directions. These photons are subsequently detected by rings of photomultiplier tubes or silicon

avalanche photodiodes (Si APD) in the PET scanner. The technique depends on the coincident detection of a pair of photons; photons that do not arrive in pairs (to within a few nanoseconds) are ignored. The position at which the annihilation event originated can be estimated by measuring the time of flight of the two photons. Using statistics collected from tens-of-thousands of coincidence events, a set of simultaneous equations for the total activity of each voxel as a function of time along many line paths can be solved, indicating the amount of isotope present.

For the intravenously injected $H_2{}^{15}O$, an arterial blood sample is measured to serve as an input function, and combined with a series of consecutive images taken at short time intervals (~1 second), to give quantitative *CBF* (Herscovitch *et al.* 1983). For the inhaled isotope ($^{15}O_2$ and $C^{15}O_2$), the image is acquired after a steady-state is reached in the blood, to give quantitative *CBV* (Martin *et al.* 1987) . In addition the *OEF* can be estimated from the ratio of the local cerebral radioactivity obtained from an $^{15}O_2$ inhalation experiment to that obtained in the same region from $H_2{}^{15}O$ administered intravenously (Hatazawa *et al.* 1995). And the product of *CBF*, *OEF* and arterial $^{15}O_2$ provides an estimate of the cerebral metabolic rate of oxygen, $CMRO_2$ (Herscovitch 1989). Thus PET imaging can produce maps estimating the *CBF*, *CBV*, *OEF* and $CMRO_2$ values.

The strength of the PET technique is its quantitative accuracy (Herscovitch *et al.* 1983; Raichle *et al.* 1983) In fact, the current *in vivo* "gold standard" for the quantitative evaluation of *CBF* is $H_2{}^{15}O$ PET. It is mainly used clinically in chronic cerebrovascular disorders to try and identify the autoregularity phase of ischaemia where elevated *OEF* values (combined with normal *CBF*, see Figure 3.1) are thought to indicate higher risk of future infarction (Young *et al.* 1996). The short half-life of the radioactive tracers makes repeated measurements possible, although repeated exposure to these small doses of radiation is not desirable. The radiation risk is just one of many substantial disadvantages in the PET methodology, including the need for an arterial catheter to measure the arterial tracer concentration, and the limited

availability of PET centres with a cyclotron to create the isotopes. In addition, the spatial resolution of PET is poor.

3.4.2 SINGLE PHOTON EMISSION COMPUTER TOMOGRAPHY

SPECT (Warwick 2004) is a technique similar to PET. However, in SPECT the radioactive substances used (often $^{99m}Tc-HMPAO$) have longer decay times than those used in PET, and emit lower energy single photons, rather than double gamma rays. As a result, SPECT images have lower sensitivity and are less detailed than PET images. Unlike PET, SPECT measurements are approximate and relative measurements of perfusion. However, SPECT is less expensive and more accessible than PET since the tracer is not formed in a proton accelerator. In addition, since the tracer is retained in the tissue, it can be administered at the bedside and the imaging can be performed later. This makes it a particularly useful technique for studying perfusion during an epileptic seizure.

3.4.3 XENON-ENHANCED COMPUTER TOMOGRAPHY

In XeCT, nonradioactive Xe is inhaled and rapidly dissolves in blood, freely crossing the BBB, and entering the brain. The Xe attenuates the x-rays providing additional contrast enhancement in regions where the Xe has accumulated. CT images are acquired at successive intervals and before and during the Xe inhalation: the time-course concentration of Xe in the blood (arterial input) and brain and the blood-brain partition coefficient for Xe are used to calculate the *CBF* (Drayer *et al.* 1978). The technique gives accurate quantitative results, but as with PET, one of the main sources of error in XeCT is the measurement of the arterial concentration. Because of the long acquisition time (~10mins) XeCT is prone to motion artefacts. Additionally, because of the radiation risk, XeCT is not recommended for children.

3.4.4 DYNAMIC PERFUSION COMPUTER TOMOGRAPHY

Dynamic CT involves the intravenous injection of a non-diffusible tracer of iodinated material that attenuates the x-rays, and therefore provides additional contrast as the tracer passes through the capillary bed. Typically images are acquired at a rate of one per second. Deconvolution analysis similar to that used in bolus tracking MRI (see Section 3.5.1) can lead to quantitative perfusion measurements. While the wide availability of CT scanners makes this a popular technique in a clinical setting, dynamic CT has limited spatial coverage, tends to over estimate *CBF* in voxels including large vessels, and radiation exposure makes it non-ideal for repeated scans (Wintermark *et al.* 2004).

3.5 MEASURING PERFUSION USING MRI

Perfusion changes can be identified non-invasively in MRI using either an exogenous or endogenous tracer. The first technique called bolus-tracking or dynamic susceptibly contrast MRI (DSC-MRI) requires the intravenous injection of a contrast agent (Section 3.5.1). The second technique called Arterial Spin Labelling (ASL) uses RF pulses to magnetically label the moving protons (Section 3.5.2). There are several advantages over other techniques in using MRI to assess cerebral haemodynamics. Importantly, it can be combined with fine anatomical MRI to resolve structure, diffusion MRI to measure the molecular mobility of water in the tissue (see Section 2.3.6 and Section 3.7), blood oxygenation measurements (via BOLD imaging, Section 2.3.3 and Section 3.8), magnetic resonance angiography (MRA) to inspect the integrity of the cerebral arteries (Zhang *et al.* 2007), and magnetic resonance spectroscopy (MRS) to investigate chemical changes within the brain (Baird *et al.* 1998). Thus it is possible to provide a very comprehensive set of information in a single examination. Combining this information into predictive algorithms is an active area of research that seeks to foretell the fate of

haemodynamically-compromised tissue (Section 3.12), and so assist the diagnosis, prognosis, and possible treatment plan.

3.5.1 BOLUS-TRACKING MRI

This thesis solely is concerned with the accurate measurement and interpretation of perfusion values obtained using bolus-tracking or DSC-MRI data, the most common clinical MR perfusion technique. This technique, together with its limitations and application in cerebrovascular diseases is described in detail in Chapter 4. In summary, DSC-MRI relies on the measurement of T2/T2* changes during the first pass of an intravascular paramagnetic tracer through the capillary bed (Østergaard *et al.* 1996b; Østergaard *et al.* 1996a). The technique requires a fast imaging technique in order to acquire images at adequate temporal resolution (~1-2s) to characterise the concentration time-course of the first-pass of the tracer both in the tissue and a feeding artery. Similar to dynamic CT, the quantification of *CBF* requires the deconvolution of the tissue and arterial curves. Unlike dynamic CT, the relationship between the signal intensity and tracer concentration is not linear. The whole brain can however be covered and there is good spatial resolution (typically ~1.5x1.5x4mm). In addition, because there is no ionising radiation involved, the examinations can be repeated periodically without further risk to the patient, thus enabling the evolution of haemodynamically compromised tissue to be studied (i.e. acute, subacute, and chronic phases). However, in order to avoid residual effects of a previous injection of paramagnetic tracer on the tissue relaxation rate, it is necessary to leave an interval of several hours between injections. In a study involving two time-separated injections, a discernable difference in the concentration time-course was observed with a two hour interval, but not a four hour interval (Levin *et al.* 1995). Such residual effects can be minimised using a smaller pre-dose of tracer, which appears to stabilised subsequent measurements (Levin *et al.* 1995).

3.5.2 ARTERIAL SPIN LABELLING

An alternative perfusion MRI technique to DSC-MRI is Arterial Spin Labelling (ASL), where perfusion is measured by monitoring the flow of magnetically labelled water through the tissue. Since this technique is less robust than DSC-MRI, it has not entered widespread clinical use, although its utility has been demonstrated for a variety of acute and chronic cerebrovascular diseases (Detre *et al.* 1999), as well as in tumours (Weber *et al.* 2004), dementia and Alzheimer's (Du *et al.* 2006) and brain activation (Wong *et al.* 1997). The design and development of accurate, robust and sensitive ASL techniques is an active area of research and numerous ways to do ASL have been described e.g. (Calamante *et al.* 1999b; Golay *et al.* 2004). In view of the fact that ASL is a major competitor to the DSC-MRI perfusion methodology used in this thesis, the underlying principles, assumptions, and limitations of ASL are summarised in this section.

ASL techniques do not require a contrast agent; rather they use endogenous water as a tracer. The perfusion measurements are based on the fact that the magnetisation and relaxation characteristics of the tissue-water protons are affected by the magnetisation of the inflowing blood-water protons in the capillaries. In general, *CBF* is quantified by acquiring two images: one in which the blood-water protons flowing into the capillary bed have been magnetically labelled using an RF pulse (termed the labelled image) and one in which the blood-water protons flowing into the capillary bed have the same magnetic state as the tissue (termed the control image). Subtraction of these two images results in an image intensity proportional to the blood flow.

Quantitative measurements of perfusion are obtained by modelling how the relaxation rates of the tissue-water protons are affected by the inflow of magnetically labelled blood-water protons.

Neglecting the effects of flow, the longitudinal relaxation in the tissue is described by the Bloch equation (see Section 2.2.4).

$$\frac{dM_z(t)}{dt} = \frac{M_z{}^0 - M_z(t)}{T_1} \qquad [3.1]$$

where $M_z(t)$ is the longitudinal magnetisation per gram of brain tissue water at time t, $M_z{}^0$ is the fully relaxed value of $M_z(t)$ and T_1 is the longitudinal relaxation time. Equation [3.1] can be modified to include the effects of blood flow f (ml/g/s), to account for the gain in magnetisation caused by the inflowing (arterial) blood-water protons $fM_a(t)$, and the loss of magnetisation due to the outflowing (venous) blood-water protons $fM_v(t)$.

$$\frac{dM_z(t)}{dt} = \frac{M_z{}^0 - M_z(t)}{T_1} + fM_a(t) - fM_v(t) \qquad [3.2]$$

Assuming the longitudinal magnetisation of the venous blood can be related to the longitudinal magnetisation of the tissue water $M_t(t)$ via the blood brain partition coefficient λ, i.e., $M_v(t) = \frac{M_t(t)}{\lambda}$, Equation [3.2] can be written (Herscovitch *et al.* 1985):

$$\frac{dM_t(t)}{dt} = \frac{M_t{}^0 - M_t(t)}{T_1} + f\left(M_a(t) - \frac{M_t(t)}{\lambda}\right) \qquad [3.3]$$

The magnetisation of the inflowing arterial blood $M_a(t)$ modifies the apparent relaxation and magnetisation of the tissue water $M_t(t)$. If $M_a(t)$ is known, Equation [3.3] can be solved for the blood flow, f.

3.5.2.1 Continuous Arterial Spin Labelling

The original ASL technique (Williams *et al.* 1992; Detre *et al.* 1992), known as CASL (Continuous Arterial Spin Labelling), involves the continuous inversion of the blood-water protons for a period of several seconds as they flow into the brain. In

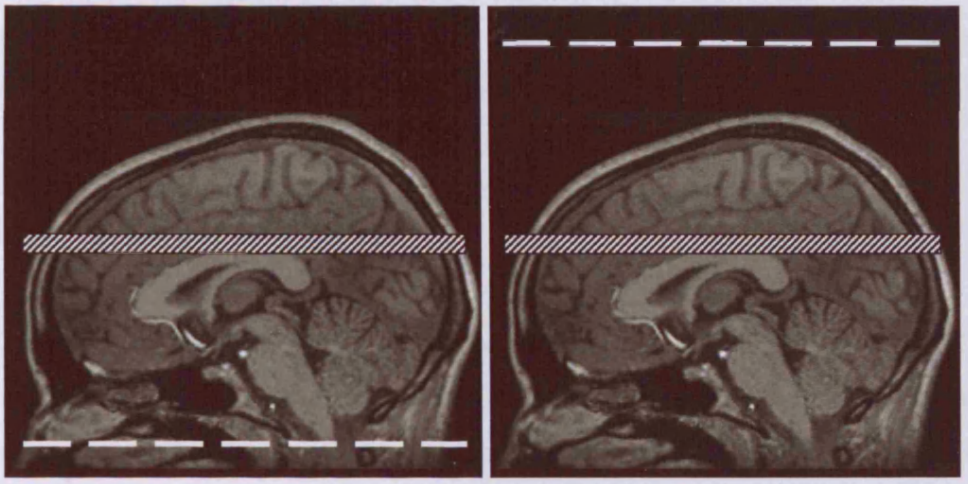

Figure 3.2: Schematic diagram illustrating the pairs of images acquired in a simple CASL experiment. The axial imaging slices are indicated by the diagonally striped regions. The dashed lines indicate the plane of inversion for arterial spins by the adiabatic fast passage RF pulses (see Section 3.5.2.1.1). The left hand image is the label and the right hand image the control.

this way, a flow dependent steady-state tissue magnetisation evolves. Figure 3.2 illustrates the continuous labelling method, where in the labelled image the arterial spins are inverted as they flow through a plane (dashed line). In the steady-state, $\frac{dM_t(t)}{dt}$ given in Equation [3.3] is equal to zero. Solving this equation for both images, leads to an equation for cerebral blood flow (Williams *et al.* 1992):

$$f = \frac{\lambda}{T_{1app}} \frac{M^{cont}{}_t - M^{label}{}_t}{2\alpha M^{cont}{}_t} \qquad [3.4]$$

f is dependent on the steady-state magnetisations of the labelled $M^{label}{}_t(t)$ and control image $M^{cont}{}_t(t)$, the spin inversion efficiency α (see Section 3.5.2.1.1), and the *apparent* longitudinal relaxation time T_{1app} of the brain tissue. This *apparent* relaxation rate determines how the longitudinal relaxation time of the tissue-water protons is affected by the inflowing labelled blood-water protons:

$$\frac{1}{T_{1app}} = \frac{1}{T_1} + \frac{f}{\lambda} \qquad [3.5]$$

T_{1app} can therefore be related to perfusion, f.

3.5.2.1.1. Adiabatic Fast Passage

In CASL, spin inversion is achieved using adiabatic fast passage (AFP) radiofrequency (RF) pulses (Abragam 1968). The AFP technique produces a rotation of the macroscopic vector. This rotation can be achieved either by sweeping the frequency of the 'inverting' RF pulse through the resonance frequency or by changing the strength of the local magnetic field (such that the resonant frequency is changed). I.e. rotation of the macroscopic magnetisation vector results from sweeping the relative frequency (with respect to the Larmor frequency) of RF pulse from positive to negative, such that the effective field experienced by the blood-water protons changes being parallel to the main field (when the RF pulse is far off-resonance) to being perpendicular (when the RF is on-resonance in the inversion plane) to being anti-parallel (when the RF is far off-resonance). In CASL, the RF pulse is applied off-resonance (to the imaging slice) in the presence of a magnetic field gradient in the direction of blood flow. As the blood water spins flow up the artery and into the brain, the effective magnetic field they experience sweeps from being parallel to the main field to antiparallel. As long as the sweep is slow enough for the spins to keep precessing around the effective field, they will switch from fully relaxed to become fully inverted. Furthermore, the duration of the inversion process should be short compared with the longitudinal and transverse relaxation times of the arterial blood water spins. This process is illustrated in Figure 3.3. The adiabatic condition to be satisfied for inversion to occur is:

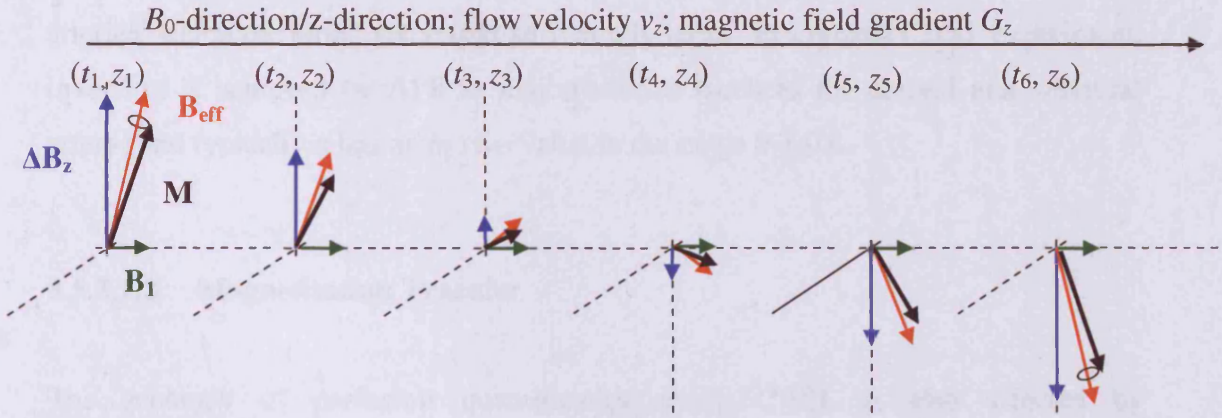

Figure 3.3: Schematic illustration of adiabatic inversion in CASL. The six axes labelled (t_i, z_i) show the macroscopic magnetisation vector $\vec{M}$ (black arrow) precessing with the effective magnetic field vector $\vec{B}_{eff}$ (red arrow) in the rotating frame (x',y',z) rotating with angular frequency $\omega(z_i) = \gamma(B_0 + G_z \cdot z_i)$. From left to right the diagrams represent adjacent points i, along the artery in the direction of blood flow v_z. $\Delta\vec{B}_z$ (blue arrow) is the magnetic field $G_z \cdot z$ that is generated by the applied field gradient G_z in the direction of flow, z. This field difference sweeps from positive to negative through the inversion plane and along the artery in the direction of flow. $\vec{B}_1$ (green arrow) is the low-power continuous RF field that is applied perpendicular to the main field. $\vec{B}_{eff}$ is the vector sum of $\Delta\vec{B}_z$ and $\vec{B}_1$. Provided the adiabatic condition is satisfied, $\vec{M}$ will follow $\vec{B}_{eff}$ and adiabatic inversion will occur.

$$\frac{1}{T_{1a}}, \frac{1}{T_{2a}} << \left(\frac{1}{B_1}\right)\vec{G}\cdot\vec{v} << \gamma B_1 \qquad [3.6]$$

where T_{1a} and T_{2a} are the longitudinal and transverse relaxation times of the arterial blood water, B_1 is the amplitude of the RF pulse, $\vec{G}$ is the magnetic field gradient, $\vec{v}$ is the velocity of the blood (in the direction of the gradient) and γ the gyromagnetic ratio of the proton. When a range of arterial blood velocities is present, this condition may not be completely satisfied and consequently there is imperfect inversion. The inversion coefficient α in Equation [3.4] is defined as 1 for perfect inversion and 0 for

no inversion. The condition in Equation [3.6] is most likely satisfied in the major arteries, where the blood velocity is sufficiently large. In a typical CASL experiment, inversion is achieved by AFP in major arteries (such as the carotid and vertebral artery) and typically α has an *in vivo* value in the range 0.7-0.8.

3.5.2.1.2. Magnetisation Transfer

The accuracy of perfusion quantification using CASL is also affected by magnetisation transfer (MT) effects caused by the off-resonance (with respect to the imaging slice) RF pulse used for the AFP. This RF can affect the magnetisation of tissue-water protons bound to macromolecules within the imaging slice (Wolff *et al.* 1989). The resonance peak of the water protons bound to the macromolecules is very wide (see Figure 3.4). Magnetisation transfer between the free and bound tissue-water protons causes the MRI signal to decrease. In order to circumvent this effect, the control image must also include an off-resonance pulse combined with a magnetic field gradient of reverse polarity: the plane of inversion is above rather than below the imaging slice so that the RF does not affect the inflowing arterial water blood spins (see Figure 3.2). In this way the MT effects are cancelled out in the subtraction of the control image from the labelled image.

3.5.2.1.3. Transit Time

One of the main problems with CASL is related to the presence of the long arterial delays for the arterial blood travelling from the labelling plane to the imaging slice, such as those related to collateral flows to stroke regions. During the time taken for the blood to flow from the point where it was inverted to the capillary bed in the imaging slice, relaxation of the spins causes the effective inversion efficiency α to decrease. This effect is accounted for by incorporating a transit time into the Bloch equation analysis (Zhang *et al.* 1992). However, in general there is a range of transit times due to the different vascular paths of the blood-water protons to the slice.

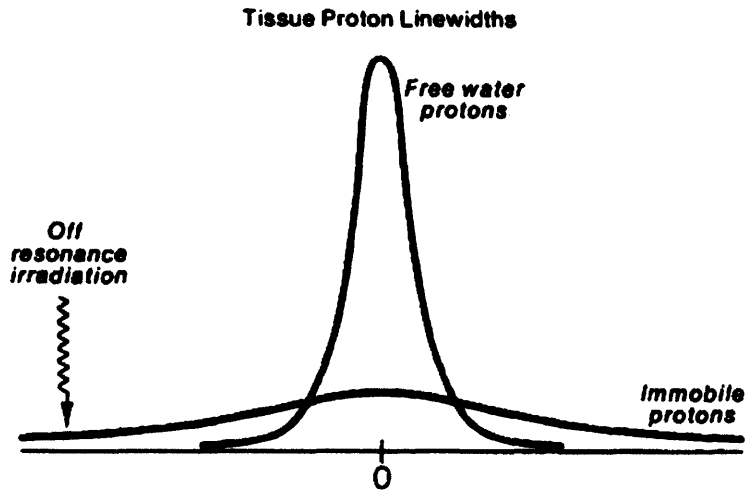

Figure 3.4: Schematic frequency spectrum illustrating the frequency response of the two different pools of protons (free water and bound (immobile) water). The immobile protons are saturated by an off-resonance pulse (respresented by the zig-zag arrow on the left) whereas the free water protons are largely unaffected. In CASL, the RF pulse applied in the inversion plane is off-resonance in the imaging slice, affecting the bound, but not the free water protons. The magnetisation of the free water protons is indirectly affected by magnetisation transfer between the two pools.

Therefore any global correction will not be accurate. Transit time insensitive approaches e.g. (Alsop *et al.* 1996) utilise a delay between the end of the labelling period and the image acquisition, which must be longer than the longest transit time present. This approach is shown to give perfusion estimates that are insensitive to transit time, on the assumption that the T_1 values of blood- and tissue-water protons are approximately the same. Although the transit time insensitivity results in better perfusion maps, the extra delay time reduces the SNR.

3.5.2.1.4. Vascular Artefacts

The tissue magnetisation M_t used in the perfusion quantifying equation, Equation [3.4], may be contaminated by blood signal from larger vessels. If the labelled blood in the vessels does not actually perfuse into the tissue in that voxel, but is just passing through *en route* to perfuse some more distant tissue, then its contribution to the

signal difference between the labelled and control images will introduce an error in the perfusion measurement. Vascular signal contamination can be eliminated by inserting a delay between the end of the labelling period and the image acquisition (as described above, (Alsop *et al.* 1996)). This allows time for the fast moving blood to flow through the slice before the image is acquired. However, a residual vascular artefact may still be present in regions fed by collateral flow, which have longer transit times. As the post-labelling delay in CASL imaging is increased, the vascular contamination and transit time sensitivity are reduced, resulting in more accurate perfusion maps. However, SNR is sacrificed. Alternatively, bipolar crusher gradients can be used to eliminate the signal from the large feeding arteries in a CASL experiment (Ye *et al.* 1997).

3.5.2.1.5. Multislice Imaging

Since it is necessary to balance the MT effects in the labelled and control CASL images, multiple slices cannot be acquire for a single control slice; a separate control image is required for each labelled image. Multi-slice CASL may be achieved if spin inversion is performed using a small surface coil placed on the neck. In this situation, the MT effects do not occur since the B_1 fields from a small coil have small extent and do not reach the imaging slice (Silva *et al.* 1995). Alternatively, a *control* (amplitude-modulated double-inversion) RF pulse designed to give MT effects equivalent to the *inversion* RF pulse (Alsop *et al.* 1998), could be used at the same location as the labelling plane.

3.5.2.2 Pulsed Arterial Spin Labelling

PASL (Pulse Arterial Spin Labelling) is an alternative ASL technique, where a relatively short RF pulse lasting 10-20ms is used to invert the arterial blood-water protons just before they enter the imaging slice. Since this inversion process does not rely on the blood velocity, it can take place in a region adjacent to the imaging slice.

A time TI (cf. Inversion-Recovery sequence in Section 2.3.4) is allowed for the blood to inflow from the inversion region into the slice, after which the labelled image is acquired. A control image of the slice is also acquired with no spin inversion. The subtraction of these two images results in an image whose signal intensity is proportional to the blood flow. Through using shorter RF pulses, PASL has considerably reduced power deposition compared with CASL.

3.5.2.2.1. PASL Techniques

The two main PASL techniques are EPISTAR (Echo-planar imaging and signal targeting with alternating radiofrequency) (Edelman *et al.* 1994) and FAIR (Flow-sensitive alternating inversion recovery) (Kwong *et al.* 1995) . Since the introduction of these techniques, many other methods have been proposed based on the concept of PASL. For example, UNFAIR (Helpern *et al.* 1997), STAR-HASTE (Chen *et al.* 1997), TILT (Golay *et al.* 1999), SMART (Kao *et al.* 1998), and FAIRER (Zhou *et al.* 1998). Since all of these methods are based on variations of EPISTAR and FAIR, only these will be discussed here. Details of the other methods can be found in the references given above.

Figure 3.5 illustrated an EPISTAR experiment. The imaging slice is first saturated to reduce unwanted signal from the static tissue water. A slab proximal to this slice is inverted and a time TI is allowed for the inverted blood to inflow before the labelled image is acquired. Equivalent MT effects must be present in the control image. This is achieved either by applying an equivalent inversion slab that is distal to the imaging slice or by applying a double inversion pulse in the same 'inversion' slab. The difference between the labelled and control image magnetisation is (Kwong *et al.* 1995):

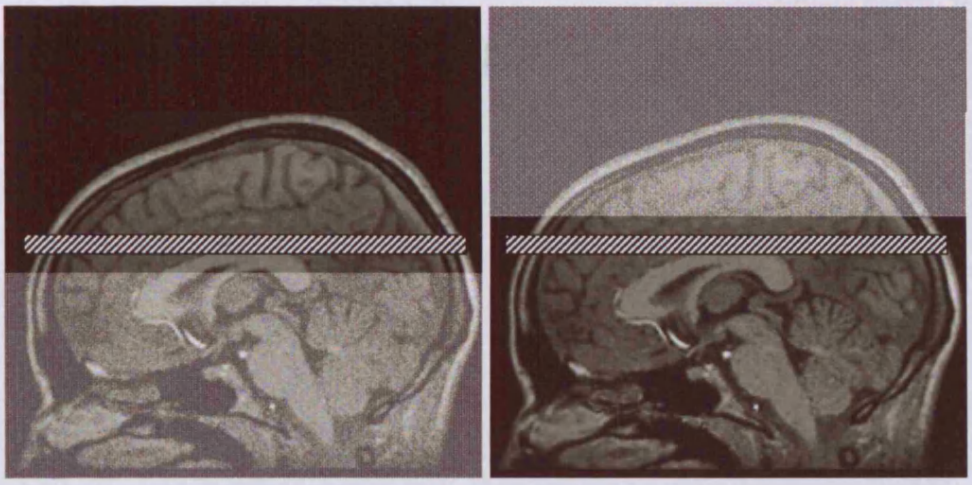

Figure 3.5: Schematic diagram illustrating the pairs of images acquired in a simple EPISTAR experiment. The axial imaging slices are indicated by the diagonally striped regions. The shaded areas indicate the regions with inverted magnetisation. The left hand image is the label and the right hand image the control. In each case the image is acquired at time TI after the inversion pulse.

$$\Delta M = 2\alpha M_t^{\,0} \frac{f}{\lambda} \left(\frac{\exp\left(\frac{TI}{T_{1app}}\right) - \exp\left(\frac{TI}{T_{1a}}\right)}{\frac{1}{T_{1a}} - \frac{1}{T_{1app}}} \right) \qquad [3.7]$$

If T_1 is assumed to be the same for blood and tissue, and if α=1 and f/λ<<1, then

$$\Delta M = 2\alpha M_t^{\,0} TI \frac{f}{\lambda} \exp\left(-\frac{TI}{T_1}\right) \qquad [3.8]$$

Although Equation [3.8] is often used to calculate PASL blood flow, the T_1 in blood and tissue may be significantly different, and this can be a significant source of error.

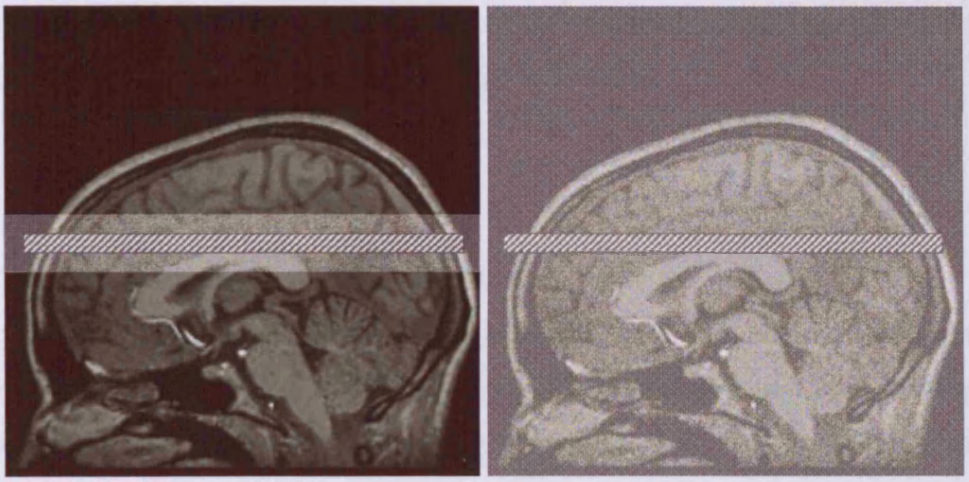

Figure 3.6: Schematic diagram illustrating the pairs of images acquired in a simple FAIR experiment. The axial imaging slices are indicated by the diagonally striped regions. The shaded areas indicate the regions with inverted magnetisation. In each case the image is acquired at time TI after the inversion pulse.

In FAIR, a slice-selective inversion pulse is applied before the first image is acquired after a time TI. The second image is similarly acquired after a global inversion pulse. Figure 3.6 illustrates the FAIR experiment. In both images, the signal from the static tissue in the slice is the same, and the difference in magnetisation comes from the inflowing blood, which is fully relaxed in the first image and inverted (but relaxing) in the second. In the first image, the inflowing relaxed blood increases the apparent relaxation rate of the tissue water. In the second image, the initially inverted inflowing blood relaxes during time TI, and so affects the relaxation rate of the tissue, but to a lesser extent than the inflowing blood in the first image. The quantification of perfusion with FAIR is identical to EPISTAR, since the signal difference in both derives from the inflowing blood being inverted in one image and fully relaxed in the other.

In practice, α, $M_t^0(t)$ and T_{1app} are determined by fitting a slice selective monoexponential inversion recovery curve to the first image series acquired at a range of inflow times TI. f and T_{1a} are then fitted to the biexponential of Equation [3.7]. In this way a proper estimate of *CBF* is obtained.

3.5.2.2.2. Slice Profile

One of the main advantages of PASL over CASL is that transit time effects are minimised owing to the close proximity of the inversion region and imaging slice. The distance the spins need to travel after inversion is only limited by the slice profiles of the labelled region and imaging slice. Ideally the slice profiles of both the imaging and inversion pulses would be infinitely sharp so that the inversion slice would be placed immediately adjacent to the imaging slice. Slice profile effects can be minimised by using adiabatic hyperbolic secant pulses, which have sharply defined edges. However there is still a necessary gap of a few millimetres to avoid slice overlap (compared with several centimetres in CASL). Even this small distance can still cause transit time effects. Sharper inversion pulses such as FOCI pulses (Ordidge *et al.* 1996) can reduce this sensitivity to some degree.

3.5.2.2.3. Inflow Effects

In PASL experiments it is important to consider the width of the labelled bolus, which must be wide enough to ensure that fresh spins that have not been inverted do not flow into the imaging slice during the inversion time TI. If this occurs, the perfusion signal will be less than predicted by the standard ASL model.

3.5.2.2.4. Vascular artefacts

Since a proper calculation of *CBF* requires a range of inflow times TI, it is possible that for some measurements, an insufficient time will have elapsed for all the spin-labelled blood to have either exchanged with the tissue or passed through the slice. This effect can be reduced by using crusher gradients to destroy the signal from moving spins (Ye *et al.* 1997).

3.5.2.2.5. Multislice Imaging

In both EPISTAR and FAIR, the introduction of multi-slice imaging introduces a range of transit times. In EPISTAR, slices are acquired further away from the inversion slab, and in FAIR, the slice-selective inversion slab is widen to accommodate more slices. For multi-slice imaging transit time insensitive techniques are therefore preferable, for example QUIPPS (see Section 3.5.2.2.6).

3.5.2.2.6. Transit Times

In PASL, various approaches have been explored to reduce the sensitivity to transit delays. One popular approach involves modifying the PASL pulse-sequence to include saturation pulses that control the time-duration of the labelled bolus (Wong *et al.* 1998). In a technique named QUIPSS (quantitative imaging of perfusion using a single subtraction) a saturation pulse is applied to the imaging slice at a time TI_1 that is longer than the longest transit time delay, and an image is acquired at time TI_2 that is shorter than the time-duration of the labelled bolus. In this way, the leading edge of the labelled bolus is 'cut off', and the perfusion signal depends on the amount of blood entering the slice between TI_1 and TI_2. In an alternative technique QUIPSS II, a saturation pulse is applied to the inversion slab at time TI_1 that is shorter than the time-duration of the labelled bolus, and an image is acquired at TI_2 that is longer than the longest transit time delay. In this way, the trailing edge of the labelled bolus is

'cut off', and the perfusion signal depends on the amount of blood entering that leaves the inversion slab in TI_1. Both these techniques have been shown to minimise the dependency of perfusion measurement on transit delays, since the bolus of labelled blood has a well defined length. These techniques may however become impractical in cases of pathology where very long transit times are present.

3.6 COMPARISON OF MR PERFUSION TECHNIQUES

DSC-MRI and ASL are the most common MR perfusion imaging modalities. They are both non-invasive, i.e. they do not require ionising radiation, a property that is very desirable for imaging children, and when multiple scans are required. Additionally, there is no need for intravenous access in ASL. The endogenous contrast agent enables multiple repeated measurements to be made in quick succession. This is a useful property for functional MRI studies (Wang *et al.* 2003). In DSC-MRI however, repeated doses of contrast agent in multiple DSC-MRI experiments is associated with persistent effects on image intensity from the previous contrast injections (Runge *et al.* 1994). Additionally it is important the maximum dose (known as "triple-dose" or 0.3 mmol/kg) is not exceeded. For this reason, a single dose (0.1 mmol/kg) is often used for repeated measurements (Grandin *et al.* 2005).

Typically, the signal difference between the label and control image acquisitions in ASL is only ~1% of the control image. Therefore perfusion monitoring using ASL requires a very high SNR and multiple signal averaging. Because the signal difference is so low, it is difficult to accurately measure blood flow lower than ~10ml/100g/min. In addition, ASL tends to underestimate high blood flow, which is partly attributable to the labelled blood having left the voxel at the time of imaging, and an incomplete exchange having occurred (Silva *et al.* 1997; Barbier *et al.* 2001). The SNR in ASL experiments can be improved by increasing the number of averages, but this increases the scan time. Although there is much higher SNR in a DSC-MRI experiment, there is still difficulty in accurately quantifying low blood flow.

However, both techniques perform well in the range of normal *CBF* values and in the absence of pathology.

The difficulty in accurately quantifying low blood flow in CASL is also exacerbated in stroke regions due to collateral circulation resulting in long transit times for the arterial blood. These additional delays can be several seconds in the ischaemic tissue, and so the SNR is further reduced. This is a fundamental limitation of the ASL technique, which in the extreme situation would result in no labelled blood arriving at the tissue and consequently no perfusion would be measured. The only way to improve this is to use higher field strengths where the T_1 is longer.

The equivalent problem in DSC-MRI is the distribution of transit times for the contrast agent between where the arterial input to the tissue is measured and the where the tissue signal itself is measured. This is a particular problem in cerebrovascular disease, particularly in cases of collateral flow to ischemic areas (see Section 4.7.2). If this effect is not accounted for, *CBF* is underestimated, and arterial dispersion is not distinguished from intravoxel dispersion by tissue microvasculature. Correcting for these effects is an active area of research, and the primary focus of this thesis.

There is a limit on the regional coverage achievable in both ASL and DSC-MRI acquisitions. In DSC-MRI, there is a trade-off between the number of slices and the time resolution. Typically 10-15 slices can be acquired using EPI at a temporal resolution of ~1.5s. Three-dimensional acquisitions are also possible, but at the expense of spatial resolution. In ASL, the number of slices is also limited by length of the labelled bolus. Typically 8-10 slices are acquired.

It is interesting to note that ASL and DSC-MRI actually measure a different effect. The labelled water in an ASL experiment is a diffusible tracer (similar to $H_2{}^{15}O$ used in PET). On the other hand, the intravascular contrast agent used in DSC-MRI is non-diffusible. Therefore the signal behaviour of both might be expected to be

different. However, it has been observed that both ASL and DSC-MRI yield highly comparable perfusion values in normal brain (Weber *et al.* 2004).

Currently the most robust MR perfusion technique is DSC-MRI, especially in patients with cerebrovascular diseases. However, although it is a commonly used clinical technique, there is still much development necessary to make it quantitatively accurate. Many of the analysis methods in popular use neglect to take into account some important factors that may lead to a misinterpretation of the acquired perfusion maps. This thesis seeks to address some of these issues, and as a result, provide the information needed for more accurate diagnosis, prognosis, and treatment plans for patients with stroke.

3.7 DIFFUSION MRI IN CEREBROVASCULAR DISEASE

Perfusion MRI can be used to identify ischaemic tissue that may be at risk of infarction. On progression to infarction, the structure of the tissue can also change, affecting the mobility of the tissue water. Therefore, water diffusion is another useful indicator of tissue status. This section describes the changes in water diffusion that accompany the changes in cerebral haemodynamics. MRI can be made sensitive to detect such changes using diffusion-weighted MRI (DWI) images (see Section 2.3.6). Busza *et al.* (Busza *et al.* 1992) found that DWI signal enhancement occurred when the *CBF* fell below a value similar to the threshold necessary to drive normal neuronal function. It has been suggested that dysfunction occurs at a blood flow of around 20ml/100g/min (Baird *et al.* 1998). When the *CBF* is severely reduced and the compensatory mechanisms are overwhelmed, less oxygen and glucose are delivered to the tissue (see Section 3.3). This results in a decrease in the amount of available adenosine triphosphate (ATP), which is the main source of cell energy. Energy is required to pump Na+ ions out of the cell and K+ ions into the cell in order to maintain homeostasis. When the ATP supply is diminished there is an accumulation of intracellular Na+ and consequently an osmotic influx of extracellular

water. This leads to cell swelling (cytotoxic oedema) and eventually cell death (Moseley *et al.* 1990). Although still a point of debate, the enhanced DWI signal is thought to be a consequence of the oedema, since the cell swelling restricts the diffusion in the extracellular space.

Serial DWI studies in animal models have demonstrated the evolution of the DWI lesion volume changes over time, which is often quantified by using the apparent diffusion coefficient (ADC) (see Section 2.3.6). These experiments have shown that although the lesion size has nearly fully evolved at around 2 hours, the magnitude of the ADC reduction continues to increase for up to 4-6 hours (Knight *et al.* 1994; Roussel *et al.* 1994). At about 24-48 hours, the ADC increases again, returning to normal after about 3 days (known as "pseudonormalisation"), and actually rises above normal values in the subsequent week (Knight *et al.* 1994). This elevated diffusion of tissue water is thought to be associated with the loss of cell membrane structure. Knowledge of the temporal evolution of the DWI signal can be used to help discriminate between acute and chronic tissue lesions. In animal models of ischaemia, both a time-threshold and an ADC-threshold for the reversibility of the DWI lesion have been demonstrated. In humans, although reversibility of ischaemic lesions has been reported e.g. (Marks *et al.* 1996), the abnormal ADC area is usually so severely affected that it is likely to infarct regardless of treatment.

3.8 BLOOD-OXYGENATION IN CEREBROVASCULAR DISEASE

In addition to detecting changes in perfusion and diffusion, MRI can be made sensitive to changes in regional tissue oxygenation status using the blood-oxygenation-level-dependent (BOLD) MRI signal (Ogawa *et al.* 1990). Since deoxyhaemoglobin is paramagnetic it promotes T_2/T_2^* relaxation of the water tissue protons. Therefore, BOLD signal intensity, usually measured by T_2^*-weighted MRI, drops immediately upon onset of ischaemia when the ratio of oxy to deoxyhaemoglobin falls due to decreased blood flowing to the tissue.

In a mild hypoperfusion condition, the T_2 values are depressed but the DWI signal remains unchanged (Calamante *et al.* 1999a). In a severe hypoperfusion condition, T_2 values are shorter and DWI signal is enhanced. Changes in T_2 are immediate and not always related to vasodilatation compensation mechanisms. The early T_2 change may therefore provide useful information as to the progression of the pathophysiological status of the affected tissue. However, the effect is small at the field strength of typical clinical studies.

3.9 PENUMBRAL TISSUE

The brain has very little capacity to store energy, and consequently cell viability is compromised within 3 minutes of a complete interruption of blood flow. Normally collateral flow preserves areas of incomplete ischaemia (and equally, these areas may have incomplete ischaemia because of collateral flow). Such areas of ischaemic but not infarcted tissue (which is still at risk of irreversible damage), are known as the ischaemic penumbra (Astrup *et al.* 1981). The concept of penumbral tissue surrounding a core of densely ischaemic and irreversibly damaged tissue was first demonstrated in experiments performed on baboons (Astrup *et al.* 1981). In these experiments, brain tissue that was identified as having lost electrical functionality, regained its function and did not undergo necrosis if *CBF* was restored early enough. In later studies, it was found that the duration of ischaemia and residual *CBF* was crucial in determining the fate of ischaemic tissue. In work conducted by Jones *et al.* (Jones *et al.* 1981), the tissue in the macaque monkey with *CBF* around 15ml/100g/min could survive about three hours of occlusion, whilst tissue with *CBF* of 5ml/100g/min could survive only about two hours.

With reduced *CBF*, tissue may remain structurally intact whilst the neurons are functionally (electrically) silent. But if the *CBF* falls further, cytotoxic oedema may occur, and cell death follows shortly after depending on the residual flow (3-500min)

(Jones *et al.* 1981). The penumbral area is general thought to correspond to where the *CBF* levels are somewhere between the electrical (neuronal) failure threshold and the membrane failure threshold (i.e. cell swelling resulting from energy failure).

3.10 DIFFUSION-PERFUSION MISMATCH

The extent of the final DWI lesion volume (indicative of cytotoxic oedema) may be larger or smaller than the acute abnormality. In a study of 13 patients with ischaemic stroke, Baird *et al.* (Baird *et al.* 1997) discovered that when the size of the initial perfusion abnormality (reduced *CBF*) exceeded the size of the initial DWI lesion volume, the extent of the final DWI lesion volume was larger than the initial DWI lesion volume. This suggests that the peripheral region of the observed acute perfusion deficit was not great enough to cause energy failure, and therefore went unnoticed on initial DWI images. The change in DWI lesion size with time depends on the underlying perfusion and possible collateral flow.

This mismatch of abnormal regions is known as the "diffusion-perfusion mismatch". The concept of diffusion-perfusion mismatch has been developed as a possible way of identifying potentially salvageable tissue in humans. It is thought that tissue that is abnormal on DWI, and has low perfusion is destined to infarction. Conversely, tissue that is normal on DWI but has reduced *CBF* (at penumbral levels) could possibly recover if the flow is restored. Studies in patients receiving thrombolysis (see Section 3.11) provide further evidence that the mismatch region is not irreversibly damaged (Schellinger *et al.* 2000).

3.11 REPERFUSION

The duration of ischaemia is a crucial consideration when treating humans. Treatment is most likely to be beneficial when administered as early as possible, since small changes in the energy demand may accelerate the progression to cell death or prolong the survival. Given that irreversible infarction of penumbral tissue can occur within a few hours, the therapeutic window for intervention may be very short.

Perfusion deficits caused by the obstruction of blood flow (e.g. a blood clot) may be treated with thrombolytic agents, such as the tissue plasminogen activator drug, tPA (Adams, Jr. *et al.* 1996). Such drugs act to break down the clot and unblock the artery. However, the use of tPA in acute stroke is controversial, since irreversibly damaged tissue will not benefit from reperfusion, and tPA may actually increased the risk of haemorrhage (Adams, Jr. *et al.* 1996).

In addition to the neuronal and cell membrane failure resulting from ischaemia and infarction, there can also be a loss of structural integrity of the blood vessels (breakdown of the BBB), partly through the release of enzymes that break down connective tissues. Additionally, ischaemia induces the production of reactive oxygen species that promote cell membrane failure and BBB breakdown. Antioxidant neuroprotective drugs have been shown to be effective in reducing the region of damaged tissue in rodents, but their efficacy has not been confirmed clinically. However, such treatment offers a promising approach to limiting infarct tissue damage without increasing haemorrhage risk (Goldberg 2007).

In light of the severe complications of thrombolysis, such treatment must be balanced against the potential benefits. For this reason it is important to assess the pathophysiological tissue status with accuracy, and to know how to combine and interpret the measurements from the various imaging modalities. Such information would enable an early and accurate identification of patients most likely to benefit from reperfusion treatments.

3.12 PREDICTION MODELS USING MR DATA

Much current research is being conducted into predicting tissue outcome in stroke by combining DWI, perfusion and T_2 parameter maps (e.g. (Hjort *et al.* 2005; Wu *et al.* 2001; Wu *et al.* 2007; Rose *et al.* 2001)). Such work involves the creation of tissue signature algorithms based on thresholding, for example ADC, *CBF* and T_2 values. These algorithms are 'calibrated' using a so-called training data set (the DWI, perfusion and T_2 MRI data), which has been obtained acutely from a group of patients, and for whom the final radiological outcome is known. A comparison of the acute and final data enables parameters for a predictive algorithm to be determined. These can then be used to infer the likelihood of infarction in subsequent patients. The output of these models is therefore a map of probability of tissue infarction, based on the patient's acute MRI data. In this way, they are aimed at helping to identify the patients that are more likely to benefit from therapy.

Models based on a voxel by voxel analysis rather than comparing volumes of tissue are more sensitive for identifying salvable tissue (Wu *et al.* 2001; Welch *et al.* 1995). However, the sensitivity and specificity remains somewhat limited, primarily because of errors in the *CBF* measurements. If either the training data or input data into the predictor-models is erroneous, then the predictions made by these models will be unreliable.

Of all the information used by these models, the input provided by perfusion MRI is the main determinant of the tissue at risk, while the remaining data (e.g. DWI and T_2 MRI) are mainly used to determine the so-called 'core' of the infarct (which is usually so severely affected that it is likely to infarct regardless of treatment (Sobesky *et al.* 2005)). Therefore, the main source of error in the predictor-models originates from inaccuracies introduced by the perfusion MRI data; this can lead to patients being treated inappropriately, with potentially serious clinical consequences. The work presented in this thesis investigates methods to improve the accuracy of the perfusion input data used in these predictive algorithms. An improved quantification of

perfusion in patients with cerebrovascular disease is an important first step in providing a robust means to assess and successfully treat such patients.

3.13 PREDICTING 'AT RISK' TISSUE USING NON-MR METHODS

An essential medical consideration when imaging a stroke patient is the speed at which the patient data can be obtained and processed. It has been shown that reperfusion treatments are more effective in salvaging tissue if they are administered as soon as possible after the ischaemic event (Hacke *et al.* 1999).

The ability of PET imaging to provide estimates of *OEF* and $CMRO_2$ in addition to *CBF* and *CBV*, leads to the concept (which is peculiar to PET) of 'misery perfusion': ischaemic/penumbral tissue characterised by a preserved $CMRO_2$, combined with a reduced *CBF* and increased *OEF*. After the first hour, the extent of the PET-defined penumbra generally decreases with time (Heiss 2001). Although PET has been shown to be a valuable tool for evaluating the perfusion and haemodynamic reserves of cerebral tissue, the main limitation in using PET in application to acute stroke is that the delay between tracer injection and imaging usually takes about 2 hours (Read *et al.* 1998). Furthermore, as discussed in Section 3.4.1, the availability of PET is limited, there is poor spatial resolution, and it uses radioactive tracers.

Both multimodal MR imaging (DWI, PWI, BOLD etc) and dynamic CT can be acquired easily and quickly. Hypodensity in non-enhanced CT scans is believed to indicate that the tissue is irreversibly infarct, but conventional CT cannot identify tissue that is at risk (Tomandl *et al.* 2003). The pixel-by-pixel time-density curve achieved using dynamic-CT can be used to extract quantitative *CBF*, *MTT*, and *CBV* data, although absolute values are unreliable. Therefore, it has been suggested that combining non-enhance CT and enhanced-dynamic CT, could be used to identify the infarct core and the ischemic penumbra (Wintermark 2005). CT offers a number of practical advantages over other perfusion imaging methods, including its wide

availability, low cost and short scanning time. However, a major disadvantage of using CT to image stroke is its limited spatial coverage. It is therefore not well suited to imaging a small stenosis or occlusion. Furthermore, in addition to the undesirable radiation risk, the methodology for identifying at-risk tissue is not as well established as the diffusion-perfusion mismatch.

3.14 CONCLUSION

The accurate measurement of cerebral perfusion is a vital first step towards predicting regions that will go on to infarction if left untreated. MR measurements of perfusion are safely obtained and easily combined with diffusion and oxygenation measurements to indicate the underlying cerebral haemodynamics and structural (cell membrane and vessel) integrity. Thus MRI provides the most comprehensive set of information, which can potentially improve the exclusion of patients who may be harmed by treatment. In fact, a lower haemorrhagic rate has been observed for MRI-selected patients (Fiebach *et al.* 2002). The most common MR method for measuring perfusion clinically is bolus tracking or DSC-MRI. Unlike ASL, there is no fundamental limitation preventing its utility in patients with abnormal flow. However, in patients with cerebrovascular disease, DSC-MRI perfusion parameter measurements may be inaccurate because of dispersion of the intravascular tracer (see Section 4.7.2). In particular, the broadened bolus in major vessels will seemingly counteract the homogenisation of flow elements, i.e. the actual *FH* decrease due to vasodilation will be hard to detect. Similarly, dispersion errors will underestimate the *CBF*, and overestimate the *MTT*. Predictions of tissue infarction made using these perfusion data are likely to be misleading. Improved predictions may be possible by identifying regions where the perfusion measurements are potentially erroneous. The work in this thesis investigates approaches to improve the quantification and interpretation of perfusion measurements using DSC-MRI. Such work is essential in order to improve the selection of patients who would benefit from intervention.

4 DSC-MRI PERFUSION MEASUREMENT

4.1 INTRODUCTION

The work presented in this thesis is based upon the technique of bolus-tracking or DSC-MRI. This is currently the most robust clinical MR method for assessing the cerebral blood flow (*CBF*). The technique involves the successive acquisition of MR images following a rapid intravenous injection of a paramagnetic contrast agent (usually Gd-DPTA). Upon reaching the brain, the bolus of contrast agent passes first through the major branches of the arterial tree, then through the capillary bed, finally draining through veins. In healthy subjects, the blood brain barrier (BBB) of the vessels is intact, so that the contrast agent remains at all times intravascular. Consequently, the passage of the Gd-DPTA bolus is detected in the tissue because the intravascular compartmentalisation of the paramagnetic material results in a susceptibility difference between the intravascular and extravascular space. The resulting magnetic field gradients that extend out from the vessel edge promote the dephasing of the extravascular tissue water spins. As the bolus passes through the capillary bed there is a measurable transient drop in the MR signal deriving from the tissue (Villringer *et al.* 1988; Rosen *et al.* 1990). The measured signal time-course in the tissue can be used to extract perfusion related physiological parameters, such as cerebral blood flow (*CBF*), cerebral blood volume (*CBV*), mean transit time (*MTT*) and flow heterogeneity (*FH*). This chapter describes the theory and methodology of perfusion quantification by means of tracking the dynamic susceptibility contrast created by the passage of the paramagnetic contrast agent bolus. The artefacts and potential problems associated with the technique are also discussed.

4.2 IMAGE CONTRAST

The most commonly used contrast agent in DSC-MRI is the paramagnetic metal ion, Gadolinium, chelated to diethylenetriaminepentaacetic acid (Gd-DTPA) (Sorensen *et al.* 1997). The BBB is impermeable to molecules of this size, and so, when the BBB

is intact, Gd-DTPA can be regarded as an intravascular tracer. Typically the injected dose is 0.1-0.3 mmol/kg body weight. Although the intravascular compartment within which the Gd-DTPA resides represents only ~2-6% of the brain tissue, the susceptibility effect (see Section 4.2.1) enables the detection and quantification of contrast agent via a suitable MR acquisition (Rosen *et al.* 1990; Villringer *et al.* 1988).

4.2.1 THE SUSCEPTIBILITY EFFECT

Image contrast in DSC-MRI images is primarily due to magnetic susceptibility differences. Magnetic susceptibility is the proportionality constant between an applied magnetic field and the resultant magnetisation established within the material.[4] The Gd ions of the paramagnetic contrast agent possess electro-magnetic dipoles attributable to the unpaired electrons on the Gd ion. These dipoles tend to align with an applied magnetic field (in the same way as the weaker nuclear magnetic dipoles of proton spins), therefore reinforcing the applied field (the magnetic susceptibility of a paramagnetic material is positive). The compartmentalisation of the paramagnetic contrast agent within the capillaries causes a susceptibility difference between the intravascular and extravascular space. The situation is illustrated schematically in Figure 4.1. Since there can be no field discontinuities (Bleaney *et al.* 1989), there is a magnetic field gradient between the two compartments. *In vivo*, these gradients extend out approximately the same distance as the vessel diameter. Consequently, there is a distribution of resonant frequencies for protons in the voxels within this region, and hence a corresponding increase in the heterogeneity of the phase distribution across the voxel (Villringer *et al.* 1988; Boxerman *et al.* 1995). As a result, the transverse T_2/T_2^* relaxation time of the extravascular tissue-water protons is shortened. For a typical DSC-MRI acquisition,

---

[4] $\vec{M} = \chi\vec{H}$, where χ is the susceptibility, $\vec{M}$ is the magnetisation of the material and $\vec{H}$ is the applied filed. The magnetic field in the material $\vec{B}$, is related to $\vec{H}$ by the relationship $\vec{B} = \mu_0(1+\chi)\vec{H}$, where μ_0 is the permeability of free space and $(1+\chi)$ is the relative permeability of the material.

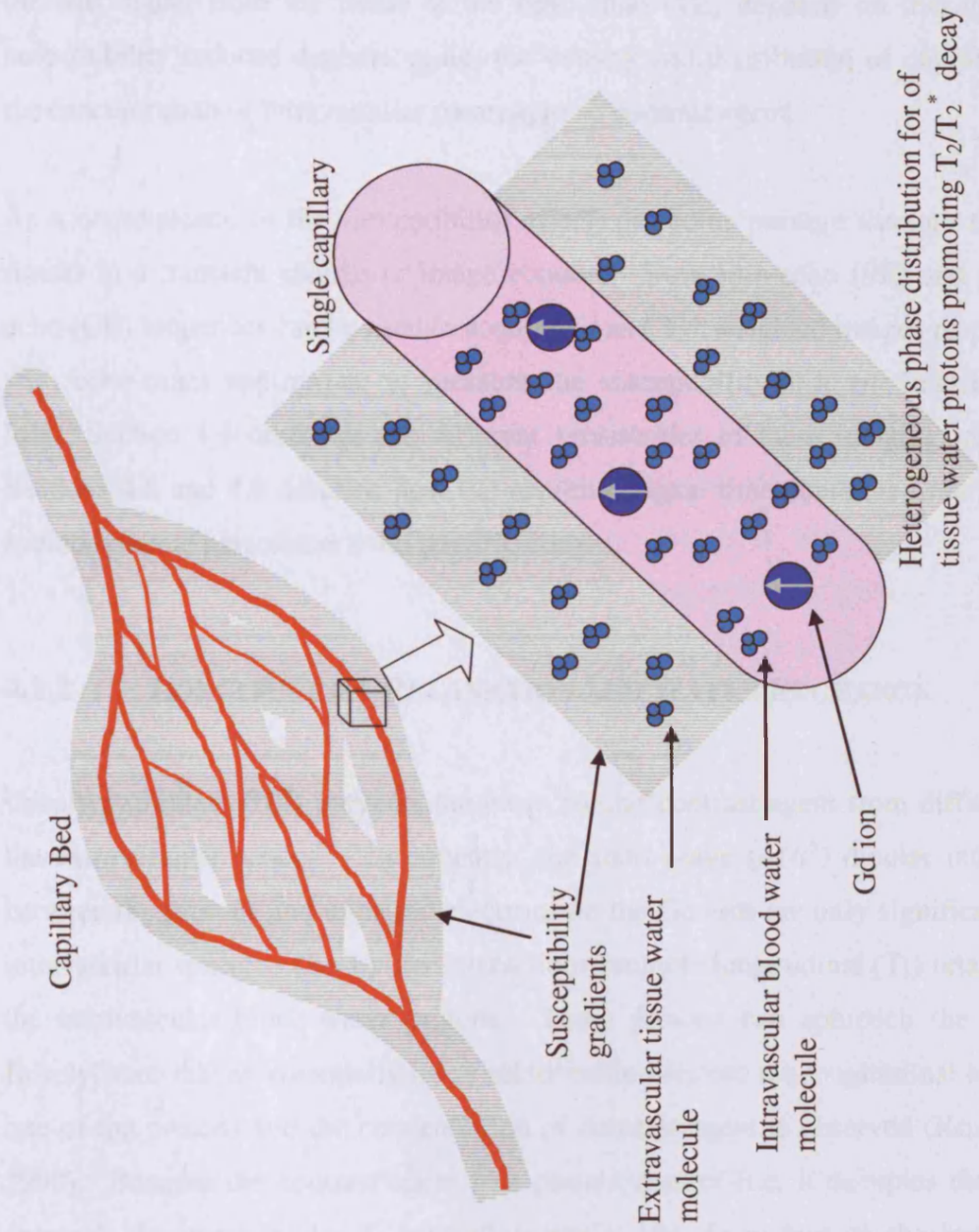

Figure 4.1: Schematic representation of the effect of intravascular compartmentalisation of contrast agent. The resulting susceptibility gradients, which promote T2/T2* relaxation, extend out from the vessel edge and consequently cause a decreased signal intensity in the tissue. If the BBB were damaged, the Gd ions would be distributed in the intravascular and extravascular space, and therefore, the susceptibility gradients would be smaller. As a result Gd- promoted T_1 relaxation would be the dominant effect.

the MR signal from the tissue at the echo time (TE) depends on the amount of susceptibility induced dephasing, i.e. the density and distribution of capillaries and the concentration of intravascular paramagnetic contrast agent.

As a consequence of the susceptibility effect, the bolus passage through the tissue results in a transient change in image contrast. Both spin-echo (SE) and gradient-echo (GE) sequences can be used to acquire T_2 and T_2* weighted images respectively, with echo-times appropriate to measure the susceptibility-different induced signal loss. Section 4.4 describes the different sensitivities of these imaging modalities. Sections 4.5 and 4.6 describe how the resulting signal time-course is used to derive haemodynamic parameters from the MR images.

4.2.2 LONGITUDINAL RELAXATION AND WATER EXCHANGE

Usually, an intact BBB prevents the intravascular contrast agent from diffusing into the extravascular space. Consequently, the short-range ($\sim 1/r^6$) dipolar interactions between the protons and unpaired electrons on the Gd ions are only significant in the intravascular space. The dipolar interactions promote longitudinal (T_1) relaxation of the intravascular blood-water protons. These protons can approach the Gd ions closely, such that an essentially linear relationship between the longitudinal relaxation rate of the protons and the concentration of contrast agent is observed (Rosen *et al.* 1990). Because the contrast agent is a plasma marker (i.e. it occupies the plasma volume), the intravascular T_1 relaxation rate is also dependent on the haematocrit levels in the blood (Kiselev 2001).

A small amount of T_1 relaxation of the extravascular tissue-water protons is induced by water exchange between the capillaries and the extravascular space. Compared with the T_2/T_2* image contrast (described in Section 4.2.1), bolus induced T_1 contrast in the tissue is not significant because the residence time of water in the capillaries is relatively long (~500msec) compared with the MR measurement time

(Boxerman *et al.* 1995). The situation is somewhat different when the BBB is disrupted. This is discussed in Section 4.7.1.

4.3 IMAGE ACQUISITION

The bolus is typically tracked through the brain by acquiring sequential echo planar images (EPI) with a short repetition time (TR <2s) (see Section 2.4.4). A fast imaging method is necessary to enable a high temporal resolution, so that the time-course of the bolus-induced signal drop is well described. In Figure 4.2, three distinct periods are labelled on the signal time-course measured in a particular region of interest (ROI) or voxel: the baseline (before the bolus has arrived in the ROI), the first passage of the bolus (~14s) and the recirculation, which corresponds to the second passage of the contrast agent through the brain. The signal time-course the takes approximately two sample points to reach the equilibrium baseline value, during which the tissue magnetisation is reaching a steady-state.

4.4 GRADIENT-ECHOES AND SPIN-ECHOES

In a GE experiment (see Section 2.3.3), signal loss is due to the decreased T_2^*; the dephasing derives from field inhomogeneities (which cause local differences in the resonant frequency) and also diffusional motion through these inhomogeneities (Boxerman *et al.* 1995). In DSC-MRI, the static field inhomogeneities are primarily the result of the susceptibility-difference induced field gradients. A SE experiment (see Section 2.3.2) can completely refocus the dephasing caused by these static field inhomogeneities. Therefore in the absence of diffusion, the tissue contrast arising from a SE acquisition would be unchanged during the passage of the contrast agent. In practice however, during spin-echo time, tissue-water protons will diffuse through the region of field gradients, causing an irreversible loss of phase coherence.

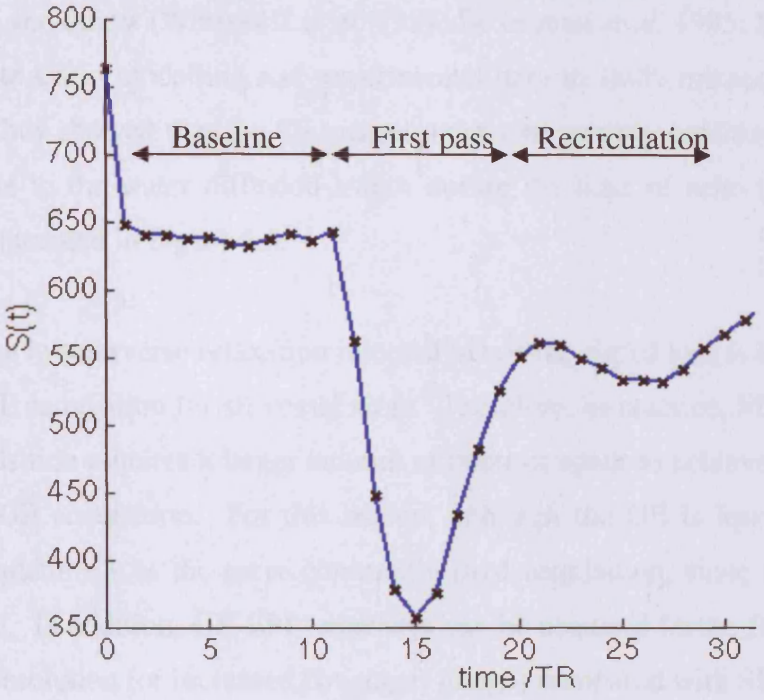

Figure 4.2: The signal time-course of a typical dynamic susceptibility contrast imaging experiment. Upon injection of contrast agent into a vein, the contrast agent reaches the brain, causing a substantial signal drop in tissue and arteries. The *baseline* section is the time before the bolus has arrived in the brain, the *first passage* is the signal drop resulting from the passage of the bolus through the cerebral vasculature, and the *recirculation* is the second passage of the bolus through the cerebral vasculature.

If the spin-echo time is sufficient to allow significant diffusion of the tissue-water protons, the irreversible phase accumulation is significant. The MR signal decrease observed in the SE experiment is therefore sensitive to diffusion effects, and hence to the diffusion-length in time TE (see Section 2.3.6). This diffusion-length is approximately the same as the diameter of the capillaries. Since the susceptibility gradients extend out approximately the same distance as the vessel diameter (Kiselev 2001), the gradients in the vicinity of large vessels will be small and consequently there will be little dephasing. Maximum irreversible dephasing occurs in the vicinity of capillaries, where the phase accumulation across the diffusion length of water is greatest (Boxerman *et al.* 1995).

Weisskoff and others (Weisskoff *et al.* 1994; Boxerman *et al.* 1995; Fisel *et al.* 1991) used Monte Carlo modelling and experimental data to study microscopic relaxation effects. They showed that the SE measurements are mainly sensitive to vessel sizes comparable to the water diffusion-length during the time of echo (~20 μm). This effect is illustrated in Figure 4.3.

The change in transverse relaxation rate and hence the signal loss is larger for the GE than the SE acquisition for all vessel sizes. Therefore, in practice, MR imaging using a SE acquisition requires a larger amount of contrast agent to achieve the same signal loss as a GE acquisition. For this reason, although the GE is less sensitive to the microvasculature, it is the more commonly used acquisition, since a higher SNR is achievable. In addition, GE-EPI sequences can be acquired faster, facilitating higher temporal resolution (or increased coverage) images compared with SE sequences.

The change in T_2/T_2^* enables perfusion to be estimated even though the vessels themselves are too small to image. In order to quantify the blood flow, the relationship between the change in T_2/T_2^* and the concentration of contrast agent (see Section 4.5) must be known.

4.5 SIGNAL INTENSITY AND BOLUS CONCENTRATION

Haemodynamic perfusion parameters are derived from DSC-MRI data using an established relationship between the MR signal and the concentration of contrast agent in the vessels. In GE sequences, the signal intensity in the tissue during the bolus passage $S_t(t)$, depends on the transverse relaxation rate $R_2^*(t)=\frac{1}{T_2^*(t)}$, longitudinal relaxation rate $R_1(t)=\frac{1}{T_1(t)}$, the echo time TE and sequence repetition time TR. For a 90° RF pulse:

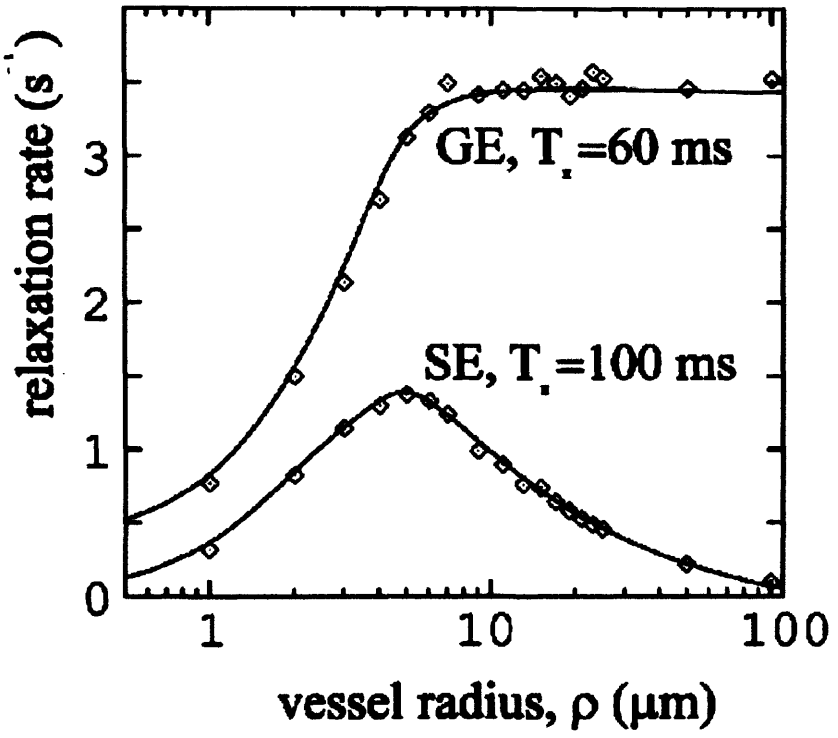

Figure 4.3: The transverse relaxation rate ΔR_2^* (TE=60ms) and ΔR_2 (TE=100ms) as a function of vessel radius for a susceptibility difference of $\Delta\chi = 10^{-7}$. ΔR_2^* exceeds ΔR_2 for all vessel sizes, reaching a plateau at larger radii. ΔR_2 is greatest for vessel radii in the range of capillaries. Thus, SE sequences are most sensitive to microvsculature while GE sequences are more sensitive to larger vessels. Reproduced from (Kiselev 2001).

$$S_t(t) = S_t(t_0)\frac{\left(1-e^{-TR\cdot R_1(t)}\right)}{\left(1-e^{-TR\cdot R_1(t_0)}\right)}e^{-TE\cdot\left(R^*_2(t)-R^*_2(t_0)\right)} \qquad [4.1]$$

$S_t(t_0)$ is the baseline signal, and $R_2^*(t_0)$ and $R_1(t_0)$ are the transverse and longitudinal relaxation rates before the arrival of the contrast agent. For a typical TE and TR, and assuming an intact BBB, the change in longitudinal relaxation rate is negligible (i.e. $\frac{\left(1-e^{-TR\cdot R_1(t)}\right)}{\left(1-e^{-TR\cdot R_1(t_0)}\right)} \approx 1$). Therefore, the measured GE signal drop in the

tissue is predominantly determined by the change in T_2* relaxation rate, $\Delta R_2^* = \frac{1}{T_2^*(t)} - \frac{1}{T_2^*(t_0)}$. Equation [4.1] simplifies to:

$$S_t(t) = S_t(t_0) e^{-TE \cdot \Delta R^*_2(t)} \qquad [4.2]$$

To derive haemodynamic parameters from DSC-MR images by tracer kinetic analysis (see Section 4.6), the concentration of contrast agent within the vessels must be known. Therefore, the relationship between observed signal changes during the bolus passage and the corresponding concentration must be known in detail for the specific pulse sequence (SE or GE-EPI). Empirical measurements (Villringer *et al.* 1988; Rosen *et al.* 1990) and theoretical simulations (Fisel *et al.* 1991; Weisskoff *et al.* 1994; Boxerman *et al.* 1995; Kennan *et al.* 1994), suggest that with the concentrations of Gd-DTPA used clinically, the change in relaxation rate measured in the tissue is approximately linearly proportional to the bolus concentration:

$$C_t(t) = \kappa_t \Delta R_2^*(t) \qquad [4.3]$$

Where κ_t is a constant depending on tissue type, the contrast agent, the field strength, and the pulse sequence (see Section 4.7.5). This relationship is a central assumption in the subsequent kinetic analysis.

Using Equations [4.2] and [4.3], the intravascular bolus concentration time-course $C_t(t)$ may therefore be written:

$$C_t(t) = -\kappa_t \frac{1}{TE} \ln\left(\frac{S_t(t)}{S_t(t_0)}\right) \qquad [4.4]$$

$S_t(t_0)$ is usually determined from the average baseline signal in the images prior to the contrast bolus arrival. *In vivo* concentration time-course data are illustrated in Figure 4.4.

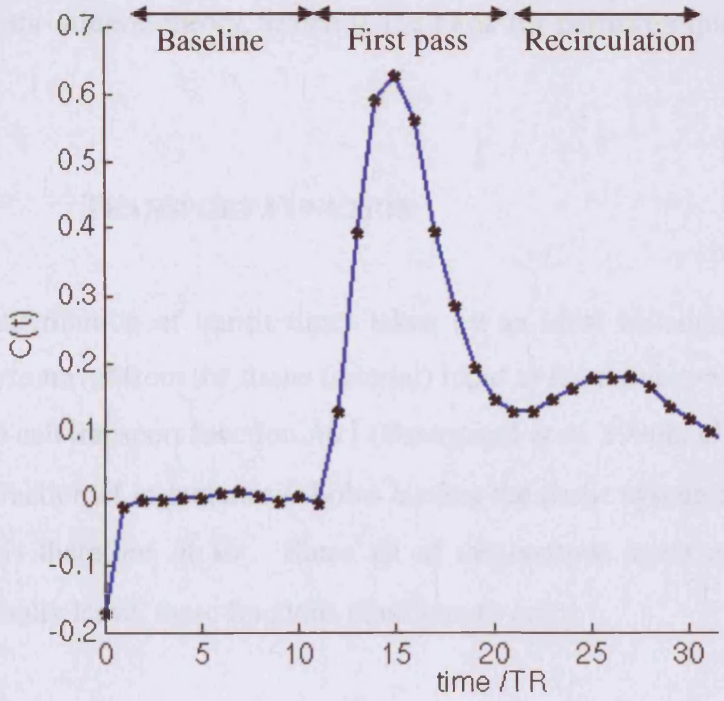

Figure 4.4: The contrast agent concentration time-course of a typical dynamic susceptibility contrast imaging experiment. The baseline, first-pass and recirculation sections are labelled.

4.6 TRACER KINETICS

The concentration time-course measured in the tissue and in an artery can be combined to quantify perfusion in the tissue. The kinetics describing the concentration time-courses of a non-diffusible contrast agent (or tracer) is described by indicator dilution theory (Zierler 1965; Meier *et al.* 1954). The theory describes the behaviour of the bolus of contrast agent (indicator) in the vasculature, assuming it is instantaneously injected into the blood stream and subsequently diluted in the circulation. For the theory to be applicable it is essential that the contrast agent remains intravascular, since if the BBB were disrupted, the contrast agent would leak and become diffusible. The following paragraphs describe the main aspects of the

indicator dilution theory, which is the basis for perfusion quantification using DSC-MRI.

4.6.1 TRANSPORT FUNCTION

The distribution of transit times taken by an ideal instantaneous bolus of contrast agent to travel from the tissue (arterial) input to the tissue (venous) output is given by the so call transport function $h(t)$ (Østergaard *et al.* 1996b; Østergaard *et al.* 1996b)). The fraction of instantaneous bolus leaving the tissue system in the time interval t to $t + dt$ is therefore $h(t)dt$. Since all of the contrast agent entering the tissue must eventually leave, these fractions must sum to one:

$$\int_0^\infty h(t)dt = 1 \qquad [4.5]$$

Accordingly, the output concentration $C_{out}(t)$ is the convolution of the input concentration $C_a(t)$ with the probability density function of transit times $h(t)$ (Meier *et al.* 1954; Zierler 1965)

$$C_{out}(t) = \int_0^t C_a(\tau)h(t-\tau)d\tau \qquad [4.6]$$

This expression can be understood by considering the input concentration $C_a(t)$ as a superposition of consecutive instantaneous boluses, $C_a(\tau)d\tau$ injected into the tissue system at time τ. For each idealised bolus, the resultant output concentration at time t, $dC_{out}(t)$, is determined by the proportion of the bolus leaving the tissue system at a later time $t-\tau$, $h(t-\tau)$:

$$dC_{out}(t) \propto C_a(\tau)h(t-\tau)d\tau \qquad [4.7]$$

The total measured output concentration $C_{out}(t)$ is the sum of all these contributions.

4.6.2 RESIDUE FUNCTION

In DSC-MRI, rather than measuring the fraction of bolus *leaving* the tissue system in the time interval t to $t + dt$, $h(t)dt$, the fraction of contrast agent *present* in the tissue system in the time interval t to $t + dt$ is measured (Østergaard *et al.* 1996b). For perfusion quantification, the 'tissue system' is often just one voxel in the capillary bed.

Assuming an instantaneously arriving bolus, the fraction of contrast agent remaining in a tissue voxel at time t is:

$$R(t) = 1 - \int_0^t h(\tau)d\tau \qquad [4.8]$$

I.e. One minus the fraction that has left. By definition, $R(0) = 1$ and $R(\infty) = 0$. Equivalently,

$$\frac{dR(t)}{dt} = -h(t) \qquad [4.9]$$

$R(t)$ is known as the tissue residue function and is a positive decreasing function of time (Østergaard *et al.* 1996b). This function provides valuable information about the retention of tracer in the capillary bed.

4.6.3 MEAN TRANSIT TIME

The mean transit time (*MTT*) of the contrast agent is the average time for the tracer to pass through the tissue from the arterial input to the venous output after an ideal bolus injection (Meier *et al.* 1954). It can be defined in terms of the probability density function of transit times as:

$$MTT = \frac{\int_0^\infty t \cdot h(t)dt}{\int_0^\infty h(t)dt} \qquad [4.10]$$

Using Equations [4.8] and [4.10] it can be shown that the *MTT* is also the area under $R(t)$.

$$MTT = \int_0^\infty R(t)dt \qquad [4.11]$$

The *MTT* is therefore longer for a broader $R(t)$, signifying prolonged retention of the blood within the capillary bed

4.6.4 MODELS FOR THE RESIDUE FUNCTION

The exact shape of $R(t)$ is unknown. It is likely to be dependent on the specific arrangement of the capillary bed and the perfusion therein. Several models have been proposed, which satisfy Equations [4.8] and [4.9]. The most simple of these models for the capillary bed is a single well-mixed compartment. In this situation, the blood is thought to drain from the tissue into the veins in an exponential manner, so that the rate at which the tracer concentration in the tissue is decreasing at time *t*, is proportional to the tracer concentration remaining in the tissue at time *t*. Assuming an instantaneous injection of bolus at *t*=0, $R(t)$ is then modelled as a decaying exponential with a time constant equal to the mean time taken for the blood to pass through the tissue from the arterial input to the venous output (*MTT*) (Østergaard *et al.* 1996b):

$$R_{\exp}(t) = e^{\left(\frac{-t}{MTT}\right)} \qquad [4.12]$$

A simple alternative model is that of plug flow, whereby the blood remains in the tissue bed for a time *MTT* before instantaneously draining into the veins (Østergaard *et al.* 1996b). In this case:

$$R_{plug}(t) = \begin{cases} 1 & 0 \le t < MTT \\ 0 & t \ge MTT \end{cases} \qquad [4.13]$$

Although the red blood cells (RBC) do to some degree prevent mixing, it is unlikely that this model accurately represents the tissue bed. Nevertheless, this model has been used in several simulation studies.

A compromise between these two extremes is the Lorentzian model (Calamante *et al.* 2003a). In this situation, the blood would have a small residue time within the tissue before it starts draining into the veins.

$$R_{lor}(t) = \frac{1}{1+\left(\frac{\pi t}{2MTT}\right)^2} \qquad [4.14]$$

The shapes of the residue functions for an *MTT*=4s are illustrate in Figure 4.5. Other models for $R(t)$ have included a triangular function, a Gaussian and a Fermi Function (Andersen *et al.* 2002; Østergaard *et al.* 1996b).

Physiological modelling of the vasculature has also been investigated to obtain the form of $R(t)$ (Mouridsen *et al.* 2006b; Østergaard *et al.* 1999; Kroll *et al.* 1996). In general, the capillary (tissue) system is modelled by N parallel tubes. Each particle entering each tube has a certain transit time. When the blood is delivered to the capillaries from an artery, it is distributed among these tubes and a density function of the transit times is obtained. Such models may provide a better description of tracer retention in the capillary bed, although at the expense of increasing complexity and introducing further parameters.

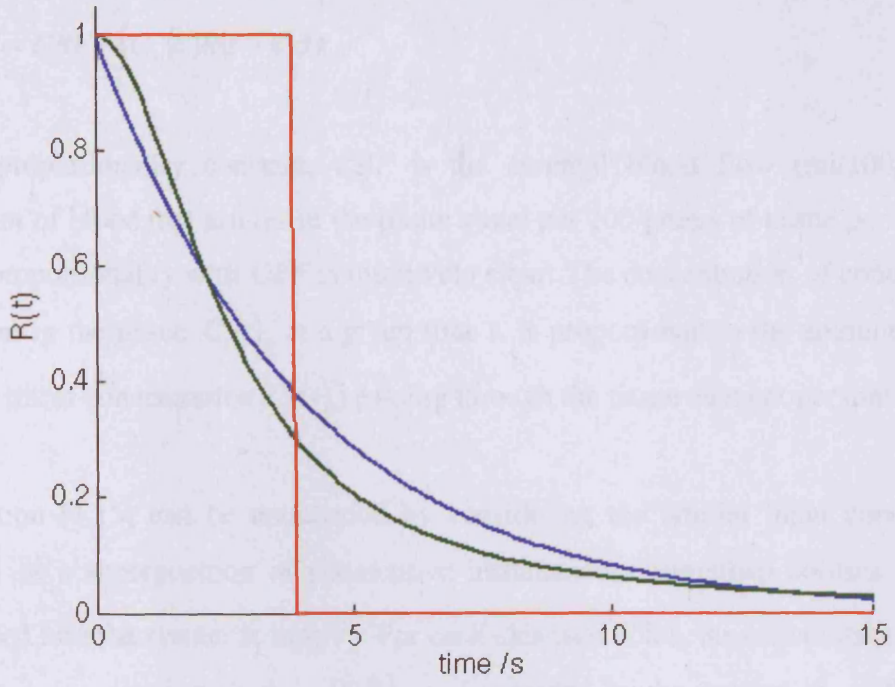

Figure 4.5: Models for the Residue Function simulated for *MTT*=4s. The blue curve is the Exponential, the green curve is the Lorentzian, and the red curve is the Plug Flow.

4.6.5 ARTERIAL CONCENTRATION

In practice, the arrival of the contrast agent in the voxel is not instantaneous. The measured concentration time-course of the contrast agent in a tissue voxel $C_t(t)$ is dependent on the shape and amount of contrast that enters the capillary bed. $C_t(t)$ is proportional to the convolution of the arterial input concentration $C_a(t)$ with the idealised (instantaneous unit input) response of the tissue, $R(t)$ (Østergaard *et al.* 1996b):

$$C_t(t) \propto CBF \cdot \int_0^t C_a(\tau) R(t-\tau) d\tau \qquad [4.15]$$

The proportionality constant, *CBF* is the cerebral blood flow (ml/100g/s):- the amount of blood that arrives in the tissue voxel per 100 grams of tissue per unit time. The proportionality with *CBF* is intuitively clear: The concentration of contrast agent present in the tissue $C_t(t)$, at a given time *t*, is proportional to the amount of blood (with tracer concentration $C_a(t)$) passing through the tissue element per unit time.

Equation [4.15] can be understood by considering the arterial input concentration $C_a(t)$ as a superposition of consecutive instantaneous (impulse) boluses, $C_a(\tau)d\tau$ injected into the system at time τ. For each idealised bolus, the concentration present in the tissue voxel at time *t*, $dC_t(t)$, is determined by the proportion of the (ideal) arterial input bolus remaining the system at a later time $t-\tau$, $R(t-\tau)$.

$$dC_t(t) \propto CBF \cdot C_a(\tau) R(t-\tau) d\tau \qquad [4.16]$$

The total measured concentration of contrast in the tissue $C_t(t)$ is the sum of all these contributions.

4.6.6 PHYSIOLOGICAL FACTORS

For a quantitative assessment of *CBF*, it is necessary to take into account the difference in the blood characteristics between the vessel in which the arterial and tissue concentrations are measured. In a large artery, the percentage of the blood volume occupied by RBC is greater than in the capillaries. This percentage is known as the haematocrit *H*, which is approximately 45% in large vessels, H_{art} (i.e. approximately 45ml of RBC per 100ml of blood) and 25% for small vessels, H_{tis} (Larsen *et al.* 1964). Because the capillaries hold a greater proportional of plasma, they also hold a greater proportion of contrast. Accordingly, the susceptibility induced MR signal drop arising from the capillaries derives from a proportionally

larger concentration of contrast agent. A correction factor k_H must be included in Equation [4.15] to indicate the plasma volume available for the contrast agent (Calamante *et al.* 1999b):

$$k_H = \frac{(1-H_{art})}{(1-H_{tis})} \qquad [4.17]$$

4.6.7 CEREBRAL BLOOD VOLUME

The cerebral blood volume (*CBV*) is a measure of capillary density or microvascular blood volume. The *CBV* units of ml blood per 100g tissue (ml/100g), are often expressed as a percentage, on the assumption that the density of brain tissue is approximately 1g/ml. *CBV* is proportional to the total amount of intravascular contrast agent in the tissue (Meier *et al.* 1954). The area under the first pass of the concentration time-course gives the entire amount of contrast agent passing through the voxel, and is therefore an indication of the capability of the region to pass blood through it. Absolute *CBV*, is calculated by normalising the area under the measured tissue concentration time-course $C_t(t)$ to the area under the arterial contrast concentration time-course, $C_a(t)$, and scaling by k_H (Calamante *et al.* 1999b). In order to obtain the correct units, the density of brain tissue ρ (100g/cm^3) must also be accounted for:

$$CBV = \frac{k_H}{\rho}\frac{\int C_t(t)dt}{\int C_a(t)dt} \qquad [4.18]$$

Normalisation to $C_a(t)$ ensures that the calculated *CBV* is independent of the amount of tracer injected. These integrals should be taken over the first pass over the bolus only in order to avoid bias introduced by the recirculation (see Section 4.7.8).

4.6.8 THE CONVOLUTION EQUATION

The central equation for the quantification of blood flow using intravascular contrast agents is (Østergaard *et al.* 1996b):

$$C_t(t) = \frac{\rho}{k_H} CBF \cdot \int_0^t C_a(\tau) R(t-\tau) dt \qquad [4.19]$$

For simplicity, the ratio ρ/k_H is often taken to be equal to 1.0 (Grandin *et al.* 2001), although in reality the ratio is unlikely to be constant (see Section 4.7.5). Deconvolution (see Section 4.8) of the concentration time-course yields $CBF \cdot R(t)$, which will be referred to as the impulse response function, as it is the tissue concentration resulting from an infinitely short ("impulse") input.

Quantitative *CBF* is estimated from the initial (t=0) value of this function, since $R(t=0)=1$, which has been shown to be the most reliable method for *CBF* quantification (Perthen *et al.* 2002). In addition to *CBV*, *CBF*, and *MTT*, the impulse response function $CBF \cdot R(t)$ can be utilised to extract additional information about the capillary blood flow characteristics of the voxel. The actual shape of the residue function is of great importance for determining the flow heterogeneity (*FH*), which is another useful indicator of tissue viability (see Section 4.6.10).

4.6.9 CENTRAL VOLUME THEOREM

With the above definitions of *CBF* and *MTT* the Central Volume Theorem states (Meier *et al.* 1954):

$$CBF = \frac{CBV}{MTT} \qquad [4.20]$$

Under constant perfusion pressure, there is a direct correlation between *CBF* and *CBV*.. If the blood vessels dilate or contract, *CBF* and *CBV* will increase and decrease

accordingly. The *MTT* is the characteristic time the time blood spends in the capillary bed, and since it is completely independent of the structure of the feeding vasculature, it is a useful indictor of physiologic tissue status. It cannot be calculated without first deconvolving $C_a(t)$ from $C_t(t)$. There are however various issues concerning the deconvolution, which make accurate estimates *CBF*, *MTT*, and flow heterogeneity *FH* difficult (see Sections 4.7.2 and 4.8).

4.6.10 FLOW HETEROGENEITY

Within a given voxel there will be a distribution of flow rates. The heterogeneity of the relative flow values, f (relative to the mean flow, *CBF*), can be described by a probability density function that assigns a probability $w(f)$ to a given flow f (Østergaard *et al.* 1999). In normal human cerebral capillaries, the flow heterogeneity is thought to indicate the tissue oxygen metabolism regulation mechanism (see Section 3.3). Cerebral blood flow heterogeneity can be measured in DSC-MRI by converting the distribution of transit times $h(t)$ (given by the slope of $R(t)$, Equation [4.9]) to the distribution of relative flow rates, $w(f)$ (Østergaard *et al.* 1999):

$$w(f)df = h(t)dt \qquad [4.21]$$

I.e. the fraction of instantaneous bolus leaving the tissue at time t to $t + dt$ is determined by the proportion of flow in the range $f + df$. Assuming all vascular paths have equal blood volume, the Central Volume Theorem, (Equation [4.20]) can be used to relate the relative flow and transit time:

$$f \cdot CBF = \frac{CBV}{t} \qquad [4.22]$$

By differentiating Equation [4.22] with respect to t, and substituting for f, the distribution of flow rates in Equation [4.21] can be re-expressed as:

$$w(f) = -\frac{t}{f}h(t) \qquad [4.23]$$

Therefore deconvolution of Equation [4.19] allows not only quantification of the mean flow in each voxel (*CBF*), but also its distribution.

4.7 PERFUSION QUANTIFICATION ISSUES

Many of the assumptions in the above theory may not be true in practice, and could cause erroneous perfusion quantification. In addition, image artefacts can further complicate the interpretation and estimation of perfusion parameters. The following paragraphs describe some of the issues that should be considered when analysing data from DSC-MRI experiments. These include BBB breakdown, delay and dispersion, quantifying the contrast concentration, partial volume effects, unknown constants, signal saturation, recirculation effects and patient motion.

4.7.1 BLOOD BRAIN BARRIER

One of the primary assumptions for perfusion quantification using DSC-MRI is that there is an intact blood-brain barrier (BBB). The contrast agent must remain intravascular for the above theory (Section 4.6) to be valid. An intact BBB ensures that the induced susceptibility difference between the intra and extra vascular space is the dominant effect. A disrupted BBB is often found in brain tumours. In such a situation, the compartmentalisation of the contrast agent is reduced, and correspondingly the related local field inhomogeneities are decreased. In addition, the extravascular contrast agent causes local T_1 shortening. Since the blood volume in a voxel is usually small (~2-6%), even a small amount of extravascular contrast agent would decrease the T_2/T_2^* effects and increase the T_1 effects (Rosen *et al.* 1990). This results in the tissue concentration time-course falling below the baseline,

introducing errors into the *CBV* calculation. Figure 4.6 schematically illustrates the tissue concentration time-course in the situation where the BBB is leaking.

Insensitivity to T_1 enhancement may be achieved using a dual-echo acquisition (Vonken *et al.* 1999b). In this acquisition, since the T_1 enhancement is the same for both TEs, the change in transverse relaxation rate can be isolated:

$$\Delta R_2^* = \frac{\ln\left(\frac{S_1(TE_1)}{S_2(TE_2)}\right) - \ln\left(\frac{S_{1,pre}(TE_1)}{S_{2,pre}(TE_2)}\right)}{TE_1 - TE_2} \qquad [4.24]$$

$S_i(TE_i)$ is the signal intensity at the i^{th} echo, TE_i, during the bolus passage and $S_{i,pre}(TE_i)$ is the average i^{th} echo intensity before the contrast arrival. When there is BBB breakdown, T_2^* image contrast is due to both intra and extravascular contrast agent, and consequently susceptibility-contrast is smaller.

For a disrupted BBB, a simple transfer constant can describe the leakage of contrast agent between the intravascular and extravascular compartments (Vonken *et al.* 1999b). If a fast exchange of mobile protons within the tissue is assumed, the same ΔR_2^* can be attributed to the intravascular and extravascular contrast. The total response function $v_{tot}(t)$ of the tissue, including the possible extravasation, can be obtained in the same manner as $CBF \cdot R(t)$, by deconvolution.

The extravascular contrast will prevent $v_{tot}(t)$ from returning to baseline (zero) after the first passage of bolus (this is a direct consequence of the shape of the tissue concentration time-course, see Figure 4.6). After a few times *MTT*, the response $v_{tot}(t)$ will reach a constant value. The tissue response with extravasation can be expressed as in terms of $CBF \cdot R(t)$ as:

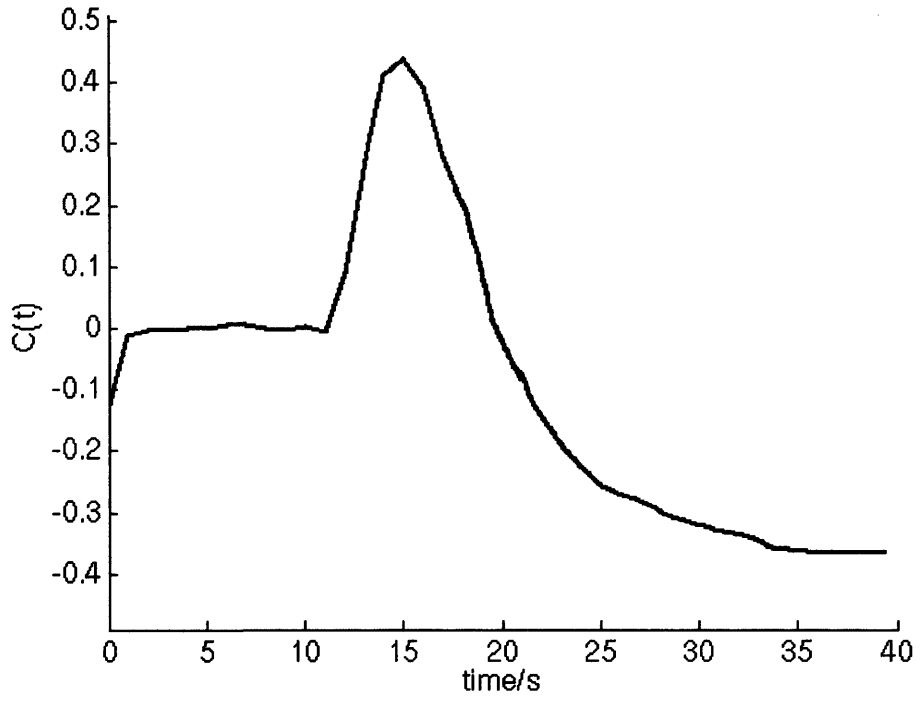

Figure 4.6: A schematic illustration of the *concentration* time-course when the BBB is leaking. In this situation, the tissue *signal* will initially decrease, but subsequent overshoot the baseline. This effect is observed because there is a significant reduction in T_1 relaxation time, which is caused by the leakage of some contrast agent into the extravascular space. The resulting signal increase causes an underestimation of the bolus concentration.

$$v_{tot}(t) = CBF \cdot R(t) + \varsigma \int_0^t CBF \cdot R(t')dt' \qquad [4.25]$$

The constant ς indicates the proportion of contrast agent leaving the circulation and can be estimated from the average baseline elevation. Using an initial guess for $CBF \cdot R(t)$, Equation [4.25] can be solved iteratively to obtain an estimate of CBF (Vonken *et al.* 1999b).

4.7.2 DELAY AND DISPERSION

Delay and dispersion of the bolus are a major source of error in perfusion quantification (Calamante *et al.* 2000). A significant part of this thesis focuses on techniques to minimise these errors, which are common in patients with cerebral arterial diseases, for example occlusions, stenosis or collateral flow (Calamante *et al.* 2002). The errors are described in detail in this section.

In the standard theory described above (Section 4.6), the concentration of contrast in the artery directly feeding the tissue is known as the Arterial Input Function or AIF. If an absolute *CBF* measure is required, then an absolute AIF must be calculated. Typically, the AIF is estimated by measuring the signal time-course in voxels within a feeding artery. In order to minimise partial volume effects (see Section 4.7.4), the AIF is typically measured in a large artery such as the carotid or middle cerebral artery (MCA) (Østergaard *et al.* 1996a; Calamante *et al.* 2002). Voxels typically chosen for the measurement are those with the earliest bolus arrival time and a high blood volume (Carroll *et al.* 2003). However, measuring the AIF in a large artery distant to the tissue leads to quantification problems resulting from bolus delay and dispersion. The delay of the bolus is the time taken to travel from the point of AIF measurement to the volume of interest. Dispersion increases the width of the bolus due for example to differing path lengths through the vascular bed, or arterial stenosis. Thus the AIF measurement is not the true input to the tissue volume of interest.

Delay-related perfusion measurement errors are purely a result of inaccuracies in the deconvolution technique used (see Section 4.8). Dispersion-related perfusion measurement errors are present regardless of the accuracy of the particular deconvolution technique employed. Dispersion may be modelled using a vascular transport function $VTF(t)$, which describes the probability distribution of transit times between the AIF measurement site and the tissue (Calamante *et al.* 2000). If

$C^{est}{}_a(t)$ is the AIF *estimated* in a large vessel such as the MCA, the *true* AIF, $C^{true}{}_a(t)$ may be expressed (cf. Equation [4.6]):

$$C^{true}{}_a(t) = C^{est}{}_a(t) \otimes VTF(t) \qquad [4.26]$$

This relationship can be interpreted in the same way as Equation [4.6]. Consider the estimated input concentration $C^{est}{}_a(t)$ as a superposition of consecutive instantaneous boluses, $C^{est}{}_a(\tau)d\tau$, injected into the vascular system at time τ. For each idealised bolus, after travelling through the vasculature, the resultant output concentration, (that is the true input to the tissue) at time *t*, $dC^{true}{}_a(t)$, is determined by proportion of the (ideal) bolus leaving the vascular system at a later time $t-\tau$, $VTF(t-\tau)$.

$$dC^{true}{}_a(t) \propto C^{est}{}_a(\tau)VTF(t-\tau)d\tau \qquad [4.27]$$

The total true input concentration $C^{true}{}_a(t)$ is the sum of all these contributions.

Using Equation [4.26], the convolution equation central to perfusion quantification using DSC-MRI becomes (Calamante *et al.* 2000):

$$\begin{aligned} C_t(t) &= \frac{\rho}{k_H} CBF \cdot \left(C^{est}{}_a(t) \otimes VTF(t) \otimes R(t)\right) \\ C_t(t) &= \frac{\rho}{k_H} CBF \cdot \left(C^{est}{}_a(t) \otimes R_{eff}(t)\right) \end{aligned} \qquad [4.28]$$

where $R_{eff}(t) = R(t) \otimes VTF(t)$ is the *effective* residue function whose shape reflects the properties of both the vasculature and the tissue. If the bolus suffers delay and/or dispersion, the deconvolution analysis with $C^{est}{}_a(t)$ will not give the true scaled residue function, $CBF \cdot R(t)$, but the impulse response function for the tissue and arterial system becomes $CBF \cdot R_{eff}(t)$. In this situation, the initial value of the deconvolved function $CBF \cdot R_{eff}(t)$ cannot be used to measure *CBF*, since $R_{eff}(t=0) = 0$. The best estimate is obtained from the maximum of $CBF \cdot R_{eff}(t)$,

although the effect of dispersion leads to an intrinsic underestimation. It should be noted that if the estimated AIF is inaccurate, dispersion-related perfusion measurement errors are always present, even if the particular deconvolution algorithm were perfectly accurate. The underestimation is wholly a consequence of the inaccurate estimation for the tissue arterial input function.

In both PET and MRI a simple exponentially decaying VTF (Iida *et al.* 1986; Calamante *et al.* 2000; Calamante *et al.* 2003b) has often been assumed to model the vascular dispersion.

$$VTF(t) = \frac{1}{\beta} e^{-\frac{t}{\beta}} \qquad [4.29]$$

β is the mean vascular transit time (MVTT) from the site of AIF measurement to the volume of interest. In PET studies, β has often been estimated in the range 0-10s, by fitting the radioactivity curve of the sampled arterial blood with the exponential (e.g. (Meyer 1989). Assuming the tissue can be represented as a well mixed compartment (Equation [4.12]), the effective residue function in DSC-MRI is then (Calamante *et al.* 2003a):

$$R_{eff}(t) = \frac{\exp\left(-\frac{t}{\beta}\right) - \exp\left(-\frac{t}{MTT}\right)}{\frac{\beta}{MTT} - 1} \qquad [4.30]$$

This model for dispersion has been previously used to assess the dispersion errors using deconvolution simulations. It was found that dispersion leads to an underestimation of *CBF* by 50% for $\beta > 2.5$ seconds and an *MTT* overestimation of 200% (Calamante *et al.* 2000).

Just as the exact form of $R(t)$ is unknown, the function describing the transport of the bolus through the vasculature, $VTF(t)$ is also unknown. The exact shape will depend on the specific configuration of the vascular network that the bolus passes through.

In particular, its shape will be dependent on stenosis and bifurcations of the vessels (Calamante *et al.* 2003b). Since the commonly assumed VTF models have limited physiological motivation, an *in vivo* study of the VTF has been conducted in Chapter 8.

Delay and/or dispersion result in four possible bolus states and corresponding $R_{eff}(t)$: No delay and no dispersion (normal), delay and no dispersion, dispersion and no delay, delay and dispersion. The shape of $R_{eff}(t)$ is illustrated in Figure 4.7 for each state. This shape can be used to indicate the bias in *CBF* and *MTT* measurements. For example, the shape can indicate whether a low *CBF* and prolonged *MTT* is a result of dispersion, or whether there is actually a true perfusion abnormality. The characterisation of the shape of $R_{eff}(t)$ is particularly important in patients with cerebral arterial disease and stroke, where bolus delay and dispersion are common due to vessel occlusion, stenosis, or collateral flow.

Some of the common deconvolution approaches used to extract the impulse response function from Equation [4.28] are discussed in Section 4.8. Many of these methods provide an unsatisfactory characterisation of the $R_{eff}(t)$, and therefore it is difficult to distinguish true hypoperfusion from the underestimation introduced by bolus delay and dispersion. The work in Chapters 6 and 7 seeks to minimise the errors introduced in the deconvolution process in order to achieve an accurate characterisation of $R_{eff}(t)$. The work presented in Chapter 9 applies these developments to the perfusion data from patients with cerebral arterial diseases, and uses the improved characterisation of $R_{eff}(t)$ to identify areas where the perfusion values are likely to be inaccurate.

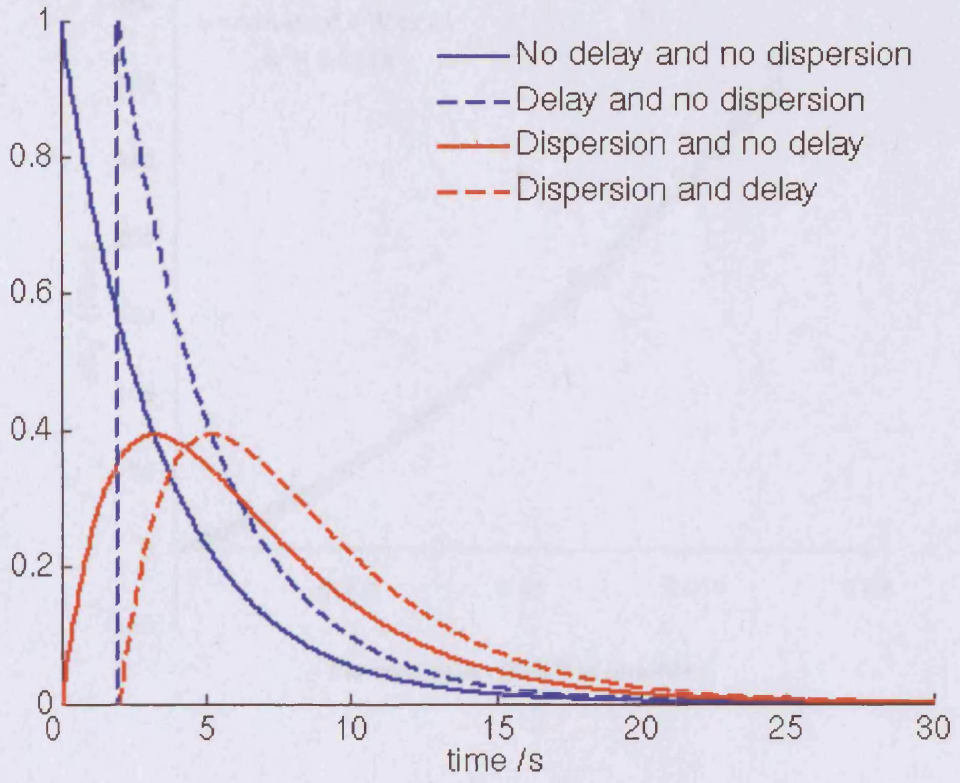

Figure 4.7: The $R_{eff}(t)$ corresponding to the four possible bolus states (delay and dispersion combinations) described in Section 4.7.2) a) No delay and no dispersion (normal), b) delay and no dispersion, c) dispersion and no delay, d) delay and dispersion.

4.7.3 Relationship Between Changes in R2/R2* and Concentration

One of the main assumptions in perfusion quantification using DSC-MRI is that the relationship between the concentration of contrast agent $C_t(t)$ and the induced change in relaxation rate (R_2/R_2*) is linear (see Section 4.5). Recent studies have actually observed a quadratic dependency between $C_t(t)$ and $\Delta R_2 / \Delta R_2^*$ (Figure 4.8). Since a higher concentration of contrast agent is found in big arteries, there may be

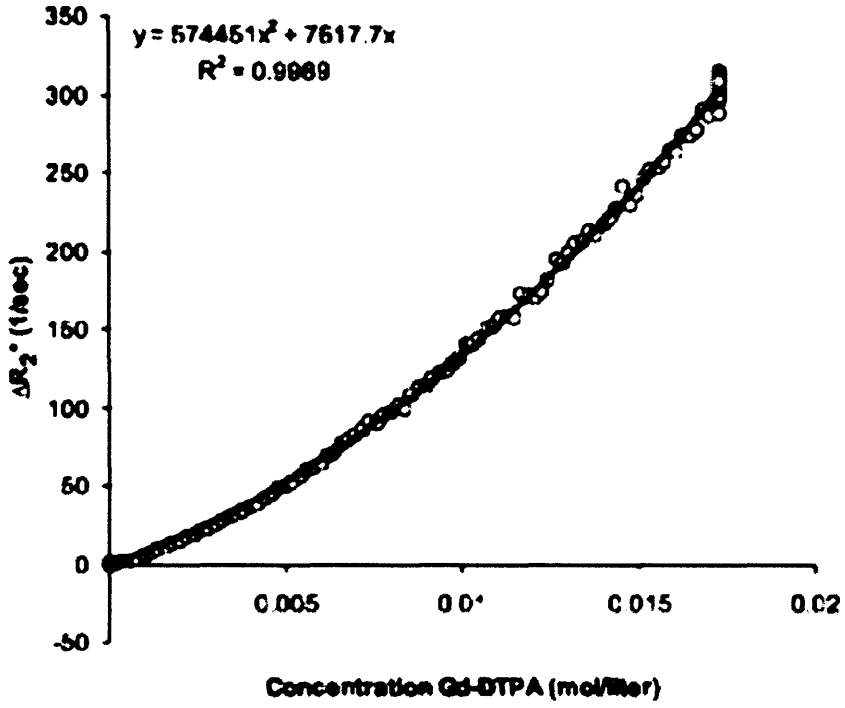

Figure 4.8: The graph shows ΔR_2^* as a function of Gd-DPTA concentration in human blood flowing in a phantom, fitted with a polynomial. The linear relationship between concentration and ΔR_2^* given in Equation [4.3] is not valid for higher concentrations of Gd-DTPA. Since high concentrations of Gd-DTPA may be present in the arteries, significant error may be introduced into the calculation of the AIF. Reproduced from (van Osch *et al.* 2003).

significant error in the calculation of AIF (van Osch *et al.* 2003). This quadratic dependency was also found to be dependent on the haematocrit levels, and will consequently vary between different patients and between different parts of the brain.

Although, not common practice, one potential way to avoid these complications is to use the phase of the signal, θ, rather than its magnitude. A linear relationship between the phase velocity $\Delta\theta/TE$ and the concentration $C_t(t)$ has been measured (van Osch *et al.* 2003). However, the interpretation of phase measurements is

complex if the artery is not parallel to the main field (van Osch *et al.* 2003). For this reason, this approach is usually only taken in the internal carotid arteries.

4.7.4 PARTIAL VOLUME EFFECTS

Even if the linear phase relationship is used, an accurate quantification of the concentration is difficult because of the limited spatial resolution of the MR images. Often the AIF is measured in the MCA, a location chosen to minimise delay and dispersion effects. However, here partial volume effects may be problematic. The total signal originating from a voxel containing both arterial blood and tissue surrounding the artery is dependent on the radius of the vessel (which determines the size of the time-dependent susceptibility gradients), the angle of the vessel with respect to the magnetic field (which determines the presence and direction of the gradients), the size of the voxel and location of the voxel with respect to the vessel, (which determine the proportion of intravascular and extravascular signal).

For *in vivo* studies, the measured signal for the AIF is likely to be a complex sum of signal arising from the tissue outside the vessel and a contrast agent dependent blood signal. If the artery in which the AIF is measured is parallel to the main field, the extravascular signal is constant throughout the measurement (Figure 4.9). As a result, for a partial volumed voxel, the complex blood signal will spiral around the contribution from the surroundings. For magnitude (ΔR_2^*) measurements, this constant offset will significantly distort calculated AIF; individual time points may be either over or underestimated, potentially giving erroneous peaks (van Osch *et al.* 2001). By using the whole complex signal, it is simple to correct for the constant phase originating from the extravascular signal (van Osch *et al.* 2001).

When the artery is not parallel to the main field (such as the MCA), the magnetic field distribution outside the artery changes as the contrast agent passes through the artery, due to the time dependent within-artery susceptibility (Figure 4.10). The signal originating from the partial volumed voxel will spiral around a non-fixed

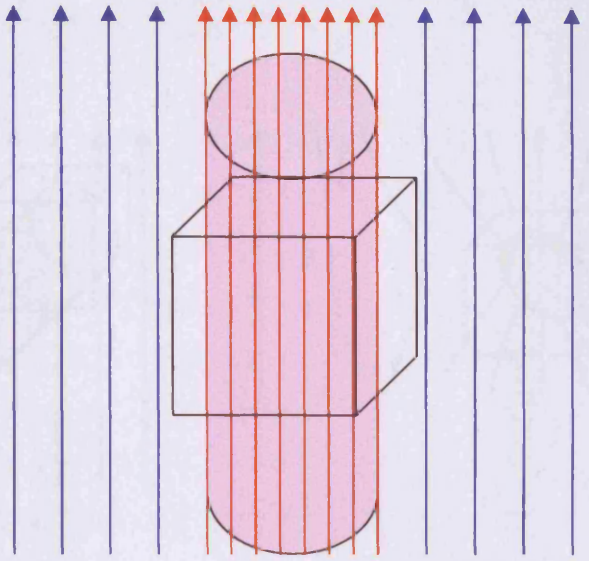

Figure 4.9: Schematic representation of the magnetic field lines arising in the tissue surrounding and artery when the bolus travels through an artery parallel to the main magnet field. The box represents a voxel located to measure the AIF, which has partial volume effects. Since the intravascular and extravascular field lines are parallel, extravascular field is unchanged by the passage of the contrast agent. The AIF can be corrected for the static contribution arising from the tissue surrounding the artery.

origin, since the contribution from the surroundings is no longer static (van Osch *et al.* 2001). Consequently, partial volume effects cannot be corrected for using the spiral method in this situation.

Partial volume contamination of the AIF could be avoided by measuring the concentration time-course in an artery whose diameter fills the whole voxel, or corrected for by measuring in an artery parallel to the field (such as the internal carotid artery). However these arteries are far away from the tissue volume of interest, and so bolus delay and dispersion are likely to introduce errors in perfusion quantification. Therefore, a compromise should be sought between these two sources of error (partial volume vs. delay and dispersion).

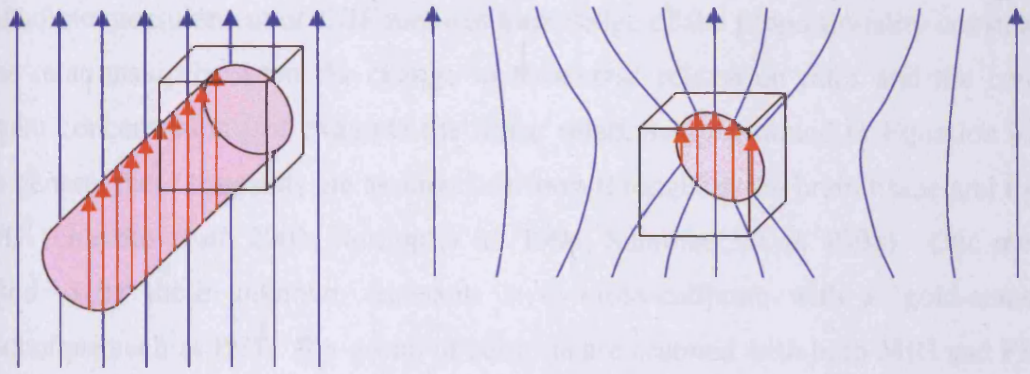

Figure 4.10: Schematic representation of the magnetic field lines arising in the tissue surrounding when the bolus travels through an artery that is not parallel to the main magnet field. The transverse view is illustrated on the left and the cross sectional view on the right. The box represents a voxel located to measure the AIF, which has partial volume effects. As the paramagnetic contrast passes through the artery, the intravascular field changes according to the concentration present at a particular time. Therefore, the density of the field lines within the artery changes during the bolus passage. Since field lines must be continuous, the field distribution in the vicinity of the artery (the extravascular field) also changes during the passage of the contrast agent. Consequently, the signal measured in the artery, cannot be corrected for partial volume effects, since the contribution from the surroundings is not static.

It is important to realise that partial volume effects may lead to both underestimation and overestimation of the individual AIF time-points. For this reason, care must be taken in selecting appropriate voxels for the AIF measurement. Voxels are often selected to have an early rise, small width, and high maximum. However, selection criteria such as these could misclassify voxels that suffer from partial volume effects as suitable for AIF measurement. This is of particular relevance for automatic methods for AIF voxel selection (Mlynash *et al.* 2005; Mouridsen *et al.* 2006a; Murase *et al.* 2001).

4.7.5 UNKNOWN CONSTANTS

Absolute measurement of *CBF* requires knowledge of the proportionality constants in the relationship between the change in transverse relaxation rates and the contrast agent concentration (for example the linear relationship assumed in Equation [4.3]). In general these constants are assumed uniform throughout the brain tissue and for the AIF (Grandin *et al.* 2001; Rempp *et al.* 1994; Schreiber *et al.* 1998). One method used to fix these unknown constants is to cross-calibrate with a 'gold-standard' technique such as PET. If a group of subjects are scanned with both MRI and PET, a global conversion factor can be calculated by plotting a graph of regional PET perfusion values against the corresponding DSC-MRI perfusion measurements, and fitting a linear regression (Østergaard *et al.* 1998a). Only a single global conversion factor is obtained using this approach, however in practice it likely to vary with changes in pathology, tissue type and for different subjects (Johnson *et al.* 2000). Therefore the conversion factor is likely to be both patient specific and time dependent (Lin *et al.* 2001). Although these common assumptions may lead to significant errors in the absolute quantification of *CBF* and *CBV*, it is interesting to note that using a universal constant has been shown to give fortuitously perfusion values consistent with the literature e.g. (Rempp *et al.* 1994). In addition, the ratio of the haematocrit levels k_H and brain density ρ is often taken to be equal to one (Grandin *et al.* 2001; Rempp *et al.* 1994; Schreiber *et al.* 1998). Furthermore, although it is assumed constant throughout the brain, the ratio is likely to change with pathology.

4.7.6 EPI ARTEFACTS

An EPI acquisition can achieve good SNR combined with high temporal resolution. However, it is important to be aware of some artefacts associated with this acquisition method that are particularly relevant for DSC-MRI.

Optimum sensitivity to T_2/T_2^* changes in tissue is achieved with a relatively long TE, (~65ms). However, because EPI uses a range of TE to acquire the data, the whole echo train cannot be optimally sensitive to the effect of the bolus, and each line of k-space will have a different T_2/T_2^* weighting. Although T_2/T_2^* decay along the frequency-encoding direction of *k*-space is negligible, decay along the phase-encoding is significant. Each line in *k*-space along the phase-encode direction is modulated by the T_2^* envelope, so that the point-spread function (which determines the image resolution, see Section 2.4.4.1) is degraded. The time dependent T_2/T_2^* during the bolus passage therefore causes a time-dependent point spread function and as a result a time-dependent resolution and partial volume effects. Furthermore, in order to maintain image resolution, the whole of *k*-space must be obtained with sufficient signal. Consequently, the echo-train should also be shorter than the shortest T_2/T_2^* seen during bolus passage.

One of the main sources of artefact in EPI imaging is related to the very low bandwidth per pixel in the phase-encoding direction (~10 Hz/pixel). Consequently, at the boundary between two regions with different susceptibilities there is voxel misregistration, whereby the voxels values are "shifted" in the phase-encoding direction. In DSC-MRI, this geometric distortion is particularly apparent for the voxels near the boundaries of the vessels, where the paramagnetic contrast agent creates local field inhomogeneities during the passage of the bolus. The resulting voxel misregistration distorts concentration time-course (Hou *et al.* 1999). This is illustrated in Figure 4.11 for voxel located close to a large vessel. Deconvolution of such a distorted time-course will give an erroneous impulse response function. Furthermore, in this voxel, the measured *CBV* (area under the first passage), will also be wrong due to the artificial negative contrast concentration. It is important to be aware that the signal close to big vessels may be distorted, and that these voxels should be excluded from the measurement of the AIF. In particular it is important to include criteria to exclude these voxels from automated AIF selection methods.

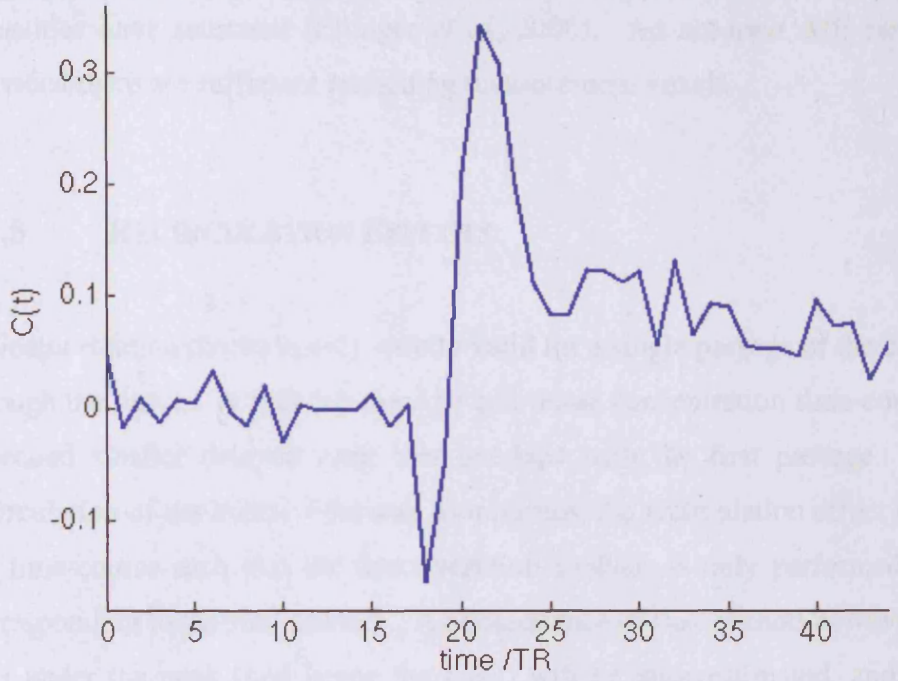

Figure 4.11: An example of the concentration time-course resulting from vessel misregistration cause by the passage of contrast agent in EPI. The time-course data has a distorted and unrealistic shape with artificially negative concentration.

4.7.7 SIGNAL SATURATION

Another common artefact that affects the measurement of the AIF is signal saturation. Because of the large concentration of contrast agent in the arteries and the relatively long TE used in DSC-MRI experiments, the signal intensity in the vessel during the first pass of the bolus can fall to the background noise levels, producing saturation in the peak of the measured AIF. Underestimating the peak of the AIF leads to an overestimation of *CBF* (Ellinger *et al.* 2000). Saturation effects can be minimised by using a dual echo sequence, in which the slice where the AIF measured is acquired with a shorter TE. However, the tissue SNR will be reduced in this slice. A more common approach is to exclude from the calculation of the AIF those voxels whose

intensities have saturated (Ellinger *et al.* 2000). An accurate AIF can be defined provided there are sufficient remaining measurement voxels.

4.7.8 RECIRCULATION EFFECTS

Indicator dilution theory is only strictly valid for a single passage of the contrast agent through the tissue. In practice the AIF and tissue concentration time-courses contain a second smaller delayed peak that overlaps with the first passage. This is the recirculation of the bolus. One way to minimise the recirculation effect is to truncate the time-course such that the deconvolution analysis is only performed on the part corresponding to the first passage. A consequence of this method however, is that the area under the peak (and hence the *CBV*) will be underestimated, and the impulse response function will be distorted. Alternatively, the recirculation can be removed by fitting a model such as the gamma-variate function to the first passage (Thompson *et al.* 1964). Care must be taken only to fit the time points that are not contaminated by the recirculation. Although this method can potentially provide reliable *CBV* estimates, it assumes that a gamma-variate function correctly models the first passage. If this is not true, it may lead to erroneous perfusion estimates and an inaccurate characterisation of the impulse response function (Levin *et al.* 1995). In addition, errors can potentially arise from inaccuracies in the non-linear fitting, which is very sensitive to noise in the data (Boxerman *et al.* 1997).

4.7.9 MOTION

Another potential artefact associated with standard 2D EPI is its sensitivity to through slice patient motion, which often occurs during bolus injection. In 2D imaging, out-off-slice spins that are suddenly shifted into the in-slice position (due to patient motion) will first need to reach a steady-state longitudinal magnetisation in order for the T_2* effect of the bolus passage to dominate the contrast. The signal time-course cannot be used for perfusion quantification if it is distorted at the end of the baseline

leading into the bolus-induced signal drop or if motion occurs during the first passage itself. However, if there is significant time between the movement and when the bolus reaches the brain, the bolus passage itself is unaffected and so the data can still be used. Care must be taken however to exclude non-steady-state images from the baseline calculation. Figure 4.12 illustrates how through-slice motion may be manifest in the signal time-course.

4.8 DECONVOLUTION

For perfusion quantification, Equation [4.28] must be solved for the impulse response function $CBF \cdot R_{eff}(t)$. There are various ways of doing this deconvolution analysis. Model-dependent approaches assume a model for $CBF \cdot R_{eff}(t)$ and calculate *CBF* by a non-linear fitting (Østergaard *et al.* 1996b; Mouridsen *et al.* 2006b). However, the model chosen may not be true for the entire brain, especially if there is pathology. As a result, model-*independent* approaches are more commonly used, for which both *CBF* and the shape of $R_{eff}(t)$ are not assumed.

Parametric methods fit a function (such as the gamma-variate) to the contrast concentration time-course data. In this situation the deconvolution is performed on a curve that is noiseless, and where there is no limitation on the temporal-resolution. In addition, the recirculation of the bolus through the brain is removed before the deconvolution is performed, enabling an accurate determination of *CBV*. However, as mentioned in Section 4.7.8 the non-linear fitting of the gamma-variate model is very sensitive to noise, potentially resulting in an inaccurate fit, and hence in an inaccurate characterisation of the deconvolved $CBF \cdot R_{eff}(t)$. Furthermore, the validity of the parametric model in all situations cannot be assured. For this reason, a *non*-parametric deconvolution approach is more commonly use, and it is the approach taken in this work.

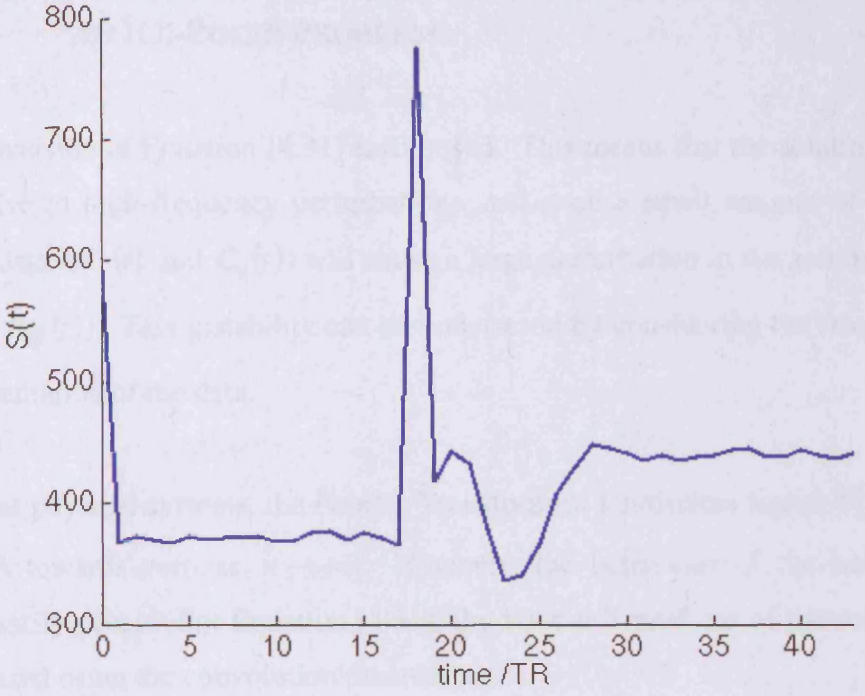

Figure 4.12: An example of the signal time-course resulting from patient motion in a 2D acquisition. In this case, the motion occurs at the beginning of the first passage of bolus. Consequently, since the new in-slice spins are still reaching an equilibrium magnetisation, the magnitude of the bolus induced signal drop is significantly reduced. Such motion would render the data set unusable for perfusion quantification.

Non-parametric methods use the actual concentration time-course data that is sampled at intervals of TR and is to some degree corrupted by noise. The noise contribution can be explicitly written into Equation [4.28]:

$$C_t(t) = CBF \cdot \left(C_a(t) \otimes R_{eff}(t)\right) \quad + \quad \textbf{noise} \qquad [4.31]$$

In DSC-MRI data, most of the noise in the system is present in $C_t(t)$, since $C_a(t)$ is often an average over many voxels. The estimated impulse response function $\tilde{r}(t) = \left(CBF \cdot R_{eff}(t)\right)_{est}$ depends both on the quality of the data and on the deconvolution technique.

4.8.1 AN ILL-POSED PROBLEM

The inversion of Equation [4.31] is ill posed. This means that the solution it is highly sensitive to high-frequency perturbations, and even a small amount of noise in the input data ($C_t(t)$ and $C_a(t)$) will cause a large perturbation in the solution (CBF and $CBF \cdot R_{eff}(t)$). This instability can be understood by considering the frequency-space representation of the data.

In most physical systems, the Fourier Transform of a noiseless signal $\mathbf{F}[g(t)] = G(\nu)$, decays towards zero as $\nu \to \infty$. However, the behaviour of the noise does not necessarily decay. For Equation [4.31], the Fourier Transform of the solution can be expressed using the convolution theorem as:

$$\mathbf{F}[\tilde{r}(t)] = \left[\frac{\mathbf{F}[C_t(t) + \mathbf{noise}]}{\mathbf{F}[C_a(t)]}\right] \qquad [4.32]$$

Thus, if $\mathbf{F}[C_a(t)] \to 0 \quad as \quad \nu \to \infty$, small changes in the high-frequency spectrum of $\mathbf{F}[C_t(t) + \mathbf{noise}]$ will be accompanied by large changes in $F[\tilde{r}(t)]$, eventually swamping the true solution $\mathbf{F}[CBF \cdot R_{eff}(t)]$. Since noise is present across all frequencies, any deconvolution of noisy data is ill-posed.

Inversion of DSC-MRI is further complicated because of discrete sampling. The noisy sample $C_t(t)$ and $C_a(t)$ have a finite frequency bandwidth, so provided there are no zero values in the discrete Fourier Transform of $C_a(t)$, there is a unique solution. However, the solution is not necessarily accurate. This is because information is lost with noise and in sampling, i.e. the $C_t(t)$ and $C_a(t)$ data are incomplete. For the simplest inversion (Equation [4.32]), small changes in the noisy $C_t(t)$ are still significantly amplified in $\tilde{r}(t)$, since the high-frequency Fourier coefficients in the denominator are still small compared with those in the numerator.

Therefore, to obtain $CBF \cdot R_{eff}(t)$, the inversion of Equation [4.31] requires some additional information. This is known as regularisation.

A stable and physically meaningful solution can only be realised using filtering or regularisation (Hansen 1994). Regularisation suppresses the high-frequency components in the data and enables a stable solution for $CBF \cdot R_{eff}(t)$ to be recovered. However, in addition to the loss of shape information introduced by the discrete sampling, suppression of high-frequency components can distort the shape of the extracted $CBF \cdot R_{eff}(t)$ further, leading to an underestimation of *CBF*. Such distortion is particularly apparent for the impulse response function deconvolved from a delayed bolus with no dispersion (see Figure 4.5). The sharp edge associated with the delay and defining the rise-to-maximum (*RTM*) is characterised by higher frequencies, which may be removed in the regularisation. In general, regularisation smoothes the edges, and in the context of DSC-MRI, causes a delayed $CBF \cdot R_{eff}(t)$ to appear dispersed.

The development of stable and accurate deconvolution methods has been an active area of research in DSC-MRI, and it is one of the issues addressed in Chapters 6 and 7 of this thesis. The following paragraphs introduce some of the model-independent deconvolution methods in common use. Each method has specific limitations, which are discussed in the context of their ability to characterise $CBF \cdot R_{eff}(t)$ and quantify perfusion.

4.8.2 DECONVOLUTION USING THE FOURIER TRANSFORM

One of the first deconvolution approaches used in DSC-MRI was the Fourier Transform (FT) (Gobbel *et al.* 1994). Since the FT of a convolution is a multiplication, Equation [4.28] can be solved as:

$$\left(CBF \cdot R_{eff}(t)\right)_{est} = \mathbf{F}^{-1}\left[\frac{\mathbf{F}\{C_t(t)\}}{\mathbf{F}\{C_a(t)\}}\right] \qquad [4.33]$$

where $\mathbf{F}^{-1}$ the inverse FT of the function in [ ]. Because of noise in the data, a stable solution to this equation can only be achieved by filtering out the high-frequency components that correspond to the small Fourier coefficients in the denominator. However, it is likely that when suppressing the experimental noise in this way, physiological information will also be lost. The FT approach to the deconvolution tends to underestimate *CBF*, especially for high flows and rapidly decaying residue functions (short *MTT*) (Østergaard *et al.* 1996b). One attraction of the FT method however, is that it is insensitive to delay between the AIF and tissue, which are common in patients with cerebrovascular disease. The intrinsic delay insensitivity of the Fourier Transform approach can be explained in terms of the Fourier shift theorem: If $\mathbf{F}[g(t)] = G(\nu)$, then $\mathbf{F}[g(t-\tau)] = e^{-2\pi\tau\nu}G(\nu)$. I.e., for a shift in time, the magnitude of the Fourier Transform remains the same, only the phase has changed. Therefore, for any delay, the same high-frequency components will be removed in the filtering process to ensure an invariant and stable solution.

4.8.3 MATRIX ALGEBRA FORMULATION OF DECONVOLUTION

Other model-independent deconvolution approaches are based on matrix algebraic techniques. If the arterial and tissue concentrations are sampled at intervals of Δt between t_0 and t_n, and assuming that $R_{eff}(t)$ and $C_a(t)$ are constant over the Δt time interval, the convolution equation (Equation [4.28]) can be discretised into matrix form (Østergaard *et al.* 1996b):

$$C_a(t_j) = \Delta t \cdot CBF \sum_{i=0}^{j} C^{est}{}_a(t_i) \cdot R_{eff}(t_j - t_i) \qquad [4.34]$$

In practice this equation is reduced to a set of linear equations:

$c = \mathbf{A}r$

$$\begin{pmatrix} C_t(t_0) \\ C_t(t_1) \\ \vdots \\ \vdots \\ C_t(t_n) \end{pmatrix} = \Delta t \cdot CBF \cdot \begin{pmatrix} C_a(t_0) & 0 & & & 0 \\ C_a(t_1) & C_a(t_0) & & & \\ \vdots & C_a(t_0) & \ddots & & \\ \vdots & \vdots & & \ddots & \\ C_a(t_n) & C_a(t_{n-1}) & \cdots & \cdots & C_a(t_0) \end{pmatrix} \cdot \begin{pmatrix} R_{eff}(0) \\ R_{eff}(t_1) \\ \vdots \\ \vdots \\ R_{eff}(t_n) \end{pmatrix} \qquad [4.35]$$

The matrix **A** has elements a_{ij} determined by the sampled AIF, vector c is the sampled tissue concentration $C_t(t)$, and vector r contains the unknown discretised product $CBF \cdot R_{eff}(t)$. In reality, $R_{eff}(t)$ and $C_a(t)$ are not constant over the sampling interval. It is possible to modify the elements of matrix **A** to produce a more accurate approximation of $R_{eff}(t)$ and $C_a(t)$ between the sample points. This is discussed further in Chapter 6.

4.8.4 DECONVOLUTION USING SINGULAR VALUE DECOMPOSITION

Due to the early simulation work done by Østergaard *et al.* comparing different deconvolution methods, the most common regularisation approach in DSC-MRI studies is truncated Singular Valued Decomposition (SVD) (Østergaard *et al.* 1996b). In SVD, a convolution matrix **A** is a real $m \times n$ matrix (where $m \geq n$) which can be decomposed into two orthogonal matrices **U** ($m \times n$) and **V** ($n \times n$), and a diagonal matrix **W** ($n \times n$), such that

$$\mathbf{A} = \mathbf{UWV}^{\mathrm{T}} \qquad [4.36]$$

and

$$\mathbf{A}^{-1} = \mathbf{VW}^{-1}\mathbf{U}^{\mathrm{T}} \qquad [4.37]$$

where

$$\mathbf{W}^{-1} = \begin{pmatrix} 1/\sigma_1 & & 0 \\ & \ddots & \\ 0 & & 1/\sigma_n \end{pmatrix} \qquad [4.38]$$

and $\sigma_1 \geq \sigma_2 \geq \ldots \geq \sigma_n$ are the diagonal elements of **W**.

The columns of **U** are called the left–singular vectors, the columns of **V** the right–singular vectors, and the diagonal elements of **W** are the singular values of the matrix **A**. The residue function is then found by solving for r

$$r = \mathbf{A}^{-1}c = \mathbf{V}\mathbf{W}^{-1}\mathbf{U}^{\mathsf{T}}c = \sum_{i=1}^{n}\left(\frac{u_i^{\,T}\cdot c}{\sigma_i}\right)\cdot v_i \qquad [4.39]$$

where u and v are the singular vectors corresponding to the orthogonal SVD matrices **U** and **V** respectively (Hansen 1994).

Because of discrete sampling, the slowly-varying portion of the arterial data (AIF time-course) is well described, while structures on fine scales or with high-frequency components are poorly represented. This is typical for all measurement processes. The singular vectors associated with the large singular values will tend to be smooth, while those associated with the small singular values will tend to be highly irregular or oscillatory (Hansen 1994). Consequently, upon inversion, these high frequencies (which can often be synonymous with noise) are amplified by their σ_i^{-1} factor, resulting in a very large random component that can completely dominate the solution. In other words, it is the diagonal elements of **W**, which are near to or equal to zero, which cause the estimated solution $\tilde{r}$ to be unstable. The rate at which the singular values of **A**, σ_i, decrease with index i, determines how ill-posed the problem is, therefore indicating how much useful information can be reconstructed from the sampled noisy data. If the singular values decrease rapidly, a high SNR is necessary for a good reconstruction.

Discarding the small singular values and replacing the corresponding diagonal entries $1/\sigma_i$ in $\mathbf{W}^{-1}$ with 0, restricts the inversion range of $\mathbf{A}$ (i.e. it reduces the number of possible solutions), yielding a more robust solution with smaller residual error ($\left\|\mathbf{A}r^{SVD} - c\right\|$). This approach is known as truncated SVD or TSVD.

In the deconvolution of DSC-MRI data, a stable TSVD solution is achieved using a fixed (Østergaard *et al.* 1996b) or adaptive (Liu *et al.* 1999) singular value threshold that depends either on SNR, or seeks to minimise oscillation in $\tilde{r}$ (Wu *et al.* 2003). The optimum threshold will actually depend on many factors including the SNR and actual shape of the impulse response function being extracted.

Calamante *et al.* (Calamante *et al.* 2003a) demonstrated using simulations that the TSVD reconstructions of a smoothly varying exponentially decaying $R(t)$, and the smoothly varying dispersed $R_{eff}(t)$ are not particularly accurate. Figure 4.13 illustrates their findings. It can be seen in Figure 4.13a that TSVD underestimates the maximum (and hence *CBF*) for the true residue function (undistorted by delay and dispersion in the vascular transport). Figure 4.13 demonstrates that the truncation of the high-frequency components in TSVD introduces oscillations in the reconstruction, adding to the distortion of reconstruction in both simulations. In addition, the accuracy of the *CBF* estimates are highly dependent on blood flow (Østergaard *et al.* 1996b) and the presence of delay (Calamante *et al.* 2000). Although the characterisation of $R_{eff}(t)$ using TSVD is not accurate enough to be able to identify and distinguish delay and dispersion in perfusion measurements, in healthy tissue SVD has been shown to give a good estimate of *CBF* (Østergaard *et al.* 1996b).

4.8.5 DECONVOLUTION USING TIKHONOV REGULARISATION

Tikhonov regularisation is an alternative deconvolution method to measure *CBF*, first presented by Calamante *et al.* (Calamante *et al.* 2003a). The truncation of singular

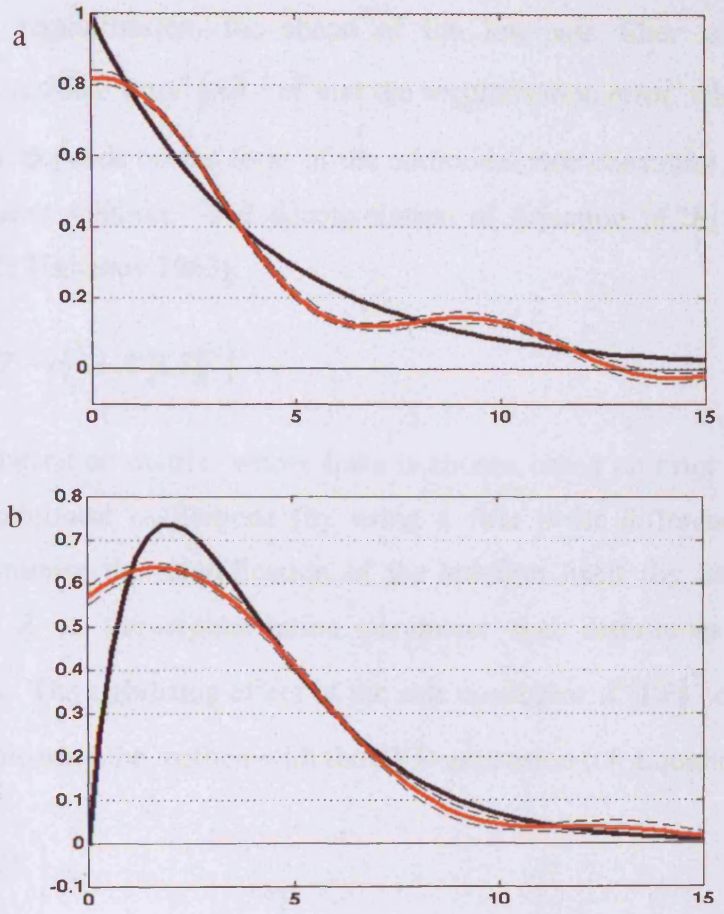

Figure 4.13: Mean solutions (for 100 simulations, CNR=20) for two models of the impulse response function calculated using the conventional TSVD. a): exponential, b): dispersed exponential. The black solid lines indicate the simulated functions (*MTT*=4s, *CBF*=60ml/100g/min), the red solid lines the mean solutions, and the dashed lines a single standard deviation of the solutions. The horizontal axes correspond to time (in seconds). The vertical axes correspond to the residue function (dimensionless). TSVD solutions exhibit oscillations and a poor shape characterisation. Reproduced from (Calamante *et al.* 2003a).

values in the SVD solution may be described in terms of filter factors f_i for each singular value that are either 0 or 1 depending on whether the singular value is below or above the chosen threshold. The oscillations introduced by truncating the singular values may be attenuated using a smoother cut-off defined by filter factors f_i that tend to zero as the corresponding σ_i decreases (Hansen 1994; Tikhonov 1963).

In Tikhonov regularisation, the shape of the low-pass filter is determined by balancing the residual error $\|\mathbf{A}\tilde{r} - c\|$ and the regularisation error, which in Tikhonov regularisation, depends on the form of the additional side constraint used to stabilise the least squares solution. The deconvolution of Equation [4.28] is expressed as (Hansen 1992; Tikhonov 1963):

$$\tilde{r}_\lambda = \min_r \left\{ \|\mathbf{A}\tilde{r} - c\|^2 + \lambda^2 \|\mathbf{L}\tilde{r}\|^2 \right\} \qquad [4.40]$$

L is the regularisation matrix, whose form is chosen based on prior information, for example to minimise oscillations (by using a first order difference operator), or simply to minimise the amplification of the solution itself (by using the identity matrix, **I**). λ is the regularisation parameter that determines the degree of regularisation. The stabilising effect of the side constraint $\lambda^2\|\mathbf{L}\tilde{r}\|^2$ can be seen most clearly by comparing the method with the SVD expansion (cf. Equation [4.39])

$$r = \sum_{i=1}^{s} f_i \left(\frac{u_i^T \cdot c}{\sigma_i} \right) \cdot v_i \qquad [4.41]$$

In the same way as SVD regularisation truncates the expansion with a singular value threshold, Tikhonov regularisation uses a λ-dependent smooth attenuation for the high frequencies. For example, for **L** = **I** (Hansen 1994):

$$f_i = \frac{\sigma^2{}_i}{\sigma^2{}_i - \lambda^2} \qquad [4.42]$$

Just as truncated SVD requires the selection of the singular value threshold, Tikhonov regularisation requires the regularisation parameter λ to be chosen. Various methods were proposed to determine this parameter. One of the most common is the L-curve (Hansen 1992). The L-curve is an L-shaped curve that results from plotting the residual norm $\|\mathbf{A}\tilde{r} - c\|$, against the constraint norm $\|\mathbf{L}\tilde{r}\|$ and is schematically

illustrated in Figure 4.14. In the vertical section, the constraint norm $\|\mathbf{L}\tilde{r}\|$ is very sensitive to changes in the regularisation parameter λ, since the solution r^{tikh} will change to fit the data better. The vertical section of the 'L' corresponds to low filtering (small values of $\|\mathbf{A}\tilde{r} - c\|$) and accordingly, $\tilde{r}$ is determined from the division by small singular values, σ, corresponding to inadequate regularisation. In the horizontal section $\|\mathbf{L}\tilde{r}\|$ is almost constant, i.e. the highly filtered solutions do not change much. However, the residual norm $\|\mathbf{A}\tilde{r} - c\|$ increases rapidly with more filtering. The corner of the L-curve has been proposed as the finding the solution that gives the best compromise.

It has been shown that Tikhonov regularisation improves the characterisation of $CBF \cdot R_{eff}(t)$ compared with TSVD (Calamante *et al.* 2003a). By carefully formulating the convolution matrix **A**, the maximum of the true residue function (undistorted by delay and dispersion in the vascular transport) is accurately recovered. In addition, the smooth low-pass filter minimises the oscillation and successfully characterises the shape in the presence of dispersion. However, the characterisation of $CBF \cdot R_{eff}(t)$ using Tikhonov regularisation deteriorates in the presence of bolus delay, retaining the smooth characteristics of regularisation, which prevents the accurate characterisation of delay. Therefore, the characterisation of $CBF \cdot R_{eff}(t)$ using Tikhonov regularisation is not accurate enough to be able to identify and distinguish delay and dispersion in perfusion measurements.

4.8.6 DECONVOLUTION USING A BLOCK CIRCULANT MATRIX

Bolus delay is common in patients with vascular abnormalities and can lead to a severe underestimation of perfusion. Calamante *et al.* performed simulations using SVD and showed *CBF* is underestimated by 35% for 1.5-2 seconds delay (Calamante *et al.* 2000). The above formulation of the matrix algebra problem is intrinsically sensitive to delay. Wu *et al.* proposed a reformulation of the convolution matrix,

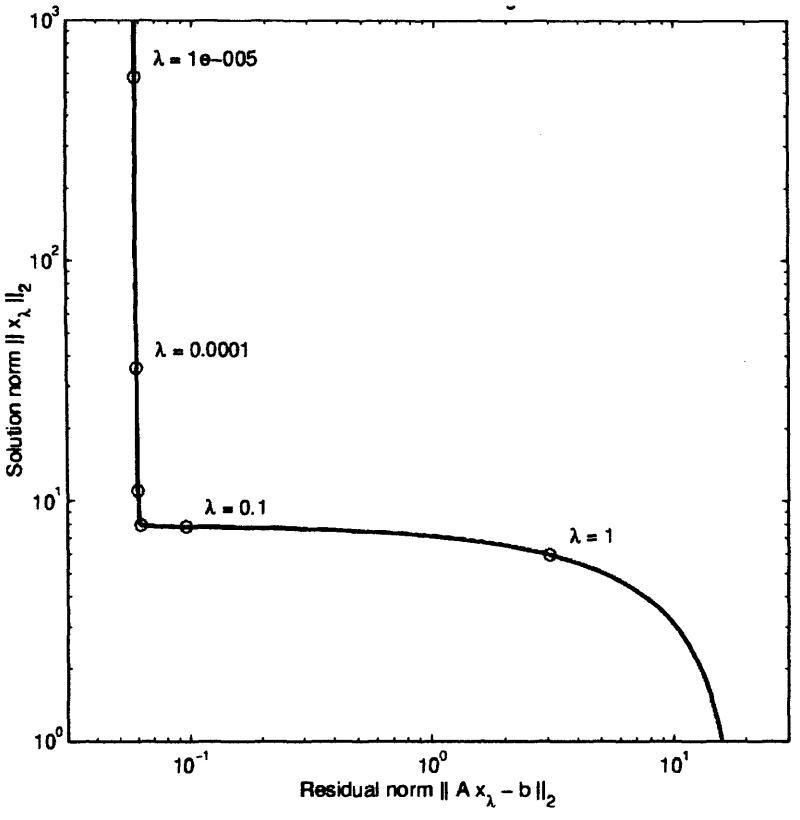

Figure 4.14: Generic L-curve for standard form Tikhonov regularisation where L=I, plotted for regularisation parameters λ=1, 10^{-1}, 10^{-2}, 10^{-3}, 10^{-4}, and 10^{-5}. A good solution for x resides just right of the corner. Reproduced from (Hansen 1992).

such that the maximum of the impulse response function is independent of bolus delay (Wu *et al.* 2003).

In delay sensitive methods, the deconvolution matrix a_{ij} of **A** take the basic form (cf. Equation [4.35]):

$$a_{ij} = \begin{cases} \Delta t C_{AIF}(t_{i-j}) & 0 \le j \le i \le n-1 \\ 0 & \text{otherwise.} \end{cases} \qquad [4.43]$$

Using this formulation, all matrix based deconvolution methods such as SVD and Tikhonov are sensitive to bolus delay. Delay sensitivity can be overcome by using a block-circulant matrix. Circular deconvolution is achieved by zero-padding the *n*-

point time series $C_a(t)$ and $C_t(t)$ to double their length, and replacing matrix **A** with a block-circulant matrix **D**, whose elements are:

$$d_{i,j} = \begin{cases} a_{i,j} & j < i \\ a_{2N+i-j,0} & otherwise \end{cases} \qquad [4.44]$$

$$\mathbf{D} = \begin{pmatrix} C_a(t_0) & 0 & \vdots & \vdots & 0 & 0 & C_a(t_n) & \vdots & \vdots & C_a(t_1) \\ C_a(t_1) & C_a(t_0) & 0 & \vdots & \vdots & 0 & 0 & C_a(t_n) & \vdots & \vdots \\ \vdots & C_a(t_1) & C_a(t_0) & 0 & \vdots & \vdots & 0 & 0 & C_a(t_n) & \vdots \\ \vdots & \vdots & C_a(t_1) & C_a(t_0) & 0 & \vdots & \vdots & 0 & 0 & C_a(t_n) \\ C_a(t_n) & \vdots & \vdots & C_a(t_1) & C_a(t_0) & 0 & \vdots & \vdots & 0 & 0 \\ 0 & C_a(t_n) & \vdots & \vdots & C_a(t_1) & C_a(t_0) & 0 & \vdots & \vdots & 0 \\ 0 & 0 & C_a(t_n) & \vdots & \vdots & C_a(t_1) & C_a(t_0) & 0 & \vdots & \vdots \\ \vdots & 0 & 0 & C_a(t_n) & \vdots & \vdots & C_a(t_1) & C_a(t_0) & 0 & \vdots \\ \vdots & \vdots & 0 & 0 & C_a(t_n) & \vdots & \vdots & C_a(t_1) & C_a(t_0) & 0 \\ 0 & \vdots & \vdots & 0 & 0 & C_a(t_n) & \vdots & \vdots & C_a(t_1) & C_a(t_0) \end{pmatrix}$$

Although the block-circulant SVD yields delay-insensitive estimates of the *CBF*, the accuracy of these measurements is actually dependent on the *MTT* of the $R_{eff}(t)$ being recovered. The *CBF* underestimation is greater for a smaller *MTT*. For *MTT*=4s, block-circulant SVD underestimated *CBF* by ~40%, independent of the amount of delay (Wu *et al.* 2003). In addition, the $R_{eff}(t)$ are distorted by the characteristic TSVD oscillations. Consequently, a delayed bolus cannot be distinguished from a dispersed bolus, and therefore a correction of the underestimation would be difficult. Nevertheless, this technique is useful for obtaining relative perfusion measurements across the brain when delays are expected. It is however important to realise that these estimated perfusion values are likely to underestimate the true values.

4.8.7 DECONVOLUTION USING MAXIMUM-LIKELIHOOD EXPECTATION-MAXIMISATION

A different approach for the deconvolution of Equation [4.28] is using maximum-likelihood expectation-maximisation (ML-EM), which seeks to improve the balance between the residual norm and the regularisation error (Dempster AP *et al.* 1977). Since a major part of the work in this thesis is based on this approach, it will be presented in more detail.

4.8.7.1 General Overview of ML-EM

A set of parameters describing a system may be estimated from measurement observations of the system. The problem becomes ill-posed when the observed data are incomplete, for example due to sampling and corruption by noise (see Section 4.8.1). The notion of *incomplete* data includes the conventional sense of missing data, but also applies to situations where the *complete* data represents what would have been available from some hypothetical experiment. The ML-EM algorithm calculates the most likely set of parameters by iteratively adjusting estimates of the parameters in order to maximise the expectation (probability) of the data. The algorithm consists of two steps. 1) The E-step, which calculates the expectation of the data given an estimate for the set of unknown parameters. 2) The M-step, which updates the parameters in order to maximise the expectation of the data. In DSC-MRI, the data are the concentration time-courses, and the set of unknown parameters is the impulse response function.

4.8.7.2 ML-EM for DSC-MRI Perfusion Quantification

For the specific problem of DSC-MRI data, the most likely form of r (the impulse response function $CBF \cdot R_{eff}(t)$) is iteratively determined by repeating the E- and M-steps (Vonken *et al.* 1999a). The observed incomplete data are the tissue contrast

concentration time-course, $C_t(t)$, and the AIF, $C_a(t)$, both of which contain noise from the system and are discretely sampled at TR. The observed data are contained in vector *c* and the convolution matrix **A** (Equation [4.35]). The unknown parameters to be estimated are the elements of vector *r*. *c* is governed by a probability density function (pdf), $g(c|r,\mathbf{A})$, which describes the likelihood of measuring *c* given the parameters governing the system. In DSC-MRI, the 'parameters' governing the form of *c* are the vector values of *r*, and matrix values of **A**. A complete-data vector *x*, can be defined, which theoretically contains all the information necessary to determine *r*. The pdf for the complete data vector is $f(x|r)$.

Because the observed data are incomplete, there is a many-to-one mapping from the complete-data sample space *X*, to the observation (incomplete-data) space *Y*. The observations *c* and **A**, (represented here as observation vector *y*) are contained within the observation space *Y*, $y \subset Y$. The complete data vector *x* (which is the inverse mapping of *y*) is contained within the subset of *X* defined by *y*, $x \subset X(y) \subset X$. Thus, the inverse of *y* has many possible mappings within $X(y)$ (Moon 1996). This situation is schematically illustrated in Figure 4.15. Hence the pdf of the incomplete data $g(c|r,\mathbf{A})$ is the sum over the pdf of the complete data $f(x|r)$ for all the possible mappings of the incomplete data $X(c,\mathbf{A})$.

$$g(c|r,\mathbf{A}) = \int_{X(c,\mathbf{A})} f(x|r)dx \qquad [4.45]$$

Or in discrete form

$$g(c|r,\mathbf{A}) = \sum_{X(c,\mathbf{A})} f(x|r) \qquad [4.46]$$

If in some hypothetical experiment the data were fully observable, the system parameters could be determined by maximising the log likelihood function for *r*, $l_x(r) = \ln f(x|r)$. Since *x* is in fact unobservable, it is necessary to maximise $\ln f(x|r)$

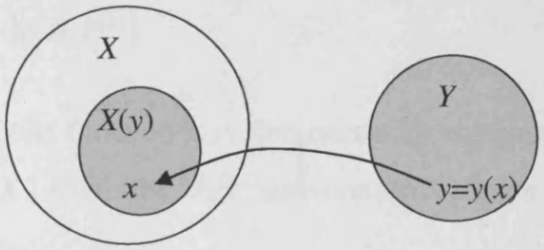

Complete Data (available from some hypothetical experiment)

Incomplete Data (actually observed in a real experiment)

Figure 4.15: Schematic representation of the 'many-to-one' problem that is the ill-posed deconvolution of DSC-MRI data. The right hand shaded circle, labelled *Y* represents the 'incomplete-data' (observation) space, from which the measurements of the dynamic contrast are made. The realisation of the measurements is represented by the observation vector *y* (contained in *Y*). Because of sampling and noise in the data, there are many possible inverse mappings of these observations *y* to the solution. The left hand white circle represents the 'complete-data' space, labelled *X*, and the grey circle within this represents the possible solutions $X(y)$, given the observation vector *y*. The complete data vector *x*, (contained in $X(y)$) is the hypothetical (true) solution to the inverse problem. The arrow indicates the inverse mapping of *y*, to the true solution *x*. The pdf of the incomplete data $g(y|x)$ is the sum of the complete data pdf $f(x)$ over all the possible mappings, $X(y)$.

given the observations *y* (*c* and **A**), and the current estimate for *r* (this is the *conditional* likelihood).

As mentioned before, the ML-EM algorithm consists of two steps, the expectation, E-step, and the maximisation, M-step. The E-step uses current estimates of the parameters *r* to reconstruct an estimate of the unobservable data *x*. Assuming a distribution for $f(x|r)$, the conditional likelihood function can then be estimated. Let $\tilde{r}^{[k]}$ be the estimate of the parameters at the k^{th} iteration. The E-step calculates the conditional expectation function, (the log likelihood $\ln f(x|r)$, given *c*, **A** and $\tilde{r}^{[k]}$) (Vonken *et al.* 1999a):

$$Q(r,\tilde{r}^{[k]}) = E\left[\ln f(x|r)\middle|c,\mathbf{A},\tilde{r}^{[k]}\right] \qquad [4.47]$$

In order to calculate this function it is first necessary to construct the complete-data subset $x \subset X(y) \subset X$ from the AIF convolution operator $\mathbf{A}$ with elements a_{ij} (Vonken *et al.* 1999a):

$$x_{ij} = a_{ij}\tilde{r}_j \qquad [4.48]$$

Combining Equations [4.46] and [4.48] reveals that the data which would have been observed if $\tilde{r}_j^{[k]}$ were the parameters is (Vonken *et al.* 1999a):

$$\tilde{c}_i = \sum_j x_{ij} = \sum_j a_{ij}\tilde{r}^{[k]}{}_j \qquad [4.49]$$

In the ML-EM algorithm adapted by Vonken *et al.* (Vonken *et al.* 1999a) the conditional probability of the complete data x_{ij}, assuming Gaussian noise is stated as:

$$P(x_{ij}) \sim \exp\left[-\frac{\left(a_{ij}\tilde{r}_j^{[k]} - N_{ij}\right)^2}{2\sigma^2}\right] \qquad [4.50]$$

where N_{ij} is the conditional (upon $\tilde{r}_j^{[k]}$, c and $\mathbf{A}$) expectation value of x (i.e $E\left[x_{ij}\middle|c,\tilde{r}^{[k]}\right]$), which in the work by Vonken *et al.* is stated as:[5]

---

[5] It should be noted that the Gaussian distribution of the complete data x_{ij} should in fact be $P(x_{ij}) \sim \exp\left[-\frac{\left(a_{ij}\tilde{r}_j^{[k]} - x_{ij}\right)^2}{2\sigma^2}\right]$, leading to the non-linear term $\left(a_{ij}\tilde{r}_j^{[k]} - x_{ij}\right)^2$. For a more accurate algorithm, this term should be expanded and expressions for both conditional expectations $E\left[x_{ij}\middle|c,\tilde{r}^{[k]}\right]$ and $E\left[x_{ij}{}^2\middle|c,\tilde{r}^{[k]}\right]$ should be used in the calculation. In addition, the result, $E\left[x_{ij}\middle|c,\tilde{r}^{[k]}\right] = N_{ij} = \frac{c_i x_{ij}}{\tilde{c}_i}$, is taken directly from work by Lange *et al.* (Lange *et al.* 1984) who applied the ML-EM technique to PET perfusion quantification. The derivation of this result is based on the assumption of a Poisson distribution $x_{ij} \sim Poisson\left(a_{ij},\tilde{r}_j^{[k]}\right)$ rather than the Gaussian distribution, which is more appropriate in the DSC-MRI context. The result however serves as a

$$N_{ij} = \frac{c_i x_{ij}}{\tilde{c}_i} \qquad [4.51]$$

Given c, $\mathbf{A}$ and $\tilde{r}^{[k]}$, the complete data pdf is:

$$f(x|r) = \Pi_i \Pi_j P(x_{ij}) \qquad [4.52]$$

Accordingly, the E-step of the ML-EM algorithm becomes:

$$Q(r|\tilde{r}^{[k]}) = E[\ln f(x|r)|c, \mathbf{A}, \tilde{r}^{[k]}] = \sum_i \sum_j \ln P(x_{ij}) = \sum_i \sum_j (a_{ij}\tilde{r}_j^{[k]} - N_{ij})/2\sigma_{ij}^2 \qquad [4.53]$$

The M-step uses the current estimate $\tilde{r}^{[k]}$ to revise the estimation of r. The conditional expectation function $Q(r, \tilde{r}^{[k]})$ is maximised with respect to r while $\tilde{r}^{[k]}$ is known and regarded as fixed. $\tilde{r}^{[k+1]}$ is the value which maximises $Q(r, \tilde{r}^{[k]})$ (Vonken *et al.* 1999a).

$$\tilde{r}^{[k+1]} = \arg\max_r Q(r, \tilde{r}^{[k]}) = \arg\max_{\tilde{r}^{[k]}} \{E[\ln f(x|r)|c, \mathbf{A}, \tilde{r}^{[k]}]\} \qquad [4.54]$$

This is calculated by taking partial derivatives of Equation [4.53] with respect to r_j and equating to zero. If all σ are equal (Vonken *et al.* 1999a):

$$\sum_i a_{ij}(a_{ij} r_j - N_{ij}) = 0 \qquad [4.55]$$

Equation [4.55] can be solved using a Newton Raphson method for the updated $\tilde{r}^{[k+1]}$. The E- and M-steps of the ML-EM algorithm are repeated until some convergence criteria are met, i.e. when $(\tilde{r}^{[k+1]} - \tilde{r}^{[k]})/\tilde{r}^{[k]} \leq \varepsilon$.

satisfactory approximation. If the above two considerations were incorporated into the algebra, the resultant formula for the E-step and subsequent M-step are long and computationally difficult.
Given that Vonken *et al.* found that the ML-EM algorithm using Equation [4.50] was successful in its recovery of the impulse response function, for ease of implementation, the same formulation will also be used in this thesis. It should be noted however that the algorithm does harbour some instabilities and an erroneous impulse in the end of the tail of the extracted impulse response function. This impulse does not however affect the previous elements, and can be overcome by setting the final elements to zero. Such problems may be attributable to the incorrect formulation of the algorithm.

Theoretically, the optimum point to stop the iterations is when the root mean squared (RMS) error in r is minimised (Kontaxakis G *et al.* 1998).

$$RMS(r)=\sqrt{\left[\sum_j\left(\tilde{r}_j^{[k]}-r_j\right)^2/\sum_j\left(\tilde{r}_j^{[k]}\right)^2\right]} \qquad [4.56]$$

This criterion cannot be used when the ML-EM reconstruction is from real data where r is not *a priori* known. An alternative measure is to calculate the residual norm (RN) agreement between the estimated and measure tissue (Kontaxakis G *et al.* 1998).

$$RN(r)=\sum_j\left(\tilde{c}_j^{[k]}-c_j\right)^2 \qquad [4.57]$$

Minimising $RN(r)$ yields the least squares solution. Given an initial uniform (k=0) guess $\tilde{r}^{[0]}$ (a small non-zero constant), the initial decrease in $RMS(r)$ is rapid, as the updated r increases in likelihood, as measured by Equation [4.53]. In the ML-EM algorithm, low spatial frequencies converge faster than higher ones, so that after the initial rapid convergence, the higher frequency components are reconstructed, and inevitably statistical noise starts to deteriorate the reconstruction as the least squares solution is realised. At this point $RMS(r)$ error begins to increase. The function $RN(r)$ is a constantly decreasing function with iteration number (Kontaxakis G *et al.* 1998). Consequently it is not possible to measure the quality of the reconstruction of r using the above criteria. Therefore, a key step in the ML-EM method is the selection of stopping criteria for the iteration. Further discussion of the convergence characteristics and suitable stopping criteria for ML-EM applied to DSC-MRI is given in Chapter 6.

The optimum number of iterations, (which minimises $RMS(r)$, and hence gives the most accurate estimate of the impulse response function), is found to be dependent on the underlying shape of the function being reconstructed, on the signal to noise ratio and on the temporal sampling resolution. Chapters 6 and 7 propose two different

automated ML-EM based methods which seek to minimise $RMS(r)$ across the brain for a wide variety of pathologies.

5 VALIDATION OF PERFUSION ANALYSIS METHODS

5.1 INTRODUCTION

DSC-MRI is the most common MR method used to quantify perfusion, and various methods have been proposed to analyse the data. However, the accuracy of the various analysis techniques cannot be determined by applying them to clinical data, since the true perfusion in a subject is not known *in vivo*. In addition, perfusion values can vary significantly between subjects, especially in the presence of vascular pathology, but also between normal volunteers. Unless the true perfusion values are known, the reliability of the perfusion estimates is uncertain.

A comparison of DSC-MRI perfusion estimates with another established technique, such as positron emission tomography (PET) is one means of validating the DSC-MRI analysis method (Østergaard *et al.* 1998a; Kaneko *et al.* 2004). PET (see Section 3.4.1) is considered to be the *in vivo* 'gold-standard' of *CBF* measurement techniques, but is not in widespread clinical use. Moreover, it involves ionizing radiation and is subject to other sources of error. Therefore, an alternative means of validation is needed for techniques used to analyse DSC-MRI data. In addition to validating the accuracy of the analysis, it is also important to know the technique's limitations, robustness and requirements, which cannot be assessed using *in vivo* data alone.

For these reasons, DSC-MRI data are simulated to model an *in vivo* situation, using realistic function and parameter values for perfusion (*CBF*, *MTT*, *CBV*, $R(t)$), vascular transport (bolus delay, dispersion, $VTF(t)$) and MR imaging (TE, TR, SNR etc). Since in the simulated data the true values of these parameters and functions are known, the accuracy and robustness of the analysis technique in recovering them from the simulated data can be investigated over many iterations, and across a broad range of values. In fact, testing on simulated data sets has become a crucial step in the development of DSC-MRI analysis techniques e.g. (Østergaard *et al.* 1996b; Andersen *et al.* 2002; Liu *et al.* 1999; Wu *et al.* 2003; Wirestam *et al.* 2005; Vonken *et al.* 1999a; Calamante *et al.* 2000; Østergaard *et al.* 1999; Calamante *et al.* 2003a;

Sourbron *et al.* 2004; Willats *et al.* 2006; Mouridsen *et al.* 2006b). The analysis methods developed in this thesis (Chapters 6 and 7) were tested on the simulated data set described in the first half of this chapter.

Although simulations provide the best means of validating an analysis method and determining the limitations and requirements, the method must also be applied to *in vivo* patient data. While the true answer is not known *in vivo*, the analysis of such data are complementary to the simulations, since the findings from analysing simulated data can be used to help interpret clinical cases. In addition, since the simulated data are purely determined from models of the microvascular and arterial retention, analysis of patient data are important to either verify or refute the modelled behaviour (see Chapter 8). The analysis methods developed in this thesis were also tested on a variety of *in vivo* data, from subjects with various cerebral arterial and perfusion abnormalities. Before the analysis is performed, several pre-processing steps are applied to the DSC-MRI data. These steps are common to all the analyses and are described in the second half of this chapter.

5.2 SIMULATIONS

In order to simulate *in vivo* DSC-MRI data, models are assumed for microvascular retention (i.e. the residue function $R(t)$), the arterial transport (i.e. the vascular transport function *VTF*), and the measured arterial input function (AIF). These models, together with the parameter ranges used in their simulation, are described in the following sections.

5.2.1 RESIDUE FUNCTION

The form of the scaled tissue residue function $CBF \cdot R(t)$ supplies valuable information about the integrity of the tissue. Provided the measured AIF accurately

represents the true input to the tissue, $CBF \cdot R(t)$ is extracted from the deconvolution of *in vivo* data. However, because there are errors in the deconvolution (see Section 4.7), the form of $R(t)$ is not precisely known, even in this ideal situation. Therefore its shape is still somewhat speculative (see Section 4.6.2), and has been an active area of research through simulation e.g. (Østergaard *et al.* 1999; Mouridsen *et al.* 2006b) and *in vivo* measurement e.g.(Calamante *et al.* 2003a; Willats *et al.* 2006).

Although the function describing $R(t)$ *in vivo* is not known, it is in general recognised to be a decreasing function of time with $R(0)=1$ and $R(\infty)=0$ (Østergaard *et al.* 1999; Mouridsen *et al.* 2006b; Calamante *et al.* 2003a; Willats *et al.* 2006). The precise shape will vary significantly between regions of healthy and ischaemic tissue, and between different subjects. Common models for $R(t)$ are described in Section 4.6.4.

For ease of comparison with other studies, the most commonly used $R(t)$ model was chosen for this work: $R(t)$ has been modelled as a decaying exponential (Equation [4.12]):

$$R_{exp}(t)=e^{\left(\frac{-t}{MTT}\right)} \qquad [5.1]$$

where *MTT* is the mean transit time of blood through the tissue. A smaller *MTT* defines a sharper residue function.

In order to simulate a broad range of physiological tissue states, $R(t)$ were simulated for a realistic range of *MTT* values. The range of *MTT* used to define $R(t)$ in Equation [5.1] were calculated from the central volume theorem (see Section 4.6.9) by varying the *CBF* in the range 10-80ml/100g/min in steps of 10ml/100g/min and the *CBV* in the range 1-6ml/100g in steps of 1ml/100g. In particular 4 combinations of *CBF* and *CBV* were considered: *CBF*=60ml/100g/min and *CBV*=4ml/100g were used to represent healthy (normal) grey-matter (GM) perfusion values;

CBF=20ml/100g/min and *CBV*=3ml/100g for ischaemic GM perfusion values; *CBF*=20ml/100g/min and *CBV*=3ml/100g for healthy (normal) white-matter perfusion values; and *CBF*=50ml/100g/min and *CBV*=6ml/100g for autoregulated GM perfusion values (Baird *et al.* 1998; Calamante *et al.* 1999b; Rempp *et al.* 1994; Schreiber *et al.* 1998).

5.2.2 ARTERIAL INPUT FUNCTION

A gamma-variate function has been proposed as a good model for the first pass of the AIF, (Thompson *et al.* 1964). The equation of the gamma-variate is:

$$C_a(t) = C_0(t - t_0)^a e^{-b(t-t_0)} \qquad [5.2]$$

C_0 determines the amplitude of the AIF, t_0 is the bolus arrival time, a primarily determines how steeply the AIF time-course reaches the maximum, and b mainly determines the shape of the tail (in the absence of recirculation). The coupling of these a and b parameters enables a wide range of shapes to be defined.

Based on typical *in vivo* data, Østergaard *et al.* (Østergaard *et al.* 1996b) suggested that a typical and realistic shape for the first pass of the AIF measured in a major artery (such as the middle cerebral artery or MCA) is given by the curve

$$C_a^{est}(t) \propto t^3 e^{-1.5t} \qquad [5.3]$$

The arrival time of the bolus is defined as time zero. $C_a^{est}(t)$ is only an *estimate* of the true arterial input function since the bolus shape may become distorted in its transit to the tissue (see Section 4.7.2).

In order to give a realistic representation of an AIF measured *in vivo*, the curve used in the deconvolution must be sampled at intervals of TR. Additionally, the recirculation of the bolus must be included, which is usually seen as a second wider delayed peak. In this work the recirculation was simulated by numerically

convolving the gamma-variate first passage with a decaying exponential of time constant of 30s, delayed by 10s with respect to the first bolus (Østergaard *et al.* 1996b). Figure 5.1 illustrates the simulated AIF with recirculation.

5.2.3 VASCULAR TRANSPORT FUNCTION

In vivo, it is difficult to measure the exact input function to the tissue. Consequently, what is extracted from the deconvolution of the DSC-MRI concentration data with measured AIF is the scaled effective residue function, or impulse response, $CBF \cdot R_{eff}(t)$. This more realistic *in vivo* situation is simulated by defining a function to describe the vascular transport. The effective residue is the convolution of the true tissue residue function and the *VTF* (see Section 4.7.2):

$$R_{eff}(t) = R(t) \otimes VTF(t) \qquad [5.4]$$

The exact form of the *VTF* will depend on the arterial path that the bolus travels and on the presence and severity of any cerebral arterial abnormalities

The vascular transport model chosen to simulate the delay and dispersion of the bolus is a delayed exponential decay (see Section 4.7.2), which has been extensively used to correct for dispersion in MRI and PET studies (Calamante *et al.* 2000; Iida *et al.* 1986).

$$VTF(t - t_{delay}) = \frac{1}{\beta} e^{-\frac{(t - t_{delay})}{\beta}} \qquad [5.5]$$

t_{delay} represents the bolus delay and β is the bolus dispersion parameter, or the mean vascular transit time (MVTT). This parameter determines the distortion of the bolus. A larger β corresponds to a larger dispersion.

In order to simulate the effect of vascular transport through a range cerebral arterial abnormalities, the bolus dispersion, β was varied from 0-6s in intervals of 1s

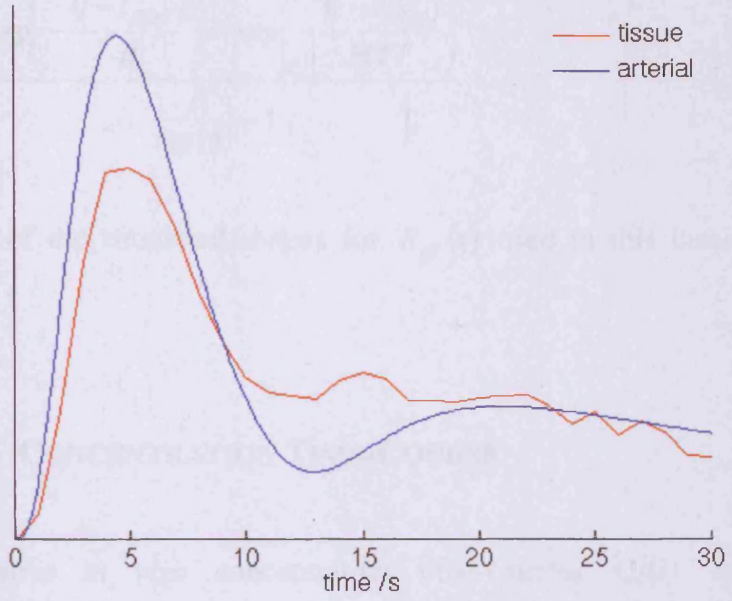

Figure 5.1: The blue curve is the AIF simulated from the gamma variate function Equation [5.3], with recirculation (see Section 5.2.2), The red curve is the tissue concentration time-course, simulated for MTT=4s, CBF=60ml/100g/min, t_{delay}=0s and β=0s, TR=1.5s, SNR=100 (see Section 5.2.4).

(Calamante *et al.* 2000), and the bolus delay t_{delay} was varied independently from 0 – 4s in intervals of 0.5s.

In practice, for the formation of the simulated data set, $R_{eff}(t)$ was calculated from the *analytical* convolution of Equations [5.3] and [5.1] (Calamante *et al.* 2000):

$$R_{eff}(t) = \frac{\exp\left(-\frac{(t - t_{delay})}{\beta}\right) - \exp\left(-\frac{(t - t_{delay})}{MTT}\right)}{\frac{\beta}{MTT} - 1} \qquad [5.6]$$

Examples of the simulated shapes for $R_{eff}(t)$ used in this thesis are illustrated in Figure 5.2.[6]

5.2.4 CONCENTRATION TIME-COURSE

Representative *in vivo* concentration time-courses $C_t(t)$ were simulated by performing the *numerical* convolution of $CBF \cdot R_{eff}(t)$ and the AIF with recirculation, (Equation [4.28]):

$$C_t(t) = \frac{\rho}{k_H} CBF \cdot \left(C^{est}{}_a(t) \otimes R_{eff}(t)\right) \qquad [5.7]$$

For simplicity, the ratio $\frac{\rho}{k_H}$ was taken as 1.0. The convolution was implemented as a matrix multiplication (Equation 4.3.5) with a sampling interval of 0.01s in order to minimise discretisation errors. Using every combination of the 11 delay, 7 dispersion, 8 *CBF* and 6 *CBV* values described above, 11x7x8x6 = 3696 unique tissue concentration time-courses $C_t(t)$ were calculated

[6] It should be noted that the effective reside functions $R_{eff}(t)$ simulated in this work have been chosen to represent a physically realistic situation. The true residue function $R(t)$ is expected to be a decreasing function of time (no delay or dispersion) (Equation [5.1]). Distortion of the bolus a due to vascular transport may result in a sharp rising edge cause by delay, and/or a skewed bell-shaped appearance caused by dispersion. Another common model for the residue function is a top-hat. This model has not been simulated because the plug flow that it represents is unlikely to occur in practice. The performance of an analysis technique to recover a top-hat shaped function would not be indicative of its accuracy in analysing *in vivo* DSC-MRI data.

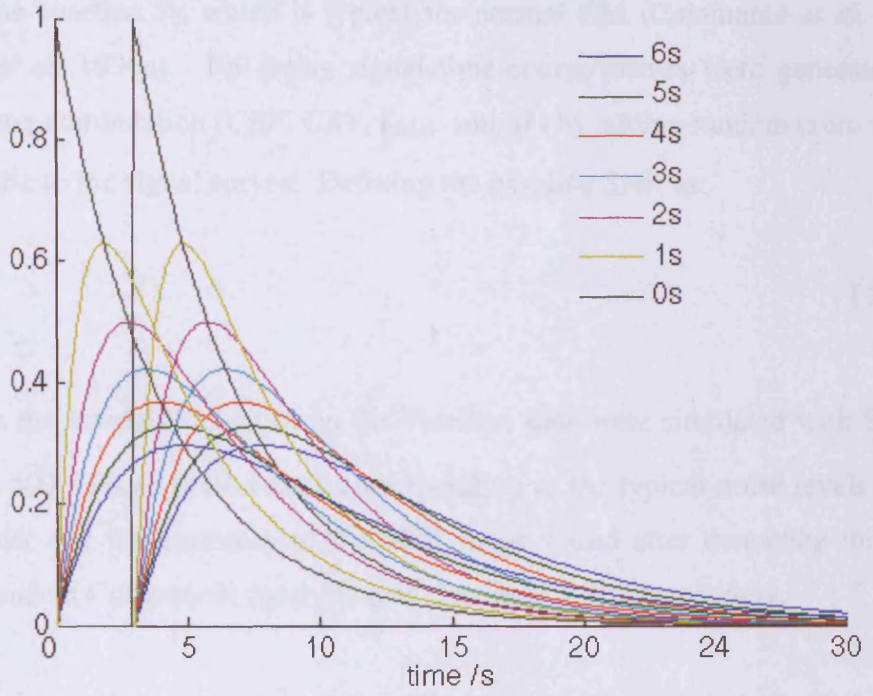

Figure 5.2: An illustrative sample of some of the shapes simulated for $R_{eff}(t)$ using Equation [5.6]. In the figure, $R_{eff}(t)$ is simulated with MTT=4s, and CBF=60ml/100g/min. The dispersion parameter was ranged from from β=0s to 6s (as labelled in the legend) and delays, t_{delay} = 0 and 3s are shown.

In a DSC-MRI experiment, the measured *in vivo* data are actually signal intensities. In order to realistically model the noise in the data, the tissue concentration time-course curves $C_t(t)$ first be converted into signal intensity curves $S_t(t)$. The $S_t(t)$ curves were generated assuming a linear relationship between the vascular concentration of the tracer and the observed susceptibility contrast (see Section 4.5):

$$S_t(t) = S_0 \exp\left(-\frac{TE}{\kappa_t} C_t(t)\right) \qquad [5.8]$$

with S_0=100 (arbitrary units), TE=65ms and κ_t=0.667. The constant κ_t was chosen such that a CBF=60ml/100g/min and CBV=4ml/100g produces a 40% signal drop

relative to the baseline S_0, which is typical for normal GM (Calamante *et al.* 2000; Østergaard *et al.* 1996a). 100 noisy signal time-course curves were generated for each parameter combination (*CBF*, *CBV*, t_{delay} and β) by adding random (zero mean) Gaussian noise to the signal curves. Defining the baseline SNR as:

$$SNR = \frac{S_0}{\sigma_{S_0}} \qquad [5.9]$$

where σ_{S_0} is the standard deviation in the baseline, data were simulated with SNR = 50, 100 and 500. These SNR values corresponding to the typical noise levels found in our scanner and the extremes of the SNR range found after denoising this data using Independent Component Analysis (see Section 5.3.2) respectively.

The noisy signal data are converted back into concentration time-course data (Equation [4.4]). In order to simulate the different temporal resolutions, separate data sets were created by sampling the curves at TR intervals in the range 0.5 – 3s at 0.5s steps. The length of the simulated data was initially 68s.[7] In total, 3 (SNR) x 6 (TR) = 18 data sets of 3696 (parameters) x 100 (repetitions) were created in order to test the techniques presented in this work. Figure 5.1 shows an example of a simulated tissue time-course.

Note that for a given SNR, different perfusion and dispersion values will give different contrast to noise ratios, CNR:

$$CNR = \frac{\max(C_t)}{\sigma_{C_0}} \qquad [5.10]$$

where σ_{C_0} is the standard deviation in the concentration baseline.. For example, for SNR=50, normal GM perfusion values (*MTT*=4s, *CBF*=60ml/100g/min), and dispersion β=0, results in CNR=20. When there is a dispersion of β=4s, CNR≈16. In ischaemic GM (*MTT*=9s, *CBF*=20ml/100g/min), and a dispersion of β=4s, the

[7] A typical DSC-MRI study might acquire 45 images at TR=1.5s

CNR falls still further, SNR=50 corresponds to CNR≈9. Thus, the accuracy of deconvolution for a given SNR is also dependent on the perfusion and vascular transport parameters.[8]

The various steps involved in a simulation study are summarised in the flow chart in Figure 5.3. The DSC-MRI analysis techniques presented in this thesis were assessed by deconvolving the simulated tissue concentration time-course data and the simulated AIF sampled at the corresponding TR.

5.2.5 IMPLEMENTATION ISSUES

When simulating an *in vivo* data set, it is important that any numerical convolution is performed with a very small sampling interval, $\Delta t << TR$. In this way, the error between the true analytical solution and the numerical convolution is minimised. In the numerical convolution, the function value at each sampling point is multiplied by the sampling interval. Therefore the numerical convolution is actually the convolution of a function that is constant across the sampling interval, i.e. a function that progresses in a step-wise manner. Since this situation is unrealistic, a very small sampling interval is desirable so that the discretely sampled function most accurately represents a continuous function.

If the numerical convolutions used to create the simulated data set were performed with $\Delta t = TR$, fewer data points and therefore less information would be used in the formation of $C_t(t)$. Therefore, there would be correspondingly fewer degrees of freedom in the deconvolution of the simulated data, and thus the instability of the inversion is artificially reduced. As a result, deconvolution using such a

[8] The definition for SNR given in Equation [5.9] is chosen because it is independent of the magnitude of the signal drop ΔS. This definition is more representative of an *in vivo* situation, where the baseline noise is constant regardless of the perfusion and dispersion. Conversely, CNR is dependent on perfusion and dispersion, so for a given SNR it will be smaller for lower perfusion and longer dispersion. Therefore, to realistically represent the *in vivo* situation it would be necessary to simulate different CNR values for healthy/abnormal tissue fed by healthy/abnormal vasculature

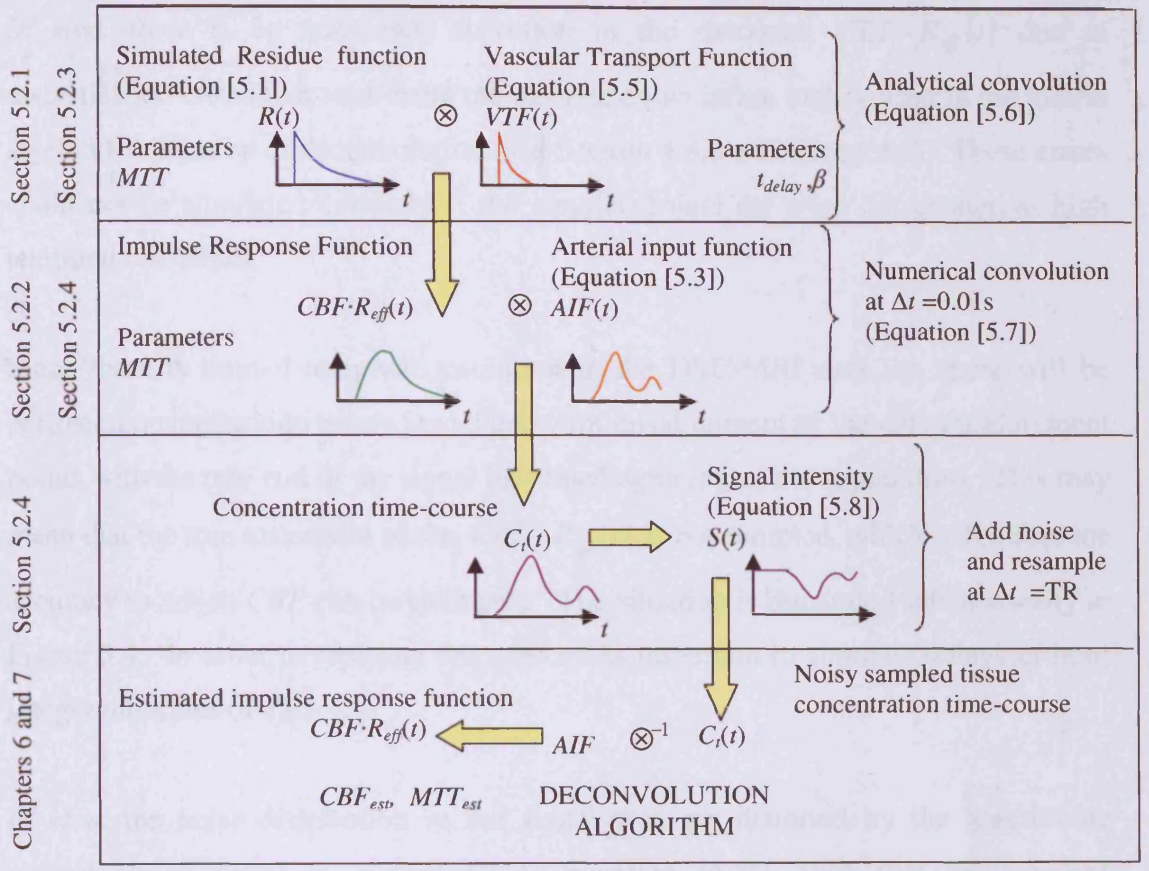

Figure 5.3: Flow chart illustrating the steps involved in simulating a DSC-MRI data set and testing a DSC-MRI analysis technique. The steps depicted in each row are described in the sections indicated on the left hand side of the figure.

(mis)simulated data set would require less regularisation and would consequently yield an artificially accurate characterisation of $CBF \cdot R_{eff}(t)$. In real data there is a many to one mapping between $CBF \cdot R_{eff}(t)$ and the sampled $C_t(t)$ and $C_a^{est}(t)$ (see Section 4.8.7.2), such that many different possible $CBF \cdot R_{eff}(t)$ could solve Equation [5.7]. Regularisation is necessary to suppress the noise related instabilities (see Section 4.8).

In vivo, there is an additional distortion in the extracted $CBF \cdot R_{eff}(t)$ due to discretisation errors that stem from the discrete convolution matrix used in the matrix algebra formulation of deconvolution (see Section 4.8.3 and Chapter 6). These errors could not be simulated correctly if the simulated data set were not created at high temporal resolution.

Since there is limited temporal resolution in the DSC-MRI data set, there will be perfusion quantification errors associated with misalignment of the data measurement points with the true end of the signal baseline/beginning of the signal drop. This may mean that the true maximum of the $CBF \cdot R_{eff}(t)$ is not sampled, which will affect the accuracy to which *CBF* can be estimated. The situation is illustrated schematically in Figure 5.4. In order to replicate this effect it is important to simulate delays of non-integer multiples of TR.

In vivo, the noise distribution in the signal data are distorted by the logarithmic conversion of signal to concentration (Equation [5.8]), such that the standard deviation of the noise in the peak is larger than the noise in the baseline (Smith *et al.* 2003). The distribution of noise in the concentration time-course data is likely to have significant impact on the ability of the various deconvolution techniques to reconstruct $CBF \cdot R_{eff}(t)$ accurately. It is therefore important that noise in the simulated data set is added to the signal rather than the concentration time-course data.

5.3 ANALYSIS OF PATIENT DATA

The reliability of the analysed DSC-MRI patient data are to some extent dependent on the quality of the *in vivo* data and the care taken in implementing the analysis method. This next section describes the steps taken to prepare the *in vivo* DSC-MRI

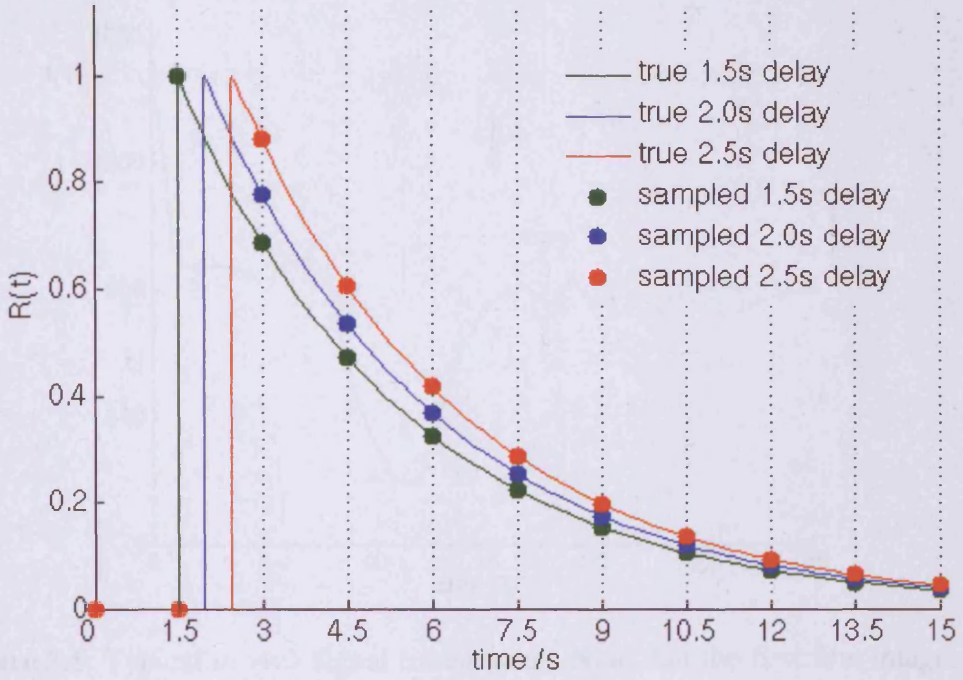

Figure 5.4: The figure shows the effect of a TR=1.5s sampling interval on the characterisation of the residue function delayed by 1.5s (green), 2.0s (blue) and 2.5s (red). When the delay is not an integer multiple of TR, the sampling time-points are not aligned with end of the baseline in the concentration time-course data. Consequently, the maximum of the impulse response may not be sampled. Underestimation is greatest when the delay is just greater than the integer multiple of TR.

data for analysis. In this way, reasonable comparisons can be made between different DSC-MRI data sets.

5.3.1 SIGNAL TO CONCENTRATION DATA

The DSC-MRI signal data are first converted to tissue concentration time-course data using the experimental TE value and the baseline value S_0 (Equation [4.4]). S_0 is calculated by averaging the first few points of the signal before the arrival of the bolus. Care should be taken to avoid the first few images, during which time the

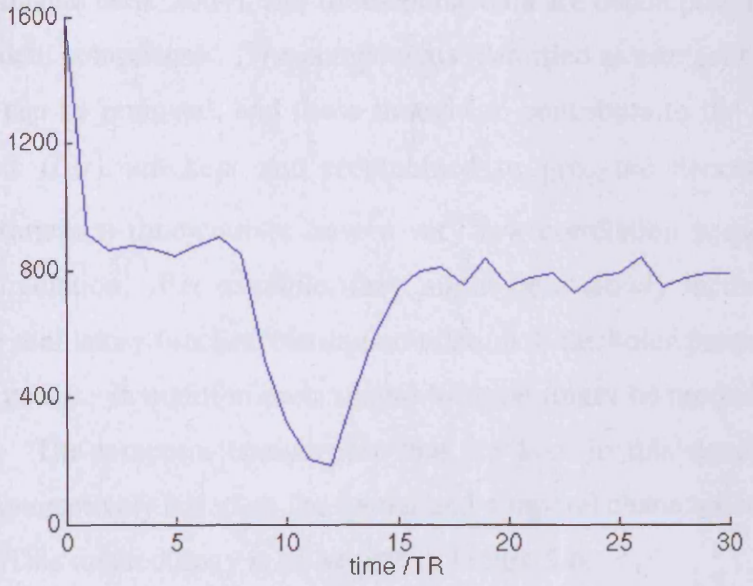

Figure 5.5: Typical *in vivo* signal time-course. Note that the first few images should be excluded from the calculation of the baseline signal.

protons have not reached a steady-state longitudinal magnetisation and the signal is artificially high. A typical signal time-course is illustrated in Figure 5.5.

5.3.2 ICA DENOISING

Often the CNRs in the data are low especially in areas of white matter or where there is low perfusion. This can make an accurate reconstruction of $CBF \cdot R_{eff}(t)$ difficult. Various denoising methods are available, e.g. (Awate *et al.* 2005; Wirestam *et al.* 2006; Bydder *et al.* 2006; Kadah 2004; Wink *et al.* 2004; Bao *et al.* 2003). In this work, noise in the concentration time-course data is minimised by decomposing the data into independent components using Independent Component Analysis (ICA) (Calamante *et al.* 2004; McKeown *et al.* 2003). ICA is a well-known denoising method that assumes the data are composed of a superposition of independent components and Gaussian noise. A Bayesian information criterion is used to determine the most likely number of independent components assuming Gaussian

noise (Calamante *et al.* 2004), and time-course data are decomposed into this number of independent components. The components identified as artefact due to either noise or motion can be removed, and those thought to contribute to the shape of the true uncorrupted $C_t(t)$ are kept and recombined to give the denoised signal. The discarded (artefact) time-courses have a very low correlation with the first passage and/or recirculation. For example, they might be a slowly increasing function of time, or an oscillatory function bearing no relation to the bolus passage (e.g. pulsation motion or noise). In addition their spatial location might be around the periphery of the image. The temporal components that are kept in this denoising process are identified interactively based on the spatial and temporal characteristics (Calamante *et al.* 2004). This methodology is illustrated in Figure 5.6.

Typically for the patient data used had a SNR of approximately 50, which after denoising improved to between 100 and 500, depending on the effectiveness of the denoising The improvement in SNR is affected by factors such as motion and perfusion levels. The ICA denoising was performed using Matlab (the code is available from the web site http://isp.imm.dtu.dk/toolboxef).

5.3.3 GLOBAL AIF SELECTION AND NORMALISATION

There are various factors to consider when selecting the best site to measure the AIF (Conturo *et al.* 2005). Ideally one would measure a unique AIF for each voxel in the image (i.e. a local AIF) (Calamante *et al.* 2004). However, because of the limited resolution of the DSC-MRI images (approx 2x2x5mm^3), physical measurement of such a local AIF is not possible. For this reason a global AIF is often measured in a large vessel such as the MCA.

a)

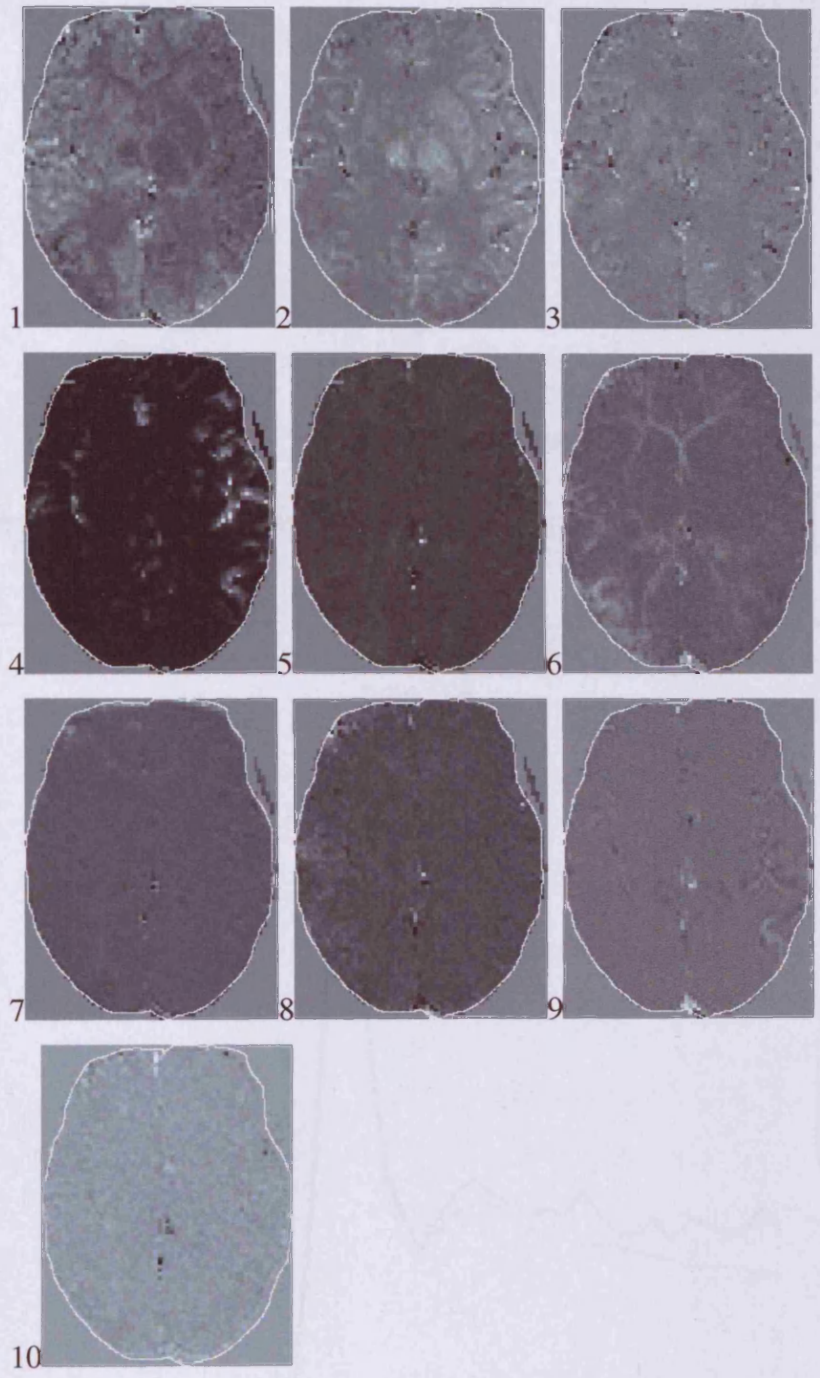

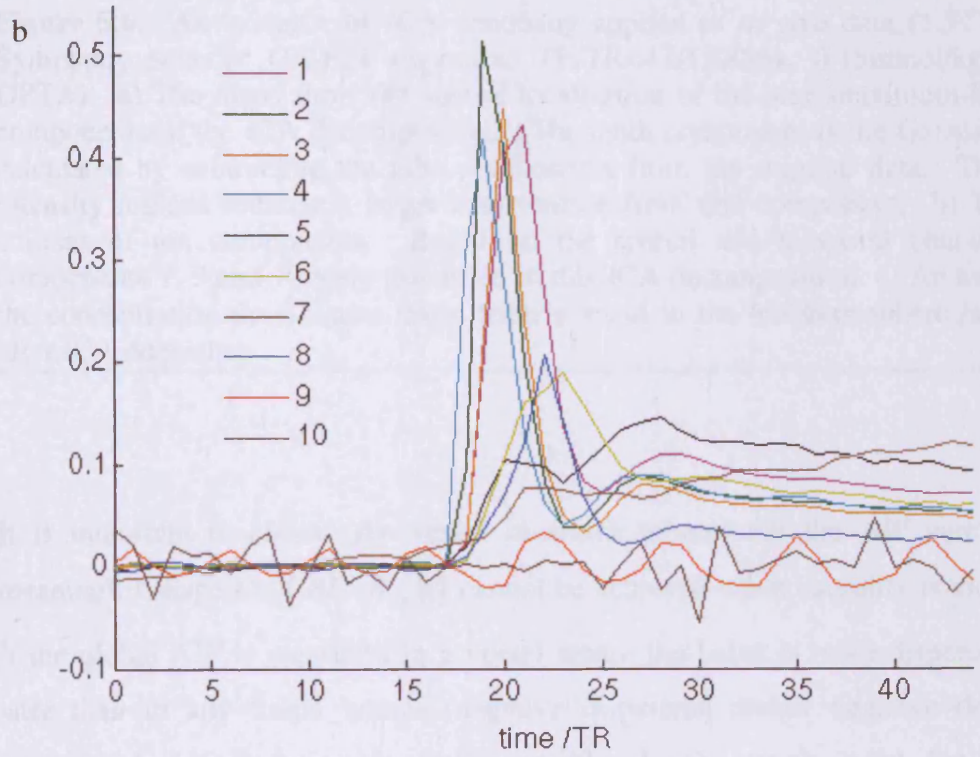
b
0.5
0.4
0.3
0.2
0.1
0
-0.1
1
2
3
4
5
6
7
8
9
10
0
5
10
15
20
25
30
35
40
time /TR

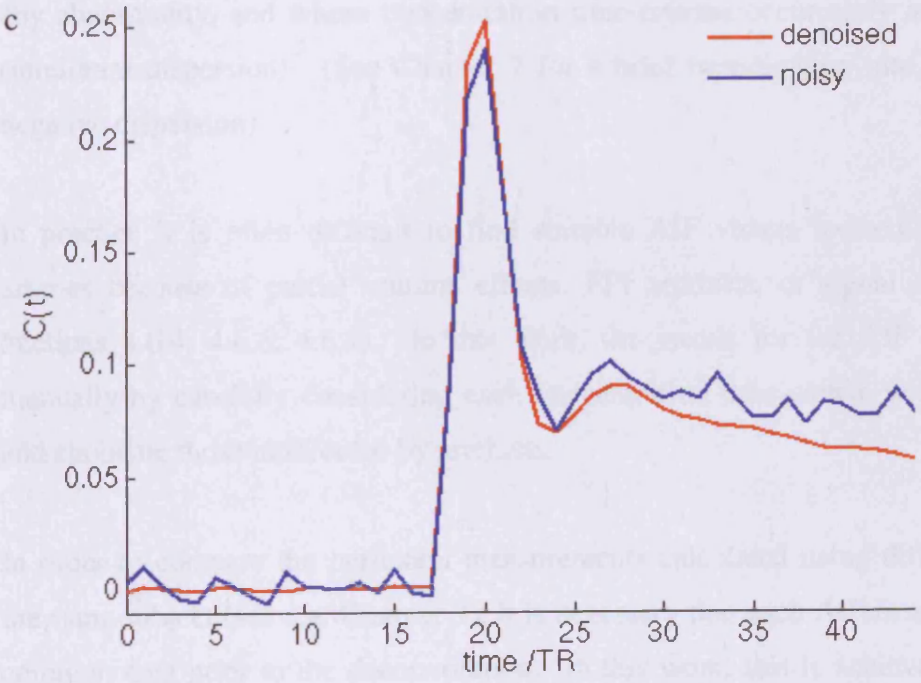
c
0.25
0.2
0.15
0.1
0.05
0
C(t)
denoised
noisy
0
5
10
15
20
25
30
35
40
time /TR

Figure 5.6: An example of ICA denoising applied to *in vivo* data (1.5T Siemens Symphony scanner GE-EPI sequence, TE/TR=47/1500ms, 0.15mmol/kg of Gd-DPTA). a) The maps show the spatial localisation of the nine maximum-likelihood components of the ICA decomposition. The tenth component is the Gaussian noise, calculated by subtracting the nine components from the original data. The higher intensity regions indicate a larger contribution from this component. b) The time-courses of ten components. Based on the spatial and temporal characteristics, components 7, 9 and 10 were discarded in this ICA decomposition. c) An example of the concentration time-course taken from a voxel in the left hemisphere before and after ICA denoising.

It is important to choose the vessel in which to measure the AIF carefully. A meaningful shape for $CBF \cdot R_{eff}(t)$ cannot be achieved when causality is violated i.e. if the global AIF is measured in a vessel where the bolus is more dispersed and/or later than in any tissue voxels (negative dispersion and/or negative delay). A meaningful deconvolution is only possible if the voxels used for the AIF measurement are carefully selected within an artery in the hemisphere contralateral to any abnormality, and whose concentration time-courses occur early and are narrow (minimum dispersion). (See Chapter 7 for a brief investigation into the effects of negative dispersion)

In practice it is often difficult to find suitable AIF voxels located in the normal arteries because of partial volume effects, EPI artefacts, or signal saturation (see Sections 4.6.4, 4.6.6, 4.6.7). In this work, the voxels for the AIF were selected manually by carefully considering each concentration time-course within the artery and choosing those unaffected by artefacts.

In order to compare the perfusion measurements calculated using different AIFs in the same subject (see e.g. Chapter 9), it is necessary that each AIF is normalised to a common area prior to the deconvolution. In this work, this is achieved by fitting a gamma-variate model (Equation [5.2]) to the first passage of the measured AIF and integrating for the area. This area is used to normalise the whole AIF.

5.3.4 PARAMETER MAPS

Deconvolution of *in vivo* DSC-MRI data prepared as described above will extract voxel by voxel estimates for the impulse response function, $CBF \cdot R_{eff}(t)$. Any error in the characterisation of this function should be purely a result of the regularisation and discretisation in the deconvolution. *CBF* maps can be made by measuring the maximum of the impulse response function, although because of delay and dispersion this measure is likely to underestimate perfusion (see Section 4.7.2). Cerebral blood volume, *CBV* maps can be estimated by fitting a gamma-variate function to the first passage of the concentration time-course in each voxel.[9] *MTT* maps can then be calculated from the ratio of the *CBV* to *CBF* in each voxel. Since both *CBV* and *CBF* are likely to be high in vessels, it can be difficult to identify regions of abnormal perfusion using these measures. It is often easier to identify abnormal regions from the *MTT* maps (see Chapter 9).

5.4 COMPUTER IMPLEMENTATION

A significant amount of the work for this thesis involved writing computer programs. For each chapter, code was written to implement the proposed techniques. In particular, the simulated data were created so that the proposed novel deconvolution techniques could be tested, and programs were written to analyse the *in vivo* data, using various deconvolution techniques. The codes were initially written and run in Matlab, but later transferred to C++ to improve the speed of implementation.

[9] It should be noted that when the gamma-variate model (Equation [5.2]) is fitted to the first passage of *in vivo* concentration data, the fitted parameter t_0 is not necessarily a good indication of the true bolus arrival time, since a relatively small t_0 could be coupled with a relatively large value of a to give approximately the same fit as a relatively large value of t_0 coupled with a relatively small value of a (Perthen 2003)

6 CHARACTERISING THE IMPULSE RESPONSE FUNCTION USING A MODIFIED ML-EM DECONVOLUTION METHOD

6.1 INTRODUCTION

Many MRI studies in acute stroke have shown the presence of a diffusion-perfusion mismatch: namely an area with an abnormality in perfusion MRI, but normal diffusion properties. This is tissue thought to be at risk of infarction but is potentially salvageable using clinical intervention such as thrombolytic therapy. Since such clinical intervention is not without risks, it is important to differentiate with accuracy, the 'at risk' tissue from the ischaemic core and from tissue not at risk. An accurate quantification of cerebral blood flow (*CBF*) is necessary to identify patients who would benefit from interventional treatment. However, as discussed in Chapter 4, there are many problems associated with the quantification of *CBF*, particularly in the presence of abnormal vasculature (Section 4.7.2), which can exaggerate a perfusion abnormality (Calamante *et al.* 2000). In order to avoid the potentially dangerous misclassification of 'at risk' tissue, it is important to recognise and interpret the potential bias in the cerebral perfusion measurements made in such patients.

In DSC-MRI, cerebral blood flow (*CBF*) is commonly estimated from the maximum of the impulse response function, $CBF \cdot R_{eff}(t)$ obtained from the deconvolution of DSC-MRI data (Østergaard *et al.* 1996b) (Equation [4.28]):

$$C_t(t) = CBF \cdot \left(C_a(t) \otimes R_{eff}(t)\right) \qquad [6.1]$$

The contrast concentration-time-course is measured both in an artery feeding the tissue $C_a(t)$, and in the tissue, $C_t(t)$. Because the arterial input function (AIF) is normally measured in a major artery, the shape of $CBF \cdot R_{eff}(t)$ often reflects the properties of both the vasculature and the tissue. Abnormal vasculature can distort the bolus, and consequently, the maximum of $CBF \cdot R_{eff}(t)$ may be an underestimation of the true perfusion (Calamante *et al.* 2000). The situation is illustrated in Figure 6.1 (reproduced from Figure 4.5),

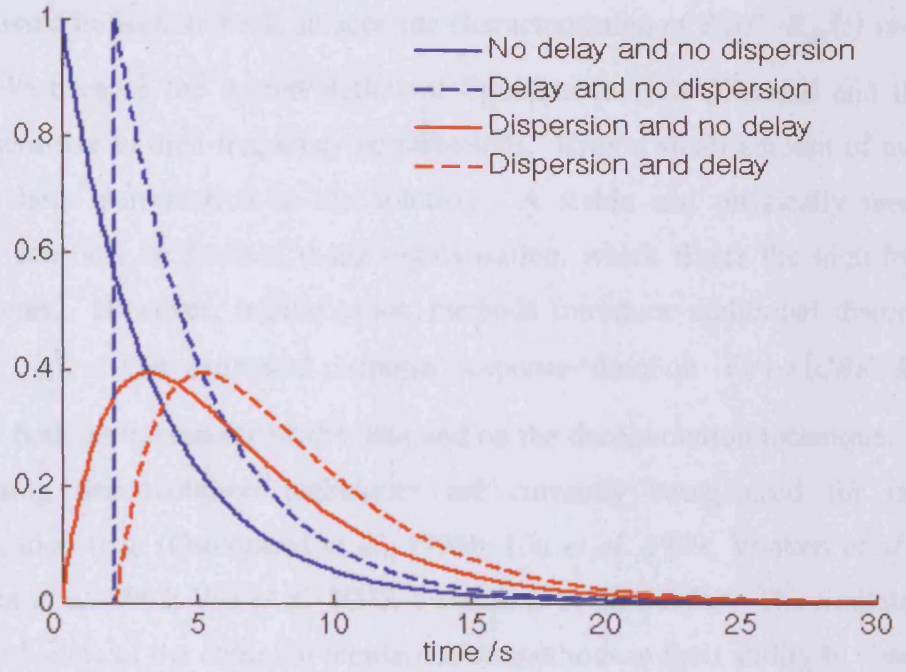

Figure 6.1: Impulse response functions illustrating the four possible combinations of delay and dispersion a) No delay and no dispersion (solid blue), b) delay and no dispersion (dashed blue), c) dispersion and no delay (solid red), d) delay and dispersion (dashed red). There is an intrinsic underestimation of *CBF* using impulse response functions derived in the presence of bolus dispersion. The regularisation and discretisation errors that accrue in the deconvolution can also cause *CBF* to be underestimated in the absence of dispersion.

which shows the form of $CBF \cdot R_{eff}(t)$ resulting from the four different combinations of bolus delay and dispersion in the vascular transport.[10] An accurate characterisation of $CBF \cdot R_{eff}(t)$ would enable the identification and distinction of bolus delay and dispersion, which may accumulate during its passage through the feeding arteries. The *CBF* underestimation introduced by bolus dispersion is largely independent of the deconvolution method used. If the bolus becomes distorted due to for example an arterial stenosis, dispersion-related perfusion measurement error will always be present. Conversely, the *CBF* underestimation arising from bolus delay is purely a consequence of the inaccuracies in the deconvolution.

[10] Note that throughout this work the simulated $R_{eff}(t)$ are formed according to Equation [5.6] in Chapter 5.

As discussed in Section 4.8.1, an accurate characterisation of $CBF \cdot R_{eff}(t)$ is difficult to achieve because the deconvolution of Equation [6.1] is ill-posed and therefore highly sensitive to high-frequency perturbations. Even a small amount of noise will cause a large perturbation in the solution. A stable and physically meaningful solution can only be realised using regularisation, which filters the high-frequency components. However, regularisation methods introduce additional distortions to $CBF \cdot R_{eff}(t)$. The estimated impulse response function $\tilde{r}(t) = (CBF \cdot R_{eff}(t))_{est}$ depends both on the quality of the data and on the deconvolution technique. Several regularising deconvolution techniques are currently being used for perfusion quantification (e.g. (Østergaard *et al.* 1996b; Liu *et al.* 1999; Vonken *et al.* 1999a; Andersen *et al.* 2002; Wu *et al.* 2003; Calamante *et al.* 2003a). The limitations and caveats of some of the common regularisation methods in their ability to characterise $CBF \cdot R_{eff}(t)$ and quantify perfusion are discussed in detail in Chapter 4 (Section 4.8). In brief, the most common is Truncated Singular Valued Decomposition (TSVD), which filters the noise using a singular value threshold (Østergaard *et al.* 1996b; Liu *et al.* 1999). The truncation of the high-frequency components introduces oscillations, adding to the distortion of $CBF \cdot R_{eff}(t)$. Another related method, Tikhonov regularisation balances the data misfit and regularisation error with an appropriate side constraint (Calamante *et al.* 2003a). The smooth low-pass filter avoids oscillation and successfully characterises dispersion. In the absence of dispersion, both TSVD and Tikhonov provide relatively accurate *CBF* estimates when there is no bolus delay. However, the characterisation of $CBF \cdot R_{eff}(t)$ and accuracy of *CBF* quantification deteriorate in the presence of bolus delay. In particular, the smoothing that is synonymous with removing the high frequencies causes a delayed $CBF \cdot R_{eff}(t)$ to appear dispersed, since in order to define the sharp edge associated with the delay (see Figure 6.1), very high frequencies must be recovered.

Because of deconvolution errors, it is difficult to interpret the contribution of the vasculature (i.e. delay and dispersion) to the shape of $CBF \cdot R_{eff}(t)$, and therefore

equally difficult to assess the related perfusion measurement errors. If unreliable measurements of perfusion are used in predictor-models, the resulting classification of 'at-risk' tissue is likely to be erroneous. Recognising the potential bias in the *CBF* estimates could avoid a misclassification of tissue at risk of infarction. Furthermore, the distinction between delay and dispersion is also important for subsequent correction of $CBF \cdot R_{eff}(t)$. For example, a delay can be corrected simply, by shifting $C_t(t)$ and re-performing the deconvolution e.g. (Ibaraki *et al.* 2005). Dispersion correction is more difficult, requiring either a model of the vascular transport function (VTF), or a more accurate measurement of the AIF (see Chapters 8 and 9).

Since the shape of $CBF \cdot R_{eff}(t)$ is crucial in the interpretation of perfusion measurements, and hence the selection of patients for treatment, a major part of this thesis focuses on the development of deconvolution techniques that are accurate in dealing with DSC-MRI perfusion data, particularly in patients with cerebrovascular abnormalities. This work in this chapter proposes a method to minimise the artefacts associated with the deconvolution using a modified maximum-likelihood expectation-maximisation (ML-EM) method, with a view to improving the characterisation of $CBF \cdot R_{eff}(t)$.

6.2 MAXIMUM LIKELIHOOD EXPECTATION MAXIMISATION

This section describes some of the observations concerning standard ML-EM (sML-EM) regularisation (Dempster AP *et al.* 1977), which have motivated the modifications employed in this Chapter.

The shape $R_{eff}(t)$ can be described in terms of a distribution of temporal frequency components that define the shape. In order to characterise and distinguish all four bolus states defined in Figure 6.1, the regularised deconvolution method must be able to reconstruct a large range of frequencies. In particular, the sharp edge of the delay

and non-dispersed $R_{eff}(t)$ is characterised by high frequencies. The iterative method of ML-EM is able to extract these high frequencies (see Section 4.8.7), but the optimum point to stop the iteration for the ill-posed DSC-MRI problem is ill-defined.

Vonken *et al.* (Vonken *et al.* 1999a) were the first to implement a sML-EM method to extract $R_{eff}(t)$. This method is described in detail in Section 4.8.7. In summary, the sML-EM algorithm maximises the probability of measuring the observed (noisy/sampled) tissue concentrations $C_t(t)$, given the estimated AIF, $C_a(t)$, an estimation of the impulse response function $\tilde{r}(t) = (CBF \cdot R_{eff}(t))_{est}$, and a noise model. Each iteration updates $\tilde{r}(t)$, linearly increasing the expectation of the measured data, such that each new estimate of $\tilde{r}(t)$ when convolved with $C_a(t)$, will give an estimate $\tilde{C}_t(t)$ that is increasingly similar to $C_t(t)$. However, the expectation provides no indication of the quality of the reconstruction (Moon 1996; Kontaxakis G *et al.* 1998). The low-frequency components defining the smooth parts of $CBF \cdot R_{eff}(t)$ are recovered first, while higher frequencies defining sharp edges converge only after further iteration. During these later iterations, noise can cause the reconstruction to deteriorate.

The number of iterations used in the reconstruction can therefore be considered as the regularisation filter. Less iteration corresponds to greater regularisation. When deciding on an appropriate fixed number of iterations, there is a trade-off between extracting the high-frequency information and allowing corruption of the parts of $R_{eff}(t)$ characterised by low frequencies. For example, the smooth tail of $R_{eff}(t)$ will be recovered with few iterations. Conversely, the rise-to-maximum (*RTM*) of $R_{eff}(t)$ will be recovered with more. The most appropriate number of iterations to use in the reconstruction is a compromise between extracting the high frequencies and corrupting the sections characterised by low frequencies. Figure 6.2 illustrates the sML-EM reconstruction of $R_{eff}(t)$ with 2s delay and no dispersion, after 1, 3, 5, 9, 20, 30, 40, 60 80, 100, 150, 200 and 250 iterations. The illustration in Figure 6.2

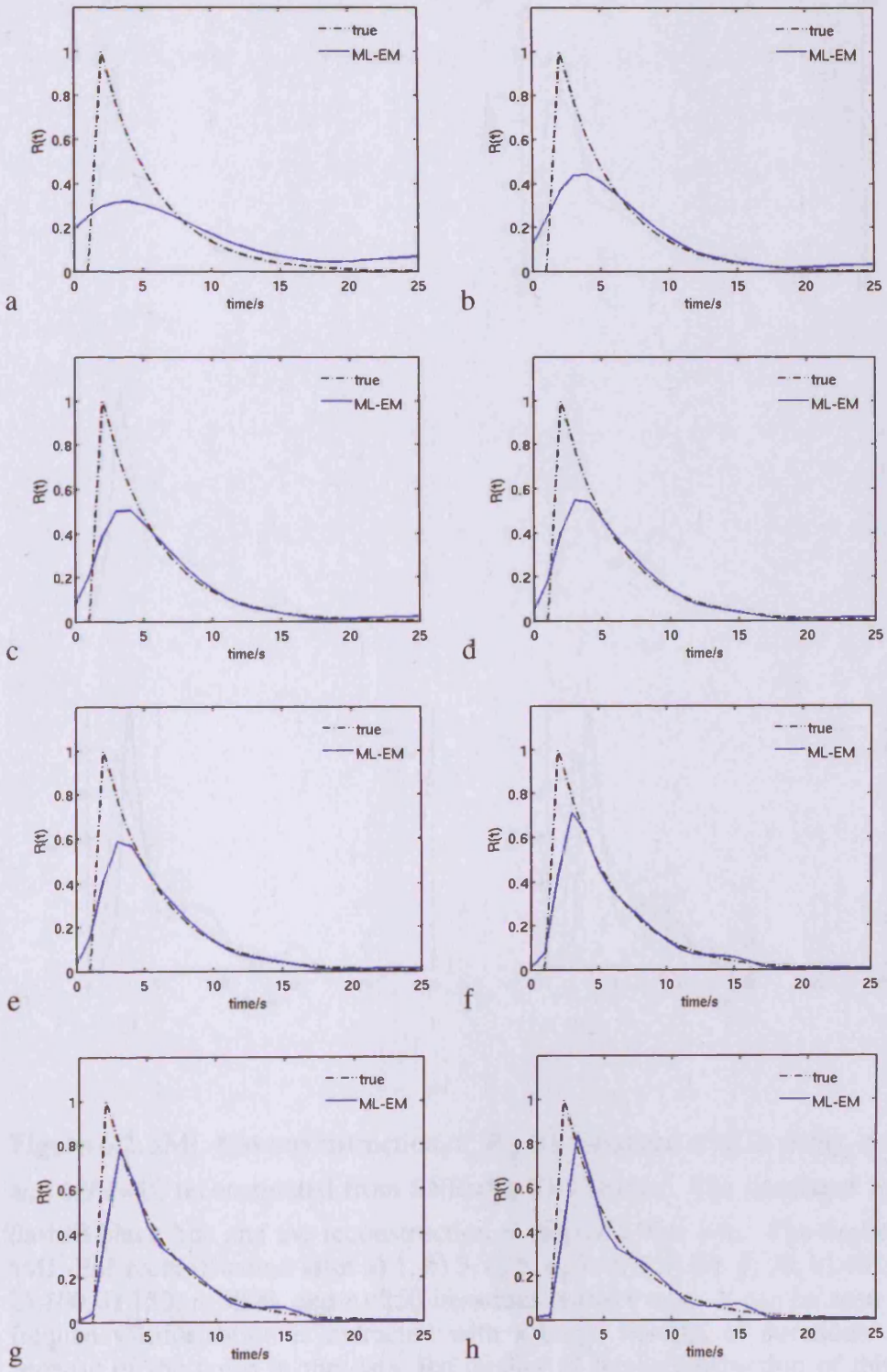
true
ML-EM
R(t)
time/s
a
b
c
d
e
f
g
h

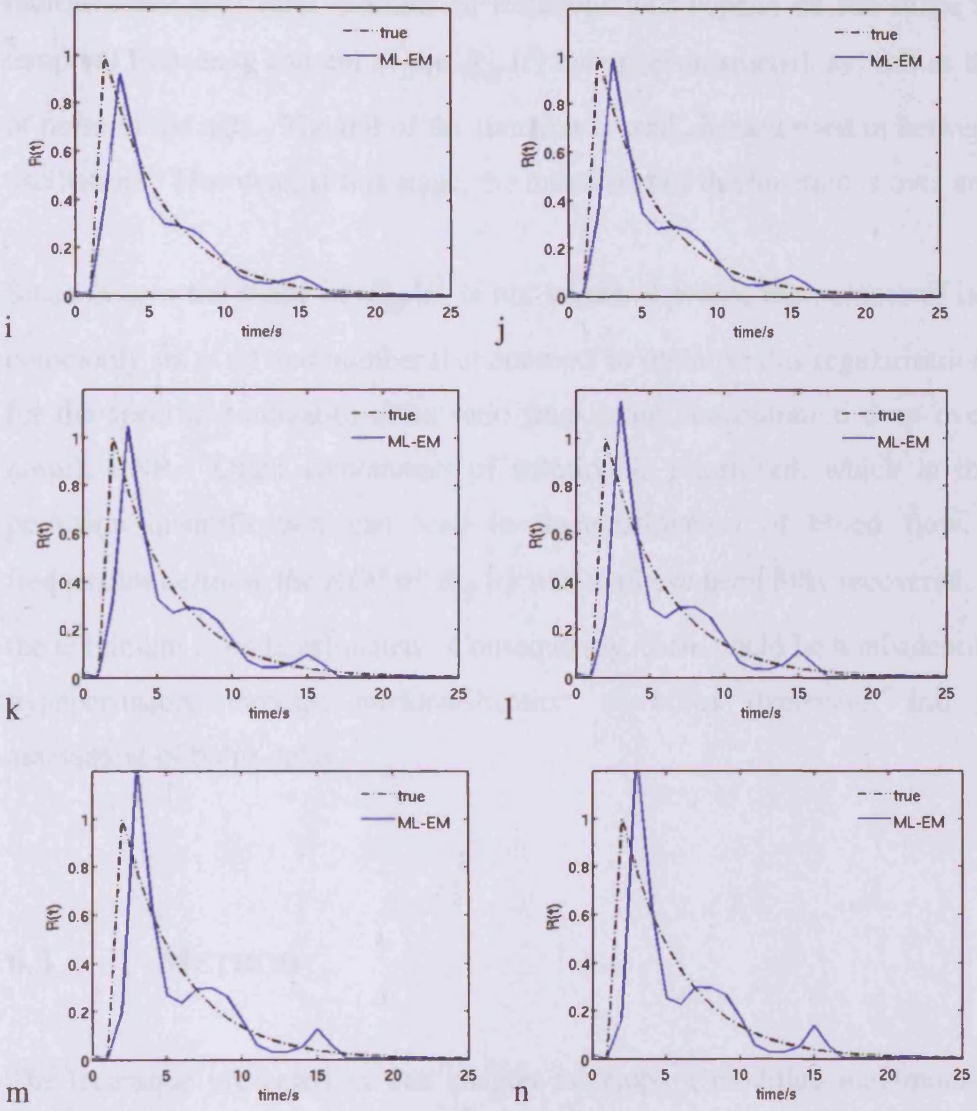

Figure 6.2: sML-EM reconstruction of $R_{eff}(t)$ simulated with 2s delay, no dispersion and *MTT*=4s, reconstructed from SNR=50, TR=1s data. The simulated $R_{eff}(t)$ is the dashed black line and the reconstruction is the solid blue line. The figures show the sML-EM reconstruction after a) 1, b) 3, c) 5, d) 7, e) 9, f) 20, g) 30, h) 40, i) 60, j) 80, k) 100, l) 150, m) 200, and n) 250 iterations respectively. It can be seen that higher frequency information is extracted with a larger number of iterations. However, because of the noise in the data, the quality of the reconstruction of this particular $R_{eff}(t)$ begins to deteriorate after about 60 iterations.

indicates that the 'ideal' number of iterations will depend on the shape and hence temporal frequency content of the $R_{eff}(t)$ being reconstructed, as well as the amount of noise in the data. The tail of the function is well characterised in between 3 and 9 oscillations. However, at this stage, the initial part of the function is over smoothed.

Since *in vivo* the shape of $R_{eff}(t)$ is not known *a priori*, the number of iterations is commonly set at a fixed number that attempts to optimise this regularisation trade-off for the specific contrast-to-noise ratio (maximum concentration drop over baseline noise), CNR. Often smoothness of solution is prioritised, which in the case of perfusion quantification can lead to underestimation of blood flow; the high frequencies defining the *RTM* of $R_{eff}(t)$ will not have been fully recovered, and hence the maximum is underestimated. Consequently, there could be a misidentification of hypoperfusion, through misidentification of bolus dispersion and inaccurate assessment of bolus delay.

6.3 METHOD

The technique presented in this chapter develops a modified maximum-likelihood expectation-maximisation (mML-EM) method, which aims to minimise regularisation-induced oscillations and discretisation errors in $CBF \cdot R_{eff}(t)$, to obtain an accurate measure of the function maximum, and a good characterisation of shape.

In order to circumvent the problem of over or under iteration, the modified ML-EM (mML-EM) method uses a *point-wise* termination criterion for the iteration. Each time-point within $R_{eff}(t)$ is reconstructed with a unique number of iterations depending on its position within $R_{eff}(t)$ and the convergence properties of the point. In this way, high frequencies defining the steep section of $R_{eff}(t)$ can be extracted, whilst preventing the corruption of the smooth sections by the fitting of experimental

noise. The method for determining the number of iterations is described in Section 6.3.2.

In addition to the error introduced through the necessary regularisation of the deconvolution, errors also arise from the discretisation of the continuous functions $C_t(t)$ and $C_a(t)$, which in the DSC-MRI experiment are sampled at intervals of TR. The Nyquist criterion determines the maximum frequency component that can be recovered, limiting the accuracy of delay and *CBF* quantification: it is not possible to reconstruct a frequency component that is higher than the 1/(2TR). The shape and hence frequency composition of $R_{eff}(t)$ is governed by the *MTT* of the tissue; $R_{eff}(t)$ is sharper in shorter *MTT* tissue. Consequently the accuracies of all deconvolution techniques are dependent on *MTT*, since regularisation removes the high frequencies. Despite this intrinsic limitation, the errors resulting from the discretisation can be minimised by carefully constructing the convolution matrix (Østergaard *et al.* 1996b). The mML-EM method presented in this chapter implements two different convolution matrices in order to minimise the discretisation errors for the particular $R_{eff}(t)$ being reconstructed. These are given in Section 6.3.1.

6.3.1 MINIMISING DISCRETISATION ERRORS

The ML-EM algorithm performs the discrete convolution of an estimate for the impulse response function $\tilde{r}(t) = (CBF \cdot R_{eff}(t))_{est}$, with $C_a(t)$, to get an approximation to the tissue concentration $\tilde{C}_t(t)$. This can be expressed in matrix form $\tilde{c} = \mathbf{A}\tilde{r}$ (Østergaard *et al.* 1996b) (Equation [4.35], Section 4.8.3). Since the sampling interval TR of these functions is of the order of 1-2 seconds, there are discretisation errors arising from the discrete convolution, which distort the reconstruction (see also Section 5.2.5). These errors can be minimised by formulating the elements of the **A** matrix to assume values of $C_a(t)$ and $R_{eff}(t)$ *between* measurement points, without subsampling. For example, Østergaard *et al.*

(Østergaard *et al.* 1996b) assumed that both $C_a(t)$ and $R_{eff}(t)$ vary *linearly* with time. The elements of the convolution matrix **A** become:

$$a_{ij} = \begin{cases} \Delta t\left(C_a(t_{i-j-1}) + 4C_a(t_{i-j}) + C_a(t_{i-j+1})\right)/6 & 0 \le j \le i \le n-1 \\ 0 & \text{otherwise.} \end{cases} \quad [6.2]$$

Calamante *et al.* (Calamante *et al.* 2003a) implemented a more generalised version for the Tikhonov regularisation method with elements of **A**:

$$a_{ij} = \begin{cases} \Delta t\left(2C_a(t_0) + C_a(t_1)\right)/6 & 0 \le i = j \le n \\ \Delta t\left(C_a(t_{i-j-1}) + 4C_a(t_{i-j}) + C_a(t_{i-j+1})\right)/6 & 0 < j < i < n \\ \Delta t\left(C_a(t_{i-1}) + 2C_a(t_i)\right)/6 & j = 0;\ 0 \le i \le n \\ 0 & \textit{otherwise.} \end{cases} \quad [6.3]$$

On the other hand, if $C_a(t)$ is assumed to vary *linearly* and $R_{eff}(t)$ is assumed *constant* between sample points the matrix elements are:

$$a_{ij} = \begin{cases} \Delta t\left(C_a(t_{i-j}) + C_a(t_{i-j+1})\right)/2 & 0 \le j \le i \le n-1 \\ 0 & \textit{otherwise.} \end{cases} \quad [6.4]$$

In this work, we denote the matrix in Equation [6.4] as $\mathbf{A_1}$ and the matrix in Equation [6.3] as $\mathbf{A_2}$.

A continuous $R_{eff}(t)$ (i.e. an impulse response function with no delay (with/without dispersion), or one with delay and dispersion) is best reconstructed with matrix $\mathbf{A_2}$, which assumes a linear progression between measurement points. However, the assumption of linearity between sample points may not apply to the discontinuity associated with the instantaneous *RTM* of a delayed but non-dispersed $R_{eff}(t)$ (see Figure 6.1). In this situation matrix $\mathbf{A_1}$ may be more suitable.

Preliminary noiseless simulations were performed to determine the suitability of each matrix to reconstruct $R_{eff}(t)$ deriving from the different bolus states represented in Figure 6.1. In the absence of noise, the discretisation effects of the two matrices $\mathbf{A_1}$

and $\mathbf{A_2}$ can be isolated from regularisation error. The $R_{eff}(t)$ were simulated with different combinations of delay and dispersion and reconstructed using both matrices. Figure 6.3 shows examples of the noiseless sML-EM reconstructions for delays of 0s, 2s, and 2.5s, and dispersions of 0s, and 4s. These are illustrative of the many delay and dispersion combinations simulated. It was found that matrix $\mathbf{A_2}$ is most appropriate to reconstruct $R_{eff}(t)$ with no delay and no dispersion (Figure 6.3a). Matrix $\mathbf{A_1}$ is better able to reconstruct the $R_{eff}(t)$ with no dispersion and a delay of an integer multiple of TR (Figure 6.3b). Matrix $\mathbf{A_2}$ cannot recover the instantaneous *RTM* of $R_{eff}(t)$ when there is a discontinuity across the sampling interval. However, matrix $\mathbf{A_2}$ gives the most accurate reconstruction for $R_{eff}(t)$ with no dispersion and a delay of TR plus half an integer TR (Figure 6.3c), i.e. when there is no measurement at the discontinuity. Matrix $\mathbf{A_2}$ was also found to give the most accurate characterisation of the $R_{eff}(t)$ with dispersion (Figures 6.3d and 6.3e).

In *in vivo* data the presence of delay and/or dispersion is unknown. Therefore, to obtain an accurate characterisation of the impulse response function, the most appropriate matrix for the reconstruction ($\mathbf{A_1}$ or $\mathbf{A_2}$) should be selected prior to the final deconvolution used for the perfusion estimates. In order to establish a possible methodology to select the matrix, simulations were performed, which extracted the sML-EM reconstruction of $CBF \cdot R_{eff}(t)$ from noisy simulated data, with various degrees of delay, dispersion, *CBF* and *CBV* (see Chapter 5). In brief, the sML-EM estimated impulse response funtions $\tilde{r}(t)$ were recovered using both $\mathbf{A_1}$ and $\mathbf{A_2}$. The number of sample points between the end of the baseline (defined as 10% of the maximum) and the maximum of $\tilde{r}(t)$, were measured for each of the curves, after 10 and 100 iterations. These measurements were found to be dependent on the choice of matrix, and the delay and dispersion combination. Using the results from these simulations, empirical criteria were formed to identify the non-dispersed $R_{eff}(t)$ delayed by a near integer number of sample points, which are best reconstructed with

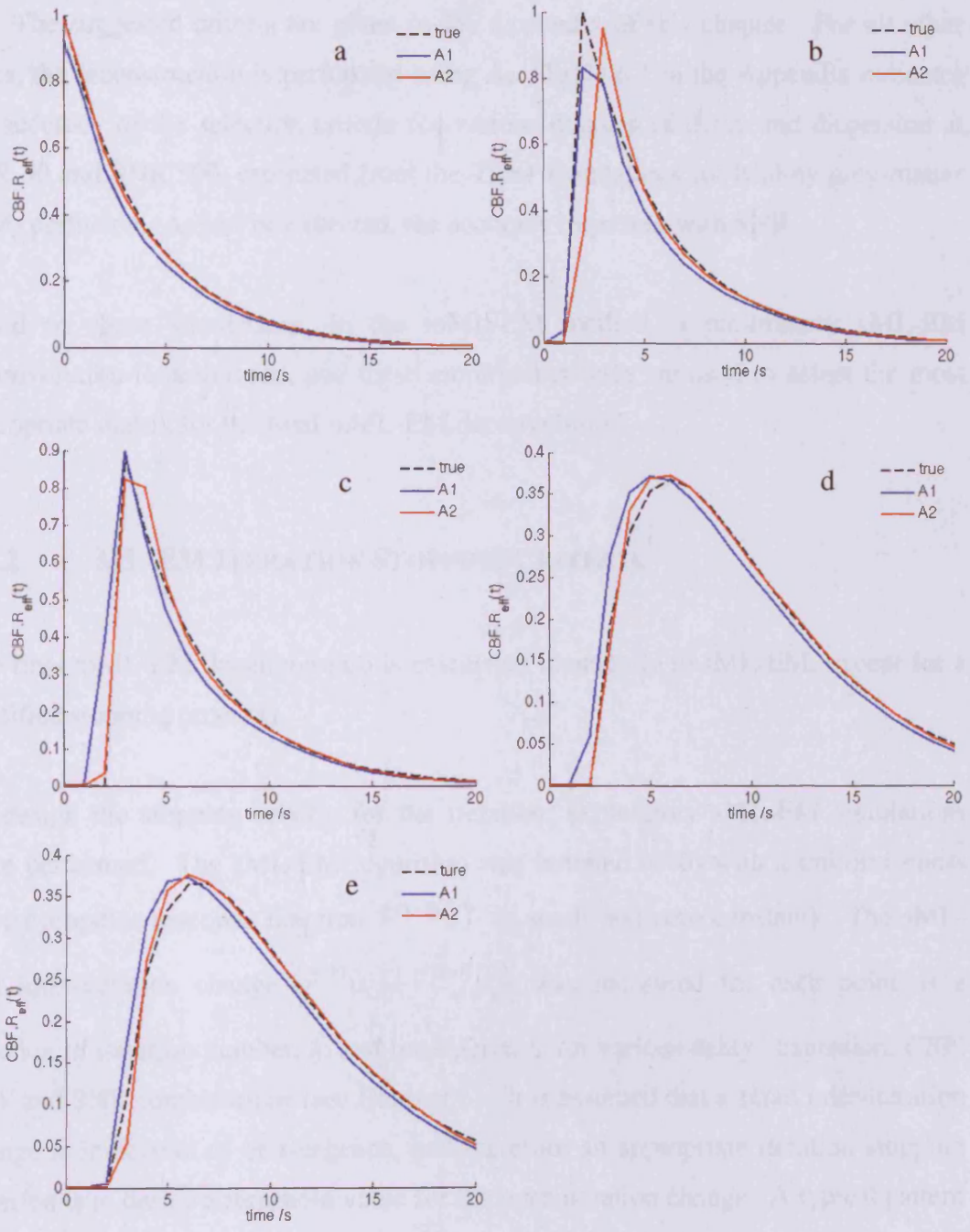

Figure 6.3: sML-EM reconstructions of $R_{eff}(t)$ with a) t_{delay}=0s delay, β=0s dispersion, b) t_{delay}=2s, β=0s, c) t_{delay}=2.5s, β=0s, d) t_{delay}=2s, β=4s, e) t_{delay}=2.5s, β=4s. Noiseless data were simulated with *CBF*=60ml/100g/min, *MTT*=4s, TR=1s. The black dashed lines are the simulated $R_{eff}(t)$, the blue solid lines are the reconstructions using matrix $\mathbf{A_1}$ and red solid lines are the reconstructions using matrix $\mathbf{A_2}$. It can be seen that matrix $\mathbf{A_1}$ gives the most accurate reconstruction in b), whereas matrix $\mathbf{A_2}$ gives the best reconstruction in a), c), d), e) and f).

$\mathbf{A_1}$. The suggested criteria are given in the Appendix of this chapter. For all other cases, the reconstruction is performed using $\mathbf{A_2}$. Table 6.1 in the Appendix indicates the accuracy of the selection criteria for various degrees of delay and dispersion at SNR 50 and SNR 500, estimated from the TR=1 simulations for healthy grey-matter (GM) perfusion. As can be expected, the accuracy improves with SNR.

Based on these simulations, in the mML-EM method, a preliminary sML-EM deconvolution is performed, and these empirical criteria are used to select the most appropriate matrix for the final mML-EM deconvolution.

6.3.2 ML-EM ITERATION STOPPING CRITERIA

The final mML-EM deconvolution is calculated identically to sML-EM, except for a modified stopping criterion.

To design the stopping criteria for the iteration, exploratory sML-EM simulations were performed. The sML-EM algorithm was initiated (k=0) with a uniform guess for the impulse response function $\tilde{r}^{[k=0]}(t)$ (a small non-zero constant). The sML-EM inter-iteration change $\left|\tilde{r}^{[k]}(t_i)-\tilde{r}^{[k-1]}(t_i)\right|$ was measured for each point as a function of iteration number, k, and time point, t_i, for various delay, dispersion, *CBF*, *CBV* and SNR combinations (see Chapter 5). It is assumed that a small inter-iteration change is indicative of convergence, and therefore an appropriate iteration stopping criterion is to define a threshold value for the inter-iteration change. A typical pattern was observed for the convergence of the individual points, which is illustrated in Figure 6.4 for $CBF \cdot R_{eff}(t)$ simulated with *CBF*=30ml/100g/min, *MTT*=4s, delayed by 2s, for noiseless data (a), and SNR=30 data (b).

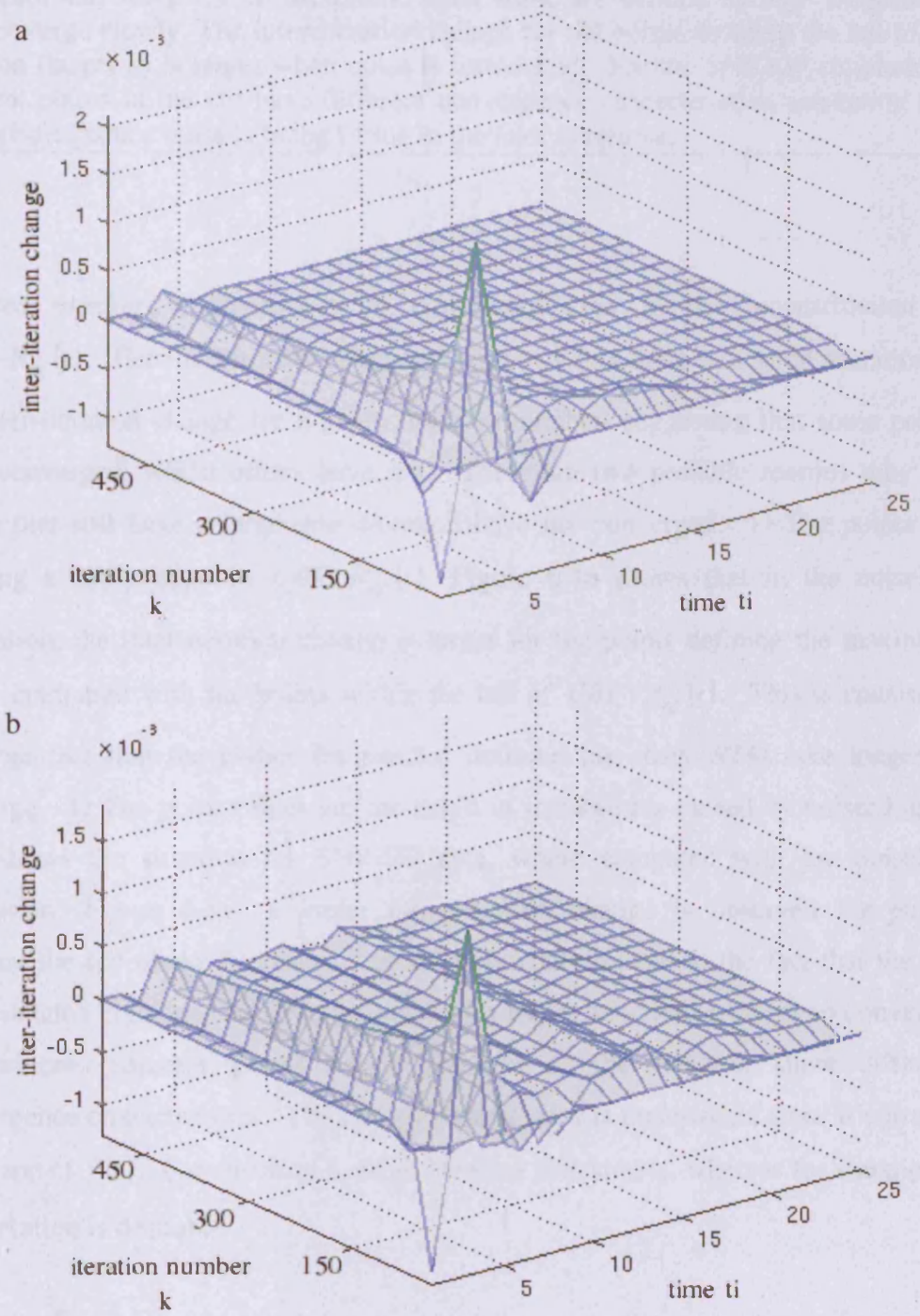

Figure 6.4: The inter-iteration change $\left|\tilde{r}^{[k]}(t_i) - \tilde{r}^{[k-1]}(t_i)\right|$ for each point as a function of iteration number, k, and time point, t_i, for a) noiselesss and b) SNR 30 sML-EM reconstructions of $CBF \cdot R_{eff}(t)$ simulated with CBF=30ml/100g/min, MTT=4s,

delay=2s, TR=1s. The inter-iteration change is largest for points defining the maximum and sharp rise-to-maximum, since these are defined by high frequencies that converge slowly. The inter-iteration change for the points defining the tail of the function (larger t_i) is larger when noise is introduced. For the SNR=30 simulations, adjacent points in the tail have different convergence characteristics, indicating that the high-frequency noise is being fitting in the later iterations.

A *fixed number of iterations* are commonly used in the reconstruction of $CBF \cdot R_{eff}(t)$. For this situation, Figure 6.4, shows that there is a large variation in the inter-iteration change for a given iteration number, suggesting that some points have converged, whilst others have not. There are two possible reasons why the points that still have a large inter-iteration have not converged. 1) The points are defining a sharp edge in $CBF \cdot R_{eff}(t)$: Figure 6.4a shows that in the noiseless simulation, the inter-iteration change is larger for the points defining the maximum (t_i~2), compared with the points within the tail of $CBF \cdot R_{eff}(t)$. This is consistent with the fact that the higher frequencies defining the sharp *RTM* take longer to converge. 2) The point values are the result of instabilities caused by noise: Figure 6.4b shows the situation for SNR=30 data, where compared with the noiseless simulation (Figure 6.4a), a larger inter-iteration change is observed for points defining the tail of the function. This is presumably related to the fact that the tail now contains high frequencies associated with noise, which take longer to converge. Furthermore, adjacent points within the tail of the function show different convergence characteristics. The fitting of such noise is undesirable since it corrupts the shape of $\tilde{r}(t)$. For situation 1, more iteration is desirable, whereas for situation 2 less iteration is desirable

Equally, if a *fixed inter-iteration change* is used to determine the number of iterations in the reconstruction of $CBF \cdot R_{eff}(t)$, Figure 6.4 indicates there would be a very large variance in the number of iterations used to calculate each point in $CBF \cdot R_{eff}(t)$ For the noiseless simulation in Figure 6.4a, such criteria would facilitate the accurate

reconstruction of any sharp edges in $CBF \cdot R_{eff}(t)$. However, for the SNR=30 simulation in Figure 6.4b, using a fixed inter-iteration change-threshold to stop the iteration would cause the complete corruption of tail points contaminated with noise.

Therefore, in order to minimise the corruption of $CBF \cdot R_{eff}(t)$, and maximise the reconstruction of the real high-frequency information actually defining the true shape, a *point-wise inter-iteration change* should be used. For example, the inter-iteration change-threshold defining the stopping criteria for the points defining the *RTM* of $CBF \cdot R_{eff}(t)$, should be smaller than the inter-iteration change-threshold defining the stopping criteria for the tail points. In this way, more iteration is used to reconstruct the *RMT* compared with the tail. In this work, such point-wise stopping criteria are formed by making the inter-iteration change-threshold $\left|\tilde{r}^{[k]}(t_i) - \tilde{r}^{[k-1]}(t_i)\right|$ for each point dependent on both the point value $\tilde{r}^{[k]}(t_i)$, and the time point t_i.

Furthermore, the inter-iteration change for each point should also be scaled according to the actual shape of $CBF \cdot R_{eff}(t)$ being reconstructed. A shorter *MTT* defines a sharper and steeper $R_{eff}(t)$, with a smaller integrated area. Because these shapes are characterised by more slowly converging high frequencies, the number of iterations used to reconstruct $CBF \cdot R_{eff}(t)$ should be inversely proportional to the integrated area of $R_{eff}(t)$, which is not *a priori* known, but can be approximated by $\sum_i \tilde{r}^{[k]}(t_i)$.[11] Therefore, for the point-wise stopping criteria used in this work, the inter-iteration change was set to be proportional to the integrated area of the reconstruction $\sum_i \tilde{r}^{[k]}(t_i)$, enabling more iteration for the steeper and sharper $R_{eff}(t)$.

[11] It should be noted that for a sharp steep $R_{eff}(t)$, the true maximum of the recovered $CBF \cdot R_{eff}(t)$ is slowly reconstructed, so the integrated area of the reconstruction, $\sum_i \tilde{r}^{[k]}(t_i)$, will take many more iterations to reach a good approximation to the *CBV* (which is the are under $CBF \cdot R_{eff}(t)$) than for a broad dispersed $R_{eff}(t)$.

Based on the simulations and inference described above, a *point-wise* termination criterion was empirically determined from preliminary simulations to optimise the reconstruction of the various shapes of $CBF \cdot R_{eff}(t)$. In this work, iteration on a particular point is stopped when the inter-iteration change in the value of that point is less than a threshold dependent on the position of the point t_i, the value of the point $\tilde{r}_i(t_i)$, as well as area of the reconstruction, $\sum_j \tilde{r}_j$:

$$\left|\tilde{r}^{[k]}(t_i) - \tilde{r}^{[k-1]}(t_i)\right| < \alpha \cdot TR^2 \cdot \left(t_i \cdot \tilde{r}^{[k]}(t_i)\right)^{\beta} \cdot \sum_i \tilde{r}^{[k]}(t_i)/N \quad k > 10; \quad 0 \le t_i \le \max(t_i)$$

[6.5]

with k the iteration number, N the number of sampling points and α and β empirically determined numerical constants. For the results presented here, the values of α and β were 0.01 and 0.33 respectively. These suggested values were determined by monitoring (iteration by iteration) the sML-EM reconstruction of many different simulated shapes for $CBF \cdot R_{eff}(t)$, and changing the values of α and β to achieve the most accurate recovery of the simulated $CBF \cdot R_{eff}(t)$. The aim of the criteria given in Equation [6.5] is to allow more iteration to reconstruct the beginning of the function, and less for the tail and for functions with a large *MTT* (i.e broad functions).

The preliminary simulations also revealed that the inter-iteration change for individual points in noisy data may *not* fall below the Equation [6.5] threshold. For this reason, in order to avoid severe corruption due to over-iteration, the maximum number of iterations allowed for the reconstruction was set to 250/TR for reconstructions using matrix $\mathbf{A_1}$. The smoother functions reconstructed with matrix $\mathbf{A_2}$ used a lower maximum of 100/TR iterations.

These stopping criteria are incorporated in the mML-EM algorithm as follows: The algorithm is initiated (k=0) with a uniform guess for the impulse response function $\tilde{r}^{[k=0]}(t)$ (a small non-zero constant). ML-EM iteration on a particular point, t_i is stopped at the k^{th} iteration when the inter-iteration change in the value of that point

$\left|\tilde{r}^{[k]}(t_i)-\tilde{r}^{[k-1]}(t_i)\right|$ is less than the threshold given in Equation [6.5]. The current value of the point, $\tilde{r}^{[k]}(t_i)$ is then placed in a separate vector and kept at this value until the inter-iteration change for all points in the estimated impulse response function have fallen below their individual thresholds. In order to extract the high-frequency information, the sML-EM estimated $\tilde{r}^{[k]}(t)$ is used to update the mML-EM algorithm at each iteration step. The resulting reconstruction will not be maximum likelihood, but corruption of $\tilde{r}(t)$ is minimised.

6.3.3 SIMULATIONS AND PATIENT DATA

The final mML-EM algorithm combines the methodology to firstly minimise the discretisation errors (Section 6.3.1) and secondly minimise the regularisation and noise induced errors (Section 6.3.2). In the first stage a preliminary sML-EM reconstruction is performed and the criteria given in Equation [6.6] (see Appendix) are used to automatically select the appropriate matrix, $\mathbf{A_1}$ or $\mathbf{A_2}$. In the second stage, the final ML-EM reconstruction is performed using the appropriate matrix and terminating the iteration with the point-wise convergence criteria, given in Equation [6.5]. This methodology was tested on the simulated data set described in Chapter 5. For comparative purposes, reported in the results (Section 6.4), are the reconstructions after 50 and 200 iterations (van Osch *et al.* 2003) of the sML-EM method.

For illustrative purposes, the mML-EM technique was applied to real image data acquired from a patient with left internal carotid artery occlusion on a 1.5T Siemens Symphony scanner using a gradient-echo EPI sequence (TE/TR = 47/1500ms) after injecting 0.15mmol/kg of Gd-DPTA. A global AIF was measured in the contralateral middle cerebral artery (MCA). Denoising of the tissue concentration data was performed using Independent Component Analysis (see Section 5.3.2). sML-EM and mML-EM deconvolution analysis were used to extract the $CBF \cdot R_{eff}(t)$ for each

voxel. The matrix selection and point-wise termination criteria used for the *in vivo* data were the same as those determined and used in the simulations.

6.4 RESULTS

6.4.1 CHARACTERISING THE IMPULSE RESPONSE FUNCTION

The four rows of Figure 6.5 and Figure 6.6 show the $CBF \cdot R_{eff}(t)$ reconstruction of the four different bolus states described in Section 4.7.2 and illustrated Figure 6.1, from data simulated at SNR=50 and 500 respectively. The delay and dispersion combinations shown are representative of the many combinations for which the simulations were performed (see Chapter 5). It should be noted that the vertical axis of the first three columns have units in ml/100 g/s (healthy GM *CBF*= 60 ml/100 g/min = 1 ml/100 g/s), and the vertical axis of the fourth column is the number of iterations.

At SNR 50 (Figure 6.5), 50 iterations of sML-EM (first column) recovers the smooth parts of all the impulse response functions well, while the iteration is terminated before the high-frequency components have had a chance to converge. The initial sections of the non-dispersed $CBF \cdot R_{eff}(t)$ (a and b) are poorly characterised because of discretisation error (affecting both (a) and (b)) and because too few iterations have been used to recover the high-frequency information defining the steep *RTM* in (b). Continuing the sML-EM iteration further causes the reconstructions at SNR=50 to become dominated by noise. After 200 iterations (second column), noise has completely corrupted the smooth parts of the $CBF \cdot R_{eff}(t)$. 200 iterations is not therefore a suitable number of iterations to use for these SNR and flow parameters.

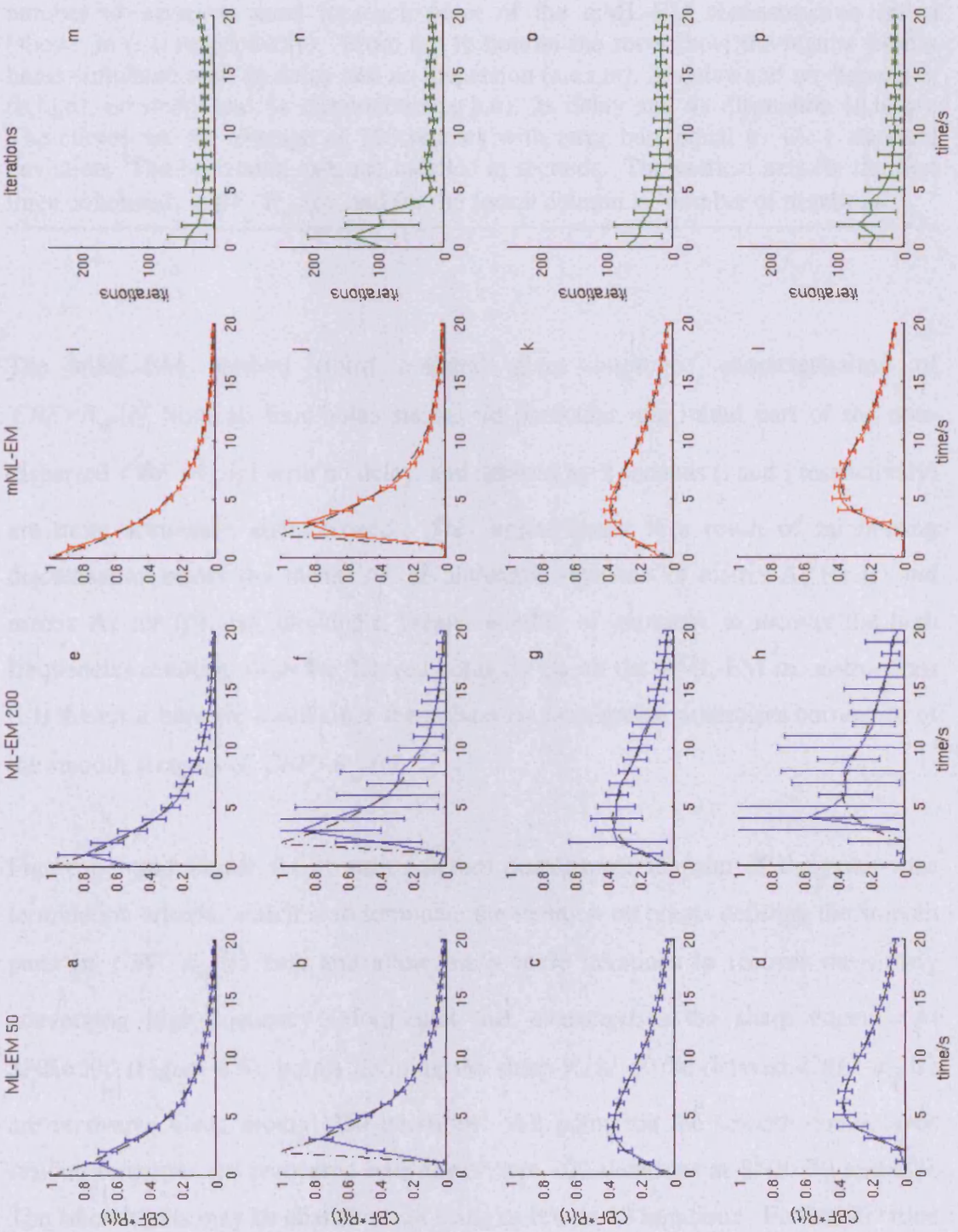
ML-EM 50
ML-EM 200
mML-EM
Iterations
CBF*R(t)
time/s
a
b
c
d
e
f
g
h
i
j
k
l
m
n
o
p

Figure 6.5: Impulse response functions reconstructed at TR=1s from data simulated with SNR=50 and healthy GM perfusion *CBF*=60ml/100g/min, *CBV*=4ml/100g, *MTT*=4s. From left to right, the columns show the reconstructions using 50 iterations of sML-EM (a-d), 200 iterations sML-EM (e-h), mML-EM (i-l), and the average number of iterations used for each point of the mML-EM reconstruction (m-p) (shown in (i-l) respectively). From top to bottom the rows show the results from a bolus simulated with no delay and no dispersion (a,e,i,m), 2s delay and no dispersion (b,f,j,n), no delay and 4s dispersion (c,g,k,o), 2s delay and 4s dispersion (d,h,l,p). The curves are the average of 100 repeats with error bars equal to +/- 1 standard deviation. The horizontal axes are labelled in seconds. The vertical axis for the first three columns is $CBF \cdot R_{eff}(t)$, and for the fourth column is 'number of iterations'.

The mML-EM method (third column) gives improved characterisation of $CBF \cdot R_{eff}(t)$ from all four bolus states. In particular, the initial part of the non-dispersed $CBF \cdot R_{eff}(t)$ with no delay, and delayed by 2 seconds (i and j respectively) are more accurately characterised. This improvement is a result of minimising discretisation errors (by means of the automatic selection of matrix $\mathbf{A_2}$ for (i) and matrix $\mathbf{A_1}$ for (j)) and allowing a greater number of iterations to recover the high frequencies resulting from the delayed bolus (j). In all the mML-EM reconstructions (i-l) the error bars are small since the point-wise termination minimises corruption of the smooth sections of $CBF \cdot R_{eff}(t)$.

Figure 6.5 and Figure 6.6 (fourth column) demonstrate the aim of the point-wise termination criteria, which is to terminate the iteration on points defining the smooth parts of $CBF \cdot R_{eff}(t)$ first and allow many more iterations to recover the slowly converging high-frequency information that characterises the sharp edges. At SNR=500 (Figure 6.6), points defining the sharp *RTM* of the delayed $CBF \cdot R_{eff}(t)$ are recovered using around 250 iterations. All points on the smooth non-delayed residue functions are recovered with fewer than 100 iterations at SNR=50 and 500. The smooth tails may be characterised using as few as 10 iterations. Further iteration on these points is likely to distort them. At SNR 500 (Figure 6.6), the point-wise termination criteria designed to minimise noise corruption become less important.

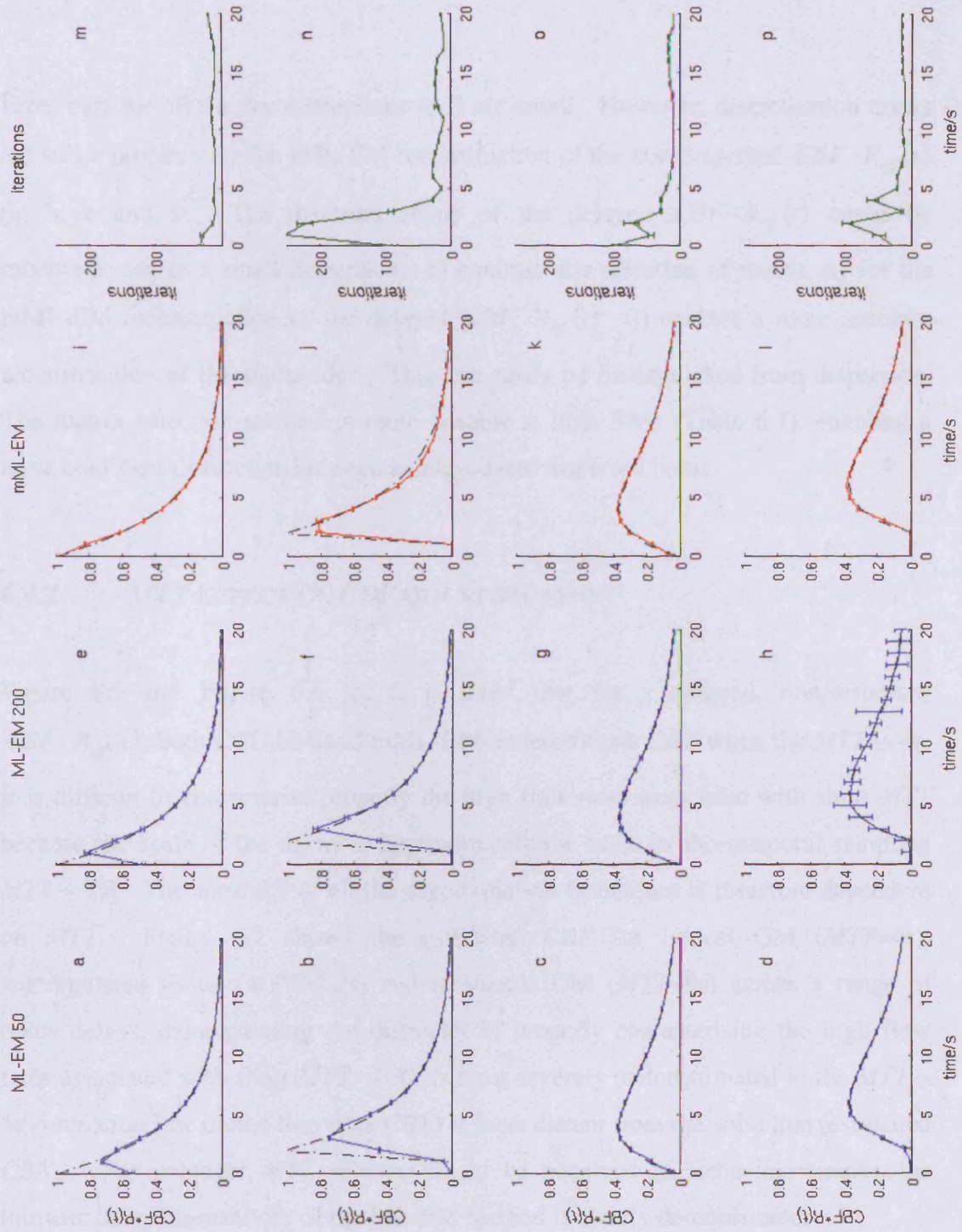
ML-EM 50
ML-EM 200
mML-EM
Iterations
CBF*R(t)
time/s
Iterations

Figure 6.6: Impulse response functions reconstructed at TR=1s from data simulated with SNR 500 and healthy GM perfusion *CBF*=60ml/100g/min, *CBV*=4ml/100g, *MTT*=4s. See Figure 6.5 legend for the labelling of the rows and columns.

Error bars for all the reconstructions (a-l) are small. However, discretisation errors are still a problem for the sML-EM reconstruction of the non-dispersed $CBF \cdot R_{eff}(t)$ (a, b, e and f). The distorted shape of the delayed $CBF \cdot R_{eff}(t)$ could be misinterpreted as a small dispersion. In contrast, the selection of matrix $\mathbf{A_1}$ for the mML-EM reconstruction of the delayed $CBF \cdot R_{eff}(t)$ (j) enables a more accurate reconstruction of the sharp edge. This can easily be distinguished from dispersion. The matrix selection method is more reliable at high SNR (Table 6.1), enabling a more confident distinction between a delayed and dispersed bolus.

6.4.2 *MTT* EFFECT ON *CBF* QUANTIFICATION

Figure 6.5 and Figure 6.6 (b, f, j) show that for a delayed, non-dispersed $CBF \cdot R_{eff}(t)$, both sML-EM and mML-EM underestimate *CBF* when the *MTT* is 4s. It is difficult to characterise properly the high flow rates associated with short *MTT* because the scale of the decay is approximately the same as the temporal sampling *MTT* ~ TR. The accuracy of all the deconvolution techniques is therefore dependent on *MTT*. Figure 6.7 shows the estimated *CBF* for typical GM (*MTT*=4s), autoregulated tissue (*MTT*=7.2s) and ischaemic GM (*MTT*=9s) across a range of bolus delays, demonstrating the difficulty in properly characterising the high flow rates associated with short *MTT*. *CBF* is most severely underestimated in the *MTT* = 4s simulation (the dotted line (true *CBF*) is most distant from the solid line (estimated *CBF*)). For a longer *MTT* =9s (as might be observed in ischaemic tissue), the intrinsic delay insensitivity of the ML-EM method is clearly demonstrated.

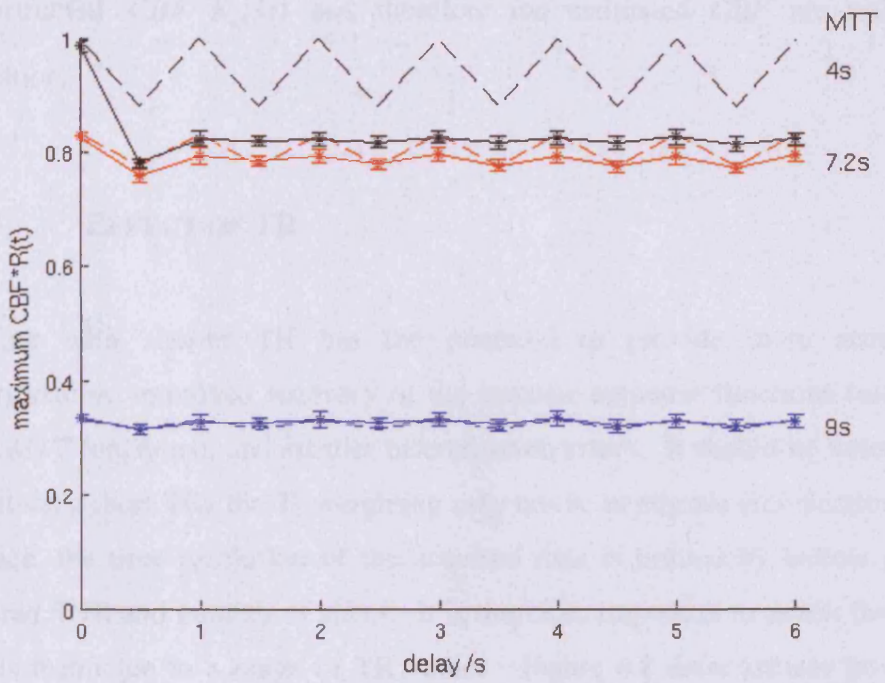

Figure 6.7: The graph shows the maximum of the $CBF \cdot R_{eff}(t)$ (vertical axis units ml/100g/s) reconstructed at TR=1s using mML-EM from data simulated (SNR 500) with no dispersion and delays (horizontal axis) of 0-6s. The solid lines show the maximum of the reconstructed $CBF.R_{eff}(t)$ for the *MTT* values indicated. The dotted lines indicate the corresponding maximum in each case of the *true* $CBF \cdot R_{eff}(t)$ measured at TR=1s. The periodicity is because the discrete sampling interval does not sample the maximum of $CBF \cdot R_{eff}(t)$ for delays which are non-integer multiples of TR. The figure shows the average of 100 iterations with error bars equal to two standard deviations

Although there is better characterisation of the *CBF* measured from impulse response functions with longer *MTT*, in such cases another artefact associated with the truncation of the concentration time-course data may be present. Simulations were performed to assess the effect of truncating the recirculation in the concentration time-course data; a situation that commonly occurs for longer-*MTT* tissue or for adispersed bolus, especially for shorter sampling lengths. It was found that found that a severe truncation of the recirculation produces an unphysical step in the tail of the reconstructed $CBF \cdot R_{eff}(t)$ (data not shown). However, the initial part of the

reconstructed $CBF \cdot R_{eff}(t)$ and therefore the estimated *CBF* are unaffected by truncation.

6.4.3 EFFECT OF TR

Imaging with shorter TR has the potential to provide more accurate delay quantification, improved recovery of the impulse response functions (especially for short *MTT* functions), and smaller discretisation errors. It should be noted, however, that at very short TRs the T_1 weighting may not be negligible (see Section 2.3.3). In practice, the time resolution of the acquired data is limited by factors such as the required SNR and number of slices. It is therefore important to assess the robustness of this technique to a range of TR values. Figure 6.8 demonstrates how the delay quantification is limited by the resolution of the sampling. The accuracy of the mML-EM reconstructions degrades as expected with increasing TR. Even if $CBF \cdot R_{eff}(t)$ were reconstructed with infinite accuracy, the particular TR and delay combination determine whether the delayed peak is actually sampled, and therefore accurate *CBF* estimates can only be obtained if the delay is an integer number of TRs (see Section 5.2.5). In order to assess delays to within 1 second, distinguish small dispersions, and enable reasonably accurate *CBF* estimates, a TR of 1 second is desirable. At the more commonly used TR value of 1.5 s, it is more difficult to assess small dispersions (This issue is discussed further in Chapter 9). The accuracy of the mML-EM reconstructions degrades as expected with increasing TR.

6.4.4 PATIENT DATA

The mML-EM method was applied to the GE-EPI image data from a patient with left internal carotid artery occlusion. The data collected had a baseline signal SNR= 50, which improved to ~500 after denoising was performed. The typical CNR in healthy GM was ~600, and in the affected side it was ~20 (compare with CNR ~ 200 in the SNR ~ 500 simulated data). The CNR is not uniform across the image because of the

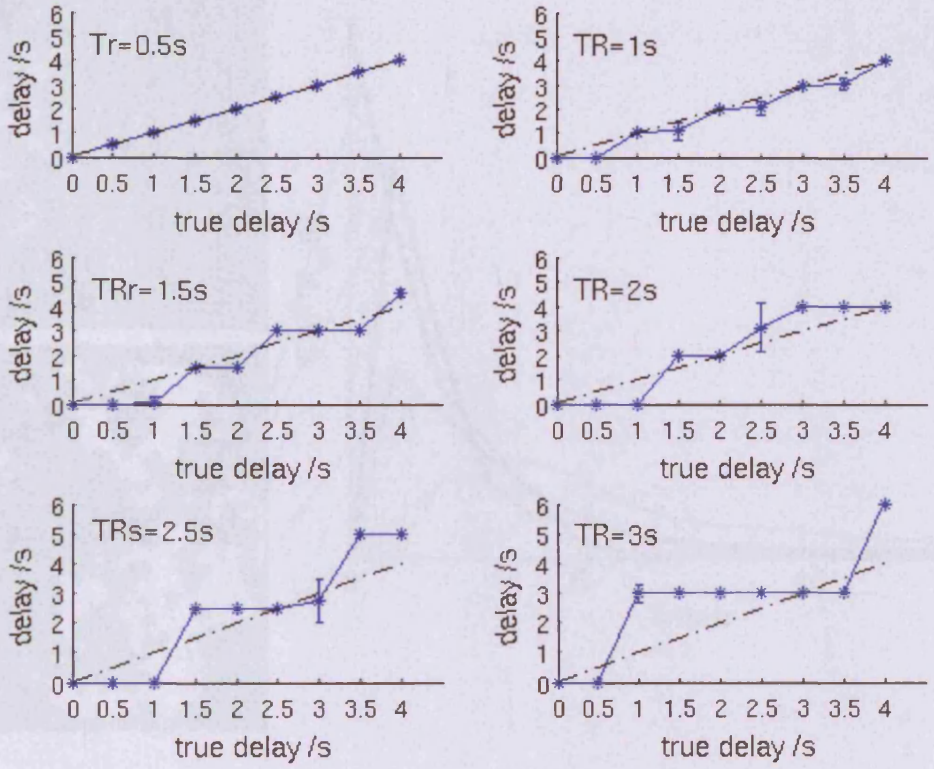

Figure 6.8: The graphs show the delay estimated (vertical axis) from the impulse response functions reconstructed using mML-EM and data simulated (SNR=500) with no dispersion and delays (horizontal axis) 0–4s, for healthy GM perfusion *CBF*=60ml/100g/min, *CBV*=4ml/100g, *MTT*=4s. The graphs show the results for sampling intervals 0.5s, 1s, 1.5s, 2s, 2.5s and 3s. The solid lines are the mML-EM estimated delay, and the dashed lines are the simulated delay. The results are the average of 100 iterations with error bars equal to two standard deviations. The periodic accuracy is caused by insufficient sampling to sample the true end of baseline for delays which are non-integer multiples of TR.

heterogeneity in the perfusion parameters and extent of delay and dispersion in various regions (see Section 5.2.4). The denoising enables a reasonably accurate selection of the appropriate deconvolution matrix, $\mathbf{A_1}$ or $\mathbf{A_2}$ (Table 6.1), and hence a good characterisation of $CBF \cdot R_{eff}(t)$ in all areas by means of the point-wise termination criteria.

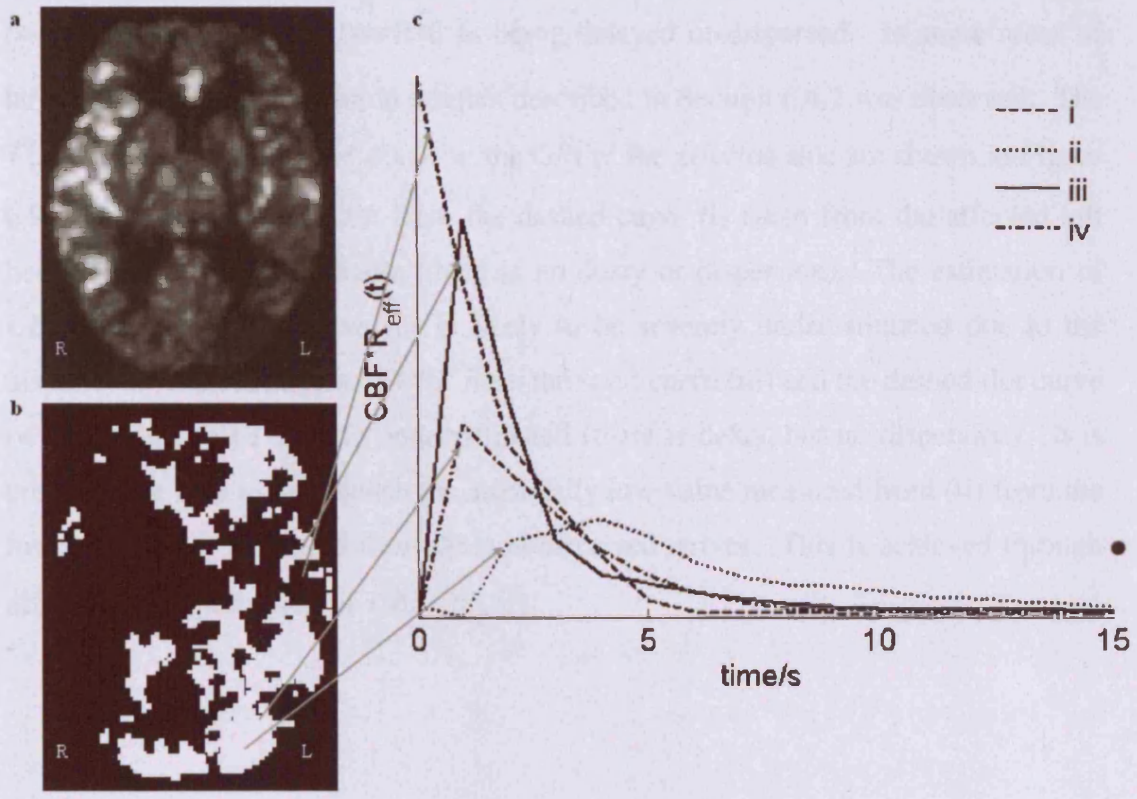

Figure 6.9: The results from the analysis of data acquired from a patient with left internal carotid occlusion a) *CBF* map calculated using the maximum of the impulse response function reconstructed using mML-EM. b) Highlighted pixels have been classified as delayed and/or dispersed according to the shape of the mML-EM reconstruction, as described in the Section 6.4.4. c) Example mML-EM recovered impulse response functions taken from i) a pixel where there is no delay or dispersion (dashed line), ii) a pixel where there is delay and dispersion (dotted line), iii) a pixel where there is delay but no dispersion (solid line), iv) a pixel with lower flow where there is delay but no dispersion (dashed-dot line).

Figure 6.9a is the *CBF* map measured from the maximum of $CBF \cdot R_{eff}(t)$ calculated using the mML-EM algorithm. Various regions of severely reduced *CBF* can be seen in the left hemisphere, and in the anterior and posterior of the right hemisphere. Figure 6.9b highlights voxels identified (from the shape of the reconstructed $CBF \cdot R_{eff}(t)$ as suffering from bolus delay and/or dispersion, many of which also show low *CBF*. If the maximum of the reconstructed $CBF \cdot R_{eff}(t)$ did not occur at

t= 0, $CBF \cdot R_{eff}(t)$ was classified as being delayed or dispersed. In some areas of large dispersion, the truncation artefact described in Section 6.4.2 was observed. The $\tilde{r}(t)$ for four representative pixels in the GM of the affected side are shown in Figure 6.9c. The estimation of *CBF* from the dashed curve (i) taken from the affected left hemisphere is low but reliable (there is no delay or dispersion). The estimation of *CBF* from the dotted curve (ii) is likely to be severely underestimated due to the dispersion. The estimation of *CBF* from the solid curve (iii) and the dashed-dot curve (iv) are likely to be slightly underestimated (there is delay, but no dispersion). It is crucial to be able to distinguish the artificially low value measured from (ii) from the low flow values measured from the non-dispersed curves. This is achieved through accurate characterisation of $CBF \cdot R_{eff}(t)$.

6.5 DISCUSSION

The methodology presented in this chapter has been shown to minimise the artefacts associated with the deconvolution algorithm, and provide an improved characterisation of $CBF \cdot R_{eff}(t)$. Previous studies suggest that tissue at risk of infarction is characterised by low *CBF* and prolonged *MTT* (Powers 1991). Since delay and dispersion have been shown to bias the estimated *CBF* and *MTT*, an accurate characterisation of $CBF \cdot R_{eff}(t)$ is vital to assess the reliability of these estimates.

It was shown that the sML-EM algorithm can lead to an unrealistic reconstruction of $CBF \cdot R_{eff}(t)$, with consequently incorrect *CBF* estimates. For the sML-EM reconstruction to give physically meaningful results, the number of iterations performed must take into account the CNR of the time-course, and the actual shape of the unknown $CBF \cdot R_{eff}(t)$. Since the contrast will not be uniform across the whole brain, the number of iterations used in the reconstruction should change accordingly.

In order to avoid corruption due to noise, iteration is often terminated prematurely, resulting in smooth but biased reconstructions. Early termination fails to extract all the information present, biasing the low-frequency information and neglecting to extract any high-frequency information that may be present (Figure 6.5 and Figure 6.6 (a-d)).

The modified ML-EM method presented in this chapter implements point-wise termination criteria. The new termination criteria enable the recovery of high-frequency information associated with $R_{eff}(t)$ whilst preventing corruption due to noise fitting, thus preserving a smooth tail (Figure 6.5 and Figure 6.6(i-l)). The point-wise termination criteria allow any slowly converging high frequencies occurring in the initial part of $CBF \cdot R_{eff}(t)$ to be reconstructed using a large number of iterations (Figure 6.5 and Figure 6.6(m-p)). If the initial section of $CBF \cdot R_{eff}(t)$ contains no high-frequency information, this part of the function converges quickly and the point-wise termination criteria allow few iterations in its reconstruction (Figure 6.5 and Figure 6.6(m)). It should be emphasised that no prior information about the delay/dispersion state of $R_{eff}(t)$ is assumed in the termination criteria. The point-wise termination criteria also automatically account for noise, allowing realistic reconstruction across a large range of SNR.

The characterisation of $CBF \cdot R_{eff}(t)$, in particular the distinction between a bolus dispersion and a delay, is further improved by the automated selection of the convolution matrix whose approximations best minimise the discretisation errors for the particular $CBF \cdot R_{eff}(t)$ being reconstructed. The improvement is particularly apparent comparing Figure 6.5 and Figure 6.6 (b and j). This distinction is important both for assessing the accuracy of the *CBF* estimate, and potential subsequent correction of the *CBF* estimate. Although, the effect of dispersion on the impulse response function cannot be *corrected* without knowing a vascular transport function (VTF) (Østergaard *et al.* 1999; Calamante *et al.* 2003a), an improved characterisation of $CBF \cdot R_{eff}(t)$ is an important first step towards this correction. Furthermore, the

identification of delay and dispersion is important for highlighting unreliable regions on the *CBF* maps, and may alter the prediction of areas thought to have increased risk of infarction. Without knowledge of delay and dispersion, it is not possible to separate an underestimation of *CBF* from a true perfusion abnormality. The information from maps indicating regions of delay and dispersion (such as the regions highlighted in Figure 6.9b) would therefore be a useful input into predictor-models (e.g.(Wu *et al.* 2001), see also Section 3.12), which assess the probability of tissue infarction using diffusion, perfusion and T_2 data. Thus, an improved $CBF \cdot R_{eff}(t)$ could avoid a potentially dangerous misclassification of 'at risk' tissue.

A reliable interpretation of DSC-MRI perfusion maps is only possible through both an accurate characterisation and accurate interpretation of the shape of $CBF \cdot R_{eff}(t)$. The *CBF* will be under-estimated when measured from the maximum of a dispersed $CBF \cdot R_{eff}(t)$; if the shape of $CBF \cdot R_{eff}(t)$ is not considered, the error in the *CBF* could be overlooked. If the *CBF* estimates are interpreted with reference to the shape of $CBF \cdot R_{eff}(t)$, the accuracy of the characterisation must also be considered. For example, in ischaemic tissue, a long *MTT* is often combined with a low *CBF*. If the ischaemic $CBF \cdot R_{eff}(t)$ were delayed, care must be taken no to misidentify the long *MTT* as dispersion (for example, if the *RTM* of $CBF \cdot R_{eff}(t)$ is not accurately reconstructed). Such a misidentification could lead to the interpretation that the *CBF* estimate has been underestimated. The tissue may in fact healthier than the *CBF* and dispersion maps suggest. In order to prevent such misdiagnosis, an accurate characterisation of $CBF \cdot R_{eff}(t)$ is vital. In this work the automatic selection of either matrix $\mathbf{A_1}$ or $\mathbf{A_2}$ improves the reconstruction of the *RTM* of $CBF \cdot R_{eff}(t)$. This permits a more accurate distinction between an impulse response function with a long *MTT* and no dispersion from one which is dispersed. In this way, a truly low *CBF* can be separated from the case in which *CBF* is underestimated because of dispersion.

For high quality data, the delayed/dispersed regions such as those highlighted in Figure 6.9b could be subcategorised into delayed and dispersed voxels. For example,

a reconstruction using matrix $\mathbf{A_1}$ would be classified as "non-dispersed and delayed by a near integer value of TR." A reconstruction using matrix $\mathbf{A_2}$ would be classified as "dispersed" if the *RTM* was greater than one measurement point, and "delayed by a near half integer value of TR" if the *RTM* was equal to one measurement point. In Chapter 7, a method of sub-categorisation is suggested and the limitations of this methodology are discussed.

In order to achieve an accurate characterisation of $CBF \cdot R_{eff}(t)$, care must be taken in selecting the AIF, so as to prevent negative delays (i.e. $C_t(t)$ arriving before $C_a(t)$). When negative delays were simulated, the same effects were observed as reported in by Wu *et al.* (Wu *et al.* 2003). Wu *et al.* circumvented this overestimation in SVD using a block-circulant matrix. However, the block-circulant modification results a uniform underestimation of *CBF* from $CBF \cdot R_{eff}(t)$ with positive, negative, and zero delays for normal *MTT* values (it is in this sense that the block-circulant SVD algorithm is delay-insensitive). The mML-EM method could be modified to use a block-circulant $\mathbf{A_1}$ matrix. However, matrix $\mathbf{A_2}$, which minimises the discretisation errors and hence achieves the most accurate *CBF* from $CBF \cdot R_{eff}(t)$ with no delay or dispersion, cannot be made block-circulant. This matrix is deliberately formed in this way because it avoids the *CBF* underestimation that is intrinsic to block-circulant methods for normal *MTT* values when t_{delay}= 0. In healthy vasculature, the most accurate *CBF* estimates can therefore be achieved through careful selection of the AIF measurement site in order to avoid negative delays, and deconvolution using the non-block-circulant matrices $\mathbf{A_1}$ and $\mathbf{A_2}$. If delay and dispersion in the vascular transport are removed from the concentration time-course data, mML-EM deconvolution with matrix $\mathbf{A_2}$ permits a reliable *CBF* estimate. In Chapter 9 a novel methodology is presented to minimise delay and dispersion in the concentration time-course data. If this minimisation is successfully achieved, a deconvolution technique that can accurately characterise the true maximum of the tissue impulse response function is especially valuable.

The mML-EM methodology applied to the patient data (Figure 6.9) clearly highlights the effect of the internal carotid artery occlusion on the DSC-MRI perfusion measurements. Figure 6.9a and Figure 6.9b reveal that areas indicating low perfusion actually correspond to regions where there is dispersion and/or delay. This suggests that the perfusion abnormality is exaggerated due to dispersion and/or delay of the bolus through the occluded vessel to into the left hemisphere. If this perfusion map were interpreted independently of the delay and dispersion map, a treatment plan may have been based on the artificially low perfusion estimates, with potentially dangerous consequences. Further examples highlighting *in vivo* perfusion measurement errors are discussed in Chapter 9.

6.5.1 LIMITATIONS

The *CBF* estimates obtained from delayed high flow regions in 6.9a should be interpreted in the light of the possible underestimation for short *MTT* tissue illustrated in Figure 6.7. The accuracy of *CBF* and delay quantification in regions of short *MTT* are Nyquist limited. In addition, discretisation errors associated with deconvolution at intervals of TR are manifest most strongly for short *MTT* delayed and non-dispersed $R_{eff}(t)$. The mML-EM reconstructions shown in Figure 6.5 and Figure 6.6 (i and j) demonstrate that these errors may be minimised by appropriately selecting the matrix $\mathbf{A}_1$ or $\mathbf{A}_2$. Although the errors associated with discretisation are independent of noise, the contrast-to-noise will affect the reliability of the matrix selection method used (see Table 6.1).

The specific point-wise termination criteria shown here were designed in the preliminary simulations to extract a physically meaningful shape for $R_{eff}(t)$ with and without bolus delay and/or dispersion. The simulations found that the values of α and β in Equation [6.5] gave good reconstructions across a range of impulse response function shapes and CNRs. However, these values were determined empirically, and thus they could potentially be improved by, for example, adapting them according to

the CNR of the pixel being deconvolved. In addition, the empirically determined criteria for selecting the $\mathbf{A_1}$ or $\mathbf{A_2}$ matrices (also determined in the preliminary simulations, (Equation [6.6] in the Appendix) could be optimised and generalised for various scanner sequence parameters. In particular, the sampling interval TR will influence the accuracy of the reconstruction, especially across the initial rise, which is used to distinguish delay and dispersion in the preliminary deconvolution. Optimisation and generalisation of all these criteria require further work. In view of these limitations, Chapter 7 extends the ideas introduced in this chapter and presents an alternative methodology that is less reliant on user determined empirical criteria.

6.6 CONCLUSION

An improved characterisation of the impulse response function can be achieved by selecting the most appropriate convolution matrix approximations and implementing point-wise termination criteria for the ML-EM iteration. These modifications to the standard ML-EM method enable the extraction of high-frequency information associated with the impulse response function itself, whilst preventing corruption due to noise. In particular, the sharp *RTM* of a delayed and non-dispersed $R_{eff}(t)$ can be reconstructed, distinguishing it from a dispersed $R_{eff}(t)$. This distinction is important for assessing the accuracy of *CBF* estimates, and therefore should have important implications for tissue outcome prediction models.

6.7 APPENDIX

This appendix describes in outline the empirical criteria used to select the most appropriate matrix **A**.

Definitions:

sML-EM solution calculated using matrix $\mathbf{A_1}$ after k iterations: $\tilde{r}_1^{[k]}$

Time point of maximum point in $\tilde{r}_1^{[k]}$: $m_1^{[k]}$

Time point at end of baseline of $\tilde{r}_1^{[k]}$: $b_1^{[k]}$

Number of time points for $\tilde{r}_1^{[k]}$ to rise-to-maximum: $n_1^{[k]} = m_1^{[k]} - b_1^{[k]}$

sML-EM solution calculated using matrix $\mathbf{A_2}$ after k iterations: $\tilde{r}_2^{[k]}$

Time point of maximum point in $\tilde{r}_2^{[k]}$: $m_2^{[k]}$

Time point at end of baseline of $\tilde{r}_2^{[k]}$: $b_2^{[k]}$

Number of time points for $\tilde{r}_2^{[k]}$ to rise-to-maximum: $n_2^{[k]} = m_1^{[k]} - b_2^{[k]}$

Method:

The sML-EM solutions after 10 and 100 iterations were calculated, and the above parameters m, b, and n were determined.

For the TR=1s simulations, the matrix selected was default set to $\mathbf{A_2}$. If the criteria below were satisfied, the matrix used in the final mML-EM reconstruction was selected to be $\mathbf{A_1}$ instead. These criteria were found from preliminary simulations to be satisfied by impulse response functions with a near integer sampling interval delay and no dispersion, and these impulse response functions were found to be most accurately reconstructed using matrix $\mathbf{A_1}$.

Default: $\mathbf{A=A_2}$

$$\left.\begin{array}{llll}
\textit{if} & n_2^{[100]} \le 3 \ \textit{and} & \dfrac{\tilde{r}_1^{[100]}(m_1^{[100]}-1)}{\tilde{r}_1^{[100]}(m_1^{[100]})} > 0.8 & \textit{and} \ \dfrac{\tilde{r}_2^{[100]}(m_2^{[100]}-1)}{\tilde{r}_2^{[100]}(m_2^{[100]})} < 0.55 \\
\textit{if} & n_2^{[100]} = 3 \ \textit{and} & \dfrac{\tilde{r}_1^{[100]}(m_1^{[100]}-1)}{\tilde{r}_1^{[100]}(m_1^{[100]})} > 0.6 & \textit{and} \ \dfrac{\tilde{r}_2^{[100]}(m_2^{[100]}-1)}{\tilde{r}_2^{[100]}(m_2)} > 0.9 \\
\textit{if} & n_2^{[100]} = 2 \ \textit{and} & \left(\dfrac{\tilde{r}_1^{[100]}(m_1^{[100]}-1)}{\tilde{r}_1(m_1^{[100]})} < 0.1 \right. & \textit{or} \ \left. \dfrac{\tilde{r}_1^{[100]}(m_2^{[100]}-1)}{\tilde{r}_1^{[100]}(m_2^{[100]})} > 0.6 \right) \\
 & \textit{and} & \dfrac{\tilde{r}_2^{[100]}(m_2^{[100]}-1)}{\tilde{r}_2^{[100]}(m_2^{[100]})} < 0.6 & \\
\textit{unless} & \ldots \ \ldots & \dfrac{\tilde{r}_2^{[100]}(m_2^{[100]})}{\tilde{r}_2^{[10]}(m_2^{[10]})} \cdot \dfrac{\tilde{r}_1^{[10]}(m_1^{[10]})}{\tilde{r}_1(m_1^{[100]})} > 0.85 & \textit{or} \quad m_2^{[10]} = 0
\end{array}\right\} \begin{array}{l} [6.6] \\ \\ \mathbf{A=A_1} \end{array}$$

SNR 500 **delay /s**

		0.0	0.5	1.0	1.5	2.0	2.5	3.0	3.5	4.0	4.5	5.0	5.5	6.0
dispersion /s	**0.0**	1.00	0.99	1.00	1.00	1.00	1.00	1.00	1.00	1.00	1.00	1.00	1.00	1.00
	1.0	1.00	1.00	0.93	1.00	0.93	1.00	0.92	1.00	0.89	1.00	0.91	1.00	0.88
	2.0	1.00	1.00	1.00	1.00	1.00	1.00	1.00	1.00	0.99	1.00	1.00	1.00	0.98
	3.0	1.00	1.00	1.00	1.00	1.00	1.00	1.00	1.00	1.00	1.00	1.00	1.00	1.00
	4.0	1.00	1.00	1.00	1.00	1.00	1.00	1.00	1.00	1.00	1.00	1.00	1.00	1.00
	5.0	1.00	1.00	1.00	1.00	1.00	1.00	1.00	1.00	1.00	1.00	1.00	1.00	1.00

SNR50 **delay /s**

		0.0	0.5	1.0	1.5	2.0	2.5	3.0	3.5	4.0	4.5	5.0	5.5	6.0
dispersion /s	**0.0**	1.00	0.96	0.60	0.94	0.72	0.92	0.74	0.93	0.77	0.98	0.58	0.92	0.60
	1.0	0.80	0.66	0.90	0.63	0.71	0.65	0.77	0.65	0.82	0.64	0.76	0.65	0.79
	2.0	0.81	0.93	0.81	0.89	0.69	0.93	0.75	0.97	0.82	0.88	0.72	0.90	0.81
	3.0	0.82	0.91	0.78	0.93	0.81	0.89	0.79	0.90	0.82	0.95	0.81	0.88	0.82
	4.0	0.89	0.86	0.90	0.91	0.90	0.91	0.95	0.91	0.90	0.91	0.94	0.91	0.88
	5.0	0.92	0.91	0.95	0.84	0.92	0.88	0.96	0.89	0.95	0.87	0.90	0.91	0.88

Table 6.1: The proportion of correctly selected matrices ($\mathbf{A}_1$ or $\mathbf{A}_2$) over 100 simulations of delay (columns) and dispersion (rows) combinations for the mML-EM TR=1s simulations at SNR 50 and 500 using healthy GM perfusion values. The shaded cells are the delay and dispersion combinations requiring reconstruction with the $\mathbf{A}_1$ matrix.

7 PERFUSION QUANTIFICATION USING OSCILLATION INDEX REGULARISED ML-EM AND WAVELET THRESHOLDING

7.1 INTRODUCTION

In Chapter 6 a modification to the iterative method of Maximum-Likelihood Expectation-Maximisation (modified-MLEM or mMLEM) was described for the deconvolution of DSC-MRI data. In the mMLEM reconstruction, suppression of noise-derived frequency components that corrupt the impulse response function $CBF \cdot R_{eff}(t)$ was achieved by means of a *point-wise* termination criterion for the ML-EM iteration (Willats *et al.* 2006). The point-wise termination criteria enable the smooth tail of $CBF \cdot R_{eff}(t)$ to be reconstructed with less iteration than its sharp rise-to-maximum (*RTM*), in situations where the bolus is delayed but not dispersed. The point-wise termination criteria were shown to minimised the fitting of experimental noise in the reconstruction, whilst recovering physiologically significant frequency components that define the shape of $CBF \cdot R_{eff}(t)$. In this way, delay and dispersion could be identified and distinguished (see Chapter 6 for more details).

In a clinical situation it is important that an analysis technique is adaptable to different scanners and scanning sequences. In addition, so it can be used in the every day scanning of patients, it should be robust, adaptable, and automated. With this in mind, the work presented in this chapter builds upon the idea of *temporally-selective* preservation of the frequencies that define the true physiological shape of the impulse response function and temporally-selective suppression of those frequency components that are associated with noise. Whereas the termination criteria used for mML-EM iteration were empirically determined and dependent on various scanning parameters (see Section 6.5.1), the regularisation approach presented here uses criteria that are less dependent on the scanning parameters or quality of the data. This is achieved by combining an *oscillation-index*-regularised ML-EM reconstruction with subsequent *wavelet* decomposition and thresholding.

This chapter begins by introducing the concept of wavelet decomposition and its implementation as a noise-suppressing filter. The concept of an oscillation index

regularised ML-EM is then explained. Finally, the combination of these two methods as an accurate and robust DSC-MRI deconvolution method for characterising $CBF \cdot R_{eff}(t)$ is demonstrated using simulations.

7.2 WAVELET THEORY

7.2.1 TEMPORAL AND FREQUENCY RESOLUTION

Standard deconvolution techniques are based on the Discrete Fourier Transform (DFT) that uses complex exponentials of different frequencies as basis functions. Using this frequency-time formulation, frequency components of a signal cannot be localised in time. The Short Term Fourier Transform (STFT) (Bracewell 1986) tries to localise the frequency components by windowing the signal over the interval which the transform is performed and then shifting this window to cover the whole signal. In accordance with the Uncertainty Principle, the width of the windowing function determines the trade-off between good frequency resolution and good time resolution. A wide window gives better frequency resolution but poor time resolution; a narrower window (said to be compactly supported) gives good time resolution but poor frequency resolution. In addition, there is no inverse transform for the STFT, so it cannot be used in deconvolution techniques.

Restrictions on temporal localisation of frequencies may be circumvented with the wavelet transform (WT). In the WT, the basis functions are no longer the complex exponentials used in the FT, but are wavelet functions that are oscillatory in the time domain and concentrated in both the time and frequency domains (see Section 7.2.2). Figure 7.1 illustrates some of the commonly used wavelet functions.

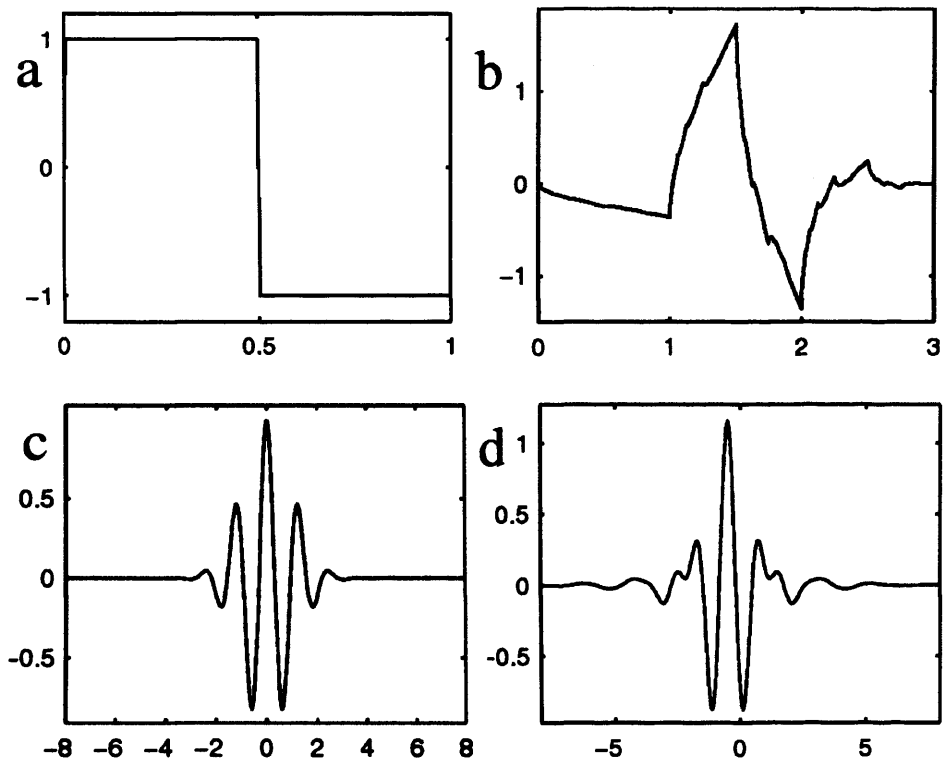

Figure 7.1: Some common wavelets, or basis functions used in the wavelet transform. a) Haar wavelet, b) Daubechies wavelet, c) Morlet wavelet, d) Myer wavelet.

The STFT picks out different frequency components by keeping the window width constant and filling it with sinusoidal oscillations of different frequencies. Conversely, the WT picks out different frequency components by keeping the number of oscillations constant (i.e. the same locally concentrated wavelet function) and varying the width of the "window" by means of contracting and dilating the wavelet. As a result, in the WT, high frequencies are characterised using a narrow window and the low frequencies using a wide window. Although the Uncertainty Principle cannot be overcome, the WT offers a variable-resolution time-frequency representation, which results in better temporal localisation of high frequencies and better frequency resolution of low frequencies. Figure 7.2 compares the coverage of the time-frequency plane for the STFT and the WT. In the FT, the time-frequency resolution is independent of time or frequency. In the WT, the time-frequency resolution is

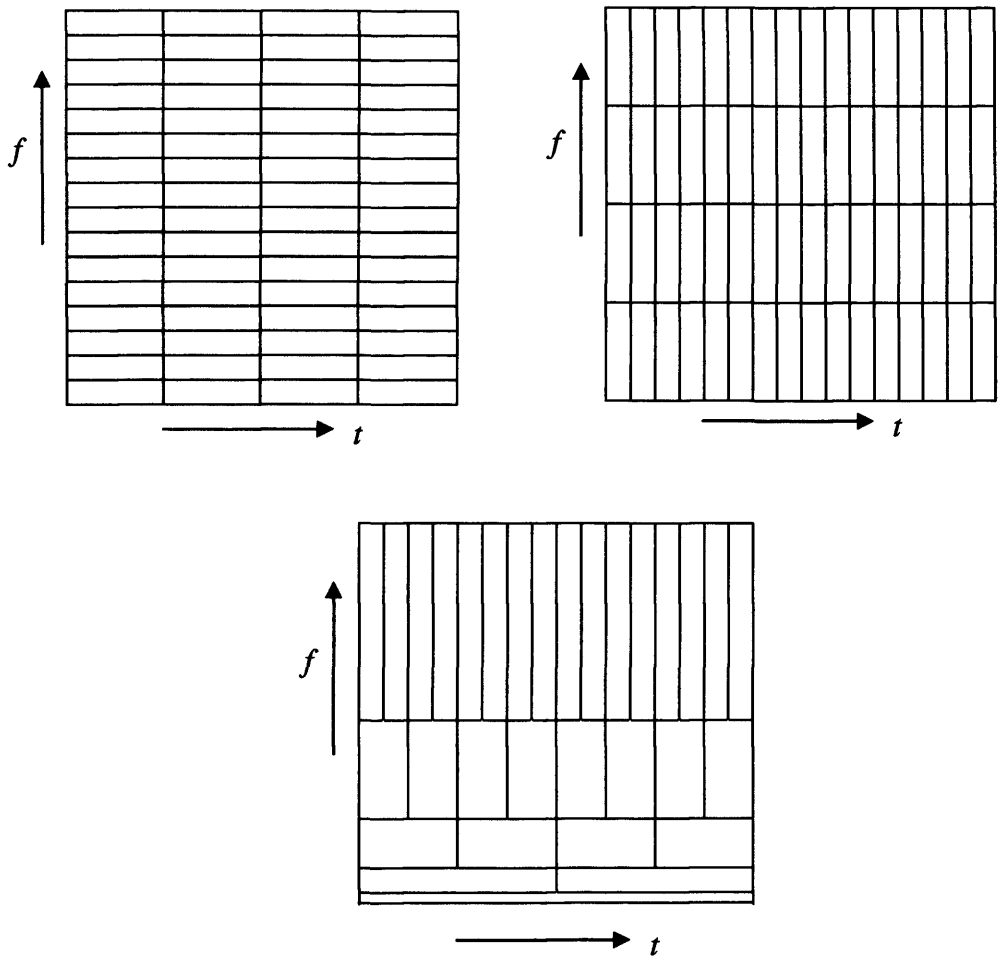

Figure 7.2: The 3 panels represent the time-frequency plane for the STFT (top row) and the WT (bottom row). The frequency increases up the vertical axis and the time increases along the horizontal axis. For the STFT, the left figure has better frequency resolution, and the right figure has better time resolution. For the WT, the higher frequencies have better time resolution, and the lower frequencies have better frequency resolution. In all diagrams, the area of each box (equal areas) is determined by Uncertainty Principle.

dependent on the time and frequency.

7.2.2 THE CONTINUOUS WAVELET TRANSFORM

The mathematic formulation of the continuous WT (CWT) is analogous to the continuous FT (Bracewell 1986). The CWT is defined as the inner-product between the signal $f(t)$ and wavelet (basis) function $\Psi_{s,\tau}(t)$, where s and τ are the scale (indicating the wavelet's width) and translation (indicating the wavelet's position) parameters respectively, (which are respectively analogous to frequency and time variables in the FT). The wavelet coefficients are defined:

$$\gamma(s,\tau) = \int f(t)\Psi^*_{s,\tau}(t)\mathrm{dt} \qquad [7.1]$$

Correspondingly, the inverse CWT (ICWT) is:

$$f(t) = \iint \gamma(s,\tau)\Psi_{s,\tau}(t)\mathrm{d}\tau\mathrm{ds} \qquad [7.2]$$

Common terminologies for describing the WT are the *Mother* and *Daughter* wavelets. The Mother wavelet function $\Psi(t)$ is the basis (wavelet) function (or analysing wavelet), and the Daughter wavelet functions $\Psi_{s,\tau}(t)$ are created by scaling and translating the Mother wavelet:

$$\Psi_{s,\tau}(t) = \frac{1}{\sqrt{s}}\Psi\left(\frac{t-\tau}{s}\right) \qquad [7.3]$$

The Mother wavelet is a continuous (real or complex) function that satisfies certain mathematical conditions: These include 1) It must integrate to 0, i.e., it is oscillatory; 2) It has finite energy, i.e., its oscillations are contained within a finite duration; 3) It satisfies the *admissibility* condition, i.e., it has a band-pass like spectrum; 4) It satisfies the *regularity* condition, i.e., it is oscillatory and finite in both the time and frequency domains. Different wavelet families (see Figure 7.1) make different trade offs between how compactly the basis functions are localised and how smooth they are. For example, the Haar wavelet (Figure 7.1a) is very compact (it can be defined using just three points), but it is not very smooth. On the other hand, the Myer

wavelet (Figure 7.1c) is smooth but less compact. Subgroups within a wavelet family are categorised according to their number of *vanishing moments m.* The number of vanishing moments is essentially the half the number of zero-crossings within the wavelet function. Formally, a wavelet has its m^{th} vanishing moment if

$$\int t^m \psi(t) dt = 0 \qquad [7.4]$$

In practice, the WT is computed by first choosing a function for the Mother wavelet. In general, the Mother wavelet is chosen to look similar to the patterns that are to be localised in the signal. The first scale s=1, is the most compressed Daughter wavelet. The Daughter wavelet is placed at t=0, multiplied by signal and integrated over all times. It is then shifted along the positive time axis by small amount τ, multiplied and integrated as before. The shifting and integration are repeated until the wavelet reaches the end of the signal. A second Daughter wavelet at a larger scale s=2 is created, and the shifting and integration are repeated as described above. This process is performed for every value of s. As the wavelet is dilated, the transform picks up lower and lower frequencies, but these are present over a larger section of the signal and so will have poorer temporal localisation. In summary, shifting the wavelet in time provides temporal localisation to the signal. Changing the wavelet scale localises the signal in scale (providing frequency resolution). The wavelet coefficients will be large if the signal has a spectral component corresponding to the current value of s and at the temporal location corresponding to the current value of τ.

7.2.3 THE DISCRETE WAVELET TRANSFORM

In most signal processing applications, the signal is discretely sampled. Therefore a discrete form of the wavelet transform is necessary to analyse the signal. In the DFT the time-frequency scale is sampled at a uniform rate. Similarly in the Discrete Wavelet Transform (DWT), the translation and scale variables are sampled at a uniform rate. Changing the frequency in the DFT enables a reduction in the sampling

rate. Similarly, the scale change in the DWT allows the sampling rate to be reduced. According to Nyquist's rule, the sampling rate must be at least twice the bandwidth in order to represent the highest constituent frequency component unaliased. At larger scales (lower frequencies), the sampling rate N can be decreased in proportion to the scale. For example, if the Nyquist condition is satisfied at the smallest scale, j, the sampling rate N_j necessary for each successive scale is

$$N_{j+1} = \frac{j}{j+1} N_j \qquad [7.5]$$

If this condition is satisfied, the original continuous time-signal can be reconstructed unaliased from its discrete samples in the wavelet domain.

Discrete scale and translation steps (j and k respectively) can be defined such that the Daughter wavelets have the form:

$$\psi_{j,k}(t) = \frac{1}{\sqrt{s_0^j}} \psi\left(\frac{t - k\tau_0 s_0^j}{s_0^j} \right) \qquad [7.6]$$

j and k are integers, s_0 is a fixed dilation step, and τ_0 is a fixed translation step. The case for which $s_0 = 2$, and $\tau_0=1$ is known as dyadic sampling of frequency and time axis. This common sampling scheme is efficient and accurate. The Daughter wavelets in dyadic sampling are given by:

$$\psi_{j,k}(t) = 2^{-j/2} \psi(2^{-j} t - k) \qquad [7.7]$$

Note that increasing j increases the wavelet scale.

The discrete wavelet coefficients of a signal $f(t)$ are:

$$\gamma(j,k) = \Delta t \sum_t f(t) \psi_{j,k}(t) \qquad [7.8]$$

And the inverse wavelet transform is:

$$f(t)=\sum_{j,k}\gamma(j,k)\psi_{j,k}(t) \qquad [7.9]$$

In accordance with the FT shift theorem (Bracewell 1986), every time the wavelet is stretched in the time domain by a factor of two (double j) its bandwidth and central frequency are halved. The shape of the band-pass spectrum for Mother wavelet is such that the band-pass spectrum of each successive scaling (Daughter wavelets) overlap each other. In this way there will be no unanalysed gaps in the spectrum. Since at each Daughter-wavelet stretch, only half the remaining low-frequency spectrum is covered by its band-pass spectrum, a *Scaling function* $\phi(t)$ with a low pass spectrum is used to cover this lowest-frequency region. The situation is illustrated in Figure 7.3.

The Scaling function is essentially a signal with a low-pass spectrum. Therefore its wavelet decomposition uses an infinite number of coefficients up to level j_n.

$$\phi(t)=\sum_{j\geq j_n,k}^{j=\infty}\gamma(j,k)\psi_{j,k}(t) \qquad [7.10]$$

Without $\phi(t)$, an infinite set of wavelets would be needed to cover the entire frequency spectrum. Including a Scaling function, the signal $f(t)$ can be expressed:

$$f(t)=\sum_{k}\lambda(j_n,k)\phi_{j_n,k}(t)+\sum_{j<j_n,k}\gamma(j,k)\psi_{j,k}(t) \qquad [7.11]$$

where j_n is the chosen cut-off scale for the wavelet dilations, and scaling function coefficients are given by:

$$\lambda(j_n,k)=\Delta t\sum_{t}\phi(t)\psi_{j_n,k}(t) \qquad [7.12]$$

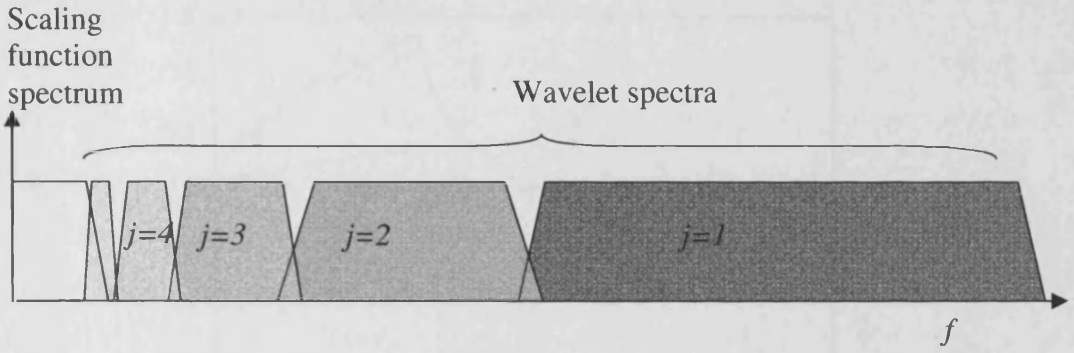

Figure 7.3: Coverage of the frequency spectrum using a finite set of wavelets and a Scaling function. Each time the Daughter wavelet is stretched by a factor of two, the band-width and central frequency of the Daughter-wavelet spectrum are halved. Consequently, at every wavelet stretch only half the remaining frequency spectrum is covered. In order to use a finite number of wavelets, a Scaling function that has a low-pass spectrum is used.

For illustrative purposes, the Scaling and Mother wavelet functions for the Daubechies-4 wavelet family are shown in Figure 7.4 together with their frequency responses. The Daubechies-4 wavelet has m=2 vanishing moments.

7.2.3.1 Multiresolution Decomposition

Practically, the most efficient way to implement DWT is using the wavelet decomposition and reconstruction algorithm proposed by Mallat (Mallat 1989). In this formulation, the signal $f(t)$ is separated into 'details' and 'approximations' by passing it through an iterated filter bank of high-pass and low-pass filters. These filters correspond to the spectra of the Daughter wavelet function and the corresponding Scaling function respectively. The first high-pass and low-pass filters (or first level *multiresolution decomposition*) bisect the signal spectrum into a high-pass and low-pass band. The output of each filter has half the bandwidth of the original signal, and can therefore be subsampled without loss of information. The subsampled output of the high-pass filter contains the smallest-scale wavelet coefficients. The subsampled output from the low-pass filter is split further, using a

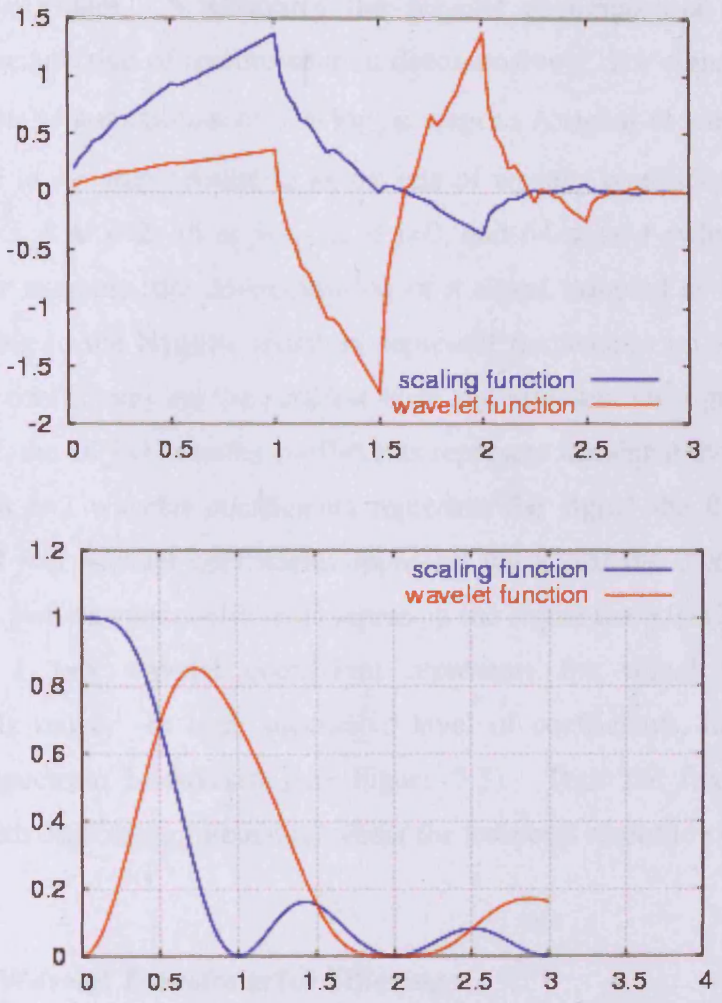

Figure 7.4: Top: The Wavelet and Scaling functions for the Daubechies-4 wavelet. Bottom: The frequency response of the illustrated Daubechies-4 Wavelet and Scaling functions. The Scaling function covers the zero-frequency region of the spectrum.

second high-pass/low-pass filter pair, into a high-pass and low-pass band. The subsampled output of the resulting high-pass band contains the next smallest-scale wavelet coefficients. The subsampled output of the resulting low-pass band is split further using another filter pair, and so on until only one sample point remains. The outcome of this multiresolution decomposition operation is a series of high-pass bands with doubling bandwidth (that form the signal details, or wavelet coefficients) and one low-pass band (that forms the approximation, or Scaling function

coefficient). Figure 7.5 illustrates the wavelet decomposition from the signal processing perspective of multiresolution decomposition. For signal of length n, the DWT consists of a maximum of $J = \log_2 n$ stages. A signal of length $n = 64$ can be decomposed in six steps, resulting in six sets of wavelet coefficients: 1 at j=5, 2 at j=4, 4 at j=3, 8 at j=2, 16 at j=1, 32 at j=0, and 64 at j=-1 (which is the original signal). For example, the decomposition of a signal sampled at 1Hz (i.e. TR=1s), can, according to the Nyquist criterion, represent frequencies up to 0.5Hz. The 32 j=0 wavelet coefficients are the smallest scale and represent the signal in the 0.25Hz-0.5Hz range, the 16 j=1 wavelet coefficients represent the signal the 0.125Hz-0.25Hz range; the 8 j=2 wavelet coefficients represent the signal the 0.0625Hz-0.125Hz range; the 4 j=3 wavelet coefficients represent the signal the 0.0625Hz-0.03125Hz range; the 2 j=4 wavelet coefficients represent the signal the 0.03125Hz-0.015625Hz range; the 1 j=5 wavelet coefficient represents the signal the 0.015625Hz-0.0078125Hz range, In each successive level of coefficients, half the remaining frequency spectrum is covered (see Figure 7.3). Thus the frequency resolution improves with decreasing frequency, whilst the temporal resolution degrades.

7.2.3.2 Wavelet Transform for Filtering

The magnitude of the wavelet coefficient indicates the contribution that particular scale (frequency) component makes to the signal at that point. The wavelet transform of a discretely sampled real signal (in this work the signal is the ML-EM–deconvolved impulse response function $CBF \cdot R_{eff}(t)$) will generally be represented by a small number of large coefficients, which determine the broad form of the signal, whilst any noise in the signal will largely be mapped to many small small-scale coefficients.

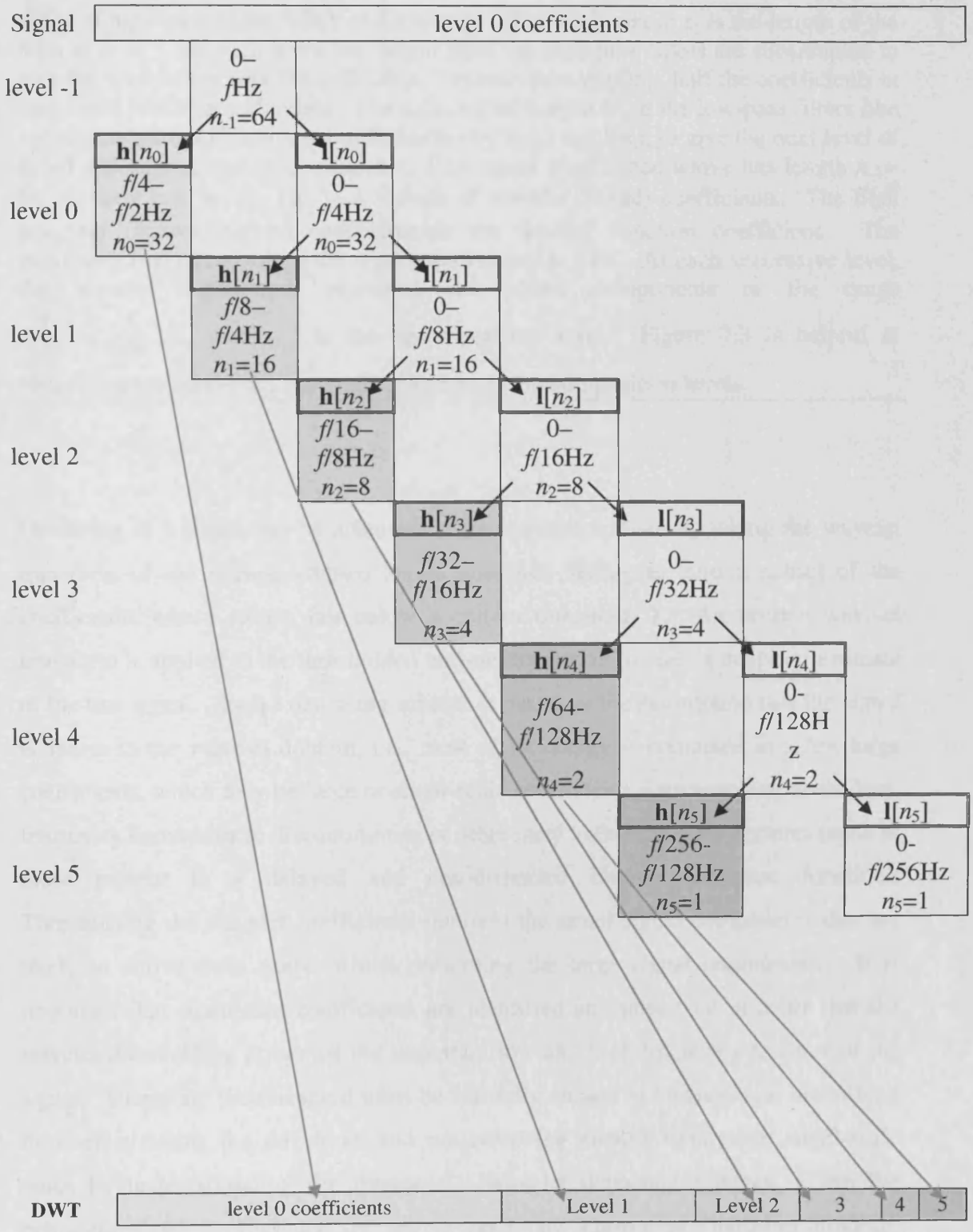

Figure 7.5: Multiresolution Decomposition analysis: The signal, (also termed level j=-1 coefficients) (depicted at the top) is split in six stages into a 6-level j=0-5 DWT (depicted at the bottom). The DWT is calculated by passing the signal through a

series of high-pass filters, h[n_j], and low-pass filters l[n_j], where n_j is the length of the filter at level j. At each level, the output from the high-pass filters are subsampled to give the wavelet (or detail) coefficients. Without subsampling, half the coefficients at each level would be redundant. The subsampled output from the low-pass filters (the approximation coefficients) are split further by h[n_j] and I[n_j], to give the next level of detail and approximation coefficients. The signal represented above has length n_{-1}= 64, so there can be $\log_2(n_{-1}) = 6$ levels of wavelet (detail) coefficients. The final low-pass (approximation) coefficient is the Scaling function coefficient. The maximum frequency within the represented signal is f Hz. At each successive level, the wavelet coefficients represent the signal components in the range $\frac{f}{2^{j+2}} \rightarrow \frac{f}{2^{j+1}}$ Hz, where j is the decomposition level. Figure 7.3 is helpful in visualising the band-pass spectrum of successive decomposition levels.

Denoising of a signal can be achieved in the wavelet domain by taking the wavelet transform of the noise-corrupted signal and then setting to zero a subset of the coefficients whose values fall below a certain threshold, T. An inverse wavelet transform is applied to the thresholded wavelet transform to yield a denoised estimate of the true signal. Such a denoising scheme is based on the assumption that the signal is sparse in the wavelet domain; i.e., most of its energy is contained in a few large coefficients, which may be large or small-scale coefficients corresponding to the low-frequency features or to discontinuities or other local high-frequency features (such as those present in a delayed and non-dispersed impulse response function). Thresholding the wavelet coefficients removes the small signal components that are likely to derive from noise, whilst preserving the large signal components. It is important that significant coefficients are identified and preserved in order that the wavelet thresholding preserves the important low and high-frequency features of the signal. Therefore, the threshold must be carefully chosen to balance over-smoothing by overestimating the threshold, and not removing enough unphysical small-scale noise by underestimating the threshold. Wavelet denoising schemes where the below-threshold coefficients are set to zero, are known as 'hard-thresholding' (Donoho *et al.* 1994). In an alternative denoising scheme known as 'soft-thresholding', the coefficients whose magnitudes fall below the threshold T are reduced in magnitude rather than eliminated all together (Donoho *et al.* 1994).

7.3 METHODS

7.3.1 WAVELET THRESHOLDING APPLIED TO ML-EM

In this work, wavelet decomposition and hard thresholding are applied to the impulse response function reconstructed using *standard* ML-EM (Vonken *et al.* 1999a). The formulation and convergence properties of the ML-EM algorithm are described in detail in Chapter 6. In summary, if a fixed number of iterations are used for the ML-EM reconstruction, it is likely that the solution will be either over or under regularised (if the number of iterations used is too low or too high respectively). Over-regularisation will result in an unrealistically smooth solution and consequently, in application to DSC-MRI deconvolution, an underestimation of *CBF*.

If few ML-EM iterations are used to reconstruct the impulse response function $\tilde{r} = \left(CBF \cdot R_{eff}(t)\right)_{estimated}$, the wavelet transform will consist of a few large-scale (low frequency) coefficients. This case is desirable for an impulse response function predominantly characterised by low temporal frequencies, for example one resulting from a dispersed bolus. However, if $CBF \cdot R_{eff}(t)$ contains higher frequency information, for example to characterise a delay, a small number of iterations may be insufficient. When few iterations are used wavelet denoising schemes such as those described in Section 7.2.3.2 are superfluous since the solution is already smooth.

A discussed in Chapter 6, a larger number of ML-EM iterations are necessary to recover the higher frequency components defining the sharp edge of the delayed $R_{eff}(t)$ compared with the tail. However, as the number of iteration increases, $\tilde{r}$ is more likely to become corrupted as the experimental noise is fitted and instabilities occur. As explained in Section 4.8.1 this is because the inverse problem in bolus tracking MRI is ill-posed. If too many ML-EM iterations are used, it is likely that unphysical oscillations and noise will be represented by large magnitude wavelet coefficients across all scales. Consequently, the wavelet thresholding regime described in Section 7.2.3.2 is unable to recover the true solution since few noise

coefficients will fall below the threshold. For efficient denoising, the ML-EM reconstruction should be sufficiently regularised to avoid corruption, but there should also be sufficient iteration to recover the main physically significant frequency components of the solution.

In this work, the iteration balance is achieved using an *oscillation index* (Wu *et al.* 2003) to indicate the quality of the impulse response function $\tilde{r}$, reconstructed using the standard ML-EM (Vonken *et al.* 1999a). This approach will be referred to as oscillation index regularised ML-EM (oML-EM) (see Section 7.3.2). Once the oscillation index of $\tilde{r}$ is exceeded the sML-EM iteration is stopped. The aim of the oscillation index is to balance the number of ML-EM iterations such that in wavelet space, the solution is dominated by a few large-scale components, but also has information contained in the smaller scale coefficients.

In Chapter 6, the four possible delay and dispersion combinations for $R_{eff}(t)$ were illustrated (see Figure 6.1). An effective deconvolution algorithm should be able to characterise these four distinct shapes and all shapes for intermediary values of delay and dispersion accurately. Figure 6.1 is reproduced in this chapter in Figure 7.6, illustrating a smooth decreasing function of time (no delay or dispersion of the bolus), a sharp-peaked delayed decreasing function of time (delay and no dispersion of the bolus), and a peaked smooth bell-shape (dispersion with of without delay of the bolus). With the exception of the delayed and non-dispersed $R_{eff}(t)$, very little information should be contained in the small-scale wavelet coefficients. For the delayed and non-dispersed $R_{eff}(t)$, the sharp *RTM* will be in part defined by the small-scale wavelet coefficients. It is likely that these physically meaningful wavelet coefficients will be large.

In this work, diadylic wavelet decompositions have been performed using the Daubechies wavelet family of maximum phase with two vanishing moments (see Figure 7.4). The DWT algorithm was implemented in C++ using the GSL scientific

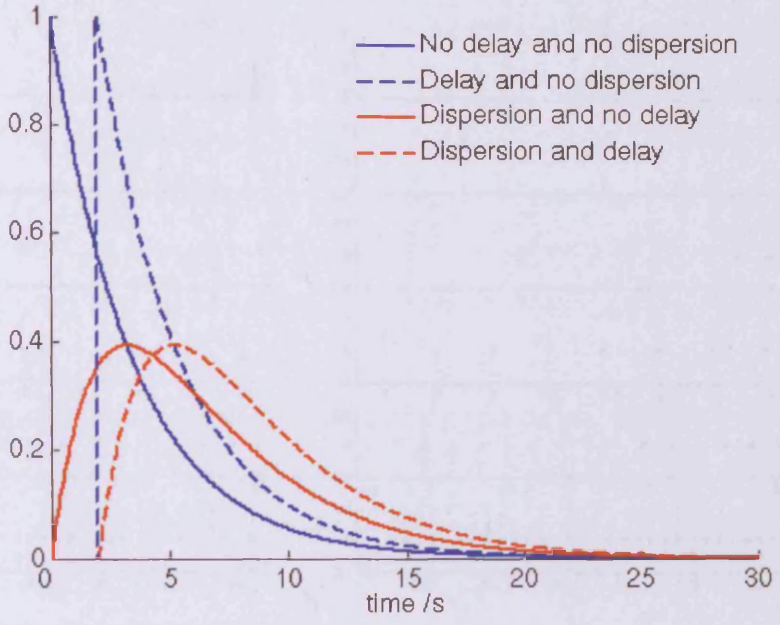

Figure 7.6: Impulse response functions illustrating the four possible combinations of delay and dispersion. a) No delay and no dispersion (solid blue), b) delay and no dispersion (dashed blue), c) dispersion and no delay (solid red), d) delay and dispersion (dashed red).

library. In this implementation, the maximum level ($J = \log_2 n$) decomposition is calculated and the scaling coefficient λ and wavelet coefficients γ are arranged in the following form

$$\left(\lambda(J-1,0);\ \gamma(J-1,0);\ \gamma(J-2,0),\ \gamma(J-2,1);\ \gamma(J-3,0),\ \ldots;\gamma(j,k),\ \ldots;\gamma(0,2^{J-1}-1)\right) \quad [7.13]$$

where j is the 'scale' index of the level $j = 0 \ldots J\text{-}1$ and k is the 'translation' index of the coefficient within each level, $k = 0 \ldots 2^{J-j-1} - 1$. I.e., the first element of the array is the scaling (approximation) coefficient $\lambda(J-1,0)$, followed by the wavelet (detail) coefficients $\gamma(j,k)$ for each level j.

For illustrative purposes, Figure 7.7 illustrates the wavelet decomposition of the four impulse response functions function illustrated in Figure 7.6. These functions were

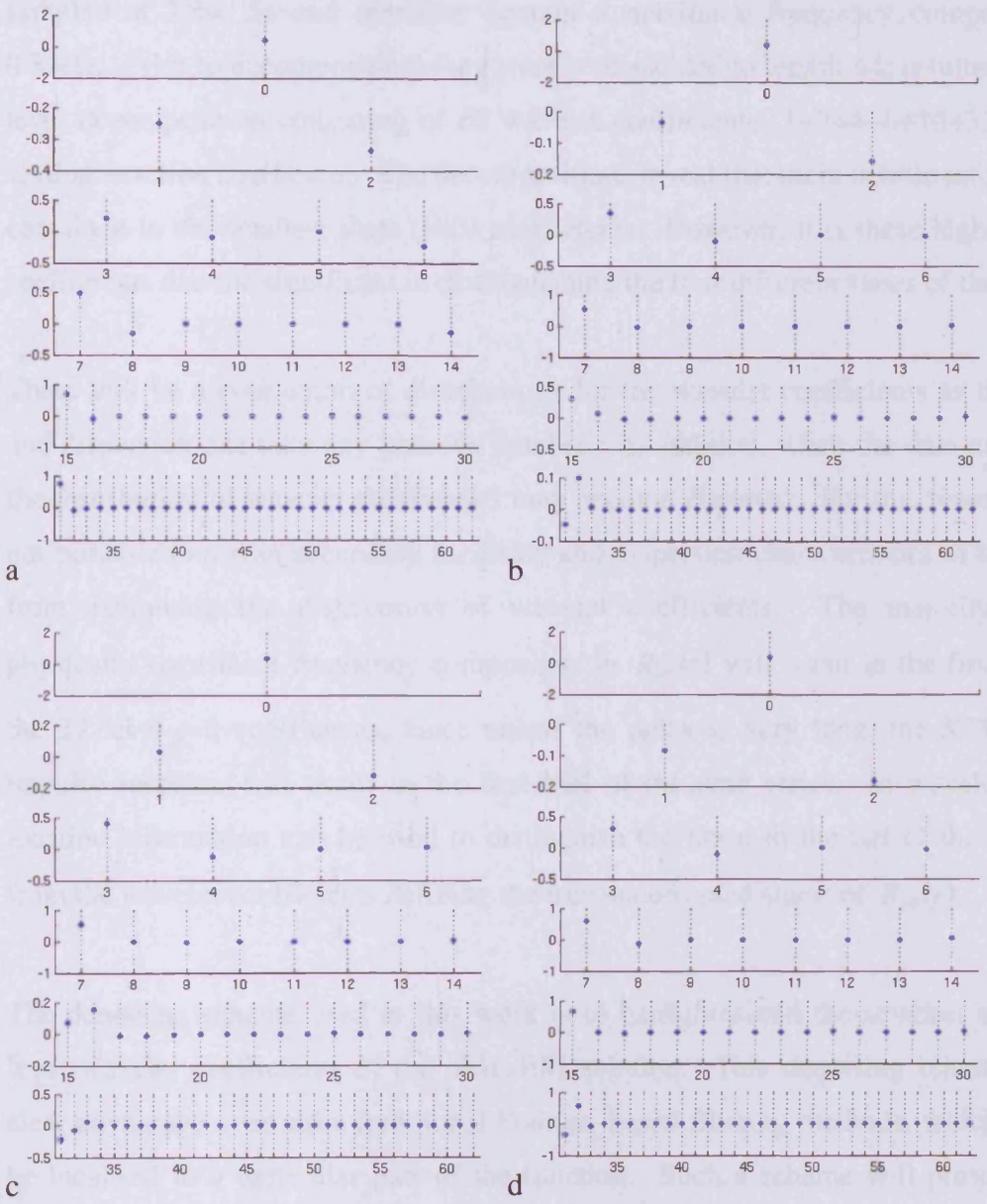

Figure 7.7: Six level wavelet decomposition of the four impulse response functions simulated with *CBF*=60ml/100g/min and *CBV*=4ml/100g for a) no delay, no dispersion, b) no delay, 4 second dispersion, c) 2 second delay, no dispersion, d) 2 second delay, 4 second dispersion. In each quadrant, the axes from top to bottom depict the j=5 (top), 4, 3, 2, 1, 0 (bottom) level wavelet coefficients, i.e. the scale decreases from top to bottom. The vertical scale indicates the relative magnitude of the coefficients. The horizontal axes indicate the translation k of the wavelet for the coefficient. An indication of the temporal location of the wavelet coefficient is given by decreasing the horizontal scale in proportion to the number of coefficients. An equivalent temporal location t for each translation k is found from $t = k \cdot 2^j \cdot TR$.

sampled at TR=1.5s and therefore contain a maximum frequency component of 0.33Hz. Prior to decomposition, they were zero-padded to length 64, resulting in a 6 level decomposition consisting of 63 wavelet coefficients (1+2+4+8+16+32) and 1 scaling function coefficient. The decompositions reveal that there is little information contained in the smallest scale (j=0) coefficients. However, it is these highest-level coefficients that are significant in distinguishing the four different states of the bolus.

There will be a continuum of distributions for the wavelet coefficients as the delay and dispersion can take any positive number. In addition, when the data are noisy, the distribution of wavelet coefficients may become distorted. For this reason it was not possible to assess accurately the delay and dispersion characteristics of the bolus from examining the distribution of wavelet coefficients. The majority of the physically significant frequency components in $R_{eff}(t)$ will occur in the first half of the 32 level j=0 coefficients, since unless the delay is very long, the *RTM* of the impulse response will occur in the first half of the time series. In wavelet space, location information can be used to distinguish the noise in the tail of the function from the wavelet coefficients defining the true uncorrupted shape of $R_{eff}(t)$.

The denoising scheme used in this work is to hard-threshold the smallest scale j=0 level wavelet coefficients of the oML-EM solution. This denoising scheme has a clear advantage over more traditional Fourier- based filtering methods, which cannot be localised to a particular part of the function. Such a scheme will preserve any large magnitude (j=0) wavelet coefficients defining the sharp peak of a delayed and non-dispersed $R_{eff}(t)$, but suppress the small magnitude (j=0) wavelet coefficients that may derive from noise. All the larger-scale (j=1 – 5) wavelet coefficients are kept on the premise that the noise in the oMLEM reconstruction will be small-scale (high-frequency). This assumption is of course dependent on the successful termination of the iterations by means of the oscillation index, which prevents the complete corruption of the ML-EM reconstruction by over iteration. The hard-threshold used on the wavelet decomposition of the oML-EM reconstruction was empirically chosen from simulations to be 5% of the value of the height of the largest

coefficient across all scales. This threshold was found to be most efficient at removing any residual oscillations in the oML-EM solution whilst at the same time preserving the coefficients defining the *RTM* of the oML-EM recovered $\tilde{r}$. Figure 7.8 shows two oML-EM reconstructions of $\tilde{r}$, one with delay and another with delay and dispersion. The different colour curves represent thresholding the level j=0 coefficients at different levels as indicated in the legends. It can be seen that removing too many of the smallest scale wavelet coefficients can actually introduce additional distortion into the reconstruction. However, removing a few of these coefficients minimises oscillations in the tail of $\tilde{r}$.[12] Although the simulations shown were performed at SNR=50, the oscillations index constrains the noise in the oML-EM reconstruction so that the wavelet denoising thresholds should be independent of the actual noise in the data.

7.3.2 OSCILLATION INDEX

In the previous section reference was made to the oscillation-index regularised or oML-EM solution. In this section the oscillation index is described.

An oscillation index (*OI*) that indicates the quality of the ML-EM reconstruction is calculated after each iteration. The iteration number p, before which a threshold value for the *OI* is exceeded, becomes the number of iteration used in the oML-EM reconstruction.

The *OI* used in this work is based on the one proposed by Wu *et al.* in (Wu *et al.* 2003). The *OI* implemented in the work by Wu was designed to determine an appropriate threshold for the suppression of singular values in an SVD deconvolution of DSC-MRI data (see Section 4.8.4 for a detailed description of SVD). The *OI* proposed in this work is similarly designed to optimise the regularisation of the deconvolution algorithm, in this case ML-EM deconvolution. The proposed *OI* is

[12] Note that the reconstructions shown in Figure 7.8 have long *MTT*. Consequently, there has been some truncation of the concentration time-course used in the deconvolution (45 time points were sampled at TR=1.5s), which results in an underestimation of points defining the tail of $\tilde{r}$.

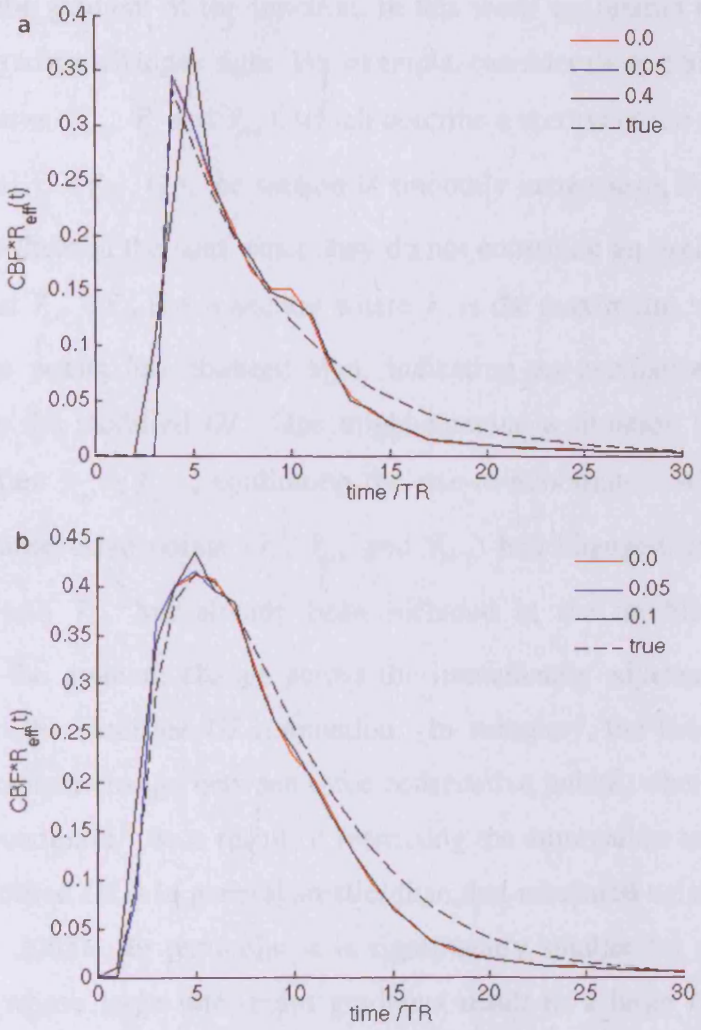

Figure 7.8: The oML-EM reconstructions of $\tilde{r}$ (from TR=1.5s, SNR=50 simulated data) a) *CBF*=20ml/100g/min, *CBV*=3ml/100g, delay=5s, dispersion β=0s, (see Chapter 5) b) *CBF*=50ml/100g/min, *CBV*=6ml/100g, delay=1.5s, β=4s. The different colour curves represent thresholding the level j=0 coefficients at different levels as indicated in the legends. The dashed curve is the true shape of $CBF \cdot R_{eff}(t)$.

subtly different from Wu's *OI* in that it is designed to be sensitive to the shape of the impulse response being recovered. An ideal *OI* would allow sufficient iteration to recover the high frequencies defining the less dispersed $\tilde{r}$, whilst at the same time preventing over iteration and consequent corruption of the reconstruction. Whereas Wu *et al.* measured the oscillations by summing over the change (between successive

points) in the gradient of the function; in this work we restrict the sum to the cases when the gradient changes sign. For example, consider three consecutive time-points in the $\tilde{r}$ curve ($\tilde{r}_{i-1}$, $\tilde{r}_i$ and $\tilde{r}_{i+1}$), which describe a section of the rise-to-maximum. If $\tilde{r}_{i-1} < \tilde{r}_i$ and $\tilde{r}_i < \tilde{r}_{i+1}$, (i.e. the section is smoothly increasing), the modified *OI* does not include them in the sum, since they do not constitute an oscillation. However, if $\tilde{r}_{i-1} < \tilde{r}_i$ and $\tilde{r}_{i+1} < \tilde{r}_i$, (i.e. a section where $\tilde{r}_i$ is the maximum), the gradient between consecutive points has changed sign, indicating an oscillation. Such points are included in the modified *OI*. One might imagine a situation where a fourth point $\tilde{r}_{i+2}$ satisfies $\tilde{r}_{i+1} < \tilde{r}_{i+2}$, continuing the rise-to-maximum. Although the gradient between consecutive points ($\tilde{r}_i$, $\tilde{r}_{i+1}$ and $\tilde{r}_{i+2}$) had changed, the gradient between points $\tilde{r}_i$ and $\tilde{r}_{i+1}$ has already been included in the modified *OI* summation. Therefore, the gradient change across the immediately adjacent three points is not included in the modified *OI* summation. In summary, the modified *OI* only sums over the gradient change between three consecutive points, where the middle point is the local maximum. As a result of restricting the summation to local oscillations in $\tilde{r}$, the modified *OI* is in general smaller than that measured using the *OI* proposed in (Wu *et al.* 2003). In particular it is significantly smaller for more steeply curved functions, whose large inter-point gradients result in a large *OI* using the method proposed by Wu *et al.* The omission of points where there is no inter-point gradient change promotes comparatively more iteration for more steeply curved functions in using the modified *OI* summation. Additionally, the maximum of $\tilde{r}$ is not included in the modified summation, leading to a smaller *OI* for sharper functions, such that they will be recovered with more iteration. The modified summation is also multiplied by the full-width-half-maximum (FWHM) and divided by the maximum value of the recovered $\tilde{r}$. These modifications respectively cause a larger *OI* (and therefore less iteration) for broad dispersed functions, and a smaller *OI* for higher flows (encouraging more iteration to recover the high-frequency components often associated with such functions). The oscillation index used in this chapter is:

$$OI = \frac{FWHM}{CBF \cdot l} \sum_{\forall i \begin{cases} r^{[k]}_{i-1} < r^{[k]}_i \\ r^{[k]}_{i+1} < r^{[k]}_i \\ r^{[k]}_i \neq \max\left(r^{[k]}\right) \end{cases}}^{l} \left| 2r^{[k]}_i - r^{[k]}_{i+1} - r^{[k]}_{i-1} \right| \qquad [7.14]$$

where k is the iteration number, l is the sample length, and FWHM is the width of $\tilde{r}^{[k]}$. Scaling by the sample length naturally accounts for the TR of the data, since there will be fewer sampling points for data recorded at longer TR. (In this chapter data simulated with TR=1s data contained 64 sample points, TR=1.5s data contained 45 sample points, and TR=2s data contained 34 sample points).

The solution $\tilde{r}^{[p]}$ is the first iteration for which $OI > \alpha$. A range of α ranging from 0.001 to 1.0 was tested in order to find a value for α that balanced the least squares and regularisation error. In this way, the subsequent wavelet denoising should be effective. The empirically chosen values of α used in this work are $\alpha = 0.01$ for $CBF \cdot R_{eff}(t)$ believed to have no delay or dispersion (i.e., the maximum of the reconstruction occurring at the first time point), and $\alpha = 0.025$ for $CBF \cdot R_{eff}(t)$ in all other cases. Figure 7.9 illustrates the recovery of a delayed impulse response function and a delayed and dispersed impulse response function, at progressive values of the oscillation index from data simulated at SNR=50.

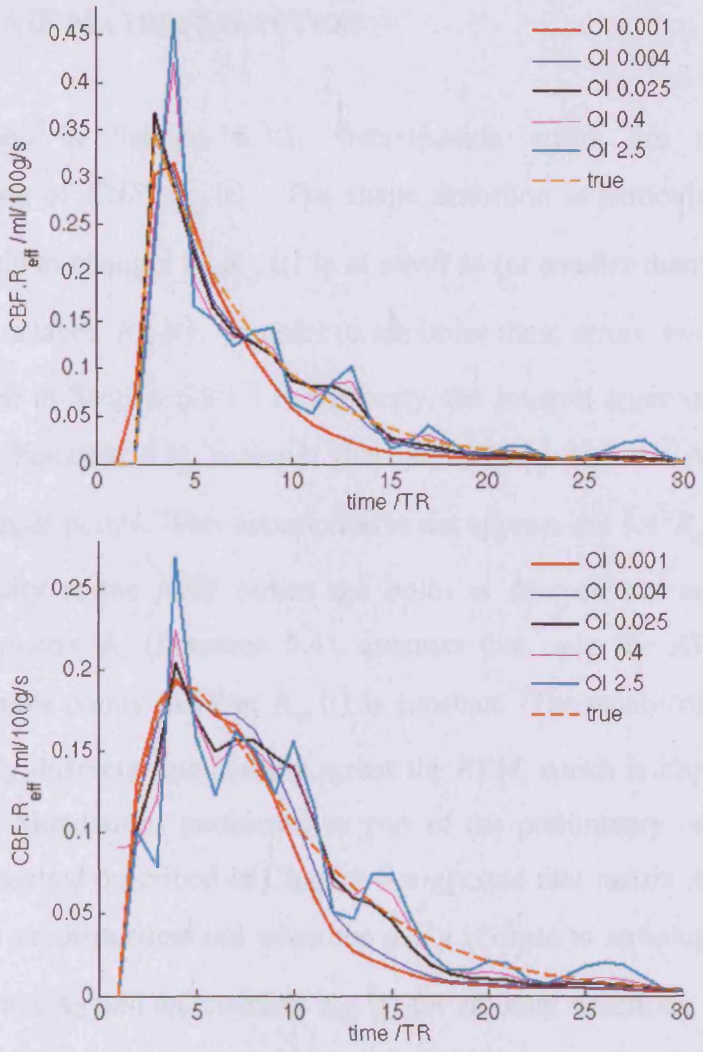

Figure 7.9: Effect of the oscillation index *OI*: sML-EM reconstructions of impulse response functions from SNR=50 TR=1.5s data simulated with ischaemic perfusion parameters *CBF*=20ml/100g/min, *CBV*=3ml/100g, for delay=2s and no dispersion (top) and for delay =1s and β=3s (bottom). The true $CBF \cdot R_{eff}(t)$ shape is shown by the orange dashed curve. It can be seen that an *OI*=2.5 is too large and the ML-EM solution is severely corrupted. An *OI*=0.001 solution has had too few iteration to properly characterise the shape. *OI*=0.025 was found to be a good balance between the least-squares and regularisation error for the range of perfusion and delay/dispersion parameters tested.

7.3.3 AIF MATRIX SELECTION

As discussed in Section 6.3.1, discretisation errors are significant in the reconstruction of $CBF \cdot R_{eff}(t)$. The shape distortion is particularly apparent when the time scale of changes in $R_{eff}(t)$ is as small as (or smaller than) TR, such as is the case with a delayed $R_{eff}(t)$. In order to minimise these errors, two different matrices are described in Section 6.3.1. In summary, the integral approximation used in the matrix, $\mathbf{A_2}$ (Equation 6.3), assumes that both $R_{eff}(t)$ and the AIF evolve linearly between sample points. This assumption is not appropriate for $R_{eff}(t)$ where there is a discontinuity at the *RTM* (when the bolus is delayed but not dispersed). An alternative matrix $\mathbf{A_1}$ (Equation 6.4), assumes that only the AIF evolves linearly between sample points and that $R_{eff}(t)$ is constant. The reconstructions with $\mathbf{A_1}$ and $\mathbf{A_2}$ are subtly different, particularly across the *RTM*, which is important in assessing dispersion. Simulations performed as part of the preliminary investigations of the mML-EM method described in Chapter 6 suggested that matrix $\mathbf{A_1}$ best reconstructs $R_{eff}(t)$ with no dispersion and when the delay is close to an integer multiple of TR, whereas matrix $\mathbf{A_2}$ best reconstructs $R_{eff}(t)$ for all other situations.

In this chapter, the matrix-selection criteria used to decide which matrix to use in the final reconstruction are given in the Equation [7.16] in the Appendix to this chapter. As with the criteria given in Appendix of Chapter 6, these criteria were also determined empirically via simulations. The new criteria were devised with a view to decrease the sensitivity to TR. 500 iterations of the standard ML-EM deconvolution were performed on the simulated data set (see Chapter 5) and relevant parameter values (*CBF*, dispersion index (*DI*) (see Equation [7.15], Section 7.5.4) and *RTM*) were recorded for combinations of *CBF*, *CBV*, delay and dispersion for each repeat at TR =1s, 1.5s and 2s. The results of a subset of these simulations (*CBF*=60ml/100g/min, *CBV*=4ml/100g at SNR=100) are shown in Figures 7.16, 7.17 and 7.18 in the Appendix. The patterns observed in the results were used to determine matrix-selection criteria given in Equation [7.16]. Table 7.1 in the

Appendix records the accuracy of these criteria for the perfusion parameters *CBF*=60ml/100g/min, *CBV*=4ml/100g at SNR=50 and 100. Further discussion about the AIF matrix selection is given in the Discussion section.

7.3.4 oML-EM-wavelet Simulations

The new deconvolution methodology (oscillation-index regularised ML-EM with subsequent wavelet decomposition and thresholding, or oML-EM-wavelet) was tested on simulated data, which were created to represent a range of physiological situations for typical scanning parameters. This data set is described in Chapter 5. A flow diagram summarising the main steps in the oM-EM-wavelet method is given in Figure 7.10.

100 repeats of the simulations were performed, and for each combination of parameters (noise, TR, *CBF*, *CBV*, delay, dispersion). The *CBF* was estimated from the maximum of the oML-EM-wavelet solution, $\tilde{r}$ and the mean and standard deviations for each point of $\tilde{r}$ were evaluated. In order to achieve high-resolution measurements of the shape, the solution $\tilde{r}$ was subsampled at TR=0.01s using a linear interpolation between sample points. The delay t_{delay} was estimated from the length of the subsampled baseline (defined to end prior to exceeding 10% of the maximum of $\tilde{r}_{subsampled}$). The dispersion characteristics were estimated using a dispersion index (*DI*) defined as:

$$\begin{aligned} DI &= FWHM\left(\tilde{r}_{subsampled}\right) \times RTM\left(\tilde{r}_{subsampled}\right) & RTM\left(\tilde{r}_{subsampled}\right) > TR \\ DI &= 0 & RTM\left(\tilde{r}_{subsampled}\right) \le TR \end{aligned} \qquad [7.15]$$

FWHM is the full-width-half-maximum (in seconds), and *RTM* is the rise-to-maximum (in seconds) from baseline. It should be noted that $R_{eff}(t)$ with a long *MTT* will have a large FWHM, as does a dispersed $R_{eff}(t)$. Therefore, the FWHM alone cannot be used to identify dispersion. Similarly, the *RTM* cannot be used as a

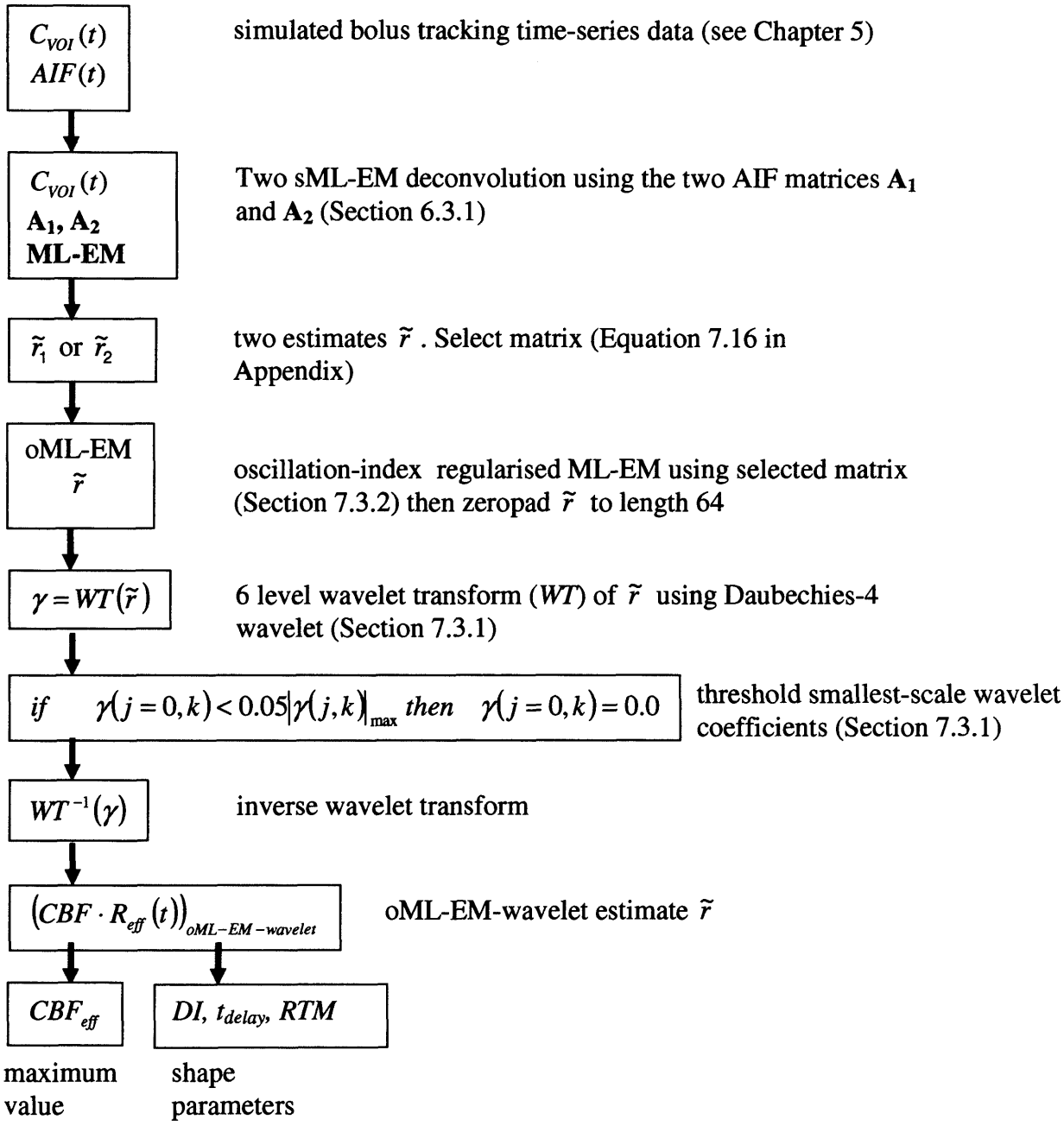

Figure 7.10: Flow diagram summarising the oML-EM-wavelet method applied to the simulated data set.

measure of dispersion, since for a given dispersion, the *RTM* increases with *MTT*. Nevertheless, by including the *RTM* in the definition for *DI*, only $\tilde{r}$ reconstructed with a *RTM* greater than or equal to one TR are classified as dispersed.

7.3.5 SIMULATING THE EFFECTS OF NEGATIVE DISPERSION

Simulations were also performed to determine the effect of negative dispersion on the shape of oML-EM-wavelet deconvolved $\tilde{r}$. In this situation the true AIF is sharper than the measured AIF. This would occur if the global AIF used to deconvolve a concentration time-course measured in tissue fed by normal vasculature, were actually measured in an abnormal artery. An AIF measured downstream of an arterial stenosis is likely to be dispersed compared with an AIF measured in a healthy artery. In practice, care should be taken to avoid such a situation *in vivo*, and the artery used to measure the AIF should be contralateral to any abnormality. It is however important to be aware of how such a mis-measured AIF distorts the reconstructed $\tilde{r}$. To simulate this situation, the AIF used in the deconvolution was generated by convolving the AIF used to simulate the tissue with an exponential model for the vascular transport function, $VTF(t) = 1.5e^{-t/1.5}$ (see Section 4.7.2). This simulates the situation of deconvolving tissue fed by a normal artery with an AIF measured in an abnormal vessel, where the mean vascular transit time is 1.5s. The situation is illustrated in Figure 7.11. The figure show that the AIF does not need to appear more dispersed than the tissue for negative dispersion to be present. The oML-EM-wavelet method described in Section 7.3.4 was used to deconvolve the simulated data set described in Chapter 5 with the modified dispersed AIF.

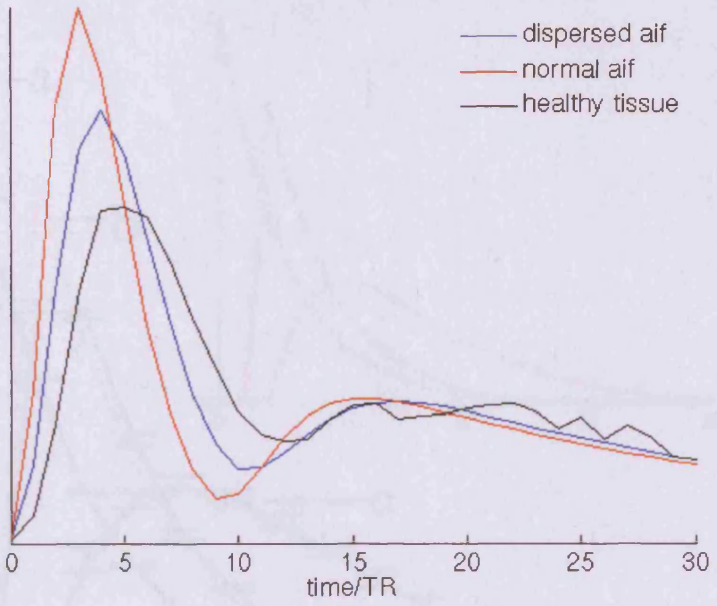

Figure 7.11: Illustration of negative dispersion in the bolus concentration time-course: The dispersed AIF (blue curve) has been created by convolving the normal AIF (red curve), with an exponential VTF with time constant 1.5s. The black curve is the simulated tissue concentration (SNR=100, TR=1.5s) for healthy tissue (*CBF*=60ml/100g/min, *CBV*=4ml/100g) fed by the normal AIF.

7.4 RESULTS

7.4.1 CHARACTERISING THE IMPULSE RESPONSE FUNCTION

The average over 100 oML-EM-wavelet reconstructions $\tilde{r}$, of three different simulated $CBF \cdot R_{eff}(t)$ functions are shown in Figure 7.12 corresponding to a) $t_{delay} = 0$, β=0s , b) t_{delay} =1.5s, β=0s, and c) t_{delay} =3s, β=6s (simulated for healthy GM tissue perfusion with *CB* =60ml/100g/min, *MTT*=4s). The error bars represent +/- one standard deviation (sd). The size of these error bars was approximately 30% larger at SNR=50 compared with SNR=100; this trend was observed for all the simulation results presented here. Representative individual reconstructions are shown in the insert of Figure 7.12. The figure demonstrates that the oM-EM-wavelet

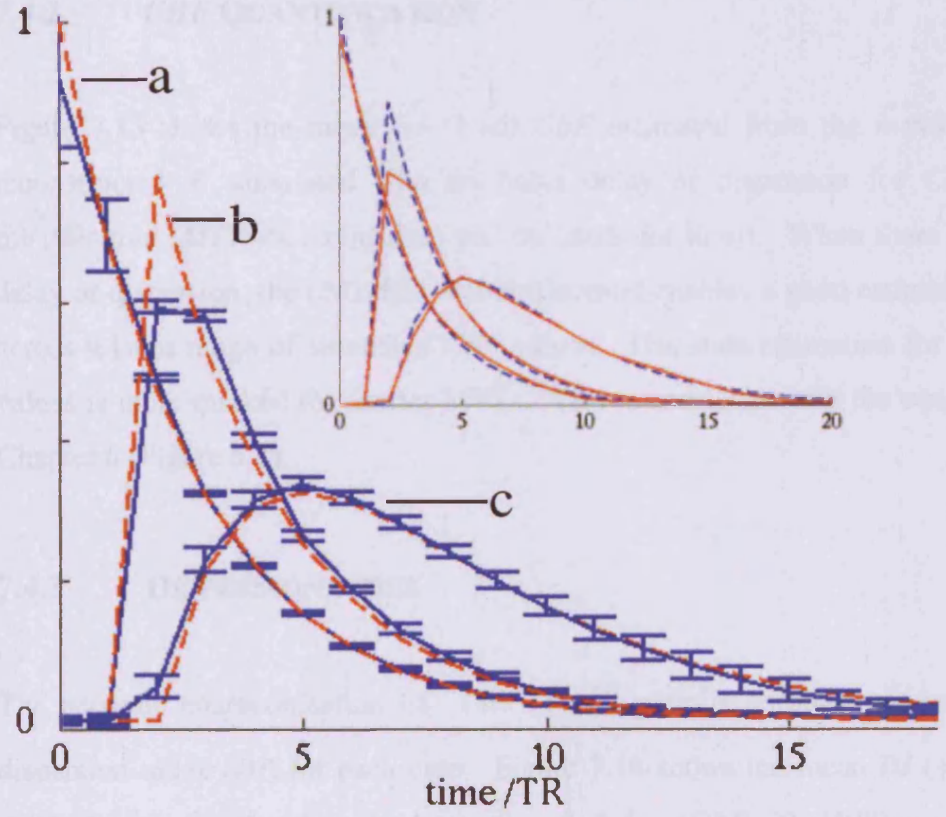

Figure 7.12: The mean (+/- 1sd) of the oML-EM-wavelet reconstruction of the impulse response function $\tilde{r}$ for three combinations of simulated delay t_{delay} and dispersion β a) t_{delay}=0s and β=0s, b) t_{delay}=1.5s and β=0s, c) t_{delay}=3s and β=6s. In all cases, *CBF*= 60ml/100g/min and *MTT*=4s. The SNR of the simulated data was 100 and TR=1.5s. The insert shows a single result of the 100 simulations. The dashed lines are the true $CBF \cdot R_{eff}(t)$ and the solid lines the estimate $\tilde{r}$.

method enables a good characterisation of a wide variety of possible shapes for $CBF \cdot R_{eff}(t)$. Good shape characterisation is necessary in order to determine the reliability of *CBF* estimates. In particular the oML-EM-wavelet method is able to characterise the sharp initial rise for the delayed and non-dispersed curves.

7.4.2 *CBF* QUANTIFICATION

Figure 7.13 shows the mean (+/- 1 sd) *CBF* estimated from the maximum of the reconstructed $\tilde{r}$ simulated with no bolus delay or dispersion for *CBF*= 10-80 ml/100g/min (*MTT*=4s (solid line) and 6s (dash-dot line)). When there is no bolus delay or dispersion, the oML-EM-wavelet method enables a good estimation of *CBF* across a large range of simulated *CBF* values. The underestimation for larger flow values is more marked for shorter MTTs. This is consistent with the observations in Chapter 6 (Figure 6.7).

7.4.3 DISPERSION INDEX

The accurate characterisation of $CBF \cdot R_{eff}(t)$ permits a robust estimation of the dispersion index (*DI*) for each case. Figure 7.14 shows the mean *DI* (+/- 1 sd) for $CBF \cdot R_{eff}(t)$ simulated with dispersion β=0-6s, (*CBF*=60ml/100g/min, *MTT*=4s (solid line) and *MTT*=2s (dashed line)) over 100 reconstructed $\tilde{r}$. As expected, the *DI* increases with the simulated dispersion β, but is also dependent on the perfusion parameters.

7.4.4 EFFECT OF NEGATIVE DISPERSION

Figure 7.15 shows a typical example of the reconstructed $\tilde{r}$ from the simulations performed to assess the effect of negative dispersion, i.e. when the AIF used in the deconvolution is wider than the true AIF. It can be seen that when a wider (abnormal) AIF is used, the *CBF* for the tissue that is fed by a healthy vessel will be severely overestimated (solid line) and the estimated impulse response function has a very large negative initial slope compared with the true $CBF \cdot R(t)$ (dashed line).

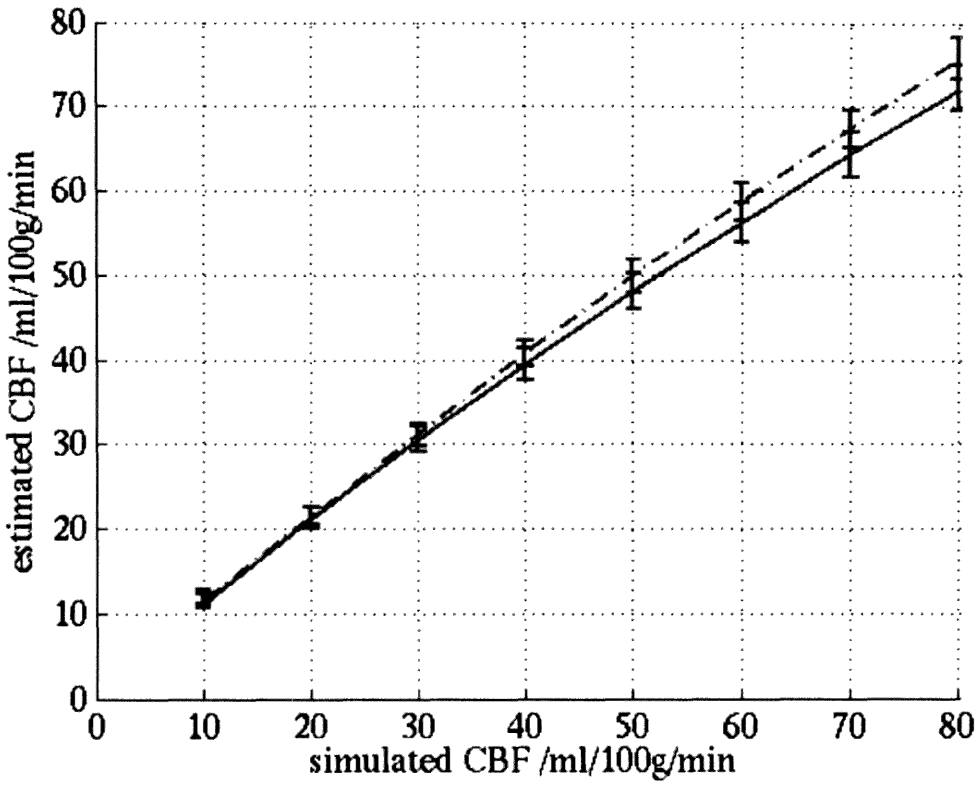

Figure 7.13: The mean (+/- 1sd) *CBF* calculate from the maximum of $\tilde{r}$ across range of simulated flows *CBF*=10-80ml/100g/min, and *MTT* = 4s (solid line), and 6s (dash-dot line). The SNR of the simulated data was 100 and TR=1.5s.

7.5 DISCUSSION

An accurate characterisation of the impulse response function $CBF \cdot R_{eff}(t)$, is essential for determining the reliability of perfusion estimates. Unless the shape $CBF \cdot R_{eff}(t)$ is known, it is impossible to determine whether the bolus was delayed and/or dispersed. Since the effect of dispersion is to cause an underestimation of perfusion, an accurate classification of hypoperfused tissue requires information about the shape of $CBF \cdot R_{eff}(t)$. Only perfusion measurements taken from $CBF \cdot R_{eff}(t)$ with no delay or dispersion can be used as a reliable indicator of tissue

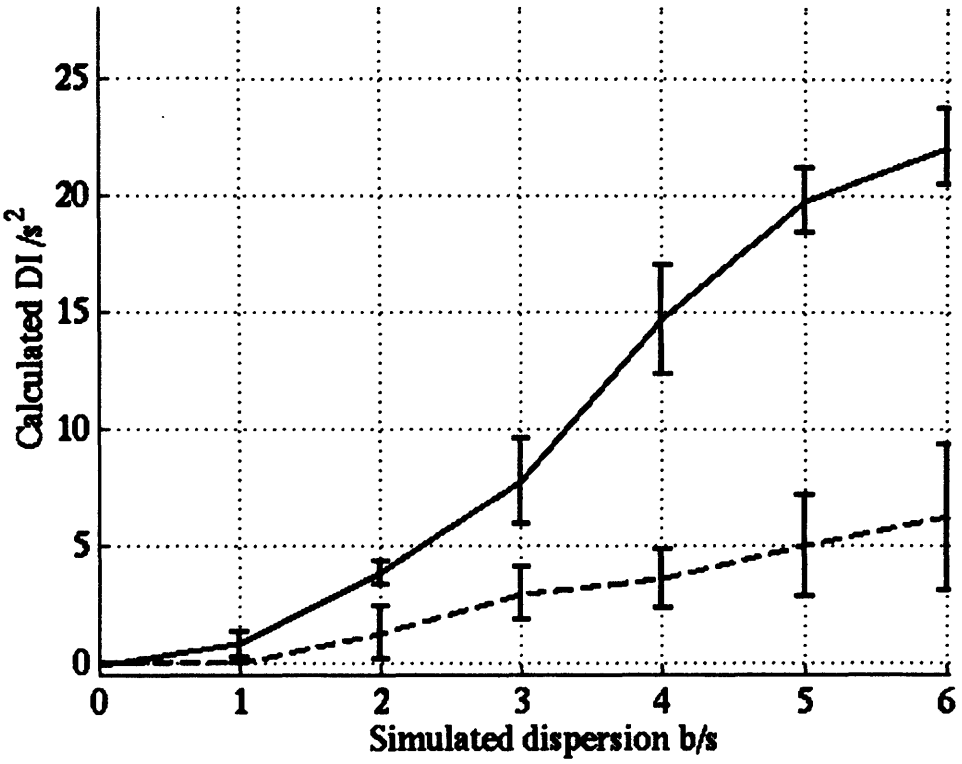

Figure 7.14: The mean (+/- 1sd) *DI* of $\tilde{r}$ measured from across range of simulated dispersions β=0-6s, and for data simulated with *CBF*=60ml/100g/min and *MTT*=4s (solid line) and 2s (dashed line). The SNR of the simulated data was 100 and TR=1.5s.

status. This has particular relevance for predictor-models, which combine perfusion estimates with other MR parameters to predict tissue fate e.g. (Wu *et al.* 2001). Bolus dispersion will lead to various degrees of underestimation for the perfusion measurements, and these errors will propagate in the predictor-models, resulting in unreliable predictions. Additional information regarding the vasculature would be a useful covariate in these models, since it may be able to counterbalance the perfusion measurement bias. In particular, maps indicating regions of delay and dispersion (which could be created using the methodology presented in this chapter), may help refine maps indicating the likelihood of infarction after stroke.

Accurate characterisation of the impulse response function is achieved in this work by combining an oscillation index regularised ML-EM and wavelet thresholding. The

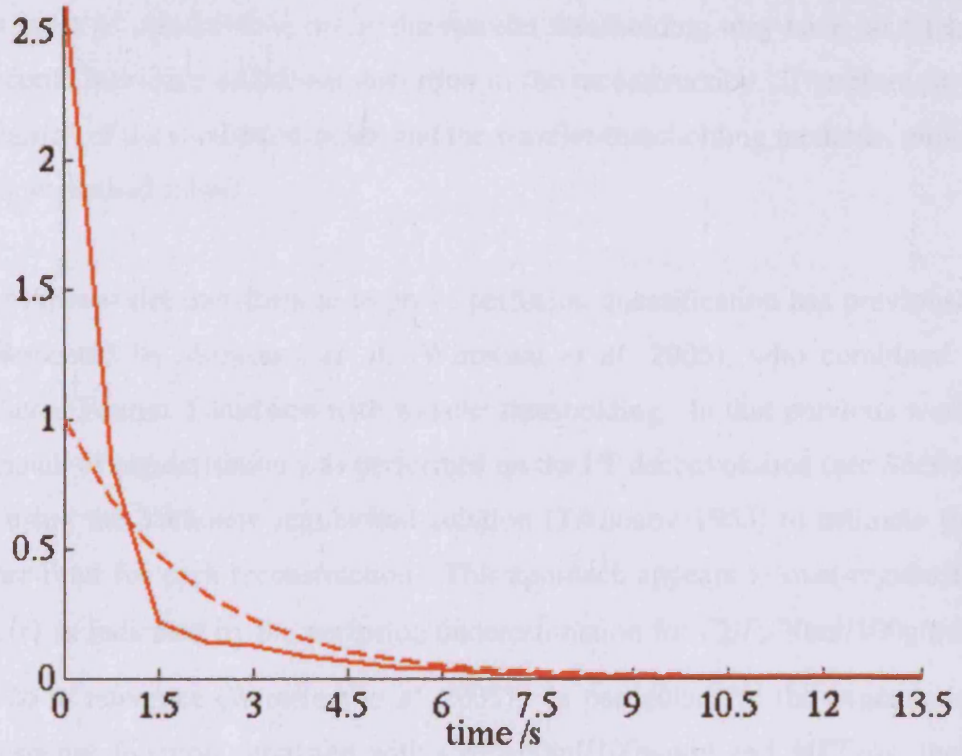

Figure 7.15: A typical oML-EM-wavelet reconstruction of the impulse response function $\tilde{r}$ (solid line) when the simulated AIF is dispersed with a mean vascular transit time of 1.5s with respect to the tissue (negative dispersion), such that the measured AIF is more dispersed than the true AIF. The dashed line shows the true shape of $CBF \cdot R_{eff}(t)$.

oscillation index constrains the noise in the ML-EM reconstruction to be approximately the same for data across a range of SNRs and imaging parameters. Although the oscillation index and wavelet threshold have been empirically determined, the criteria are more universal than those found for our previously proposed mML-EM reconstruction (Chapter 6). The convergence criteria in mML-EM were found to be dependent on various imaging parameters, due to the fact that the data points in the reconstruction converged at different rates depending on the imaging parameters (e.g. TR, which governs the maximum represented frequency). The oscillation index in oML-EM constrains the distribution and magnitude of wavelet coefficients such that the wavelet thresholding can be universal. Without an

oscillation index to constrain the noise, the wavelet thresholding may have no effect, or worse, could introduce additional distortion in the reconstruction. Therefore, it is the *combination* of the oscillation-index and the wavelet-thresholding methods, which make the new method robust.

The use of the wavelet transform to improve perfusion quantification has previously been implemented by Wirestam *et al.* (Wirestam *et al.* 2005), who combined a Weiner filtered Fourier Transform with wavelet thresholding. In that previous work, a small amount of regularisation was performed on the FT deconvolution (see Section 4.8.2) by using the Tikhonov regularised solution (Tikhonov 1963) to estimate the best Weiner filter for each reconstruction. This approach appears to over-regularise $CBF \cdot R_{eff}(t)$ as indicated by the perfusion underestimation for *CBF*>30ml/100g/min in Figure 2b in reference (Wirestam *et al.* 2005). In particular, for the exponential impulse response function simulated with *CBF*=60ml/100g/min and *MTT*=4s, their average estimated *CBF* was ~45 ml/100g/min. In comparison, Figure 7.13 shows that the equivalent estimate with oML-EM-wavelet method is *CBF*~55ml/100g/min. Over-regularisation is largely avoided using the oML-EM-wavelet method, which can characterise both delayed and dispersed $CBF \cdot R_{eff}(t)$ (Figure 7.12), and leads to better *CBF* estimates (Figure 7.13). Although the *OI* used in this current study may cause the tail of $CBF \cdot R_{eff}(t)$ to become corrupted, these unrealistic oscillations can be removed with the wavelet thresholding. As discussed in Chapter 6, because the deconvolution problem is ill-posed, it is very difficult to recover delayed impulse response functions, and most methods fail. However, the method presented in this work provides a good characterisation of delayed curves.

It should be noted that the severity of dispersion cannot be reliably estimated reliably from $\tilde{r}$. Although Figure 7.14 shows a positive correlation between the simulated dispersion (using an exponential VTF) and the measured *DI*, the relationship is highly dependent on the *MTT* of the tissue. Therefore, although the *DI* can be used as an indication of the presence of dispersion, the actual quantitative value cannot be determined reliably from this measure.

On its own, *DI* cannot distinguish a prolonged *MTT* in the tissue from bolus dispersion in the artery. For a dispersed $R_{eff}(t)$ it is not possible to determine whether the shape is due to a prolonged *MTT* in the tissue and small dispersion of bolus in the feeding artery, or whether the shape is due to a large dispersion of bolus in the vessel and a normal *MTT* in the tissue. It is therefore difficult to develop a model of the vasculature purely from the shape of $CBF \cdot R_{eff}(t)$ that will correct the $R_{eff}(t)$ for perfusion errors caused by bolus dispersion. Over-compensating for dispersion will cause the true *MTT* to be underestimated (see Figure 7.15), where negative dispersion artificially inflates the *CBF*. An accurate correction of dispersion is possible with a suitable VTF model, whose specific form is likely to be strongly dependent on the specific vasculature of the patient (Calamante *et al.* 2003b; Østergaard *et al.* 1999; Mouridsen *et al.* 2006b). Separating the components of microvascular and arterial dispersion is a difficult task, requiring either a voxel-specific model for the VTF or a voxel-specific arterial input function An investigation into a suitable model for the VTF is investigated in Chapter 8 using *in vivo* data from patients with a range of cerebral arterial abnormalities. In Chapter 9 two alternative means to correct dispersion are investigated.

In order for the *DI* and delay to be meaningful parameters, it is important that the global AIF is correctly measured. The global AIF should be measured in an artery without any abnormality to ensure that it is not delayed and/or dispersed compared with the bolus concentration measured in tissue fed by a different artery. If the global AIF were measured in an abnormal artery, then tissue that is fed by a normal artery could be deconvolved with a wider input function leading to an erroneous $\tilde{r}$ being extracted for the healthy tissue (see Figure 7.15). In this situation, tissue would mistakenly be classified as having high *CBF* and short *MTT*. In the extreme case where the AIF is more dispersed than the bolus in the tissue itself, deconvolution does not make mathematical sense. In practice, the risk of distorting $\tilde{r}$ by negative dispersion can be minimised by carefully selecting the global AIF from voxels within a normal artery whose concentration time-courses occur early and are narrow (minimum dispersion).

Figure 7.13 shows that in the ideal situation where there is no bolus distortion, the new deconvolution method can recover reasonable estimates of the true perfusion values, especially so in the clinically interesting cases where there are long MTTs. These perfusion measurements can therefore be used to improve the reliably of prediction of tissue that is likely to infarct. This is essential for the appropriate selection of patients for treatment.

Although a full correction of the dispersion errors may not be possible at present, the new deconvolution method presented here is the first step towards accurate perfusion maps, as it gives an accurate and robust reconstruction of $CBF \cdot R_{eff}(t)$ as well as providing parameters indicating delay and dispersion, which indicate the reliability of the estimated perfusion parameters. Such information regarding the vasculature would be valuable information in models used to predict tissue outcome in stroke. Chapter 9 investigates the application of the oML-EM-wavelet method to patient data, demonstrating its utility in identifying regions of delay/dispersion-related perfusion measurement errors, and their subsequent correction.

7.6 APPENDIX

This appendix gives the criteria used in this work to decide which AIF matrix use in the oML-EM-wavelet deconvolution. These criteria were determined from simulations.

500 iterations of standard ML-EM deconvolution were performed on the simulated data set (Chapter 5). Parameter values (*CBF*, dispersion index (*DI*) and *RTM*) were measured from the extracted impulse response functions $\tilde{r}$ for TR =1s, 1.5s and 2s data. Figures [7.16], [7.17], and [7.18] show the measured parameter values from SNR=50 data with TR =1s, 1.5s and 2s respectively. They reveal that when there is no dispersion, and the delay is an integer multiple of TR, the *CBF*, *DI* and *RTM* are larger using matrix $\mathbf{A}_2$. These trends were incorporated into the matrix-selection

criteria to select the matrix $\mathbf{A_1}$ for such cases. For dispersed impulse response functions, the *RTM* is larger, and it is desirable to reconstruct such functions using matrix $\mathbf{A_2}$. Similarly, when the *RTM* is zero (i.e. no delay or dispersion) matrix $\mathbf{A_2}$ should be used.

The above described information was used to determine the matrix-selection criteria given in Equation [7.16] below:

$$\begin{array}{lll} \textit{if} \quad CBF_{A_1} \le CBF_{A_2} \quad \textit{and} \begin{cases} DI_{A_1} \le DI_{A_2} \\ RTM_{A_1} \le RTM_{A_2} \end{cases} & \mathbf{A} = \mathbf{A_1} & \\ \quad \textit{unless} \;\; RTM_{A_1} > 2TR \;\; \textit{or} \;\; RTM_{A_1} < TR & \mathbf{A} = \mathbf{A_2} & [7.16] \\ \textit{else} & \mathbf{A} = \mathbf{A_2} & \end{array}$$

The accuracy of these criteria is given in Table 7.1. The table indicates that the criteria give a reasonably accurate selection of the $\mathbf{A_1}$ matrix for a non-dispersed response with an integer TR delay. For the SNR=100 data (SNR=50 data), at TR=2s, there is 84%(61%) and 91%(64%) success rate for 2s and 4s delay respectively, at TR=1.5s, there is 84%(61%) and 96%(68%) success rate for 1.5s and 3s delay respectively, at TR=1s, there is 93%(68%), 92%(67%), 90%(66%) and 81%(60%) success rate for 1s, 2s, 3s, and 4s delay respectively. In general the accuracy is higher for the higher SNR simulations.

It was found that even at high SNR, the criteria were not very accurate in selecting the $\mathbf{A_2}$ matrix for impulse response functions with small dispersions and particular values of delay. It is very difficult to distinguish such a small dispersion from a delay. Example ML-EM reconstructions of impulse response functions with 1s delay and 1s dispersion, from data simulated at TR=2s and TR=1s, are shown in Figures 7.19 and 7.20 respectively . The figures reveal that although $\tilde{r}$ are different using $\mathbf{A_1}$ (red curve) and $\mathbf{A_2}$ (blue curve), it is difficult to distinguish which one better characterises the true impulse response function (black dashed curve).

The accuracy of the selection criteria is therefore only of primary importance when there is no dispersion in the impulse response function. Such a situation is illustrated

in Figure 7.21. The figure shows that matrix $\mathbf{A}_1$ provides the better characterisation of the delayed and non-dispersed impulse response function. Table 7.1 shows that the matrix-selection criteria used in this work are reasonably accurate in correctly selection the $\mathbf{A}_1$ matrix to reconstruct non-dispersed impulse response functions that have an integer TR delay (first column), although the matrix selection is less accurate for lower SNR. Typically, after denoising (with for example, independent component analysis (Calamante *et al.* 2004)) the SNR of *in vivo* data lies in the range 100-500 depending on the quality of the initial data, (which itself depends on the particular MRI scanner, the sequence parameters and amount of contrast).

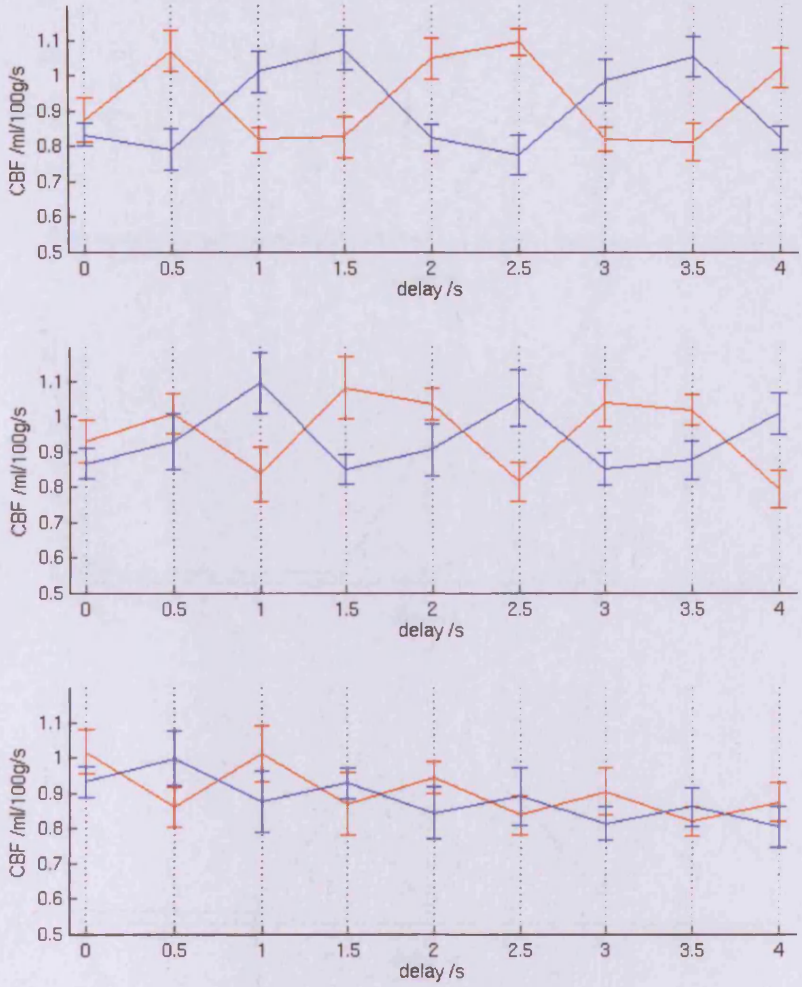

Figure 7.16: The mean (+/- 1 sd) *CBF* recorded as a function of delay for the ML-EM (500 iterations) reconstruction of $CBF \cdot R_{eff}(t)$ (*CBF*=60ml/100g/min, *CBV*=4ml/100g, dispersion β=0s) using matrix $\mathbf{A_1}$ (blue line) and matrix $\mathbf{A_2}$ (red line) for TR=2s (top), TR=1.5s (middle) and TR=1s (bottom) from SNR=50 simulated data over 100 repeats. There is a periodicity in the measured *CBF*, which is dependent on the convolution matrix.

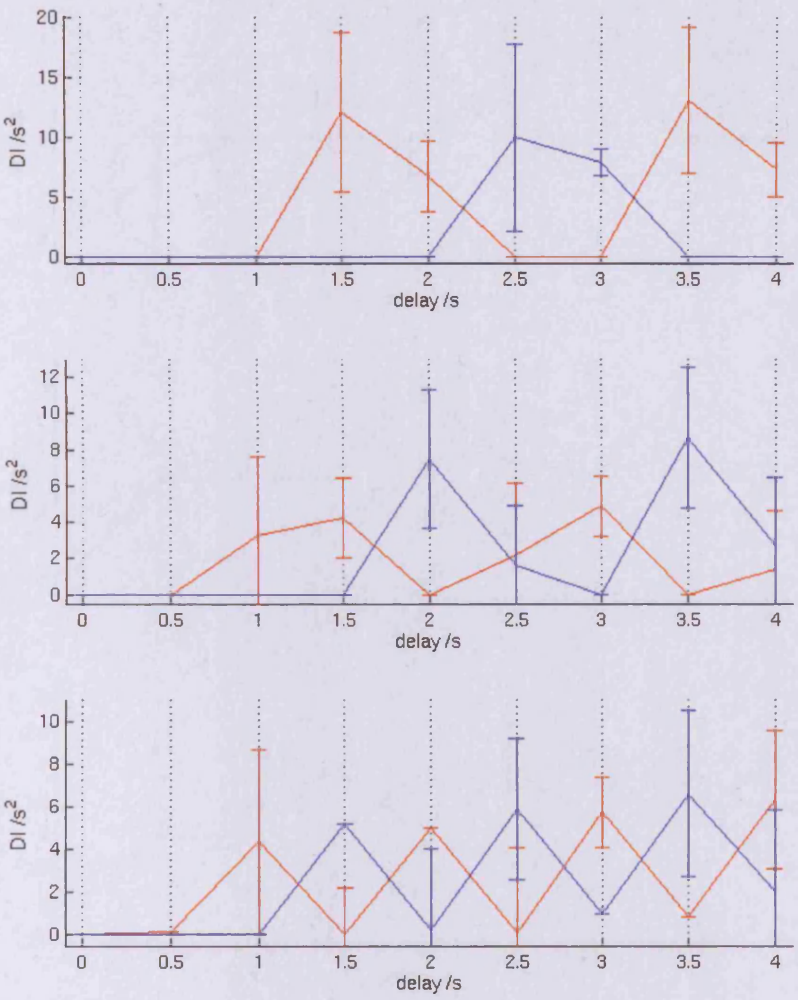

Figure 7.17: The mean (+/- 1 sd) *DI* recorded as a function of delay for the ML-EM (500 iterations) reconstruction of $CBF \cdot R_{eff}(t)$ (*CBF*=60ml/100g/min, *CBV*=4ml/100g, dispersion β=0s) using matrix $\mathbf{A_1}$ (blue line) and matrix $\mathbf{A_2}$ (red line) for TR=2s (top), TR=1.5s (middle) and TR=1s (bottom) from SNR=50 simulated data over 100 repeats.. There is a periodicity in the measured *DI*, which is dependent on the convolution matrix.

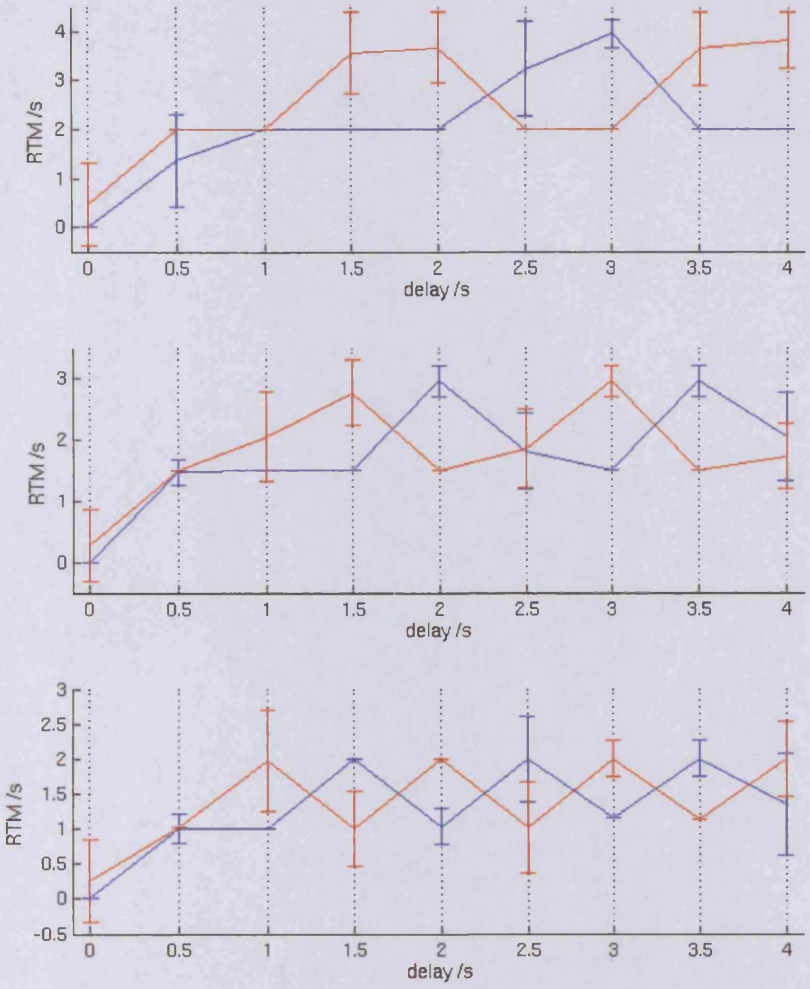

Figure 7.18: The mean (+/- 1 sd) *RTM* recorded as a function of delay for the ML-EM (500 iterations) reconstruction of $CBF \cdot R_{eff}(t)$ (*CBF*=60ml/100g/min, *CBV*=4ml/100g, dispersion β=0s) using matrix $\mathbf{A_1}$ (blue line) and matrix $\mathbf{A_2}$ (red line) for TR=2s (top), TR=1.5s (middle) and TR=1s (bottom) from SNR=50 simulated data over 100 repeats.. There is a periodicity in the measured *RTM* which is dependent on the convolution matrix.

		dispersion /s						
TR=2.0s SNR=100		**0.00**	**1.00**	**2.00**	**3.00**	**4.00**	**5.00**	**6.00**
delay /s	**0.00**	1.00	1.00	1.00	0.99	0.99	0.97	0.91
	0.50	1.00	1.00	0.91	0.84	0.68	0.80	0.72
	1.00	1.00	0.34	0.55	0.79	0.88	0.92	0.98
	1.50	1.00	0.83	1.00	1.00	1.00	1.00	1.00
	2.00	*0.84*	1.00	1.00	1.00	1.00	0.99	0.94
	2.50	1.00	1.00	0.86	0.85	0.89	0.79	0.81
	3.00	1.00	0.47	0.69	0.92	0.93	0.94	0.94
	3.50	1.00	0.86	0.99	1.00	1.00	1.00	1.00
	4.00	*0.91*	1.00	1.00	1.00	0.99	0.99	0.96
TR=1.5s SNR=100								
delay /s	**0.00**	1.00	0.99	0.93	0.87	0.82	0.79	0.85
	0.50	1.00	0.69	0.33	0.80	0.90	0.98	0.95
	1.00	1.00	0.64	1.00	1.00	0.99	0.99	0.98
	1.50	*0.84*	1.00	0.99	0.96	0.88	0.81	0.81
	2.00	1.00	0.77	0.25	0.93	0.86	0.90	1.00
	2.50	1.00	0.46	0.99	1.00	0.99	0.99	0.99
	3.00	*0.96*	1.00	1.00	0.97	0.94	0.87	0.86
	3.50	1.00	0.76	0.29	0.93	0.90	0.95	0.96
	4.00	1.00	0.31	1.00	1.00	1.00	1.00	1.00
TR=1.0s SNR=100								
delay /s	**0.00**	1.00	0.88	0.65	0.77	0.92	0.95	1.00
	0.50	0.99	0.35	0.94	0.99	0.99	0.99	0.95
	1.00	*0.93*	1.00	0.86	0.90	0.93	0.97	0.99
	1.50	1.00	0.29	0.96	0.99	0.99	1.00	0.98
	2.00	*0.92*	1.00	0.90	0.92	0.95	0.99	0.99
	2.50	1.00	0.49	1.00	0.99	1.00	1.00	1.00
	3.00	*0.90*	1.00	0.97	0.93	0.99	0.97	1.00
	3.50	1.00	0.66	0.99	1.00	1.00	1.00	0.99
	4.00	*0.81*	1.00	0.98	1.00	1.00	0.99	0.99

		dispersion /s						
TR=2.0s SNR=50		**0.00**	**1.00**	**2.00**	**3.00**	**4.00**	**5.00**	**6.00**
delay /s	**0.00**	1.00	1.00	0.95	0.87	0.95	0.90	0.92
	0.50	1.00	0.98	0.74	0.79	0.83	0.86	0.93
	1.00	1.00	0.47	0.76	0.91	0.88	0.95	0.99
	1.50	0.99	0.87	1.00	1.00	0.98	0.99	0.98
	2.00	*0.61*	1.00	0.98	0.92	0.91	0.93	0.88
	2.50	1.00	1.00	0.86	0.70	0.83	0.85	0.90
	3.00	1.00	0.53	0.80	0.91	0.91	0.97	1.00
	3.50	1.00	0.85	0.98	1.00	1.00	0.99	1.00
	4.00	*0.64*	1.00	1.00	0.97	0.97	0.93	0.96
TR=1.5s SNR=50								
delay /s	**0.00**	1.00	0.94	0.87	0.80	0.80	0.87	0.89
	0.50	1.00	0.61	0.67	0.85	0.90	0.97	0.94
	1.00	0.95	0.69	0.98	0.97	0.95	0.94	0.89
	1.50	*0.61*	0.99	0.91	0.88	0.79	0.84	0.86
	2.00	0.98	0.74	0.60	0.88	0.92	0.91	0.97
	2.50	0.96	0.56	0.98	1.00	0.98	0.91	0.95
	3.00	*0.68*	0.99	0.85	0.84	0.84	0.87	0.91
	3.50	0.94	0.71	0.63	0.81	0.89	0.95	0.99
	4.00	0.51	0.56	0.99	0.98	0.99	0.98	0.91
TR=1.0s SNR=50								
delay /s	**0.00**	1.00	0.72	0.69	0.83	0.95	0.94	0.96
	0.50	0.98	0.72	0.96	0.92	0.89	0.95	0.95
	1.00	*0.68*	0.83	0.71	0.90	0.93	0.98	0.98
	1.50	0.97	0.66	0.97	0.95	0.93	0.94	0.97
	2.00	*0.66*	0.93	0.72	0.85	0.94	0.99	1.00
	2.50	0.96	0.63	0.96	0.99	0.93	0.93	0.94
	3.00	*0.67*	0.95	0.85	0.91	0.92	0.98	0.98
	3.50	0.97	0.64	0.95	0.98	0.94	0.94	0.96
	4.00	*0.60*	0.98	0.88	0.95	0.97	1.00	0.93

Table 7.1: The proportion of 'correctly' selected matrices ($\mathbf{A}_1$ or $\mathbf{A}_2$) (given by Equation 7.1g) over 100 simulations of delay (rows) and dispersion (columns) combinations for the oML-EM-wavelet at TR=2.0s, 1.5s and 1.0s simulations at SNR 100 and 50 using healthy GM perfusion values (*CBF*= 60ml/100g/s, *CBV* = 4ml/100g). The shaded cells are the delay and dispersion combinations for which it is desirable to use the $\mathbf{A}_1$ matrix.

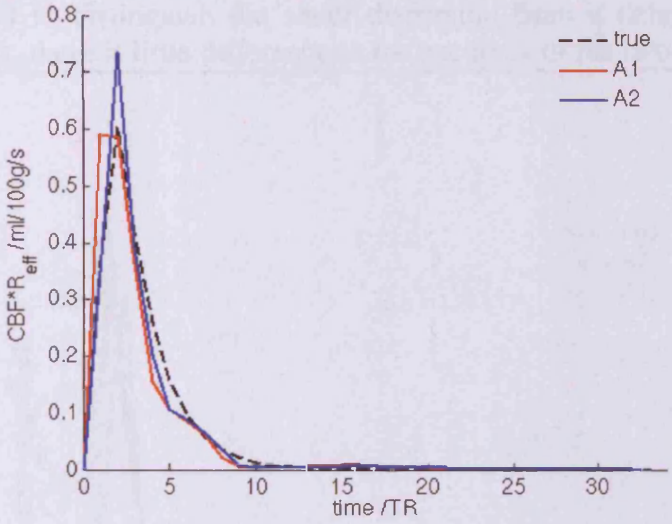

Figure 7.19: A single reconstruction of $\tilde{r}$ from data simulated with β=1s dispersion and t_{delay}= 1s, *CBF*=60ml/100g/min, *CBV*= 4ml/100g, TR=2s, SNR=100, using 500 ML-EM iterations. The red curve is the reconstruction using matrix $\mathbf{A_1}$, and the blue curve is the reconstruction using matrix $\mathbf{A_2}$. The true $CBF \cdot R_{eff}(t)$ is shown with the black dashed line. Using either matirx it is difficult to distinguish the small dispersion from a delay. The ability to characterise the sharp shape of $CBF \cdot R_{eff}(t)$ is poor for both matrix reconstructions at this temporal resolution.

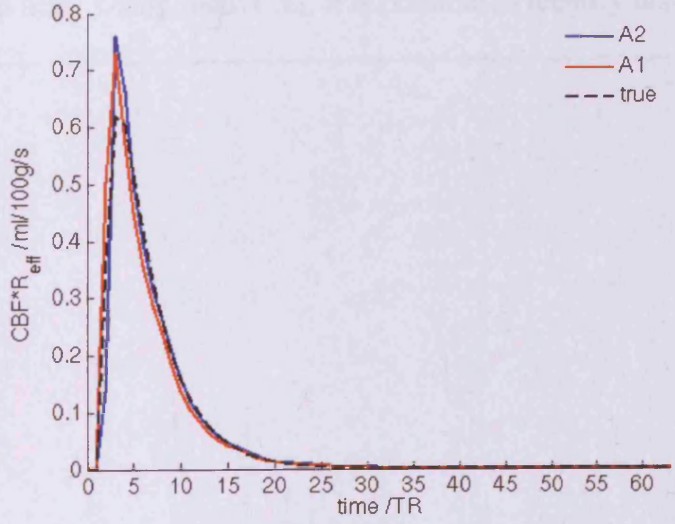

Figure 7.20: A single reconstruction of $\tilde{r}$, from data simulated with with 1s dispersion and 1s delay, *CBF*=60ml/100g/min, *CBV*= 4ml/100g, TR=1s, SNR=100, using 500 ML-EM iterations. The red curve is the reconstruction using matrix $\mathbf{A_1}$, and the blue curve is the reconstruction using matrix $\mathbf{A_2}$. The true $CBF \cdot R_{eff}(t)$ is shown with the black dashed line. Even at a high temporal resolution (TR=1s), it is

still difficult to distinguish the small dispersion from a delay using either matrix. Furthermore, there is little difference in the accuracy of the two reconstructions.

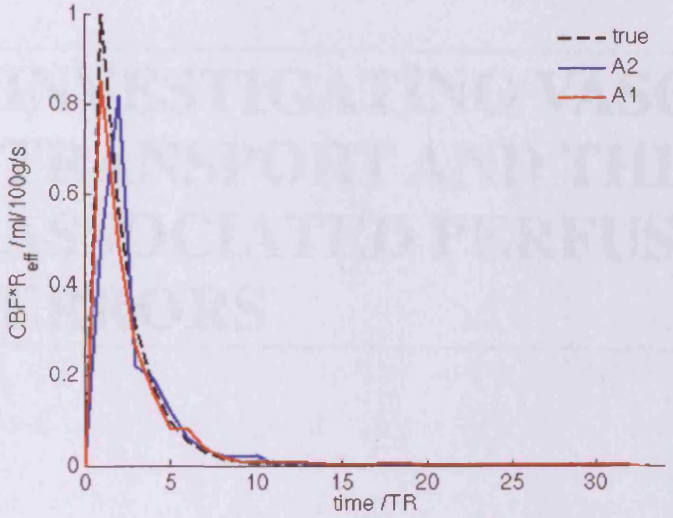

Figure 7.21: A single reconstruction $\tilde{r}$ with no dispersion and 1s delay, from data simulated with TR=2s, SNR=100, *CBF*=60ml/100g/min, *CBV*= 4ml/100g, using 500 ML-EM iterations. The red curve is the reconstruction using matrix $\mathbf{A}_1$, and the blue curve is the reconstruction using matrix $\mathbf{A}_2$. The true $CBF \cdot R_{eff}(t)$ is shown with the black dashed line. Using matrix $\mathbf{A}_1$, it is possible to identify that there is delay and no dispersion.

8 INVESTIGATING VASCULAR TRANSPORT AND THE ASSOCIATED PERFUSION ERRORS

8.1 INTRODUCTION

The novel ML-EM-based deconvolution techniques presented in Chapters 6 and 7 of this thesis were tested using the simulated DSC-MRI data described in Chapter 5. Although this approach is now well accepted in the perfusion MRI field, and it is considered an essential step in the development of analysis methods, the accuracy of these simulated data in replicating an *in vivo* situation will depend on specific assumptions about the unknown form of the microvascular and arterial retention models, i.e. the $R(t)$ and *VTF*. It is important that deconvolution techniques are tested using realistic DSC-MRI data sets, so that the accuracy and robustness of perfusion parameters maps can be extrapolated to the *in vivo* situation.

In order to simulate a realistic DSC-MRI data set, it is essential to know values for experimental and physiological parameters. There is little difficulty determining realistic values for the experiment parameters of signal intensity, noise, TR and TE, since these can either be measured directly from the DSC-MRI images, or determined from the scanning sequence. Similarly, the parameters for the arterial input function (AIF) model, known as the gamma-variate model, (Thompson *et al.* 1964) were determined from patient data (Østergaard *et al.* 1996b). A great deal of research has been conducted into values for the physiological parameters, *CBF*, *CBV*, and *MTT* under various haemodynamic and pathophysiological conditions e.g. (Lythgoe *et al.* 2000; Østergaard *et al.* 1998b), and a realistic range has been established. Similarly, although the form of the tissue residue function $R(t)$ is still somewhat speculative (see Section 4.6.2), it has been an active area of research through simulation e.g. (Østergaard *et al.* 1999; Mouridsen *et al.* 2006b) and *in vivo* measurement e.g. (Calamante *et al.* 2003a; Willats *et al.* 2006). In contrast, very little research has been conducted into the form for the vascular transport of the bolus, given by the so called vascular transport function (VTF) (see Section 4.7.2). Dispersion in the vascular transport can however introduce significant errors into perfusion quantification (Calamante *et al.* 2000; Calamante *et al.* 2003b), since its contribution distorts the

shape of the $R(t)$, which is used to estimate *CBF*. Therefore, it is very important that the form of the vascular transport and the size of the resultant perfusion errors are investigated. A functional form for the VTF would facilitate the design of a realistic simulated data set, which in addition to testing DSC-MRI analysis methods would enable investigation into dispersion and the related perfusion measurement errors.

The shape and significance of the distortion introduced in the concentration time-course curves because of abnormal arterial flow is unknown. The simulated data described in Chapter 5, were constructed using a delayed exponential decay to represent the vascular transport, $VTF(t-t_{delay})=\frac{1}{\beta}e^{-\frac{(t-t_{delay})}{\beta}}$, where t_{delay} represents the bolus delay and β the bolus dispersion. This exponential model has been extensively used to correct for dispersion in PET studies. However, in this case, the dispersion is primarily due to the cannula used to withdraw blood samples (Iida *et al.* 1986), so it is related to a different phenomenon from that found in arteries *in vivo*. In work performed by Calamante *et al.*(Calamante *et al.* 2003b), a patient specific fluid dynamical model for arterial blood flow constructed from anatomical and physiologic MR data, found that a single exponential model could properly characterise the dispersion in the four subjects studied. However, this study only included patients with very mild stenosis in extracranial arteries. Therefore, the validity of this monoexponential decay to model intracranial sources of dispersion remains to be shown.

The implications in using an incorrect VTF model could be dangerous, since *in vivo* predictions based on inaccurate simulations might be misleading. An incorrect model for the VTF may therefore indirectly contribute to misdiagnosis of patients with cerebral arterial disease. It is therefore important to use a realistic form of the VTF in simulations.

In this chapter, a methodology was developed to extract the *in vivo* VTFs. This was applied to a number of subjects with a diverse range of cerebral arterial abnormalities

with a view to verify whether the single exponential is appropriate to model dispersion in all situations. Furthermore, these VTFs were used to propose an improved and flexible parameterised mathematical model, with the potential to simulate DSC-MRI data that accurately replicates a diverse range of cerebrovascular situations *in vivo*.

Once a suitable model is identified, it is essential to determine a realistic range for its parameters. This is analogous to determining a realistic *in vivo* range for *CBF* in order to simulate realistic tissue states. The commonly assumed single exponential model for vascular transport has been used by Calamante *et al.* (Calamante *et al.* 2000) to gauge the severity of dispersion-related perfusion measurement error. Their simulations showed that a dispersion of β=2.5 seconds causes *CBF* to be underestimated by 50% and *MTT* to be overestimated by 200%. However, a realistic range for the β parameter found *in vivo* is not currently known. The largest β measured *in vivo* in (Calamante *et al.* 2003b), was ~0.6s, resulting in *CBF* errors of the order 15-20%. However, as mentioned before, this was a small group of patients all with mild stenosis, and an extensive investigation into the severity of dispersion and the related *CBF* errors has not yet been conducted *in vivo*. Such an investigation is of great importance, since this potential source of bias could have very important implications; for example, some tissue areas with benign oligemia (areas with normal or slightly decreased perfusion that will survive independently of treatment effects (Sobesky *et al.* 2005)) could be misclassified as penumbral tissue, with potentially serious clinical consequences for patient management. Therefore, in addition to informing a mathematical model for vascular transport, the collection of *in vivo* VTFs was used to determine a realistic range of dispersion-related perfusion measurement errors encountered *in vivo*.

Simulations are a vital tool for understanding *in vivo* data; equally, *in vivo* data are needed for the simulation of realistic data sets. This chapter investigates vascular transport in a group of patients with a range of cerebral arterial abnormalities. The chapter has three aims: 1) to determine a realistic model for the vascular transport function, 2) to determine the typical *in vivo* range for the model parameters, and 3) to

investigate *in vivo* the dispersion-related perfusion errors resulting from the vascular transport of the bolus through abnormal arteries. An improved characterisation of the vascular transport will facilitate more accurate testing of analysis techniques, and an improved understanding of the impact of dispersion *in vivo*.

8.2 PATIENT DATA

An *in vivo* investigation into vascular transport necessitates a patient cohort with a diverse range of arterial abnormalities. For this reason, the patients included in this study had various unilateral abnormalities in major cerebral arteries and had areas with severe DSC-MRI abnormalities (as identified in time-to-peak (TTP) maps of the bolus concentration time-course). The latter criterion was chosen to identify patients likely to have areas affected by bolus delay and dispersion (TTP maps are sensitive to these effect). Fifteen patients were identified; their abnormalities included stenosis, occlusion or dissection of a major cerebral artery (see Table 8.1). In some instances, the concentration time-course in different regions of the same patient were found to have different temporal characteristics. In such cases, two regions of interest (ROIs) were selected for the analysis. The age of the patients ranged from 0.8-19.6 years (mean 8.3 years)[13]. The MRI scans were done for clinical reasons and their analysis was approved by the local research ethics committee.

Data were acquired on a 1.5T Siemens Symphony scanner using a gradient-echo EPI sequence after the injection of a bolus of 0.15 mmol/kg of Gd-DTPA using an MR-compatible power injector (Medrad). The following sequence parameters were used: TE/TR=47/1500 ms, 12 slices, 5 mm slice thickness, 128×128 matrix, 240 cm field of view. The slices were acquired in an interleaved order with a gap of 4mm. Prior to

[13] In Chapter 6, the mML-EM technique was found to be less accurate in quantifying higher *CBF*.(see e.g. Figure 6.7). Although *CBF* is expected to be higher in children, (Biagi *et al.* 2007), accurate *CBF* quantification is not important in this chapter. The *CBF* values should not affect the characterisation of the vascular transport as this only requires information about the local and global AIFs. However, due to the smaller arteries in children, partial volume effects may be more significant. Care was taken to avoid voxels with partial volume contamination when selecting the global AIF.

	Age	Left				Right			
	(years)	ICA	MCA	PCA	ACA	ICA	MCA	PCA	ACA
Patient 1 - ROI 1	9.6		×		×				
Patient 1 - ROI 2	9.6		×		×				
Patient 2	0.8					×	×		×
Patient 3	3.2						×		×
Patient 4	1.5		×						
Patient 5 - ROI 1	9.9						×		
Patient 5 - ROI 2	9.9						×		
Patient 6	12.6						×		
Patient 7	6.9		×						
Patient 8	5.5					×	×	×	
Patient 9	12.4		×						
Patient 10	16.9	×	×		×				
Patient 11 - ROI 1	9.8						×	×	×
Patient 11 - ROI 2	9.8						×	×	×
Patient 12 - ROI 1	4.3	×							
Patient 12 - ROI 2	4.3	×							
Patient 13 - ROI 1	5.3						×		
Patient 13 - ROI 2	5.3						×		
Patient 14	12.4		×		×				
Patient 15	13.5					×	×		

Table 8.1: Location of vascular abnormalities in each patient. The symbol × indicates an abnormality (detected by MR angiography). ICA: Internal carotid artery; MCA: middle cerebral artery; PCA: posterior cerebral artery; ACA: anterior cerebral artery.

analysis, ICA denoising was performed on the concentration time-course data (see Section 5.3.2).

8.3 METHODS

8.3.1 MEASURING OF VASCULAR TRANSPORT

In order to investigate and model vascular transport, *in vivo* VTFs must be determined. A methodology was developed to experimentally determined VTFs in each of the 15 patients given in Table 8.1.

As discussed in Section 4.7.2, the VTF is defined from the convolution relating the local AIF (the true input to the tissue) and the global AIF :

$$C_a^{global}(t) = C_a^{local}(t) \otimes VTF(t) \qquad [8.1]$$

where $C_a^{local}(t)$ is the *local* AIF, and, $C_a^{global}(t)$ is the estimated *global* AIF.

The local AIF $C_a^{local}(t)$, were calculated for each patient using an Independent Component Analysis technique (Calamante *et al.* 2004). In summary, the concentration time-course of each voxel within the slice is decomposed into linearly independent components. A Bayesian information criterion is used to select the most likely number of independent components. Components are discarded (based on their spatial and temporal characteristics) if they are identified as being artefact (e.g. motion or scanner drift), or from the veins. The remaining components are thresholded to select those with significant contribution and a clear arterial spatial distribution. A Gaussian weighting factor is then used to interpolate the arterial signal to all the voxels. The resulting dataset is smoothed to represent the local AIF. A more detailed description of the AIF can be found in (Calamante *et al.* 2004).

For each patient, a global AIF, $C_a^{global}(t)$, was measured in the M1 segment of the contralateral middle cerebral artery (MCA). This estimation of the AIF can be considered a good approximation to the true AIF in the ipsilateral hemisphere in the absence of dispersion.

In this work the VTFs were calculated directly from the deconvolution of Equation [8.1]. The deconvolution was performed using the modified ML-EM method described in Chapter 6. This deconvolution technique was chosen because it has been shown to give a good characterisation of the impulse response function (in the present case, the VTF), even in the presence of bolus delay and/or dispersion, especially at high SNR. The temporal resolution of the patient data was TR=1.5s. Since the time scale of the VTF variations can be in the order of 1.5s, deconvolution at this resolution would lead to discretisation error, possibly biasing the fitting of a mathematical VTF model. Moreover, if there are too few non-zero time-points within the experimental VTF, it becomes increasingly difficult to fit a parameterised model. For this reason, prior to deconvolution, the AIF curves (local and global) were fitted using a gamma-variate function (see Section 5.2.2.) and subsampled with a resolution of 0.1s. This methodology is further discussed in the Discussion section. The extracted VTFs are reported in Section 8.4.1.

8.3.2 CHARACTERISING VASCULAR TRANSPORT

The random variation common in data from many scientific disciplines is often described by a skewed distribution. Many studies have shown that these distributions often closely fit the *lognormal distribution*, which is characterised in terms of the log-transform variable, using as parameters the mean and standard deviation of its distribution. The next few paragraphs present 1) a description of the mathematical form of the lognormal, 2) the physiological reasoning behind why the lognormal distribution might be an appropriate model for the VTF 3) a derivation of the lognormal parameter combinations used to describe delay and dispersion. In the Appendix to this chapter, a physical description of the lognormal is given.

A random variable t is lognormally distributed if ln(t) has a normal distribution. (Note that this definition is base on natural logarithms). The probability density function of such a random variable is:

$$f(t)=\frac{1}{(t-t_0)\sigma\sqrt{2\pi}}\exp\left(-\frac{1}{2\sigma^2}(\ln(t-t_0)-\mu)^2\right) \qquad [8.2]$$

Only positive values are possible for the shifted parameter (t-t_0). The shape of the lognormal distribution can be thought of in terms of the skewness (given by σ) the location (given by t_0) and the scale (given by μ).

A skewed distribution such as the lognormal is an appropriate model for distributions that have a mean value, a large variance, and values that cannot be negative. This is the situation for a vascular network with asymmetric branching and random variation at each bifurcation (fractal modelling of the vascular tree). It has been shown that with a large enough network with a significant number of generations, fractal behaviour and lognormal flow distributions naturally arise from this model (Qian *et al.* 2000; Karch *et al.* 2003). It has also been suggested that turbulent flow has a lognormal profile (Jung *et al.* 2005). Thus, the turbulent flow through the stenosis could also be considered as having a lognormal flow distribution.

The flow distribution that governs the VTF in MRI is drawn from a large network of bifurcations, which represent the capillary network feeding the tissue (Figure 8.1). Thus, one would expect the VTF to have an approximately lognormal distribution of transit times. The form of the VTF is dependent on the structure of the vascular bed and also on the pathology. The parameters μ and σ are therefore determined by the delay and dispersion of the bolus.

The variance of the VTF (variance-vascular-transit-time VVTT) around its mean (mean-vascular-transit-time MVTT) can be used to quantify the spread of the VTF and hence provide a measure of the degree of dispersion.

Figure 8.1: The vascular tree can be represented by a large network of bifurcations. Reproduced from (Karch *et al.* 2003).

$$VVTT = \frac{\int_0^\infty (t - MVTT)^2 \cdot VTF(t)dt}{\int_0^\infty VTF(t)dt} \qquad [8.3]$$

where the *MVTT* is given by the ratio of the first- to the zero-th moment of the VTF:

$$MVTT = \frac{VTF^{(1)}}{VTF^{(0)}} = \frac{\int_0^\infty t \cdot VTF(t)dt}{\int_0^\infty VTF(t)dt} \qquad [8.4]$$

Solving these equations for the lognormal function (Equation [8.2]) provides the following analytical expressions for MVTT and VVTT respectively:

$$MVTT = \exp\left(\mu + \frac{\sigma^2}{2}\right) + t_0 \qquad [8.5]$$

$$VVTT = \left(\exp(\sigma^2) - 1\right)\exp(\sigma^2 + 2\mu) \qquad [8.6]$$

The three parameter (σ, t_0 and μ) lognormal distribution was fitted to the twenty VTF extracted from the patient group in this study (Table 8.1). A multidimensional non-linear least-squares minimisation program was written in C++, implementing the Simplex algorithm from the GSL library. For each fitted VTF, in addition to recording the parameter values (σ, t_0 and μ), the MVTT and VVTT were calculated. The quality of the lognormal fit to the *in vivo* VTF was assessed and the range of lognormal parameter values required to characterise a broad range of dispersion in this patient group was obtained (Section 8.4.2).

8.3.3 SIMULATING VASCULAR TRANSPORT

One of the motivations for finding a mathematical model to describe vascular transport was to design simulated data sets that can describe a variety of cerebrovascular abnormalities. Therefore a realistic range of lognormal parameter values needs to be determined. The values found for each set of parameters (σ, μ and t_0) in the fitted *in vivo* data were analysed and realistic ranges were defined (see Section 8.4.2). The shift parameter t_0 does not influence the shape of the curve, but simply shifts the origin. For this reason, since the simulations were primarily performed to investigate the influence of the lognormal parameters on the function shape, it was not necessary to simulate the entire experimental range of t_0 values. The values for MVTT and VVTT corresponding to the simulated lognormal parameters were also calculated. The simulated VTF are reported Section 8.4.3.

8.3.4 PERFUSION ERRORS

Once a characterisation of the VTF has been made, a measure of the degree of dispersion in the vascular transport can be obtained (as measured by the variance (Equation [8.6]). The *in vivo* VTFs enable an investigation into a relationship between dispersion and the related perfusion errors *in vivo*.

The perfusion errors introduced by the bolus dispersion in the vascular transport were assessed using a similar methodology to that used in reference (Calamante *et al.* 2004) (see below). It is important that perfusion errors related to delay (which are wholly a result of regularisation and discretisation error in the deconvolution) are not wrongly assigned to dispersion-related perfusion measurement errors. If these errors are not made distinct, then any relationship found between the dispersion in the vascular transport and dispersion-related perfusion measurement errors would be biased by delay. Consequently, if the relationship were used *in vivo*, it could result in an incorrect correction of the perfusion measurement errors. In this analysis, in order to ensure that any *CBF* bias is solely a consequence of dispersion, delay in the concentration time-courses was removed prior to the deconvolution. This was achieved by shifting the curves to common origin, taking into account the differences in slice acquisition time between the global AIF and local AIF measurement slices.

An estimate of the perfusion, free from dispersion-related bias, was obtained by performing the mML-EM deconvolution (see Chapter 6) of Equation [8.7]:

$$C_t(t) = CBF \cdot C_a^{local}(t) \otimes R(t) \qquad [8.7]$$

where $C_t(t)$ is the tissue concentration measured in a region around the place where the local AIF was sampled, and $C_a^{local}(t)$ is the local AIF itself. This deconvolution recovers an estimate of the residue function $R(t)$ scaled by *CBF*, which is assumed to be the true *CBF*, free from dispersion error. This estimate of perfusion will be referred to as CBF_{local}, because it is calculated using the local AIF. CBF_{global} is the *CBF* estimation obtained by performing the deconvolution of Equation [8.8]:

$$C_t(t) = CBF \cdot C_a^{global}(t) \otimes R_{eff}(t) \qquad [8.8]$$

where $C_a^{global}(t)$ is the global AIF, which is measured in a contralateral branch of the MCA, and $R_{eff}(t) = R(t) \otimes VTF(t)$ is the effective residue function (see Section 4.7.2). In this situation, because of dispersion, CBF_{global} is calculated from the maximum of the extracted response function. i.e. $CBF_{global} = (CBF \cdot R_{eff}(t))_{max}$. Based on the assumption that the local AIF provides a more accurate estimate of *CBF* (by accounting for dispersion effects), the *% CBF* error introduced by bolus dispersion was defined as:

$$\%CBF_{ERROR} = \frac{(CBF_{global} - CBF_{local})}{CBF_{local}} \cdot 100 \qquad [8.9]$$

The results are reported in Section 8.4.4.

8.4 RESULTS

8.4.1 MEASURING OF VASCULAR TRANSPORT

In the 15 patients, twenty estimates for the local AIF were obtained, and these were used to calculate twenty VTFs. Some examples of the VTF calculated in the patients with abnormalities ranging from mild to severe dispersion are shown in Figure 8.2. All the VTFs were found to have a skewed distribution with various lengths of baseline.

The *in vivo* results illustrated in Figure 8.2 indicate that a function that is zero at the baseline and decreasing for $t > t_{delay}$ (as the exponential model assumed previously in some MRI and PET studies (Calamante *et al.* 2000; Calamante *et al.* 2003b; Iida *et al.* 1986) is a reasonable model for mild stenosis/small dispersions (e.g. Patients 2 and 12ROI1). This model for the VTF has been commonly used in simulations performed to assess the effects of delay and dispersion on perfusion quantification

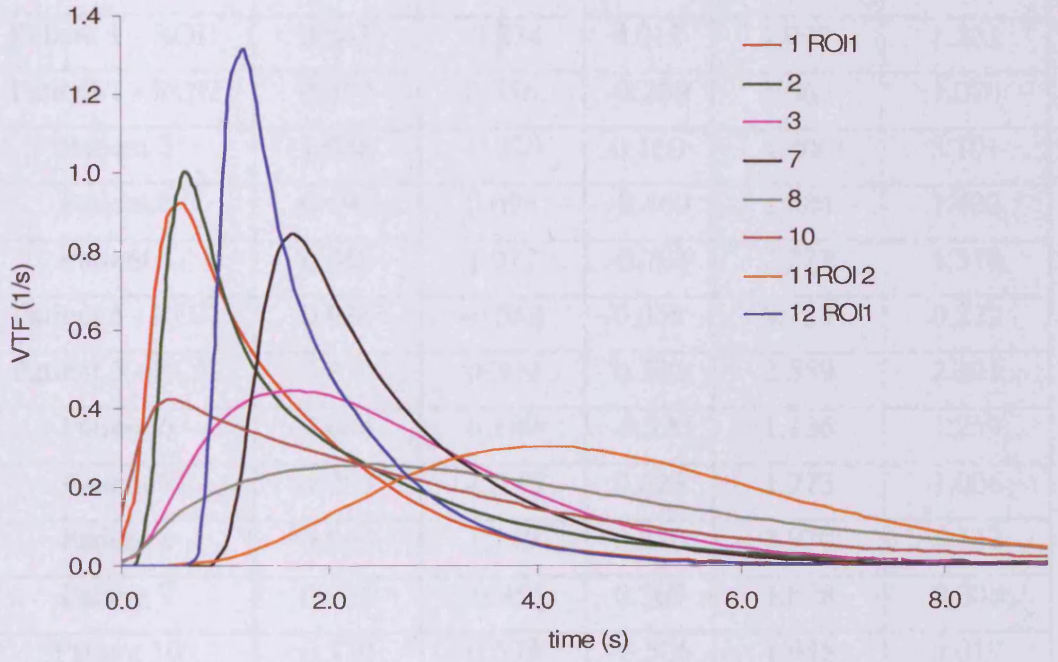

Figure 8.2: Illustrative examples of the vascular transport functions (VTF) for eight patients (listed in Table 8.1 and indicated in the figure legend) ranging from mild to severe dispersion. All curves are normalised to unit area.

(see Chapters 6 and 7). However, a more 'peaked' shaped function (as also previously used (Calamante *et al.* 2003a; King *et al.* 1993; Bassingthwaighte 1966)) may be a more suitable VTF model in many cases with moderate and severe dispersion (e.g. Patients 3 and 11ROI2). The VTF extracted from the patient data were found to be skewed to varying degrees according to the severity of the stenosis. This is consistent with the lognormal function used describe random variation in many scientific disciplines.

	σ /s	μ /s	t_0/s	MVTT /s	VVTT /s^2
Patient 1 - ROI1	0.843	-0.274	0.012	1.097	1.221
Patient 1 - ROI2	0.559	0.356	-0.299	1.369	1.020
Patient 2	1.048	-0.329	0.160	1.406	3.101
Patient 3	0.492	0.696	-0.460	1.804	1.402
Patient 4	0.369	1.032	-0.781	2.225	1.318
Patient 5 - ROI1	0.626	-0.580	0.058	0.739	0.222
Patient 5 - ROI2	0.730	0.309	0.782	2.559	2.221
Patient 6	0.664	0.189	-0.370	1.136	1.259
Patient 7	0.753	-0.145	0.625	1.773	1.006
Patient 8	0.565	1.149	0.270	3.970	5.142
Patient 9	0.935	-0.853	0.369	1.028	0.608
Patient 10	0.779	0.593	-0.506	1.945	5.019
Patient 11 - ROI1	0.476	0.406	0.170	1.851	0.717
Patient 11 - ROI2	0.304	1.497	-1.368	3.313	2.117
Patient 12 - ROI1	0.915	-0.667	0.536	1.316	0.797
Patient 12 - ROI2	0.517	1.571	-0.537	4.963	9.285
Patient 13	0.475	-0.079	0.240	1.274	0.270
Patient 14 - ROI1	0.673	-0.121	1.821	2.932	0.709
Patient 15	0.599	0.250	0.768	2.305	1.021
average	0.648	0.263	0.078	2.053	2.024

Table 8.2: Lognormal parameter values σ, t_0, and μ fitted for the VTFs in each patient, and the corresponding derived values of MVTT and VVTT.

8.4.2 CHARACTERISING VASCULAR TRANSPORT

Table 8.2 shows the fitted lognormal parameters (σ, μ, t_0) for the 15 subjects together with the average values. The average values for these parameters were: for the skewness variable, $<\sigma>$ = 0.65 (range 0.30 to 1.05); for the scale variable $<\mu>$ =0.26 (range -0.85 to 1.57s); for the shift variable $<t_0>$ = 0.08 (range -1.37 to1.82s); for the mean, <MVTT> = 2.05s (range 0.74 to 4.96s); and for the variance, <VVTT> = 2.02s^2 (range 0.22 to 9.29s^2), where <> indicates the average. The average was taken over 19 VTFs. The lognormal parameters of the VTF for ROI2 of Patient 14 converged with values σ=0.00017s, μ=10.38, and t_0= -32262.3s, which are very inconsistent with the lognormal parameter values fitted for the other patients. Inspection of the VTF curve for ROI2 of Patient 14 reveals there is a slight negative skew to this VTF, whereas the VTFs for the other patients all have varying degrees of positive skewness.

Figure 8.3 illustrates the lognormal function fitted to five of the *in vivo* VTF. The lognormal model was found to be able to characterise broad range of dispersion. For example, a more skewed distribution can be reproduced using a larger σ, while a broader distribution requires a larger value of μ.

The VTF for the 15 subjects show a large variation in shape, which is reflected in the large range of lognormal parameter values needed to fit the experimental VTF shapes.

8.4.3 SIMULATING VASCULAR TRANSPORT

Following the results of Section 8.4.2, VTFs were simulated for every combination of σ ranging 0.2 to 1.2s in steps of 0.2s, for μ ranging -1.5 to 2.0s in steps of 0.5s, and t_0 ranging -1.0 to +1.0s in steps of 0.2. This gave a very diverse range of VTF shapes. Not every combination of σ, t_0, and μ were found to give values of MVTT and VVTT within the ranges found experimentally in the *in vivo* data (Section 8.4.2). The

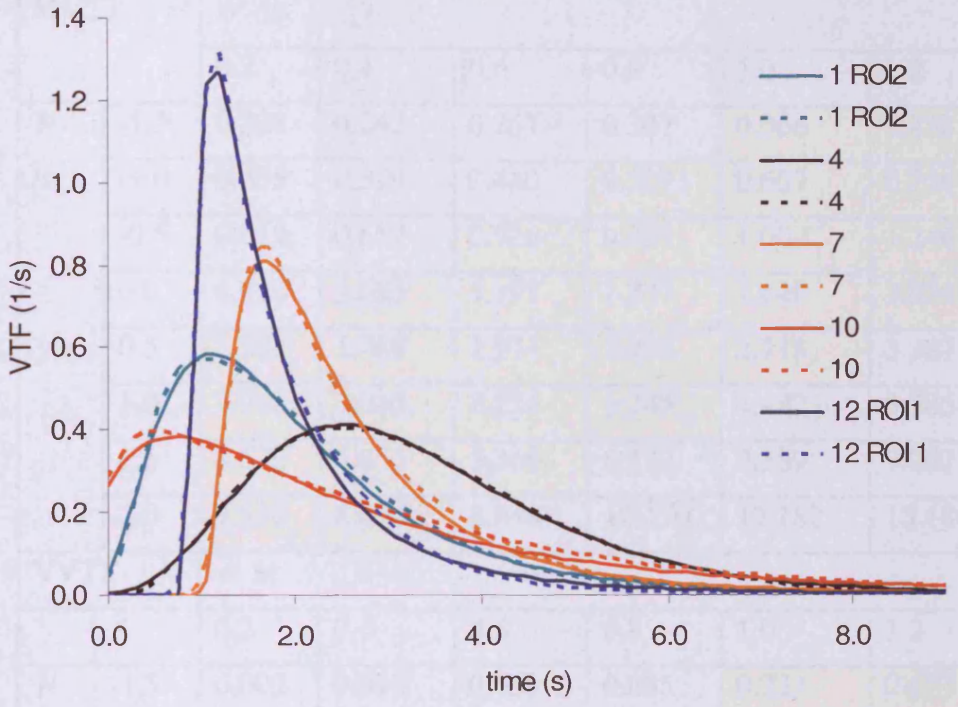

Figure 8.3: Five empirically determined *in vivo* VTFs (dashed lines) and their lognormal fit (solid lines). The legend indicates which subject the data were obtained from (Table 8.1 and Table 8.2).

simulated combinations of σ and μ, and the corresponding MVTT and VTTT values are given in Table 8.3. The highlighted cells correspond to those combinations of σ and μ that combine to give to a MVTT and VVTT consistent with the experimental ranges. Figure 8.4 illustrates some of the simulated log-normal VTFs lying within the experimental range of parameters (highlighted cells in Table 8.3). The VTFs shown in this figure were simulated with t_0=0s. Each graph shows the VTF simulated for a particular value of σ ranging from 1.2 to 0.2s. Each of the curves within the graph represents a particular value of μ that lies within the experimentally observed range and also gives rise to values for MVTT and VVTT that are consistent with the ranges observed *in vivo*. It can be seen that the large values for σ correspond to VTFs that decay from a maximum to zero in an approximately exponential manner. As σ is decreased, the VTF become more bell-shaped. For each σ, the smallest

MVTT		σ /s					
		0.2	0.4	0.6	0.8	1.0	1.2
μ /s	-1.5	0.228	0.242	0.267	0.307	0.368	0.458
	-1.0	0.375	0.399	0.440	0.507	0.607	0.756
	-0.5	0.619	0.657	0.726	0.835	1.000	1.246
	0.0	1.020	1.083	1.197	1.377	1.649	2.054
	0.5	1.682	1.786	1.974	2.270	2.718	3.387
	1.0	2.773	2.945	3.254	3.743	4.482	5.585
	1.5	4.572	4.855	5.366	6.172	7.389	9.207
	2.0	7.538	8.004	8.846	10.176	12.182	15.180
VVTT		σ /s					
		0.2	0.4	0.6	0.8	1.0	1.2
μ /s	-1.5	0.002	0.010	0.031	0.085	0.233	0.677
	-1.0	0.006	0.028	0.084	0.230	0.632	1.840
	-0.5	0.016	0.075	0.228	0.625	1.718	5.001
	0.0	0.042	0.204	0.621	1.700	4.671	13.594
	0.5	0.115	0.553	1.688	4.622	12.696	36.951
	1.0	0.314	1.505	4.589	12.563	34.513	100.444
	1.5	0.853	4.090	12.475	34.149	93.815	273.034
	2.0	2.319	11.117	33.911	92.826	255.016	742.184

Table 8.3: The table shows the MVTT and VVTT values corresponding to the simulated lognormal parameters. The highlighted cells correspond to the parameter combinations that combine to give experimentally consistent MVTT and VVTT values.

(experimentally consistent) value for μ gives rise to the sharpest VTF. As μ is increased the VTF become broader, and the maximum is shifted in time.

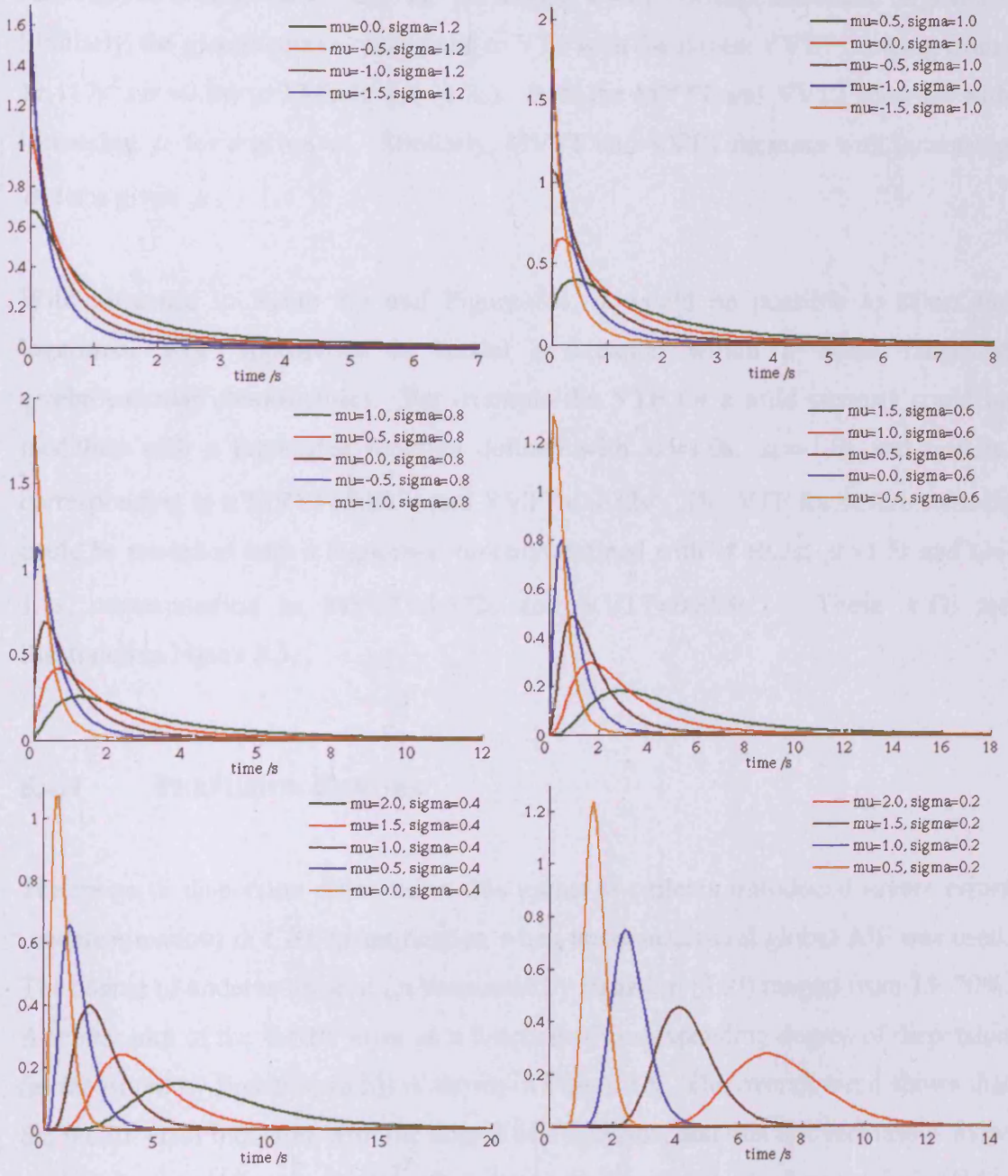

Figure 8.4: The graphs illustrate the simulated lognormal VTFs with parameters corresponding to the highlighted cells in Table 8.3. These VTF have realistic MVTT and VVTT when compared with *in vivo* data.

The orange curves in Figure 8.4 correspond to the lognormal functions with the smallest VVTT for the simulated σ. The orange-curve VVTT ranges from 0.115 s^2

(σ=0.2s) to 0.233s^2 (σ=1.2s). I.e. the largest VVTT corresponds to the largest σ. Similarly, the greens curves correspond to VTF with the largest VVTT, ranging from 11.117s^2 (σ=0.2s) to 13.954s^2 (σ=1.2s). Both the MVTT and VVTT increase with increasing μ for a given σ. Similarly, MVTT and VVTT increase with increasing σ for a given μ.

With reference to Table 8.3 and Figure 8.4, it would be possible to select the lognormal VTF appropriate to model a situation within a broad range of cerebrovascular abnormalities. For example the VTF for a mild stenosis could be modelled with a lognormal function defined with σ=1.0s, μ=-1.0s and t_0=0.5s, corresponding to a MVTT=0.607s and VVTT=0.632s^2. The VTF for severe stenosis could be modelled with a lognormal function defined with σ=0.2s, μ=1.5s and t_0=-1.1s, corresponding to MVTT=4.572s and VVTT=0.853s^2). These VTF are illustrated in Figure 8.5.

8.4.4 PERFUSION ERRORS

The range of dispersion observed in this group of patients introduced severe errors (underestimation) in *CBF* quantification when the contralateral global AIF was used. The degree of underestimation (as measured by Equation [8.9]) ranged from 13–70%. A scatter plot of the *%CBF* error as a function of corresponding degree of dispersion (as measured by Equation [8.6]) is shown in Figure 8.6. The overall trend shows that the *%CBF* error increases with the degree of dispersion, and that this increase is more marked for variances up to ~4s^2. For comparison purposes, the figure also includes the results found in previous numerical simulations (Calamante *et al.* 2000) which used an exponential function to model the VTF.

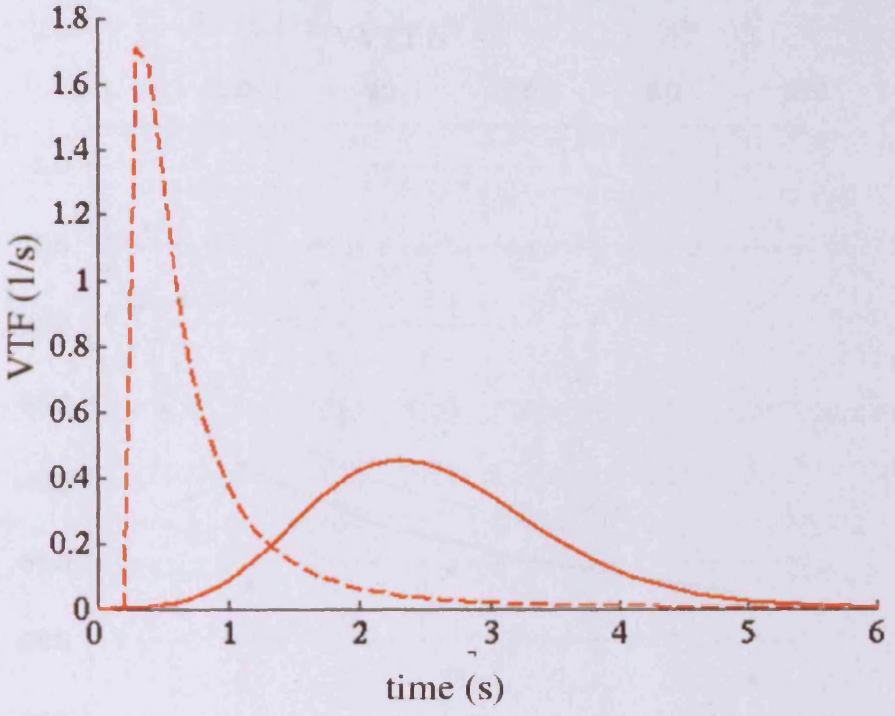

Figure 8.5: The figure exemplifies two simulated VTFs: The dashed line represents a mild stenosis (σ=1.0s, μ=-1.0s and t_0=0.2s, MVTT=0.607s and VVTT=0.632s^2). The solid represents a more severe stenosis (σ=0.2, μ=1.5 and t_0=-1.1s, MVTT=4.572s and VVTT=0.853s^2.

8.5 DISCUSSION

The empirically determined VTF from the patients used in this study indicate that it is reasonable to model the VTF for a mild stenosis with an exponentially decaying function (Calamante *et al.* 2000; Calamante *et al.* 2003b; Iida *et al.* 1986). This model for the VTF has been commonly used in simulations studies. However, it is clear from the experimental data that this model is not appropriate for the VTF describing a more severe stenosis (see Aim 1 in the Introduction). This work has demonstrated that a lognormal model for the VTF is flexible enough to define the shape of the VTF for both a mild and severe stenosis. A range of values for the lognormal parameters appropriate for modelling realistic VTFs for various degrees of dispersion has also been determined. The example VTFs illustrated in Figure 8.4

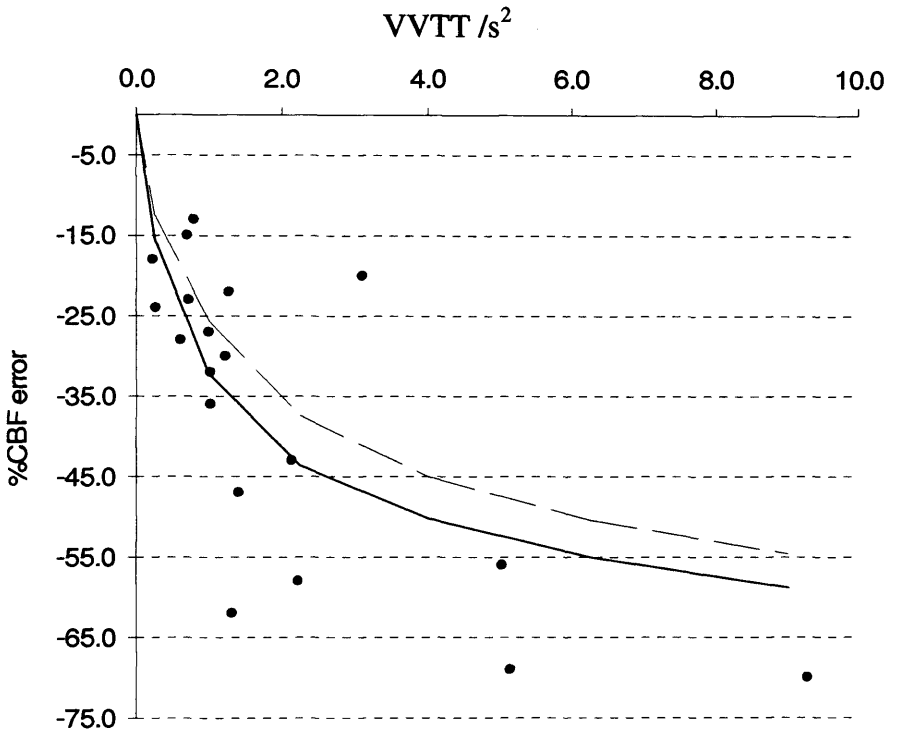

Figure 8.6: *% CBF* errors (Equation [8.9]) as a function of degree of dispersion (VVTT, Equation [8.6]). The *CBF* errors correspond to the errors in the quantification when the contralateral global AIF is used for deconvolution of the concentration time-course, i.e. when the dispersion effects are not accounted for. Negative errors correspond to *CBF* underestimation. The solid dots show the data collected in the present work. For comparison purposes, the solid and dashed lines indicate the results found in previous numerical simulations (using a simple exponential VTF model) for a typical child and a typical adult AIF cases, respectively (Calamante *et al.* 2000).

demonstrate the versatility of the lognormal to model very different cerebral arterial abnormalities

The lognormal parameter values found for the VTF to one of the regions analysed in Patient 14 were not consistent with the parameters derived from all the other VTFs. This suggests that there could be a bimodal range of experimental lognormal parameters describing the *in vivo* VTF: one for positively skewed, and one for negatively skewed. With the exception of ROI2 of Patient 14, all the extracted VTFs

were found to have some degree of positive skewness. Consequently, it was possible to gauge the range of realistic lognormal parameters in this case, which gave experimentally consistent values for MVTT and VVTT. Extracting VTFs and performing the lognormal analysis on data from many more subjects, may facilitate characterising a realistic lognormal parameter range for negatively skewed VTFs. In addition, the prevalence of negative skewness could be investigated.

Despite the need for further investigation, the experimentally informed parameterised VTF model for dispersion presented in this chapter will be useful for creating realistic and flexible simulated data sets that model DSC-MRI data in various cerebrovascular situations. Such simulated data are valuable for a comprehensive assessment of new methodologies such as the adapted ML-EM techniques presented in this thesis.

In the patient group studied, *CBF* error was found to increase with the degree of dispersion, with a more marked increase for VVTF values up to ~4s^2 (see Figure 8.5). This finding is consistent with the results from previous published numerical simulations (Calamante *et al.* 2000). Although the errors are qualitatively similar, the single exponential VTF for $t > t_{delay}$ (as used in the numerical simulations (Calamante *et al.* 2000)) do not closely follow the *in vivo* trend. The spread of *%CBF* error for a given dispersion should also be considered when assessing patient data. Furthermore, smoothly decreasing function of time for $t > t_{delay}$ seems only appropriate for mild and moderate dispersion, while a more 'peaked' shaped function is required to describe accurately some of the moderate and severe dispersion cases in this study (Figure 8.2).

In this study, and in this group of patients, the *CBF* bias (underestimation) introduced by the unaccounted dispersion has a large range (13–70% underestimation). This degree and range of dispersion-related perfusion measurement errors cannot be neglected in the interpretation of perfusion maps obtained from DSC-MRI data. A strategic use of these maps has been in combination with diffusion- and T_2-weighted images. The information is combined into models to predict the fate of the tissue in acute stroke (Section 3.12), with the final aim of identifying the patients that are more

likely to benefit from therapy. However, this work and previous works have shown that the presence of bolus dispersion can introduce large errors in *CBF* (i.e. underestimation) and *MTT* (i.e. overestimation) (Calamante *et al.* 2000), potentially biasing the prediction.

In light of the severity of the *%CBF* error in the patient data, predictive algorithms designed to assess the likelihood that ischaemic tissue will progress to infarction, (and which used the CBF_{global} perfusion estimates), should also include information about dispersion. Although currently it may not be practically possible to correct for dispersion (since this requires knowledge of the VTF for each voxel), information about the presence, extent and severity of dispersion, should be included. In Chapter 7 a dispersion index is proposed to indicate the presence, extent, and severity of dispersion. The findings of this chapter indicate that such a measure would indeed be a valuable parameter, for example, providing a measure of reliability for the predictions, or to use within the algorithm itself to improve the prediction. In Chapter 9 this dispersion index is utilised in a methodology to minimise the dispersion-related perfusion measurement errors. Such minimisation may make accurate *CBF* estimates possible. These would be a reliable input into predictor-models.

The main assumption in the assessment of dispersion and characterisation of the VTF in this study, is that they can be characterised using the locally defined AIF – i.e. the estimated local AIF is a good estimator of the true input to the tissue. Despite the need for validation, the locally defined AIF provides the best method currently available to estimate the VTF and the degree of bolus dispersion.

One potential means to validate this study would be in cross validation with an alternative technique. A method has recently been proposed to quantify the degree of dispersion in the renal blood flow of rabbits using a hyperpolarised tracer (Johansson *et al.* 2004). Since there are similarities between the renal and cerebral perfusion (i.e. the compartmentalisation of the tracer), the use of such a technique could potentially complement the methodology described in the present study. However, the requirement for such a tracer would limit the widespread used.

Another potential source of error in the methodology used to characterise the VTF, is that the lognormal function was fitted to pre-fitted data. The *in vivo* VTFs were calculated from the deconvolution of the local and global AIFs (Equation [8.1]), which had already been fitted with a gamma-variate curve. Based on the findings of the current study, the lognormal model has been suggested as a flexible and accurate characterisation of the vascular transport. Further work could now be performed to confirm this finding using more formal methods. For example, Mouridsen *et al.* (Mouridsen *et al.* 2006b) used a Bayesian deconvolution approach to estimate the parameters of a function describing the microvascular circulation. A similar approach could be taken here to estimate the lognormal parameters for the VTF from the direct deconvolution of the measured local and global AIFs. Such a model-dependent approach has the advantage of improving the stability of the deconvolution (compared with model-independent approaches) by reducing the degrees of freedom for function characterisation, and ensuring that the VTFs are smooth.

8.6 CONCLUSION

A simple mathematical function, the *lognormal*, has been suggested to describe the vascular transport of the bolus in DSC-MRI. As well as motivating the form of a mathematical model, the *in vivo* data were used to determine a realistic range of parameter values for flow through a variety of cerebral arterial abnormalities. This characterisation should facilitate the simulation of DSC-MRI data to describe a variety of cerebrovascular situations. Testing on simulated data sets (where the true perfusion values are known) has now become a crucial stage in the development of any DSC-MRI analysis technique (Chapter 5, 6 and 7). In addition to testing the robustness and accuracy of DSC-MRI analysis techniques, a realistic model of the VTF can facilitate further investigation into dispersion-related perfusion measurement errors. An understanding of the severity of perfusion errors is of primary importance for the assessment of patients with acute stroke, as well as for the accuracy of the predictor-models currently being used for determining the tissue outcome in stroke

e.g. (Wu *et al.* 2001). This study confirms that it is very important to consider the effect of dispersion in the assessment and management of patients with acute stroke, since the *CBF* errors can be significant. Neglecting these errors can lead to tissue misclassification and possibly to the inappropriate selection of patients for treatment, such as arterial thrombolysis.

8.7 APPENDIX: PHYSICAL DESCRIPTION OF THE LOGNORMAL

A physical model for the *normal* distribution can be visualised using a "Galton board" (Figure 8.7a). Particles leaving a funnel at the top fall down the slanting board and are deviated by rows of decision points (the tips of triangle obstacles) an equal distance c, left or right with equal probability p. A particle leaving the funnel at the top meets the first row obstacle and is deviated left or right by a distance c with equal probability. It then meets the corresponding triangle in the second row, is deviated again, and so on. The deviated particle from one row to the next is the realisation of a random variable with possible values $+c$ and $-c$, and equal probability for both. After passing through r rows of triangles, the particle falls into one of $r+1$ receptacles at the bottom of the board. The probability of ending up in receptacles numbered $0,1,\ldots r$ follow a binomial law with parameters r and p=0.5. When many particles have fallen down the board, the height of the particles piled in the receptacles will be approximately proportional to the binomial distribution. According to the central limit theorem, for a larger number of rows of obstacles, the probabilities approach the *normal* distribution. The central limit theorem states that the sum of many independent identically distributed positive random variables has approximately a normal distribution as $r \rightarrow \infty$.

If the Galton board is modified such that the obstacles are scalene rather than equilateral triangles (Figure 8.7b), the deviation of the particles a certain distance left or right will no longer have equal probability. The probability of particles falling into any particular receptacle at the bottom of the board follow the same binomial law, but

with parameters r and q=(1-p). The height of the accumulated particles is correspondingly skewed. For a large number of rows, the multiplicative version of the central limit theorem determines that the heights approach the *lognormal* distribution. The multiplicative version of the central limit theorem states that the product of many independent identically distributed positive random variables has approximately a lognormal distribution as $r \to \infty$.

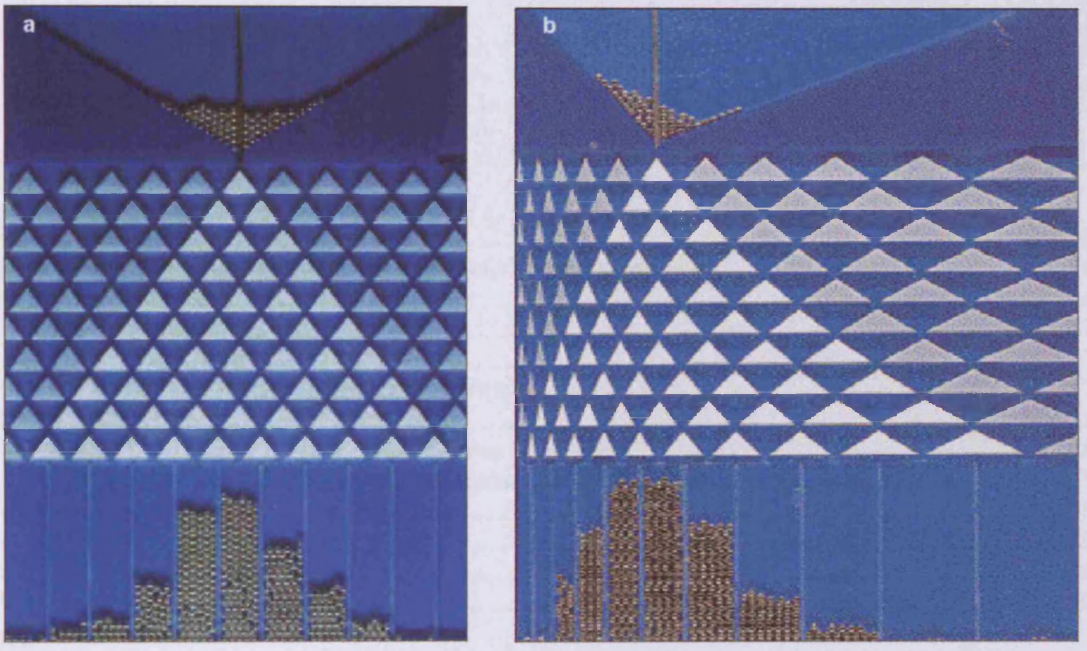

Figure 8.7: Physical models illustrating the genesis of the normal and lognormal distributions. Particles fall from a funnel onto tips of triangles, where they are deviated to the left or to the right with equal probability (0.5) and finally fall into receptacles. The median of the distributions remain below the entry points of the particles. If the tip of a triangle is at a distance x from the left edge of the board, triangle tips to the right and to the left below it are places at x + c and x – c for the normal distribution (panel a), and x.c' and x/c' for the lognormal (panel b), c and c' being constants. The distributions are generated by many random effects (according to the central limit theorem) that are additive for the normal distribution and multiplicative for the lognormal. Reproduced from (Limpert *et al.* 2001).

9 CORRECTING DISPERSION ERRORS IN DSC-MRI

9.1 INTRODUCTION

Although delay-related perfusion measurement errors have been recognised and are now accounted for in many studies (Rose *et al.* 2004; Ibaraki *et al.* 2005; Smith *et al.* 2004; Wu *et al.* 2003; Wu *et al.* 2004), dispersion errors are seldom taken into account when using DSC-MRI perfusion data to predict the fate of brain tissue in acute stroke. This is presumably related to the fact that it is difficult to correct for the effect of bolus dispersion. In Chapter 8, the size of dispersion-related perfusion measurement errors *in vivo* were found to be as large as 70%. In view of the severity of these errors and potentially dangerous consequences of misguided therapeutic decisions, this chapter investigates two approaches to correct for dispersion and as a result minimise the corresponding perfusion errors. The first method investigates whether a relationship between delay and dispersion exists *in vivo* and subsequently whether a post-deconvolution correction of dispersion is possible using such a relationship. The second method seeks to improve the estimated (global) arterial input function (AIF), using a *regional* AIF, such that the dispersion is minimised before the deconvolution.

The first method is a preliminary exploration into the possibility of using the more easily measured bolus delay to correct for the dispersion *in vivo*. An extensive investigation of delay and dispersion has not yet been performed *in vivo*. This work, which uses data from a group of patients with a large range of cerebral arterial abnormalities, will therefore provide new and useful insight. If a simple delay-dispersion relationship were identified, the degree of dispersion could be predicted from the more easily measured delay. In Chapter 8, the lognormal function was shown to model the extracted *in vivo* vascular transport functions accurately. If the lognormal parameters could be inferred from the degree of delay, one could potentially correct for dispersion. In addition, a simple relationship between delay and dispersion would be useful for the further development of vascular models.

The second method is a natural extension of Chapter 7, where the oML-EM-wavelet deconvolution technique was shown to characterise the tissue impulse response function with sufficient accuracy to identify bolus delay and dispersion. When this deconvolution technique is applied to DSC-MRI data from patients with vascular abnormalities, regions of delay and dispersion can be identified. An awareness of the potential underestimation of *CBF* in these regions is valuable information in the assessment of patients. In particular, the probability maps created using predictor-models can be interpreted with consideration to the potentially erroneous perfusion estimates. Furthermore, it may be possible to refine predictions made by these models if the bias was first removed from the perfusion measurements. Previous studies have suggested that it is possible to minimise the errors introduced by delay and dispersion by defining the AIF closer to the tissue, either using a *local* or *regional* AIF (Calamante *et al.* 2004; Alsop *et al.* 2002; Knutsson *et al.* 2006; Christensen *et al.* 2004; Lorenz *et al.* 2006).

In the *local* AIF method, the concentration time-course in each individual voxel is deconvolved with a unique (local) AIF (Calamante *et al.* 2004; Alsop *et al.* 2002). Since the direct measurement of a local AIF is problematic due to for example partial volume effects (see Section 4.7.4), methods have been proposed, which infer the expected form of the local AIF in each voxel from the larger scale data (Alsop *et al.* 2002; Calamante *et al.* 2004). The main limitation of such techniques is their validation, due to a lack of a 'gold-standard' for the AIF.

The search for an improved AIF can be restricted by using a *regional* AIF method where, rather than defining the AIFs on a voxel by voxel basis, a smaller number of region-specific AIFs are used (Knutsson *et al.* 2006; Christensen *et al.* 2004). In this chapter, a method is proposed to extract regional AIFs from regions where the bolus is identified as delay and/or dispersed. By first identifying regions of delay and/or dispersion, the search for a more accurate AIF is restricted, and targeted to areas known to have *CBF* errors.

The two studies reported in this chapter examine two very different approaches to correct dispersion. The first approach seeks to establish a new methodology for a simple dispersion correction *in vivo*, using information from the *in vivo* VTFs extracted in Chapter 8. The second *regional*-AIF method is a development of an already established theoretical means of minimising dispersion, which uses a more specific AIF. These techniques were conducted at different stages of the PhD, and as a result there is only a small overlap in the group of patients used in the investigations.

9.2 RELATIONSHIP BETWEEN BOLUS DELAY AND DISPERSION

In this study, an *in vivo* investigation into bolus delay and dispersion is conducted, with a view to establish if there is a relationship between the two. This investigation was performed using the patient group described in Chapter 8 (Section 8.2), which encompasses patients with a diverse range of cerebral arterial abnormalities. In Chapter 8, *in vivo* VTFs were extracted from these patients and fitted to a lognormal function in order to study vascular transport and the resulting perfusion errors. In this present chapter, the fitted (lognormal) VTFs are used for an investigation into delay and dispersion in the vascular transport. The methodology for the extraction and fitting of the VTFs can be found in Section 8.3 of Chapter 8.

9.2.1 METHODS

For the *in vivo* investigation of delay, two different measurements are considered. The first measure is taken directly from the bolus concentration time-course and the second requires knowledge of the VTF itself.

The first delay parameter is defined as the difference in the bolus arrival times (BAT) measured for the global and local AIFs, $\text{delay}_{\text{BAT}}$, where the BAT is the length of the

concentration time-course baseline. This definition is somewhat artificial since it only represents the delay for the *fastest* transit. Nevertheless, it is a parameter commonly used to assess brain haemodynamics.

An alternative and more representative delay parameter is the mean vascular delay, which can be calculated directly from the VTF. The mean vascular transit time (MVTT) is (cf. Equation [8.4]):

$$MVTT = \frac{VTF^{(1)}}{VTF^{(0)}} = \frac{\int_0^\infty t \cdot VTF(t)dt}{\int_0^\infty VTF(t)dt} \qquad [9.1]$$

An analytical expression can be calculated from the lognormal fit to the VFT (cf. Equation [8.5]):

$$MVTT = \exp\left(\mu + \frac{\sigma^2}{2}\right) + t_0 \qquad [9.2]$$

where σ, μ and t_0 are the lognormal parameters.

The MVTT definition of delay may be considered to be of less practical use than $delay_{BAT}$, since its quantification requires knowledge of the VTF, or the local AIF (Calamante *et al.* 2006). If these are known then the dispersion itself is known, and so it is unnecessary to predict it from the delay. Thus, even if a simple relationship were found, it would serve little practical use as a surrogate marker of dispersion. It should be also noted that a correlation between the MVTT and the bolus dispersion as measured by the VVTT is to be expected, since a wider VTF will not only lead to a larger dispersion, but also a longer first moment. The BAT definition of delay would therefore be of a more practical use for correcting bolus dispersion. Since both definitions of delay have specific limitations, both have been included with the present work.

An interleaved multi-slice acquisition order was used in the DSC-MRI sequence; accordingly the various slices were acquired at different times relative to the bolus injection. Therefore, for both definitions of delay, this extra time delay between the acquisitions of the corresponding slices for the global and local AIF (or the tissue concentration) was included in the calculation of delay.

The *in vivo* estimate of dispersion is taken from Chapter 8 as the variance of the VTF (variance-vascular-transit-time, VVTT) around its mean (MVTT) (cf. Equation [8.3]).

$$VVTT = \frac{\int_0^\infty (t - MVTT)^2 \cdot VTF(t)dt}{\int_0^\infty VTF(t)dt} \qquad [9.3]$$

An analytical expression can be calculated from the lognormal fit to the VFT (cf. Equation [8.6]):

$$VVTT = \left(\exp(\sigma^2) - 1\right)\exp(\sigma^2 + 2\mu) \qquad [9.4]$$

where σ, μ and t_0 are the lognormal parameters.

9.2.2 RESULTS

The MVTT (Equation [9.2]) and VVTT (Equation [9.4]) calculated from lognormal fit to the VTF data of the 15 patients (Table 8.1, Chapter 8) are recorded together with their lognormal parameters σ (skewness), μ (scale) and t_0 (shift) in Table 8.2 in Chapter 8. These values are reproduced in Table 9.1 with the addition of the corresponding $delay_{BAT}$ for each patient. The average estimate of $delay_{BAT}$ was $<delay_{BAT}>$ = 1.34s (range 0.76 to 3.27s). From Chapter 8, <MVTT> = 2.05s (range 0.74 to 4.96s), <VVTT> = 2.02s^2 (range 0.22 to 9.29s^2), $<\sigma>$ = 0.65 (range 0.30 to 1.05); for the scale variable $<\mu>$ =0.26 (range -0.85 to 1.57s); for the shift variable $<t_0>$ = 0.08 (range -1.37 to1.82s).

	σ /s	μ /s	t_0/s	MVTT /s	VVTT /s^2	delayBAT /s
Patient 1 - ROI1	0.84	-0.27	0.01	1.10	1.22	0.76
Patient 1 - ROI2	0.56	0.36	-0.30	1.37	1.02	1.03
Patient 2	1.05	-0.33	0.16	1.41	3.10	0.91
Patient 3	0.49	0.70	-0.46	1.80	1.40	1.44
Patient 4	0.37	1.03	-0.78	2.23	1.32	1.85
Patient 5 - ROI1	0.63	-0.58	0.06	0.74	0.22	0.80
Patient 5 - ROI2	0.73	0.31	0.78	2.56	2.22	0.87
Patient 6	0.66	0.19	-0.37	1.14	1.26	0.97
Patient 7	0.75	-0.15	0.63	1.77	1.01	1.95
Patient 8	0.57	1.15	0.27	3.97	5.14	1.68
Patient 9	0.94	-0.85	0.37	1.03	0.61	1.05
Patient 10	0.78	0.59	-0.51	1.95	5.02	0.90
Patient 11 - ROI1	0.48	0.41	0.17	1.85	0.72	2.12
Patient 11 - ROI2	0.30	1.50	-1.37	3.31	2.12	3.28
Patient 12 - ROI1	0.92	-0.67	0.54	1.32	0.80	1.35
Patient 12 - ROI2	0.52	1.57	-0.54	4.96	9.29	1.24
Patient 13	0.48	-0.08	0.24	1.27	0.27	1.56
Patient 14 - ROI1	0.67	-0.12	1.82	2.93	0.71	0.77
Patient 15	0.60	0.25	0.77	2.31	1.02	1.08
average	0.65	0.26	0.08	2.05	2.02	1.35

Table 9.1: The table shows the lognormal parameters σ, μ, and t_0, dispersion parameter VVTT and delay parameters, MVTT and $\text{delay}_{\text{BAT}}$, for the 15 patients used to study bolus delay and dispersion *in vivo*.

The relationships between the degree of dispersion and bolus delay, and between the lognormal parameters and the bolus delay, were investigated using the two delay definitions. Figure 9.1a shows a plot of VVTT, as a function of the $\text{delay}_{\text{BAT}}$. There is no correlation between the amount of delay (as measured by $\text{delay}_{\text{BAT}}$) and the

degree of dispersion (as measured by VVTT); in particular, the longest delays did not correspond to the largest dispersions. There is however a weak correlation between lognormal parameters σ, μ and t_0 and delay_{BAT}, as shown in Figures 9.1b, 9.1c, and 9.1d respectively. The correlation coefficients of σ, μ and t_0 with delay_{BAT} are respectively R^2=0.38, 0.28, and 0.22. Figure 9.2a shows a plot of VVTT as a function of MVTT. Using this delay definition, there is a correlation between the mean delay (as measured by MVTT) and the degree of dispersion (as measured by VVTT), with correlation coefficient $R^2 = 0.58$. Figures 9.2b, 9.2c, and 9.2d show the lognormal parameters σ, μ and t_0 as a function of MVTT. There is no correlation between the amount of delay (as measured by MVTT) and the lognormal shift parameter (as measured by t_0); in particular, the longest t_0 did not correspond to the longest MVTT. The correlation coefficients of σ, and μ with MVTT are respectively R^2=0.18, and 0.62. Although there is a significant correlation in Figures 9.2a and 9.2c, there is also a large scatter, so the prediction intervals are correspondingly large. Note that weak correlation and scatter in the other figures is not a consequence of the range of vascular abnormalities in the patients included in the study. For example, in Figure 9.1a the six patients (from whom seven VTF lognormal fittings were made) with vascular abnormalities restricted to their middle cerebral artery (MCA) (circled points) show no correlation with delay_{BAT}.

9.2.3 DISCUSSION

This study has revealed that for this group of patients with unilateral abnormalities in major cerebral arteries, the degree of dispersion (as measured by VVTT) that is present in any *given* patient cannot be inferred reliably from the amount of delay (measured either by delay_{BAT} or MVTT). The presence of a relationship between the degree of delay and dispersion might be expected since a longer transit of the bolus (e.g. due to abnormal blood supply) would most likely involve a larger spread of its width (the longer the transit, the longer the available time for the spread of the bolus). However, no significant correlation was found in the present study using the delay_{BAT}

a

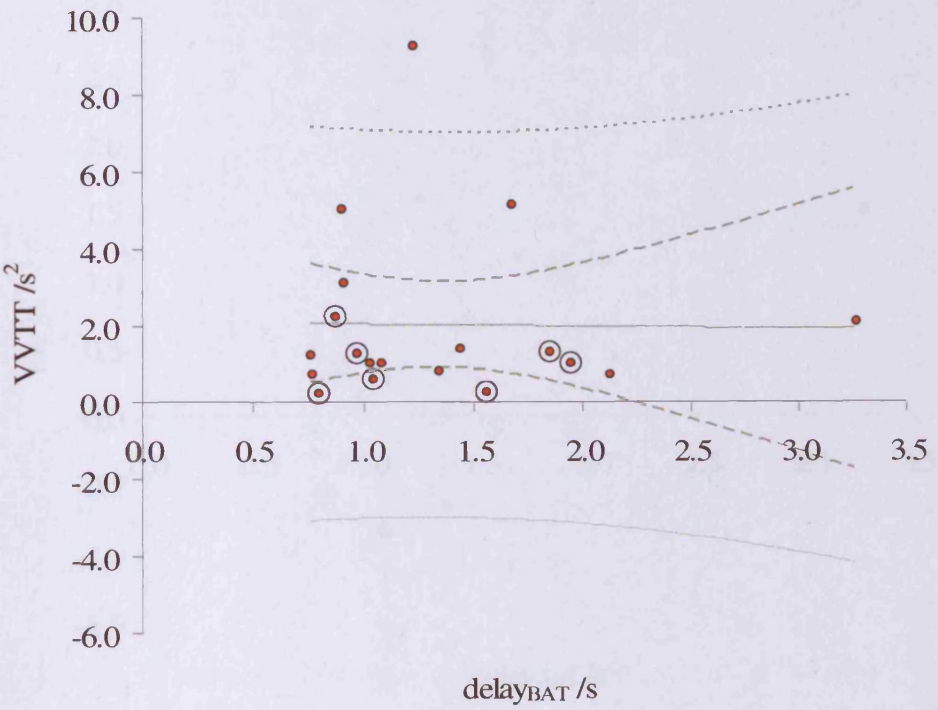
10.0
8.0
6.0
4.0
2.0
0.0
-2.0
-4.0
-6.0
VVTT /s²
0.0
0.5
1.0
1.5
2.0
2.5
3.0
3.5
delayBAT /s

b

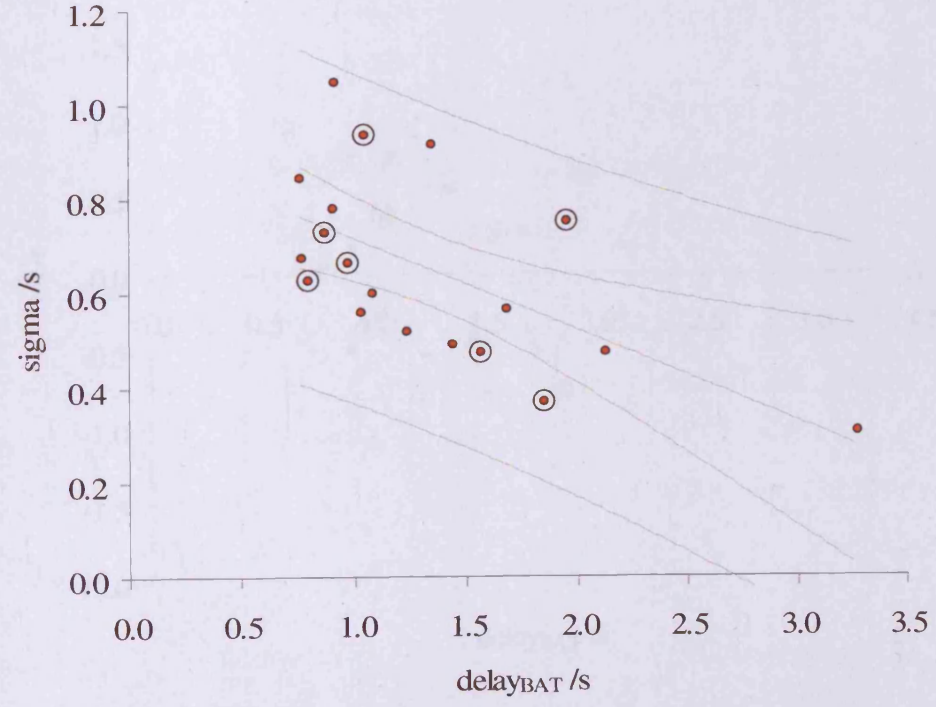
1.2
1.0
0.8
0.6
0.4
0.2
0.0
sigma /s
0.0
0.5
1.0
1.5
2.0
2.5
3.0
3.5
delayBAT /s

c

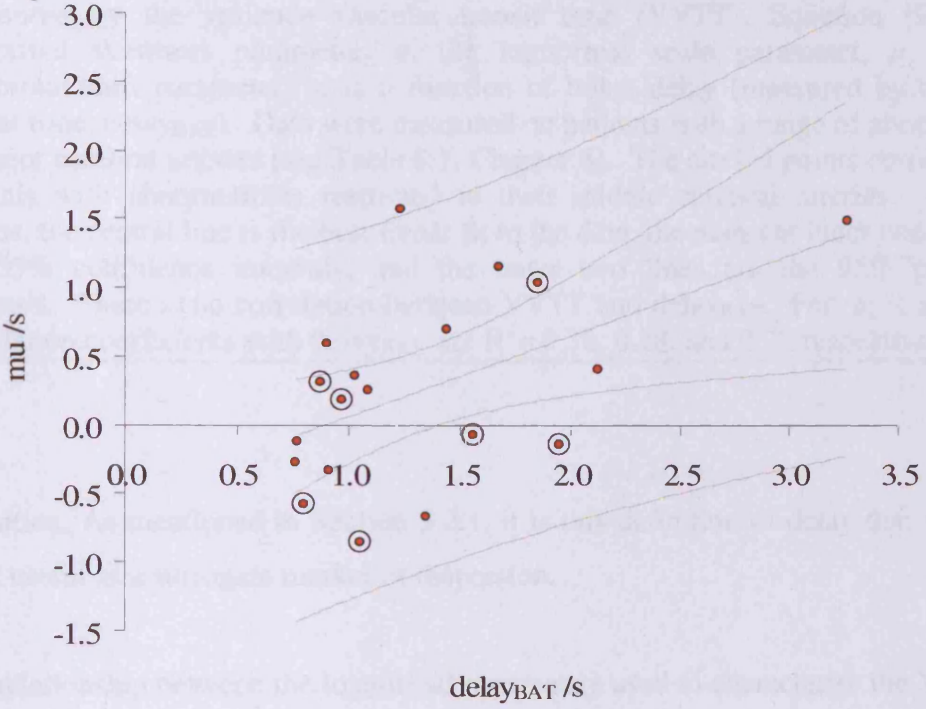
3.0
2.5
2.0
1.5
1.0
0.5
0.0
-0.5
-1.0
-1.5
mu /s
0.0
0.5
1.0
1.5
2.0
2.5
3.0
3.5
delayBAT /s

d

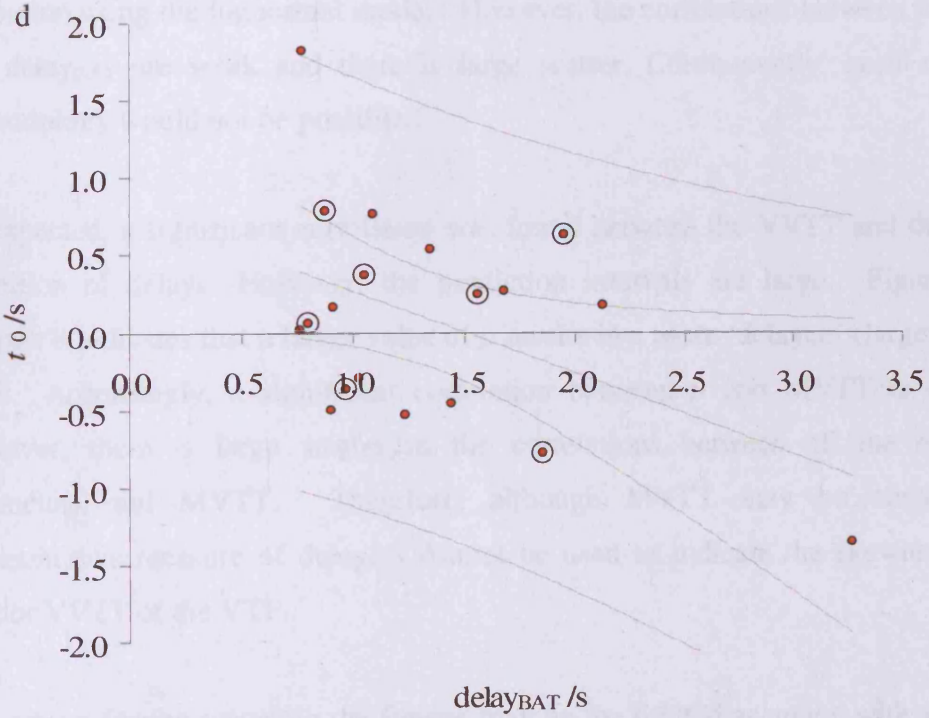
2.0
1.5
1.0
0.5
0.0
-0.5
-1.0
-1.5
-2.0
t0 /s
0.0
0.5
1.0
1.5
2.0
2.5
3.0
3.5
delayBAT /s

Figure 9.1: Graphs a, b, c, and d respectively show the degree of dispersion (measured by the variance vascular transit time (VVTT), Equation [9.3]), the lognormal skewness parameter, σ, the lognormal scale parameter, μ, and the lognormal shift parameter, t_0 as a function of bolus delay (measured by the bolus arrival time, $delay_{BAT}$). Data were measured on patients with a range of abnormalities in major cerebral arteries (see Table 8.1, Chapter 8). The circled points correspond to patients with abnormalities restricted to their middle cerebral arteries. On each graphs, the central line is the best linear fit to the data, the adjacent inner two lines are the 95% confidence intervals, and the outer two lines are the 95% prediction intervals. There is no correlation between VVTT and $delay_{BAT}$. For σ, μ, and t_0 the correlation coefficients with $delay_{BAT}$ are R^2= 0.38, 0.28, and 0.22 respectively.

definition. As mentioned in Section 9.2.1, it is this definition of delay that would be most useful as a surrogate marker of dispersion.

The relationship between the lognormal parameters used to characterise the VTFs and $delay_{BAT}$ was also investigated. If a clear relationship were found, the form of the VTF could have been inferred from $delay_{BAT}$, thus providing a means for dispersion correction using the lognormal model. However, the correlations between σ, μ and t_0 and $delay_{BAT}$ are weak and there is large scatter. Consequently, such correction methodology would not be possible.

As expected, a significant correlation was found between the VVTT and the MVTT definition of delay. However, the prediction intervals are large. Figure 8.4 of Chapter 8 indicates that a larger value of μ results in a more 'delayed' (larger MVTT) VTF. Accordingly, a significant correlation between μ and MVTT is expected. However, there is large scatter in the correlations between all the lognormal parameters and MVTT. Therefore, although MVTT may be considered a representative measure of delay, it cannot be used to indicate the skewness, scale, shift or VVTT of the VTF.

One reason for the scatter in the figures may be the limited accuracy with which the delay, dispersion and lognormal parameters can be estimated in practice. In addition, it is probable that the specific configuration of the vascular bed will influence bolus

a

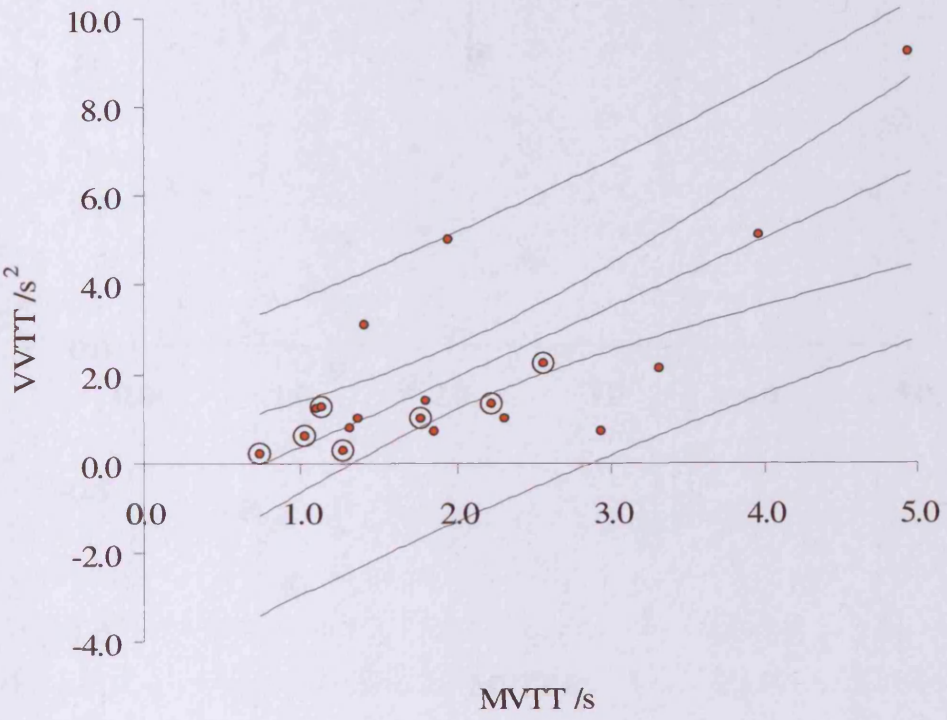
10.0
8.0
6.0
4.0
2.0
0.0
-2.0
-4.0
VVTT /s2
0.0
1.0
2.0
3.0
4.0
5.0
MVTT /s

b

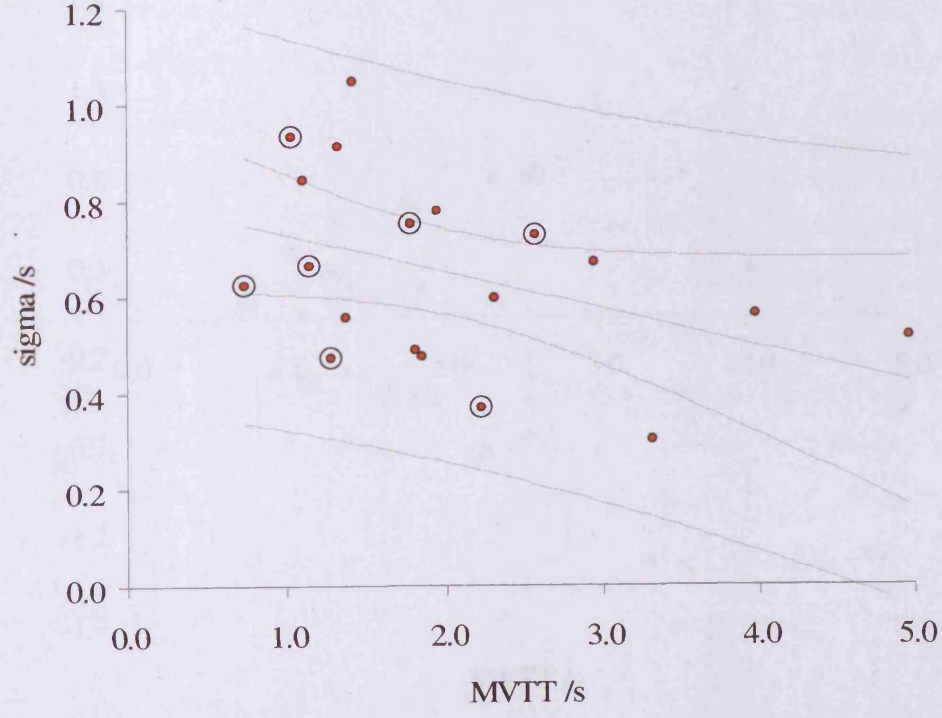
1.2
1.0
0.8
0.6
0.4
0.2
0.0
sigma /s
0.0
1.0
2.0
3.0
4.0
5.0
MVTT /s

Figure 9.2: Graphs a, b, c, and d respectively show the degree of dispersion (measured by the variance vascular transit time (VVTT), Equation [9.3]), the lognormal skewness parameter, σ, the lognormal scale parameter, μ, and the lognormal shift parameter, t_0 as a function of bolus delay (measured by the bolus arrival time, MVTT (Equation [9.2]). Data were measured on patients with a range of abnormalities in major cerebral arteries (see Table 8.1, Chapter 8). The circled points correspond to patients with abnormalities restricted to their middle cerebral arteries. On each graphs, the central line is the best linear fit to the data, the adjacent inner two lines are the 95% confidence intervals, and the outer two lines are the 95% prediction intervals. There is no correlation with MVTT for t_0. For the VVTT, σ, and μ, the correlation coefficients with MVTT are R^2= 0.58, 0.18, and 0.62 respectively.

dispersion independently of the time taken for it to travel to the tissue of interest. The degree of stenosis, the presence of arterial occlusion, vessel tortuosity, and degree of collateral flow will all contribute to the degree dispersion, although not necessarily to the same degree as they contribute to the mean delay. Furthermore, the precise vascular path will determine the shape distortion of the bolus, and therefore the skewness, scale and shift parameters of the lognormal.

In this group of patients, no simple relationship was found between the degree of bolus delay and dispersion, or the degree of bolus delay and the lognormal parameters used to characterise the VTF. Therefore a simple correction of dispersion is not possible. However, knowing that there may not be a correlation is important information for the accurate interpretation of perfusion maps in patients with cerebral arterial abnormalities. Since the presence of delay does not necessarily indicate the presence of dispersion, it might be possible to calculate an unbiased perfusion map simply by correcting for delay. Conversely, a delay may have a dispersion associated with it, and therefore, delay-corrected perfusion could still be inaccurate due to dispersion-related errors. For this reason, when analysing DSC-MRI data using a global AIF, it is important to assess the delay and dispersion independently, since one is not necessarily related to the other.

In light of the severity of the *in vivo* perfusion error found using a global AIF deconvolution (reported in Chapter 8), predictive algorithms designed to foretell the

fate of ischaemic tissue e.g. (Gottrup *et al.* 2005; Rose *et al.* 2001; Wu *et al.* 2007), (and which used the CBF_{global} perfusion estimates), should also include information about the delay and dispersion. Although it may not be practically possible to correct for dispersion using the delay estimate, information about the presence, extent and severity of dispersion are likely to improve the accuracy of predictor-models. Such information could be used to provide a measure of reliability to the predictions, or within the algorithm itself to improve the prediction.

9.3 REGIONAL ARTERIAL INPUT FUNCTIONS

When using a global-AIF analysis of DSC-MRI data, abnormally low *CBF* and long *MTT* estimates may be a consequence of a delayed and/or dispersed bolus, while the true perfusion in the tissue may in fact be sufficient to maintain tissue viability. Since the reperfusion treatments may increase the risk of cerebral haemorrhage, it is undesirable to administer such treatment in cases where perfusion is already sufficient. It is therefore important to separate the effect of vascular transport from the perfusion estimates.

In Chapter 7, a new algorithm (oML-EM-wavelet) was proposed for the deconvolution of DSC-MRI data. Simulations demonstrated that this deconvolution method is sufficiently accurate to distinguish and estimate delay and dispersion using the extracted impulse response function $CBF \cdot R_{eff}(t)$, the shape of which depends on both the arterial vascular transport (given by the vascular transport function VTF) and microvascular retention (given by the tissue residue function $R(t)$). Separating the microvascular retention from the arterial retention in the impulse response function would enable the correction of vascular transport related perfusion measurements errors. However, such methodology is difficult and impractical (e.g. Section 9.2).

In this second study, the perfusion measurement errors resulting from the vascular transport (delay and dispersion) are minimised by lessening the contribution of the VTF to the shape of $R_{eff}(t)$. This is achieved by improving the estimated AIF. A two-stage methodology is proposed. The first stage estimates perfusion using a global AIF and ascertains whether the perfusion estimates are likely to be inaccurate because or delay and/or dispersion. The second stage seeks to minimise these potential perfusion measurement errors arising from the vascular transport of the bolus. The perfusion errors present in the regions identified in stage one are minimised by finding a more accurate estimation for the arterial input to the tissue (a *regional* AIF) in stage 2.

9.3.1 METHODS

The methodology developed in this study is illustrated on data from six patients with severe vascular abnormalities. Two adult[14] patients were imaged on each of three different scanners 1) 1.5T Siemens scanner GE-EPI sequence: TE/TR=47/1500ms, 128*128 matrix, 0.15mmol/kg of Gd-DPTA. 2) 1.5T General Electric scanner GE-EPI sequence: TE/TR=60/2000ms, 128*256 matrix, 0.15mmol/kg of GD-DPTA. 3) Siemens scanner GE-EPI sequence: TE/TR=40/2000ms, 128*128 matrix, 0.15mmol/kg of GD-DPTA. The MRI scans were done for clinical reasons and their analysis was approved by the local research ethics committee. The signal intensity data were pre-processed as described in Section 5.3. Table 9.2 summarises the arterial abnormalities in the six patients, the scanner with which they were imaged, and the phase of ischaemia. In all patients, a global AIF was measured in a branch of the MCA contralateral to any abnormality (Section 5.3.3 describes the selection of a global AIF *in vivo*).

[14] Although the accuracy of the oML-EM-wavelet *CBF* quantification is degrades slightly at higher flows (e.g. Figure 7.13), it reasonable to assume that the accuracy of *CBF* quantification will be similar for all patients, since in adults *CBF* does not show much age dependency (Biagi *et al.* 2007).

	Arterial Abnormality	**Scanner**	**phase**
Patient 11	Right MCA, PCA and ACA	1. Siemens	chronic
Patient 12	Left ICA	1. Siemens	chronic
Patient 16	Left CCA	2. General Electric	chronic
Patient 17	Left ICA and CCA	2. General Electric	subacute
Patient 18	Right MCA	3. Siemens	acute
Patient 19	Left MCA	3. Siemens	acute

Table 9.2: Patients analysed using the regional AIF method. Patients 11 and 12 were also used in the delay/dispersion study described in Section 9.2. The table indicates the arterial abnormalities and the scanner on which the data were acquired. Details of the imaging sequence are given in Section 9.3.1. MCA: middle cerebral artery, PCA: posterior cerebral artery, ACA: anterior cerebral artery, ICA: internal carotid artery, CCA: common carotid artery .

9.3.1.1 Stage 1: Identifying Regions

Stage 1 involves calculating perfusion maps using a global AIF and identifying regions where the perfusion estimates are likely to be unreliable. The patient data were analysed using the oML-EM-wavelet methodology described in Chapter 7. Using the global AIF, the impulse response function $\tilde{r} = \left(CBF \cdot R_{eff}(t)\right)_{est}$, was estimated for each voxel, and maps of blood flow, $CBF = (\tilde{r})_{\max}$ and MTT (see Section 5.3.4) were created.

The first step in identifying regions where the perfusion estimates are unreliable is to identify delay and/or dispersion in the vascular transport. This can be achieved by way of an accurate characterisation of the impulse response function $CBF \cdot R_{eff}(t)$. As described in Chapter 7, in order to achieve high resolution measurements of shape,

the oML-EM-wavelet solution $\tilde{r}$ was subsampled at TR=0.01s using a linear interpolation between sample points. The bolus delay, t_{delay} was estimated from the length of the subsampled baseline (defined to end at the last subsampled baseline point with a value less than 10% of the maximum of $\tilde{r}_{subsampled}$). The dispersion characteristics were estimated using a dispersion index (*DI*) defined in Chapter 7 as:

$$\begin{aligned} DI &= FWHM\left(\tilde{r}_{subsampled}\right) \times RTM\left(\tilde{r}_{subsampled}\right) & RTM\left(\tilde{r}_{subsampled}\right) > TR \\ DI &= 0 & RTM\left(\tilde{r}_{subsampled}\right) \leq TR \end{aligned} \qquad [9.5]$$

FWHM is the full-width-half-maximum (in seconds), and *RTM* is the rise-to-maximum (in seconds) from baseline.

For the global AIF deconvolution, parameter maps of t_{delay} and *DI* were created. When the dispersion index (*DI*) in a voxel was found to be greater than zero, the *CBF* estimated in that voxel was identified to be an unreliable indicator of the true perfusion in that tissue. Although the t_{delay} parameter is used to indicate delay, the measurement cannot be entirely separated from dispersion. This is because a small dispersion may result in the *RTM* of $\tilde{r}$ having a value less than TR, and therefore, although it will not be detected on the *DI* map, it will have a small value on the t_{delay} map. Consequently, a non-zero t_{delay} may also indicate the presence of a small dispersion, and therefore it is possible that the *CBF* measurements in these voxels are also underestimated. Accordingly, the presence of delay and/or dispersion indicates that the global AIF is not a good approximation to the true AIF for this region of tissue.

In order to minimise the effects of delay and dispersion it is desirable to define a new more accurate AIF for the regions identified as having bolus delayed and/or dispersed. In practice, the regions with significant clusters of delay and/or dispersion voxels were identified interactively and delineated by manually drawing around each region. The voxels outside the region were masked.

9.3.1.2 Stage 2: Minimising Vascular Transport Effects

Stage 2 methodology seeks to correct delay and dispersion in the vascular transport by finding *regional* AIFs for the regions defined in Stage 1, thereby minimising perfusion measurement errors.

A regional AIF for the delayed/dispersed masked region is extracted using Independent Component Analysis (ICA) (Calamante *et al.* 2004) of the (non-ICA-denoised) concentration time-course data *within* the masked region. The number of independent components in the decomposition was determined using a Bayesian information criterion (Calamante *et al.* 2004). It is assumed that the ICA decomposition will decompose the concentration time-course data into artefact (i.e. noise or motion), tissue, venous, and arterial components. These components are identified interactively by analysing their temporal and spatial characteristics (Calamante *et al.* 2004; Carroll *et al.* 2002; Martel *et al.* 2003): Arterial components have a relatively early arrival time, narrow shape and spatial localisation within the vessels. The component that is most arterial in nature is selected as a better estimate for the AIF feeding the tissue within the delay/dispersed region.

The regional AIF is then used to re-perform the oML-EM-wavelet deconvolution on the (ICA-denoised) concentration time-course data within the masked region only. In order to avoid the possibility of negative dispersion in the remaining brain (outside the masked region), it is important to restrict the use of regional AIF to within the masked region from which it was defined. In (Section 7.4.4, it was shown that negative dispersion causes an overestimation of *CBF* and underestimation of *MTT*. Within the masked region, new estimates of $\tilde{r} = \left(CBF \cdot R_{eff}(t)\right)_{est}$, and maps of $CBF = (\tilde{r})_{\max}$, t_{delay} and DI are computed.

The regional AIF provides a more reliable estimate of perfusion in the regional voxels where t_{delay} and/or DI are smaller than those calculated using the global AIF. If in some voxels t_{delay} and/or DI are still significant, the *CBF* is still likely to be

underestimated in these voxels. If these voxels are clustered in a distinct area, a subregion can be defined within the original masked region. A new regional AIF can be defined for this subregion in the same way as before; everywhere other than the subregion is masked out, and the ICA analysis is performed within the subregion to find a more appropriate (sub)regional AIF, which is then used to calculate new (sub)regional perfusion parameters. This methodology may be repeated so that any residual delay/dispersion is minimised by iteratively improving the AIF (according to (sub)regional arterial ICA components), within iteratively defined (sub)regions. At each iteration, the shape of the deconvolved impulse response functions were inspected to ensure that negative dispersion had not been introduced. For each region initially identified as delayed/dispersed from the global AIF analysis, the above procedure was typically found to converge within 1-3 iterations. Once the values within and area of the delay/dispersion regions were reduced to minimal sizes, improved perfusion maps were calculated for the whole brain by combining the global, regional, and subregional perfusion estimates.

The regional AIF methodology is summarised in the flow chart in Figure 9.3.

9.3.2 RESULTS

The *CBF* and *MTT* maps calculated using the global AIF are shown in Figure 9.4 for each of the patients in Table 9.2. These maps reveal areas of apparent perfusion abnormality (identified by low *CBF* (dark areas) and prolonged *MTT* (bright areas). Figure 9.5 shows the corresponding parameter maps of t_{delay} and *DI*. In some patients a single region of delay/dispersion was identified (Patients 11, and 19). In other patients there were multiple regions of delay/dispersion, displaying different delay and dispersion characteristics (Patients 12, 17, and 18). These areas are highlighted in Figure 9.5 with the pink ovals, and also indicated in column 2 of Table 9.3.

The regional AIF analysis was performed on the five of the six patients indicated in Table 9.2. For Patient 16, the global AIF analysis failed for a significant number of

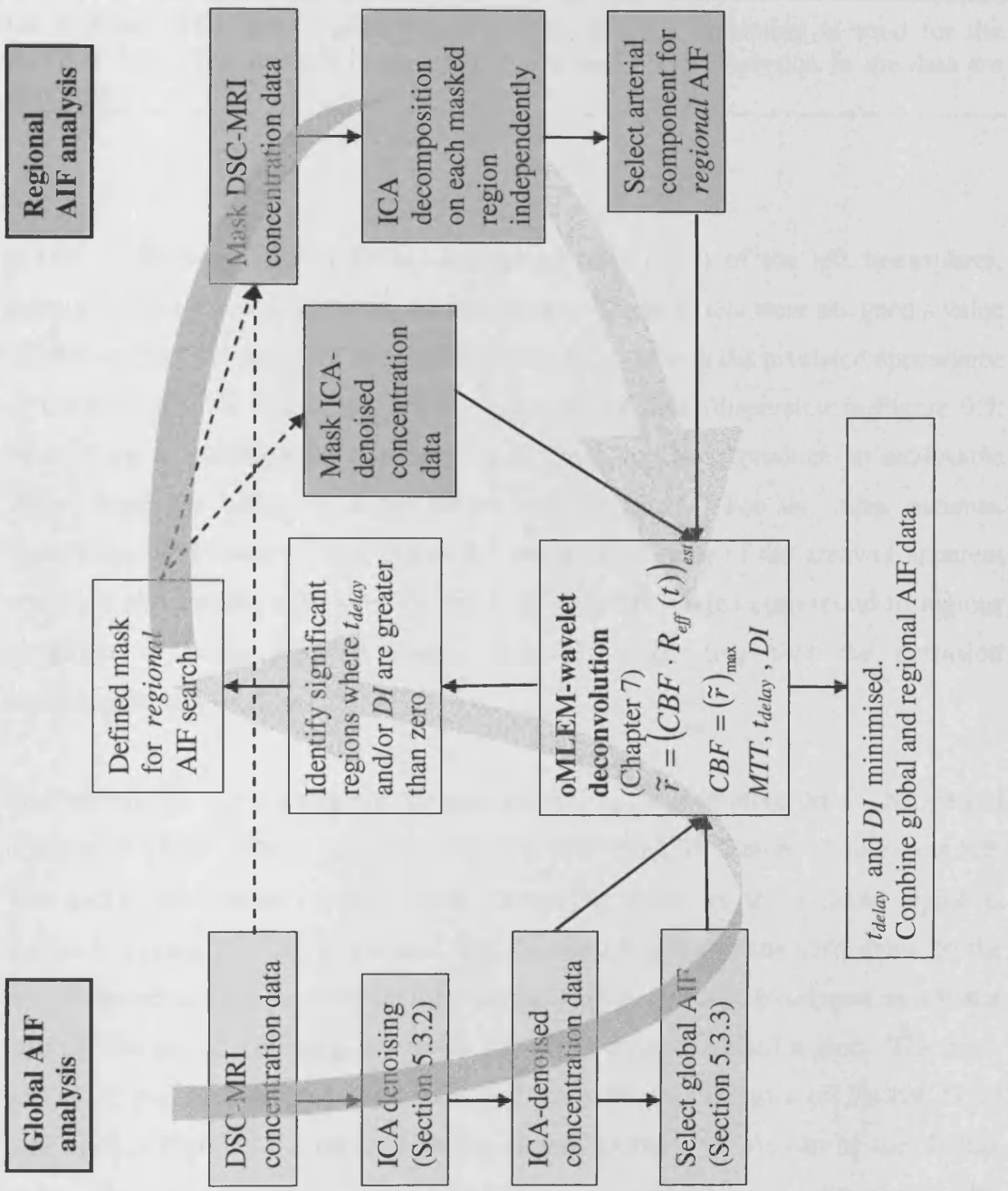

Figure 9.3: Flow chart summarising the steps involved in minimising delay and dispersion effects in DSC-MRI data by means of a regional arterial input function analysis. The left arrow depicts Stage 1 and the right arrow depicts Stage 2 of the methodology. An initial global AIF analysis using the oML-EM-wavelet deconvolution, enables the identification of regions where the global AIF is an inappropriate approximation for the input to the tissue. These regions are delineated and an ICA decomposition is performed on the concentration time-course data within

the regions. The most arterial component in this decomposition is used for the regional AIF. The analysis is repeated so that delay and dispersion in the data are minimised.

voxels in the white matter (WM) and grey-matter (GM) of the left hemisphere, because too little contrast arrived in these voxels. These voxels were assigned a value of zero on the *CBF* and *MTT* maps in Figure 9.4, explaining the pixelated appearance of the *MTT* map in Figure 9.4 and apparent lack of delay/dispersion in Figure 9.5. Since there is insufficient bolus arriving in these voxels to produce an analysable signal drop, the tissue is under severe hypoperfusion. For the other patients, examination of Figure 9.4 and Figure 9.5 reveals that many of the areas of apparent perfusion abnormality (observed on the *CBF* and *MTT* maps) correspond to regions identified as being delayed and/or dispersed, suggesting that the perfusion abnormalities are exaggerated.

To illustrate the various steps of the regional AIF method in more detail, the manual delineation of the delayed/dispersed region is illustrated for Patient 11 in Figure 9.6. The spatial localisation of the arterial component found for this masked region is shown in Figure 9.7. In this figure, the localised bright regions correspond to the spatial distribution of the arterial component. This component is selected as a better estimate for the AIF feeding the tissue within this delay/dispersed region. The time-course of the ICA-defined (regional) AIF used for the analysis of Patient 11 is illustrated in Figure 9.8 together with the original global AIF. As can be seen in this figure, the regional AIF is delayed and dispersed with respect to the global AIF. Column 3 of Table 9.3 reports the number of AIF iterations used to update the AIF within each region of each patient.

Figure 9.9 shows the *CBF* and *MTT* maps recalculated using the regional AIFs and the maps in Figure 9.10 indicate the residual delay and dispersion after this analysis. To assess the impact of the regional AIF method, Figure 9.9 should be compared with Figure 9.4, and Figure 9.10 should be compared with Figure 9.5. In all five of the

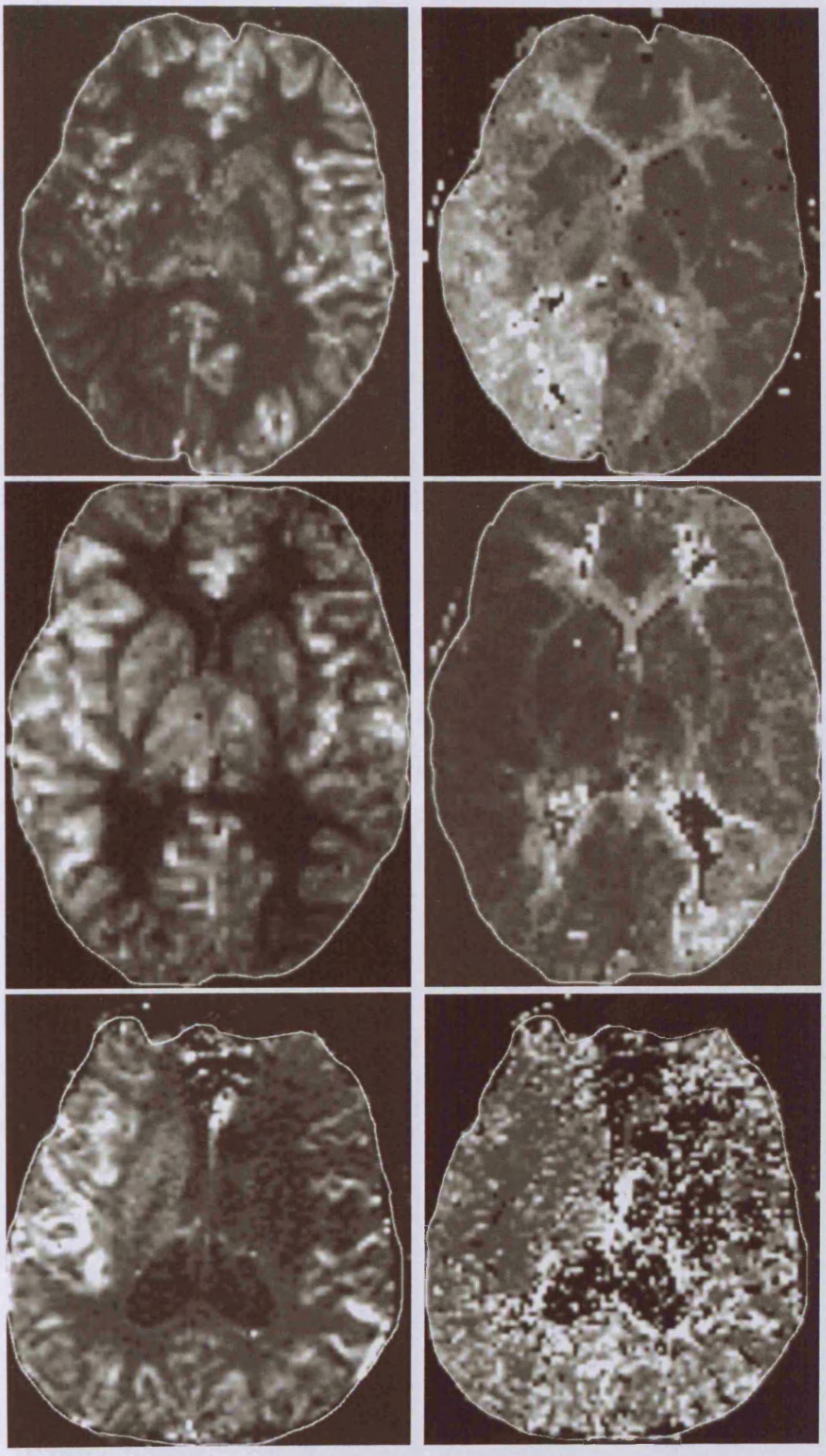
11
12
16

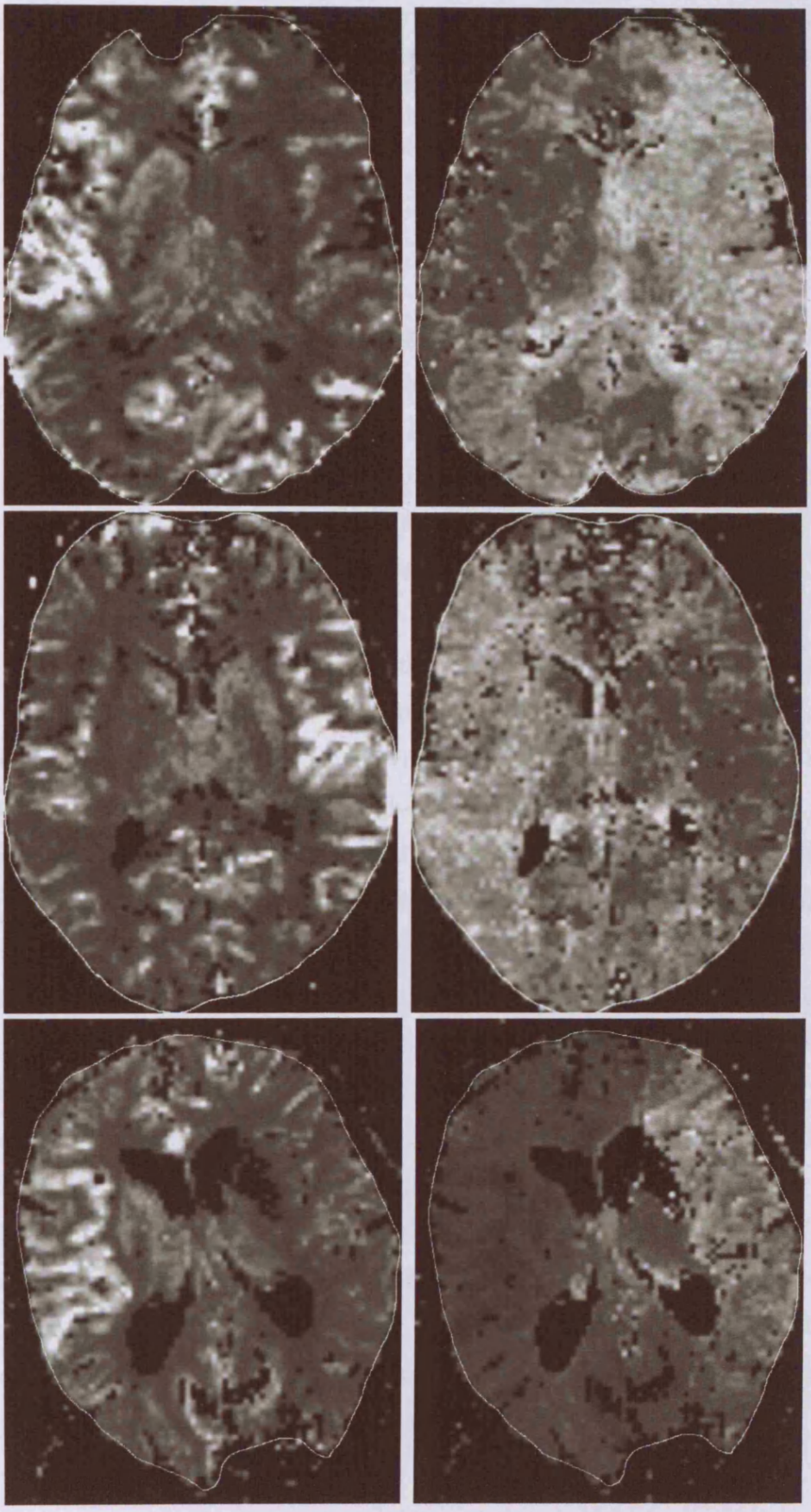

17

18

19

Figure 9.4: *CBF* (left column) and *MTT* (right column) maps calculated (using oML-EM-wavelet) for the six patients in Table 9.2 using a global AIF measured in a branch of the MCA in the healthy hemisphere. There appear to be significant areas of perfusion abnormality (identified by low *CBF* (dark areas of left column) and prolonged *MTT* (bright areas of right column)). The images are displayed in radiological convention: the left side of the image is the right side of the brain.

analysed patients, the *CBF* and *MTT* maps in Figure 9.9 illustrate both a reduction in the severity and extent of the perfusion abnormalities compared with the *CBF* and *MTT* maps in Figure 9.4. In addition, the regions of t_{delay} and/or *DI* are smaller in Figure 9.10 compared with the t_{delay} and *DI* maps in Figure 9.5. This suggests that the original perfusion deficits are partly an artefact of an inappropriate AIF for that region, and that the regional AIF is more appropriate.

Table 9.4 summarises the findings of the regional AIF and global AIF analyses for the six patients. The values in the table were obtained by averaging the values of voxels within a user-defined ROI drawn in the GM inside the mask where delay and dispersion were identified using the global AIF analysis. For comparative purposes, regions were also defined in GM in the normal hemisphere. In combination with Figure 9.10, columns 3 and 4 of Table 9.4 indicate that the residual t_{delay} and *DI* values are small for all patients with the exception of the *DI* in a small area in the posterior region of the left hemisphere of Patient 12. The small residual t_{delay}, and *DI* values indicate that in general, the regional AIF method is effective in minimising delay and dispersion in the data. For the left posterior region of Patient 12, there remains a significant dispersion. However, in this patient, there has been a significant reduction in the size of the delay/dispersed region. This area was not analysed further, since the regional AIF methodology is unlikely to be successful. With fewer voxels there is a decreased likelihood that a true arterial component will exist. In particular, for the small regions in the deep white-mater (particularly in the border zone between two major arterial territories) where residual delay and/or dispersion are probable, and the arteries are too small for the spatial resolution of MRI.

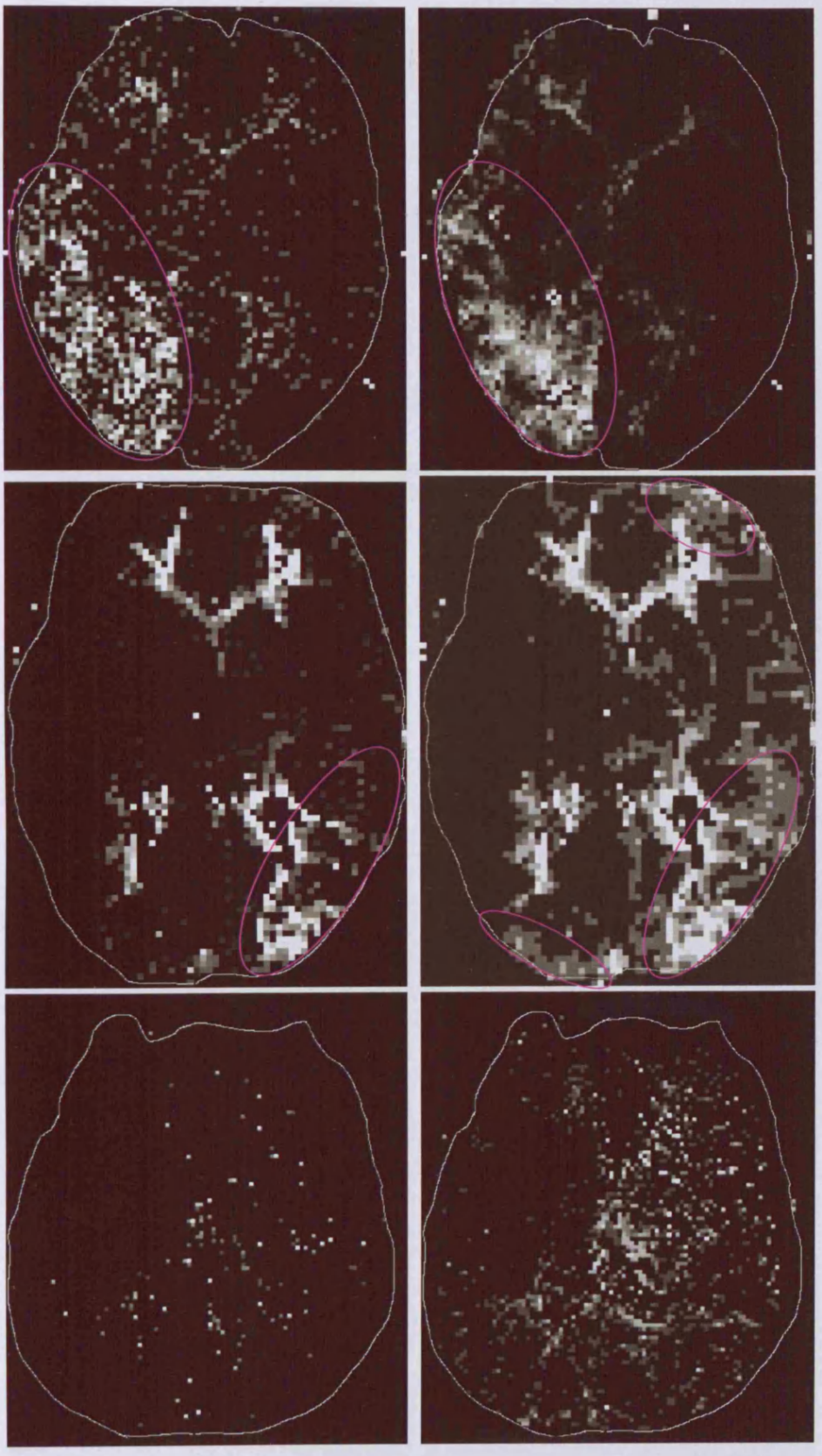
11
12
16

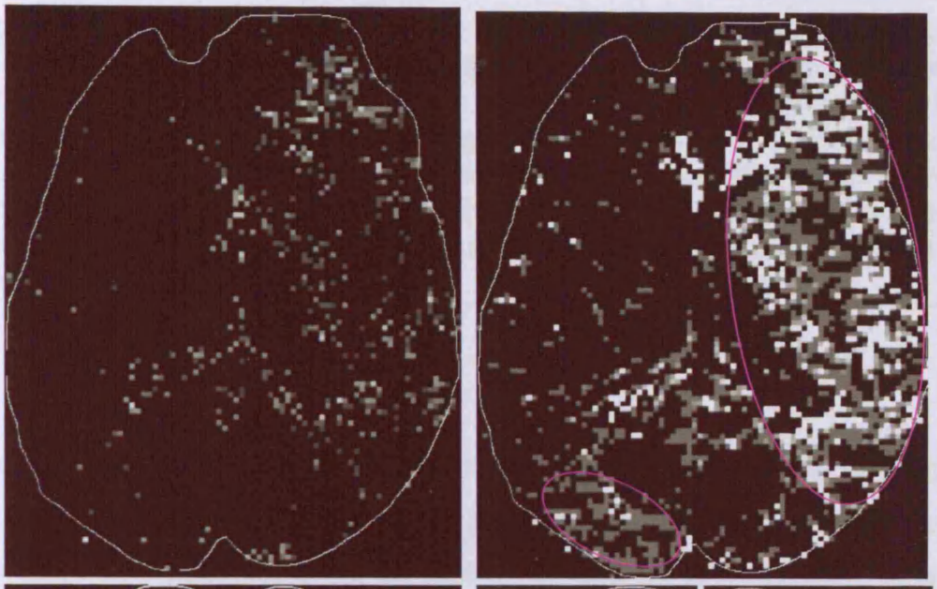

17

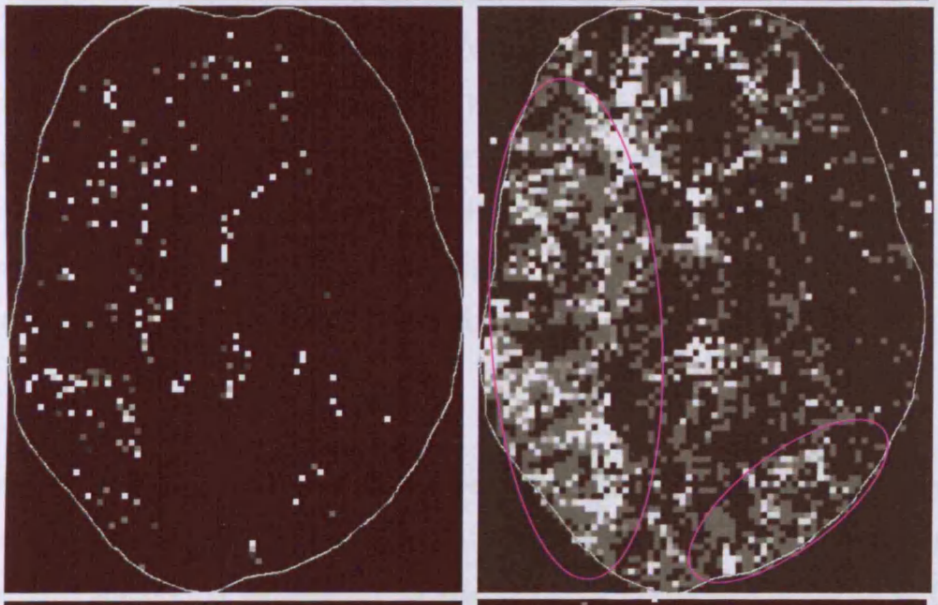

18

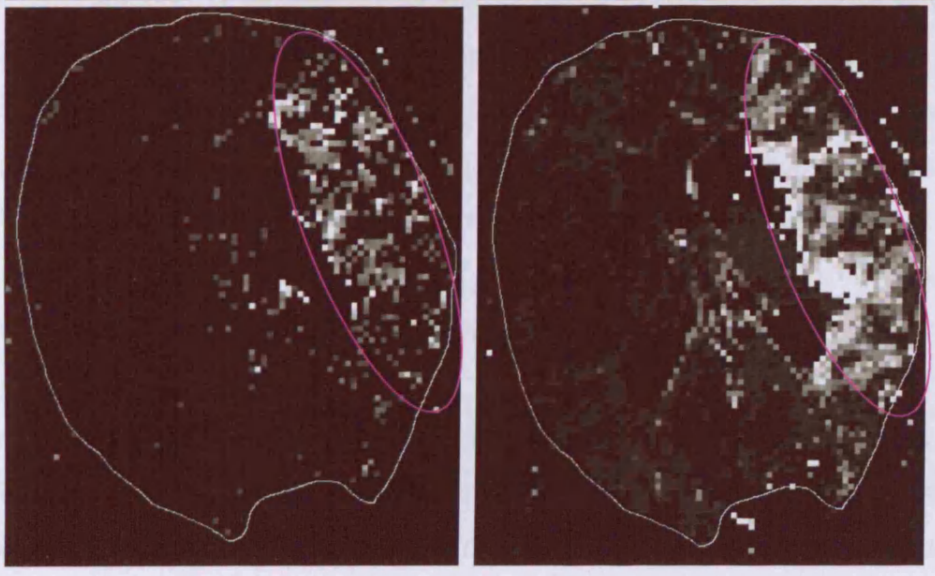

19

Figure 9.5: *DI* (left column) and t_{delay} (right column) maps calculated (using oML-EM-wavelet) for the six patients in Table 9.2 using a global AIF measured in a branch of the MCA in the healthy hemisphere. With the exception of patient 16 where there is no distinct region of delay and/or dispersion, the regions of delay and/or dispersion correspond to the abnormal areas shown in the *CBF* and *MTT* maps in Figure 9.4. The pink ovals highlight the regions where the regional AIF analysis was performed. The images are displayed in radiological convention: the left side of the image is the right side of the brain.

The effectiveness of the regional AIF method in minimising delay and dispersion in the data is further demonstrated by the percentage difference between the t_{delay} and *DI* parameter measurements using the global AIF and the regional AIF. A negative % indicates a decrease in value using the regional AIF. For all patients t_{delay} and *DI* are smaller in the regional AIF analysis. (In patient 18, the posterior region of the left hemisphere reported zero *DI* in both the global and regional AIF analyses, explaining the 0% change in *DI*). In addition to minimising the magnitude of these parameters, a comparison of Figure 9.10 with Figure 9.5 indicates that the extent of the delayed/dispersed regions are also reduced in size or removed completely.

The size of the percentage reduction of the t_{delay} and *DI* parameter measurements using the global AIF and the regional AIF is different for different regions and in different patients. This variance is also reflected in the size of the % difference in *CBF* between the global AIF and regional AIF analyses in the same region. Column 7 of Table 9.4 reports that for all regions in all the patients, there is a significant increase in the *CBF* estimates made with the regional AIF method compared with the global AIF analysis. The size of the percentage increase however, does not appear to be directly correlated with the size of the percentage decrease in the t_{delay} and *DI* parameter measurements (see Discussion).

It is informative to compare the *CBF* estimates in delayed/dispersed regions using the global and regional AIFs with those made in a ROI of normal GM in the normal hemisphere (where there is no delay or dispersion). This comparison gives an

	Number of delay/dispersed regions	Number of iterations required for each region
Patient 11	1 RHS	1
Patient 12	3: 2 LHS, 1 RHS	1 for each
Patient 16	N/A	N/A
Patient 17	2: 1 LHS, 1 RHS	1 for each
Patient 18	2: 1 LHS, 1 RHS	2 for LHS, 1 for RHS
Patient 19	1 LHS	3

Table 9.3: Summary of the number of regional AIFs calculated for each patient and the number of iterations required to minimise the delay and dispersion parameters using the regional AIF analysis.

indication of the severity of the perfusion abnormality in the abnormal regions determined using each method. The apparent perfusion abnormality in all the regions is smaller when using the regional AIF compared with the global AIF (columns 8 and 9 of Table 9.4). Within some regions (e.g. in Patients 12 and 17), the *CBF* measurements using the regional AIFs are still significantly lower than those in the normal region, even though delay and dispersion (that can cause *CBF* underestimation) have been significantly reduced. Within other regions (e.g. in Patients 11, 18 and 19) the minimisation of delay and dispersion by means of the regional AIF has resulted in regional *CBF* measurements that are comparable to the normal region.

As an illustration of the oML-EM-wavelet characterisation of the impulse response functions $\tilde{r} = \left(CBF \cdot R_{eff}(t)\right)_{est}$, examples of those extracted using the global and regional AIF analyses are shown in Figure 9.11 for Patient 12. The three regions of delay /dispersion from which the $\tilde{r}$ are taken are indicated in the figure. Although

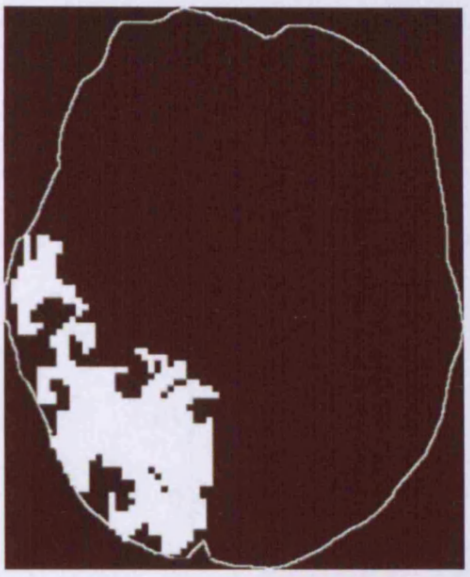

Figure 9.6: Manually drawn mask for the delay and dispersed region of Patient 11.

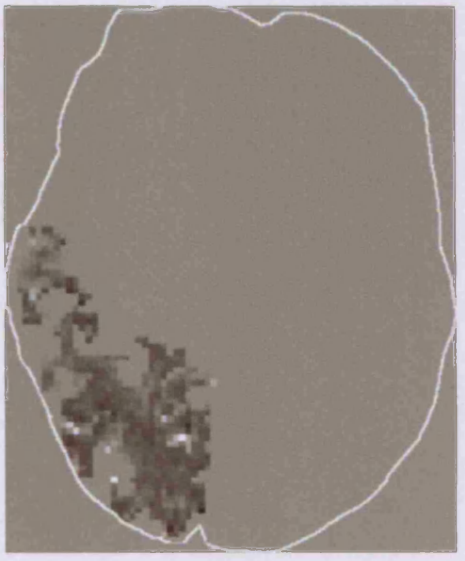

Figure 9.7: Intensity and spatial distribution of the arterial ICA component used for the regional AIF in Patient 11.

for all three voxels chosen, the delay and dispersion have been completely eliminated using the regional AIF method, the maximum value of $\tilde{r}$, (used to indicate blood flow) is still low in the right hemisphere compared with the left. The simulations performed in Chapter 7 demonstrated that the oML-EM-wavelet method accurately quantifies *CBF* when there is no delay or dispersion. Therefore, the *CBF* and *MTT* measured in voxels where there is no residue delay or dispersion should be a good estimate of the true perfusion values.

9.3.3 DISCUSSION

Decisions on therapeutic intervention are commonly based on a standard global AIF analysis of DSC-MRI data e.g.(Hjort *et al.* 2005; Ostrem *et al.* 2004). However, since such therapeutic intervention is not without risk, it is important to realise the potential

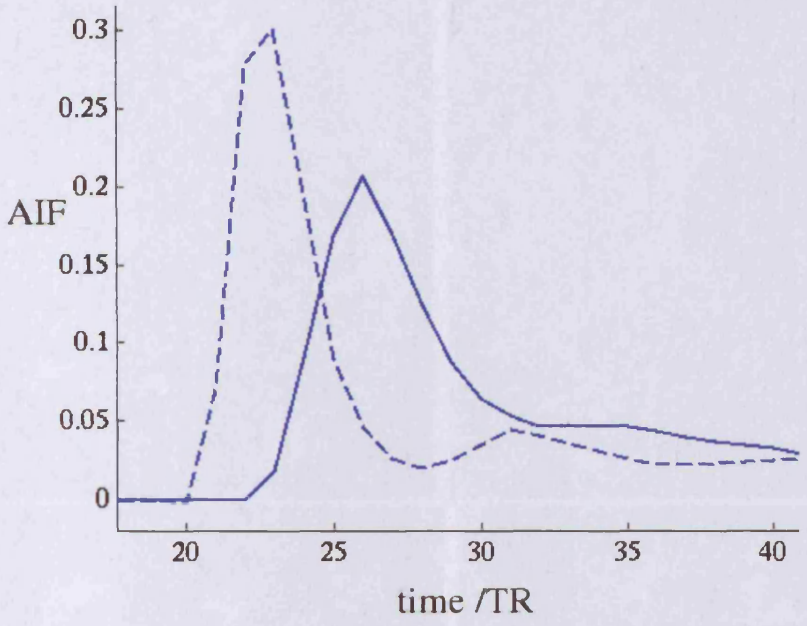

Figure 9.8: The global AIF (dashed line) and regional AIF (solid line) for Patient 11. The regional AIF is the arterial ICA component whose spatial distribution is illustrated in Figure 9.7. It can be seen that the region AIF is both delayed and dispersed with respect to the global AIF. This is consistent with the *DI* and t_{delay} maps for Patient 11 shown in Figure 9.5.

bias in these perfusion estimates. In the presence of arterial abnormalities, a standard global AIF analysis can lead to an underestimation of perfusion levels, possibly leading to unnecessary and dangerous treatment (e.g. increase risk or cerebral haemorrhage). This study has demonstrated a *regional* AIF methodology that identifies and minimises the biasing effects of vascular transport on the estimation of perfusion parameters. Such methodology can be used to minimise the risk of misdiagnosis.

Using the global AIF analysis, all six patients would have been diagnosed as having severe perfusion deficits. The *CBF* values in these regions were found to be between 15% and 40% of those found in the normal side. Such low blood flow is indicative of ischaemic tissue that will progress to infarction if flow is not restored (e.g. by

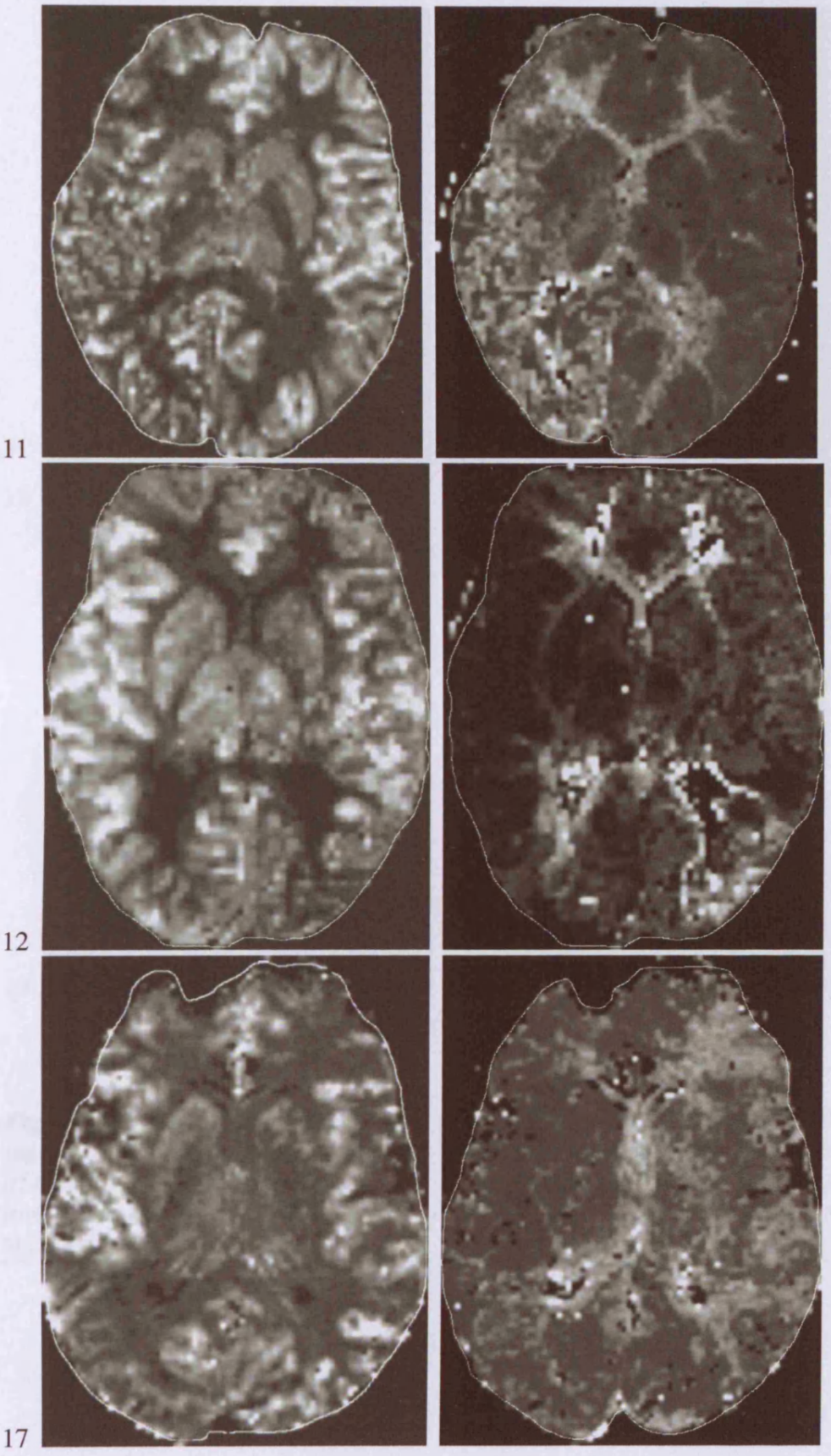
11
12
17

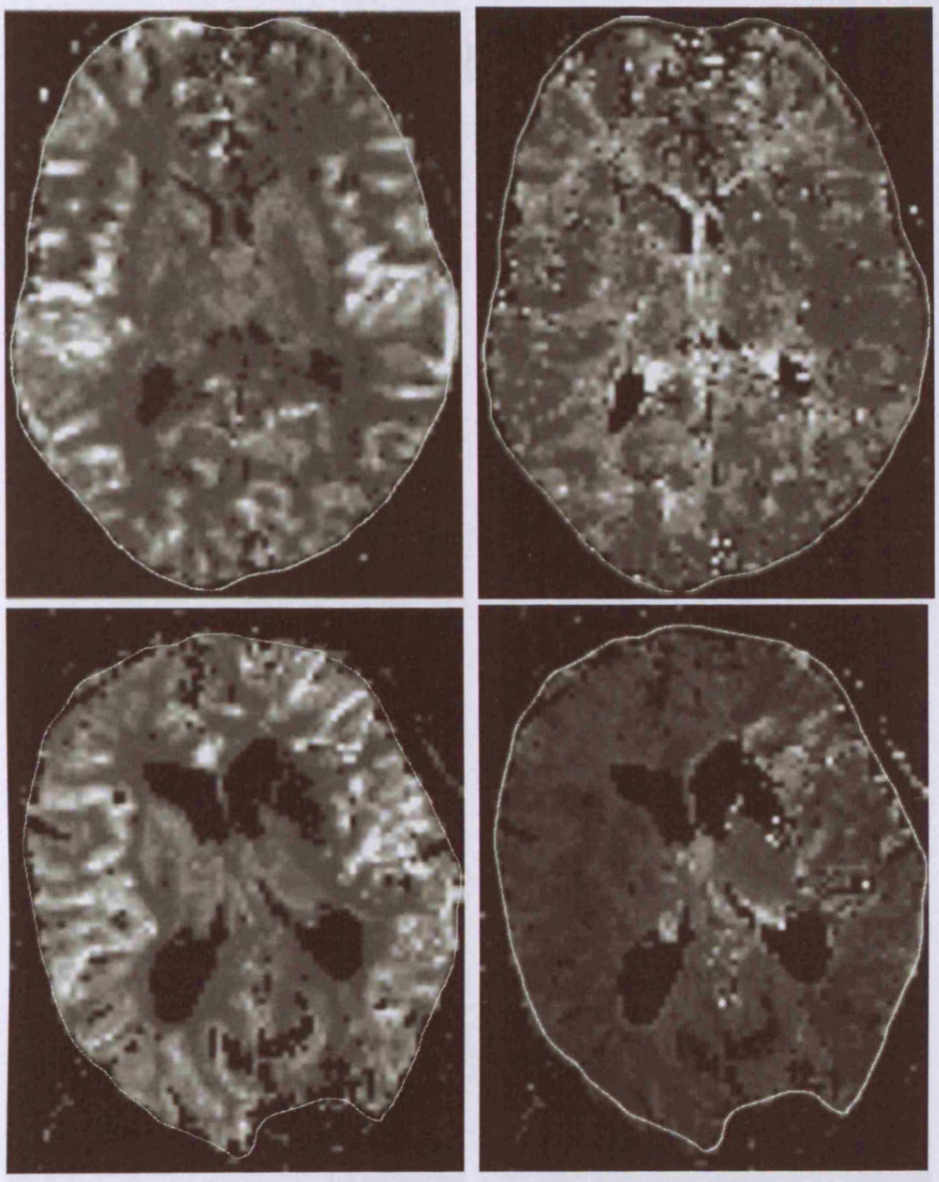

Figure 9.9: *CBF* (left column) and *MTT* (right column) maps calculated using regional AIFs. In comparison with the global-AIF maps in Figure 9.4, many regions of abnormality (identified by low *CBF* and prolonged *MTT*) have been reduced. The images are displayed in radiological convention: the left side of the image is the right side of the brain.

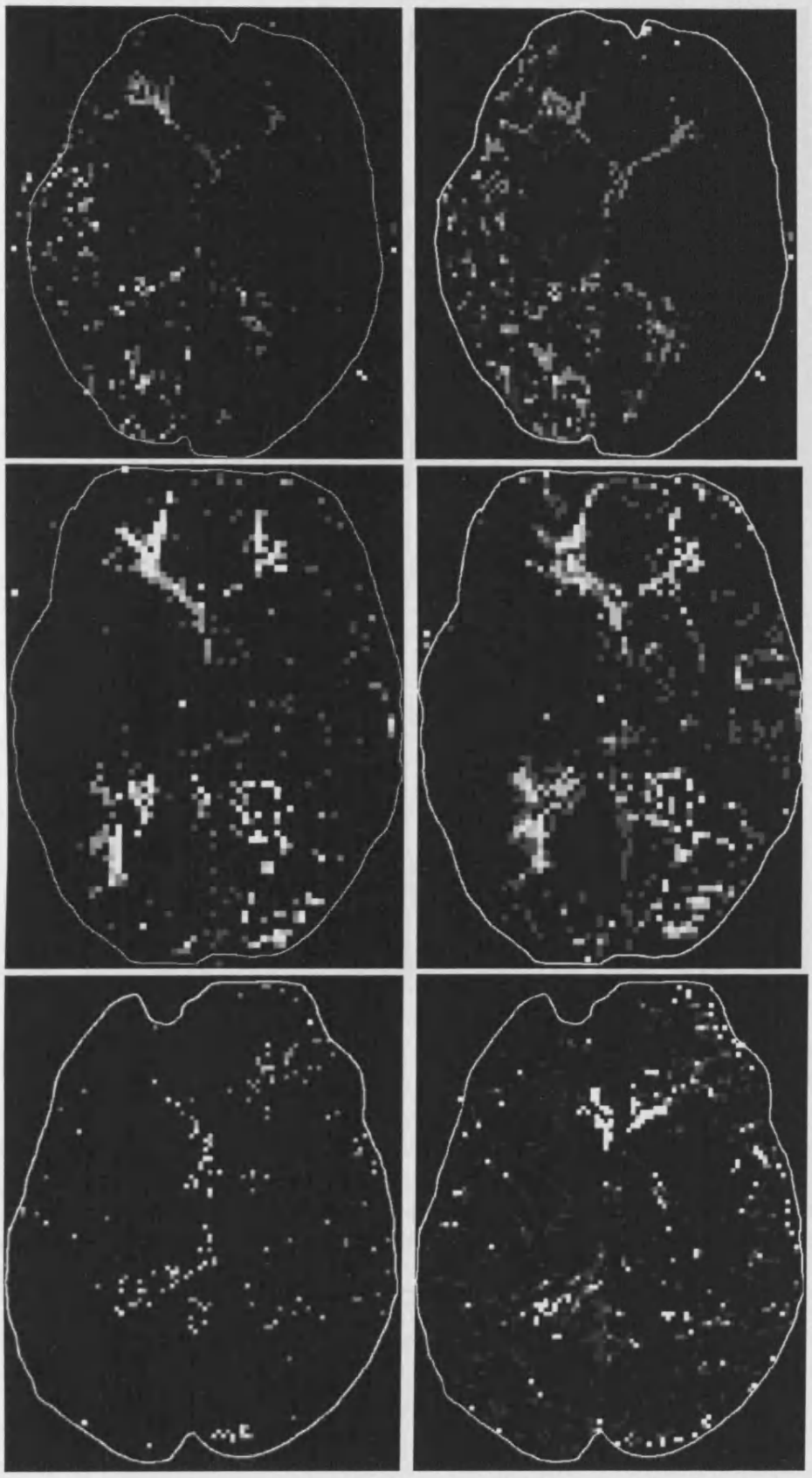
11
12
17

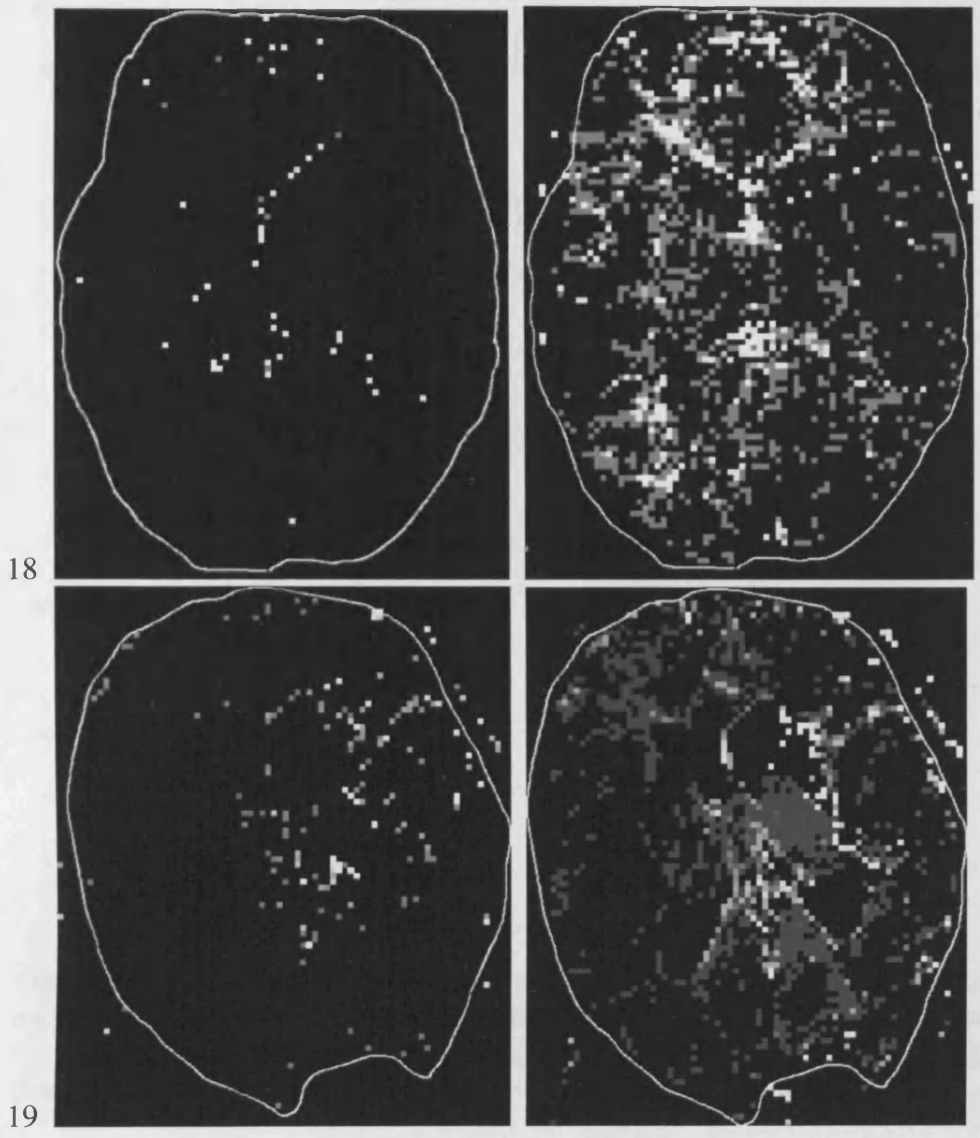

Figure 9.10: *DI* (left column) and t_{delay} (right column) maps calculated using regional AIFs. In comparison with the global-AIF maps in Figure 9.5, delay and dispersion in the grey mater regions has been reduced or removed completely. The images are displayed in radiological convention: the left side of the image is the right side of the brain.

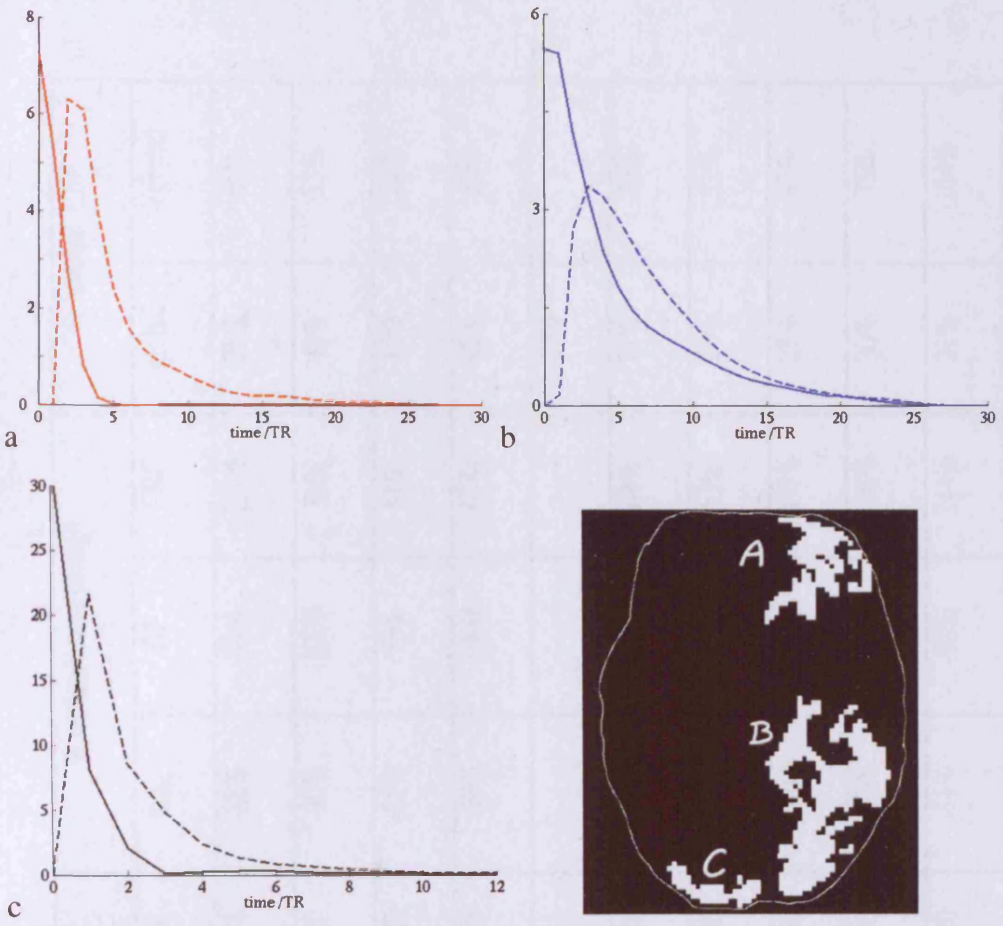

Figure 9.11: Example impulse response functions deconvolved in Patient 12 using the global (dashed lines) and regional (solid lines) AIFs, corresponding to the delayed/dispersed regions A, B and C indicated in the bottom right figure. For the voxels chosen, delay and dispersion have been eliminated.

thrombolysis). However, a diagnosis based on these global AIF measurements would be unreliable, since reanalysis using the new regional AIF method found that in five of the nine regions *CBF* values were greater than 66% of those found in the corresponding normal side. This level of perfusion is likely to correspond to the clinical state of oligemia (see Chapter 3, Section 3.3). In this state, autoregulatory mechanisms (i.e. vasodilation and increased oxygen extraction fraction) are at work to preserve cerebral oxygen metabolism at levels sufficient for neuron functionality. Such oligemic tissue is not at risk of infarction.

		residual		% measurement change			% 'normal' *CBF*	
	delayed/dispersed region	t_{delay}	*DI*	t_{delay}	*DI*	*CBF*	global	regional
Patient 11	R	0.09	0.78	-88%	-91%	131%	29%	66%
Patient 12	L anterior	0.05	0.00	-90%	-100%	36%	40%	53%
	L posterior	0.45	5.29	-56%	-73%	61%	15%	24%
	R posterior	0.00	0.00	-99%	-100%	67%	40%	67%
Patient 16	L	0.21	0.11				23%	
Patient 17	L	0.15	0.26	-75%	-82%	64%	21%	35%
	R posterior	0.02	0.00	-80%	-100%	63%	26%	42%
Patient 18	R	0.00	0.00	-100%	-100%	237%	28%	95%
	L posterior	0.01	0.00	-93%	N/A	198%	30%	75%
Patient 19	L	0.32	0.20	-81%	-98%	344%	21%	104%

Table 9.4: The table summarises the results of the regional AIF and global AIF analyses for the six patients. The first two columns indicate the patient and identify the delay/dispersed regions (these regions are circled in Figure 9.5) R=right hemisphere, L=left hemisphere. The measurements given in this table were taken by averaging the values within a user-defined GM region of interest. The columns under the heading 'residual' indicate the remaining delay and dispersion after the regional AIF analysis (except for patient 16, where the values indicate the left hemisphere GM measurements). The columns under the heading '% measurement change' show the percentage difference between the parameter measurements of t_{delay}, *DI*, and *CBF* using the global AIF and the regional AIF. A positive % indicates an increase, whereas a negative % indicates a decrease in value using the regional AIF compared with the global AIF. The columns under the heading '% normal *CBF*' compare the measurements of *CBF* in the 'normal' region of GM with no delay or dispersion, with the *CBF* measurements taken in the abnormal GM regions using the global and regional AIF deconvolution.

The global AIF apparent perfusion deficits (column eight Table 9.4) in the regions defined in Patient 11, the right hemisphere of Patient 12, Patient 18 and Patient 19, were significantly corrected using the regional AIF analysis (column nine Table 9.4). In these patients small perfusion abnormality remains in Patient 11, the right hemisphere of Patient 12, and the left hemisphere of Patient 18. However, these perfusion levels are likely to be sufficient to maintain tissue viability. In the right hemisphere of Patient 18 and in Patient 19, the perfusion estimates are no longer abnormal. For the reanalysed regions in Patient 17 and the left hemisphere of Patient 12, the perfusion abnormalities remain, although are less severe using the regional AIF analysis. Therefore, reanalysis of the DSC-MRI data using the regional AIF methodology would probably not change the diagnosis and treatment plans for Patient 17 and the left hemisphere of Patient 12. However, for Patient 11, the right hemisphere of Patient 12, Patient 18 and Patient 19, the regional AIF analysis would suggest a different diagnosis and treatment plan.

This study highlights the fact that apparently abnormal perfusion values may be partly or fully a consequence of vascular transport. Improving the estimate of the AIF can minimise or completely remove the apparent perfusion abnormality. It is important to realise that the perfusion map created using a global AIF deconvolution analysis in a

patient with arterial abnormalities is likely to be unreliable because of the vascular transport of the bolus. Therefore, it is essential that diagnosis and treatment are not determined on the basis of the global AIF deconvolution analysis alone. These perfusion maps must be interpreted in conjunction with maps indicating the presence and severity of delay and dispersion. In this way, the reliability and potential underestimation of the perfusion estimates can be considered. However, if the data are reanalysed using the regional AIFs, and if delay and dispersion are removed from the vascular transport, then the resulting perfusion maps are reliable and an accurate diagnosis can be made. The perfusion maps in Figure 9.9 therefore provide more reliable information about the tissue perfusion.

Recently there have been a number of clinical trials that utilise a global-AIF defined diffusion-perfusion mismatch region (see Section 3.10) to select patients for thrombolysis, and to assess the response to this treatment e.g. (Hacke *et al.* 2005; Butcher *et al.* 2005). The trial reported by Butcher *et al.* found that the benefits of reperfusion could not be related to the mismatch volume. This implies that some of the identified mismatch region was actually oligemic. The regional AIF analysis of the patient data in this chapter suggests that a global AIF analysis is likely to underestimate the true perfusion values, and has shown that such methodology could in fact misidentify oligemic tissue as ischaemic. Therefore, the hypothese of clinical trials that use a global-AIF defined diffusion-perfusion mismatch cannot be accurately investigated.

It should be noted that for the TR of the *in vivo* data analysed in this study, the measure of delay t_{delay}, may be a more sensitive measure of abnormal vascular transport than the dispersion index *DI*. As discussed in Section 9.3.1.1, the t_{delay} parameter could actually also indicate a small dispersion. This is probably the case in the left hemisphere region of Patient 18, where the *DI* was zero using the global and regional AIF analysis, and the regional AIF minimisation of the t_{delay} parameter significantly increased the *CBF* values. Similarly, the lack of correlation between the size of the *% DI* reduction and the *% CBF* increase could also be because the t_{delay} parameter accounts for some of the dispersion.

The patient data used in this study were taken from three different scanners with different scanning sequences; consequently the quality of the data is varied. The robustness of the oML-EM-wavelet method is demonstrated in this chapter, since in spite of this variability, the method was effective in characterising the impulse response function and estimating the delay and dispersion parameters.

The proposed regional AIF methodology is specifically targeted to regions where the bolus is identified as being distorted in transit through the arterial tree. Since distorted vascular transport has been shown to introduce significant errors in perfusion quantification, it is in these regions where an improved estimate of the arterial input to the tissue is most important. Other regional AIF methods have also been proposed e.g. (Knutsson *et al.* 2006) (Christensen *et al.* 2004). However, these methods do not selectively target areas of known perfusion measurement errors, and may actually fail in such regions. In work by Knutsson *et al.*, regional AIFs are defined for the whole brain using factor analysis of dynamic studies (FADS) on the concentration time-courses. A subsequent automatic AIF identification algorithm selects the AIF voxels, which are used to form the regional AIF within the FADS-defined regions. In addition to complications arising from peak saturation, geometric distortion and partial volume effects of the concentration time-course (see Section 4.7), the automated AIF identification algorithm in (Knutsson *et al.* 2006) is likely to fail under certain circumstances, such as severe arterial delay or dispersion. It is in these situations where an improved estimate of the AIF is most vital. Christensen *et al.*, proposed a regional AIF method that manually selects AIF voxels within presupposed major arterial territories. Although the different timing of the vascular-territory-specific AIFs can provide information about major vessel abnormalities, these AIFs cannot account for intra-region delay and dispersion, i.e. if there is an abnormality further down the arterial tree.

The main limitation of the ICA-defined regional AIF technique is the necessity for user input. For example, the masking of the delay/dispersed regions, the selection of the arterial (ICA) component, and checking for negative dispersion. Automated methods are necessary for the efficient and robust implementation of analysis in a

clinical environment. To achieve this aim further work is required. For example, a clustering and thresholding algorithm could be developed to delineate the delay/dispersed regions, and spatial-localisation/temporal-shape criteria could be proposed for the automated selection of the ICA arterial component. Although there is no 'gold-standard' with which to validate this ICA-defined regional AIF methodology, the residual t_{delay} and *DI* parameters signify the reliability of the final perfusion maps.

9.4 GENERAL DISCUSSION

It has been shown that the presence of bolus delay and dispersion can introduce large errors in *CBF* (i.e. underestimation) and *MTT* (i.e. overestimation) (Calamante *et al.* 2000). This potential source of bias can have very important implications for patient diagnosis and decisions concerning therapeutic intervention. In particular, inaccurate estimates of perfusion will bias the predictions of tissue outcome made by predictor-models. Since therapeutic intervention risks reperfusion injury, there is a need to improve therapeutic decision making. In this chapter, two methods have been explored to correct for the perfusion errors.

Various methods have been proposed to correct for delay-related perfusion measurement errors. For example, the tissue concentration time-course and the AIF can be realigned to a common origin (i.e. a common bolus arrival time) before the deconvolution analysis is performed (Calamante *et al.* 2000; Ibaraki *et al.* 2005; Rose *et al.* 2004). Alternatively, a delay-insensitive deconvolution algorithm can be used (Wu *et al.* 2003; Smith *et al.* 2000). Furthermore, the use of these methods in predictor-models in stroke has been emphasised (Rose *et al.* 2004; Ibaraki *et al.* 2005; Wu *et al.* 2004)

The effect of bolus dispersion is more difficult to deal with; to account for dispersion requires a model for the vascular bed (see Chapter 8), or the use of a more locally

defined AIF (Calamante *et al.* 2004; Alsop *et al.* 2002; Knutsson *et al.* 2006; Christensen *et al.* 2004; Lorenz *et al.* 2006). Neither approach is commonly used, although both are being actively investigated. Because dispersion errors are difficult to assess, they are not usually taken into account when using diffusion and perfusion MRI data to predict the fate of brain tissue in acute stroke, and to identify the patients at highest risk of infarction.

For this reason, the first part of this chapter (Section 9.2) sought to find a simple and quick correction of dispersion. The simplicity and speed of the investigated method would have been beneficial for widespread routine clinical application, enabling analysis by a non-expert and prompt administration of treatment. However, the *in vivo* investigation into delay and dispersion concluded that the delay could not be used to predict and correct for dispersion due to the lack of correlation and the spread between the parameter values.

Consequently, the second part of the chapter (Section 9.3) sought an alternative methodology to correct for dispersion by improving the estimated arterial input to the tissue. This regional-AIF methodology is targeted to regions known to have perfusion measurement errors. Within these regions, delay and dispersion are minimised, resulting in more accurate perfusion estimates. The comparisons between the global and regional AIF perfusion estimates emphasise the implications of using an inappropriate AIF for the deconvolution of DSC-MRI data. The regions identified using the global AIF deconvolution as having dangerously low perfusion, were found to have higher perfusion using the regional AIF analysis. In some patients the reanalysed perfusion levels would likely result in alternative diagnoses.

It is important to realise that the *a priori* it is impossible to know which patients will have significant delay and dispersion-related errors. Low perfusion values calculated using a global AIF analysis may be real in some patients, partly real in other patients and wholly artefact in other patients. The distinction can only be made by further analysis of the impulse response function, i.e. by extracting parameters such as t_{delay} and *DI*.

9.5 CONCLUSION

In conclusion, if the effects of delay and dispersion are not taken into account (e.g. by using an appropriate regional AIF), it is not possible to predict the extent of the error that will be present in the *CBF* maps reliably. These errors can lead to tissue misclassification, and finally to the inappropriate selection of patients for treatment, such as arterial thrombolysis. The findings from this chapter have very important implications for assessment and management of patients with acute stroke, as well as for the accuracy of the predictor-models currently being used for determining the tissue outcome in stroke.

10 GENERAL DISCUSSION

10.1 OVERVIEW OF WORK

In recent years significant developments have been made in both the treatment of acute ischaemic stroke and in neuroimaging methods. These advances have focussed on improving the simplicity, robustness, and accuracy of the diagnosis and management of patients with stroke. Of all the neuroimaging techniques, MRI has emerged as a powerful way to assess brain pathophysiology non-invasively, and within the last decade or so it has gained widespread clinical acceptance. Within this context, perfusion MRI has been shown to play a central role in identifying at an early stage regions of brain tissue that are compromised but likely to recover given the appropriate treatment. The only perfusion MRI technique that can currently be used easily in the clinical setting of acute stroke is DSC-MRI or bolus tracking. However, current methodology for perfusion assessment using DSC-MRI is prone to errors, which could lead to patient misdiagnosis with potentially dangerous clinical consequences.

This thesis presented a detailed investigation of several limitations in the analysis and interpretation of perfusion DSC-MRI data that currently hinder the accurate diagnosis of patients with ischaemic stroke and cerebrovascular disease. A first important step towards good patient management is to be able to identify regions on the DSC-MRI perfusion maps where the measurements are inaccurate, i.e. those regions where there is delay and dispersion of the bolus. Perfusion in these regions is likely to be underestimated, and so treatment plans based on these erroneous measurements would be inappropriate and potentially dangerous. Identification of these regions can only be achieved with an accurate analysis method. This is the motivation behind the methods presented in Chapters 6 and 7, which minimise the regularisation and discretisation errors manifest in the deconvolution of the noisy sample DSC-MRI data.

In order to determine the accuracy, robustness, and limitations of new analysis methods, they must be thoroughly tested using methodology as described in Chapter

5. It is important that the testing is comprehensive and a realistic representation of *in vivo* situations. Therefore in application to stroke, it is essential to know the degree and extent of delay and dispersion, and also the size of the related perfusion measurement errors *in vivo*. The *in vivo* investigation conducted in Chapter 8 provided some insight into this by characterising the vascular transport in a group of patients with cerebral arterial abnormalities.

In addition to identifying delay and dispersion, the analysis techniques presented in Chapters 6 and 7 aim to give an accurate quantification of perfusion in the absence of delay and dispersion (i.e. when the estimated input to the tissue accurately represents the true input). Thus, if delay and dispersion of the bolus could be removed from the data, accurate perfusion estimates should be obtained. The use of these accurate perfusion values in predictor-models would increase the model's specificity and sensitivity to 'at-risk' tissue. Therefore, obtaining unbiased perfusion measurements is an important proceeding step towards the goal of improved patient diagnosis and management. Methodology for the correction of errors introduced by vascular transport was developed in Chapter 9.

Improvements in perfusion imaging are expected to benefit a large number of patients presenting with stroke. Clinical DSC-MRI data are commonly used in the prediction of tissue outcome. Therefore, if implemented in a clinical context, the methodological developments in this thesis could be influential in improving the diagnosis and management of patients with stroke. The use of these developments would be a significant step towards reducing morbidity and disability. Improved patient outcome would ultimately contribute to lessening the socio-economic impact of cerebrovascular diseases.

10.2 ABSOLUTE PERFUSION

Although the methodologies presented in Chapters 6, 7 8, and 9 make considerable progress towards improving the robustness, accuracy and interpretation of DSC-MRI perfusion measurements, the measurements are still not quantitatively accurate, and therefore cannot be used to define perfusion thresholds for ischaemia. Even if a high accuracy is obtained in the data acquisition (i.e. good SNR, high temporal and spatial resolution, accurate AIF selection) and processing (i.e. accurate deconvolution), there are still some fundamental model assumptions which prevent absolute perfusion measurements from being obtained (see Chapter 4, Section 4.7). These include the simplification of the relationship between transverse relaxation rate and tracer concentration, which takes different forms in the tissue and artery. As a consequence there are significant systematic errors in the perfusion measurements and characterisation of the impulse response function (Kiselev 2001). The magnitude of the errors depends on microvascular architecture, properties of the contrast agents, and contribution of the intra and extravascular compartments to the total signal (Kiselev 2001). Using DSC-MRI, the goal of absolute perfusion values can only be obtained with additional information regarding the blood and microvascular compositions. Such information could potentially be obtained through monitoring blood samples and blood pressure, and by acquiring data using a variety of pulse sequences together with fitting a multiparametric model of signal relaxation (Kiselev 2005). Absolute DSC-MRI perfusion values would be invaluable for defining thresholds of irreversible brain damage. In combination with other MR imaging modalities they would greatly assist in understanding the underlying pathophysiology of ischaemic stroke.

10.3 PREDICTING FUTURE INFARCTION

10.3.1 PERFUSION-DIFFUSION MISMATCH

Achieving absolute DSC-MRI perfusion values is very challenging. However, through optimising the current acquisition and analysis methods, robust *relative* measurements of perfusion can be achieved. Such measurements are valuable for example, to compare perfusion values in the normal and abnormal hemispheres in patients with unilateral arterial abnormalities (see Chapter 9). Furthermore, their utility in combination with other MR imaging modalities such a DWI has been demonstrated (Sobesky *et al.* 2005; Gonzalez 2006; Kidwell *et al.* 2004). In particular, mismatch between a larger perfusion abnormality and a smaller diffusion lesion has been postulated to represent the ischemic penumbra, in which tissue is at risk of infarction but also potentially amenable to salvage (Kidwell *et al.* 2003). The identification of such a mismatch region does not necessitate absolute perfusion measures, rather an identification of an area that is abnormal compared with the rest of the brain. However, there is currently no agreement what degree of hypoperfusion is dangerous, i.e. ischaemic rather than oligemic tissue.

Using the mismatch to identify penumbral tissue is further complicated by the lack of a standardised measure of perfusion. Various perfusion parameters have been used, for example time-to-peak (TTP) concentration, first-moment-transit time (FMT) of the impulse response, *MTT*, *CBF* etc (Butcher *et al.* 2005). It has been shown that summary parameters such a TTP are highly dependent on the AIF and may therefore be an inaccurate indicator of the true perfusion (Perthen *et al.* 2002). Similarly, the tissue impulse response function obtained from a global AIF deconvolution is also prone to substantial error (see Chapters 8 and 9). Since these error-prone perfusion parameters are commonly used in defining the mismatch region e.g. (Butcher *et al.* 2005), it is unsurprising that as yet the mismatch region has not been proved a particularly sensitive or specific indicator of ischaemic tissue.

The perfusion-diffusion mismatch has recently been the focus of several clinical trials that aim to select patients for thrombolysis and to predict the response of the tssue to the treatment (Butcher *et al.* 2005; Hacke *et al.* 2005). A more robust definition of the mismatch region could potentially reduce some of the uncertainty currently associated with identifying and treating penumbral tissue. The methodologies described in Chapters 6, 7, and 9 of this thesis were shown to minimise many of the errors in the perfusion measurements related to the deconvolution and vascular transport, and consequently present significant progress toward the goal of an accurate and robust definition of the perfusion-diffusion mismatch.

10.3.2 PREDICTOR-MODELS

The development of multi-parametric algorithms that combine all the available MRI information is currently the forefront of research into predicting infarction in acute human cerebral ischaemia. When applied in a voxel-by-voxel manner, these models have high spatial resolution, therefore enabling a detailed insight into the evolution of the ischaemic lesion, and sensitivity to detecting changes resulting from therapeutic intervention.

One of the most popular predictive methods uses a generalised linear model (GLM) (e.g (Wu *et al.* 2001). In summary, this algorithm models the outcome of the tissue using a binary variable, where the value 1 indicates tissue infarction and the value 0 indicates tissue viability. The probability of tissue infarction is represented by a sigmoid shaped function, which initially increases in an exponential manner, slows to linear growth, and approaches unity with an exponentially decaying gap. The parameter determining the precise curvature of this sigmoid is a function of the acute MRI data (e.g. T_2, ADC, *CBF*, *CBV*, and *MTT*), which are weighted by a vector of coefficients. The coefficients reflect the impact of the data from each modality to the final patient outcome, and are determined using training data sets comprising of acute and follow-up data. These GLM coefficients can then be used to estimate risk of

infarction in a voxel-wise basis from acute data in a new patient. Such predictions would valuably inform a patient-specific treatment plan.

Without increasing the complexity, these models have the potential to include more imaging and non-imaging parameters, such as delay, dispersion (see Chapter 7), time of scan, age of patient, site of arterial abnormality, etc. More information is likely to improve the predictive accuracy of these models (Wu *et al.* 2005).

One limitation of these models is that the GLM coefficients are specific to the training data set, i.e. the MR imaging parameters, the normalisation of the data, the analysis methods etc. For example, in order to investigate if vascular transport is an important covariate of tissue outcome above and beyond the induced perfusion measurement errors, different GLM coefficients should be obtained for when bolus delay and dispersion parameters are combined with corrected perfusion measurements (calculated using a local or regional AIF), and for when they are combined with uncorrected perfusion measurements (calculated using a global AIF). This also highlights the importance of training data set, which should be acquired and analysed identically to the actual input data. Therefore, in order for these models to have widespread clinical impact, it would be necessary to standardise the acquisition and analysis of the imaging data.

In addition to providing a promising metric for the diagnosis of individual patients, another potential use of predictor-models is in the development of new therapeutic drugs. A recent study (Wu *et al.* 2007) used a GLM to predict the tissue infarction in an animal stroke model, and to evaluate the value of therapeutic intervention. Comparing the actual outcome after therapy with the model-predicted outcome without therapy provides a means to determine the efficacy of the treatment, and to investigate effective dose levels and therapeutic time-windows. Such methodology could be used to speed up and improve drug development, with the only limitation being the accuracy of the predictor model.

Currently, the prediction capability of these models remains limited in a significant number of cases, owing to errors in the perfusion quantification. The methodologies described in Chapters 6, 7, and 9 of this thesis were shown to minimise many of the errors in the perfusion measurements, and furthermore provide additional parameters indicating the vascular transport. The incorporation of these input data (perfusion, delay, and dispersion) could potentially improve the prediction of future infarction in patients with various vascular abnormalities, where currently the models have low sensitivity and specificity.

10.4 EXTENDING THE TIME-WINDOW

In most cases of ischaemic stroke, the lesion consists of small regions of complete ischaemia surrounded by a larger area of incomplete ischaemia where collateral flow is able to preserve the tissue for a limited time-window. This ischaemic by not infarcted region is at risk of irreversible damage. If flow is not restored (e.g. by thrombolysis), or if the toxic biochemical cascade is not impeded (e.g. by neuroprotective agents), then the 'at-risk' tissue progresses to irreversible infarction within a few hours (Hossmann 1994). There is therefore thought to be a very short therapeutic time-window for thrombolytic therapy.

Although thrombolytic therapy has not been proven effective beyond 3 hours, there is some evidence that individual patients may respond to reperfusion strategies up to 6 hours after symptom onset (Hacke *et al.* 1999). On the contrary, some patients treated at later times have suffered haemorrhage as a result of thrombolysis (Hacke *et al.* 1999). Consequently, the use of thrombolysis has been the subject of considerable debate. Treatment plans should therefore balance the potential benefits and risks of intervention. The assessment of the patient specific risk requires accurate information concerning tissue perfusion.

The precise time that tissue can survive is determined by the energy demands and residual blood flow, which can either prolong or accelerate the progression to cell death in the penumbral tissue. Given the logistic problem of treating patients within the short time-window, any approach that extends this period will lead to a significant increase in the number of identified patients that are likely to benefit from treatment. The approach taken in this thesis is to improve the accuracy of the perfusion measurements, by minimising dispersion (Chapter 9) and combining with an accurate DSC-MRI analysis technique (Chapters 6 and 7). Knowledge of the underlying tissue perfusion is important information for assessing the risk and time-scale of progression to infarction.

In a recent ASL study that investigated tissue outcome after reperfusion of ischaemic tissue in rats (Bardutzky *et al.* 2007), it was found that after reperfusion, a substantial amount of perfusion-diffusion mismatch tissue was salvaged *independent* of ischaemia duration. The severity of *CBF* reduction during ischaemia appeared to be the main deciding factor for determining tissue fate. This study underlines the importance of achieving accurate DSC-MRI perfusion information in a clinical context, since residual perfusion levels play a crucial role in determining tissue fate. Therefore, the techniques presented in this thesis could be significant for improving patient management.

Interestingly, the same study (Bardutzky *et al.* 2007) also found that early reperfusion salvaged a substantial number of the initially defined core infarct voxels. Therefore, whilst delayed reperfusion may in some cases be beneficial, early reperfusion is still likely to be more effective.

10.5 RECENT TECHNOLOGICAL ADVANCES

The technical developments presented in this thesis focused on improving the accuracy and robustness of the analysis of DSC-MRI data. The implementation of

such techniques on standard clinically acquired DSC-MRI images was shown in Chapter 9 to provide a better understanding of the haemodynamic status of the brain tissue. However, the amount and the accuracy of the information that can be extracted using the proposed analysis techniques is limited by the quality of the DSC-MRI data. Noise, temporal and spatial resolutions, image artefacts, and suboptimal sequence parameters, are all contributing factors to data quality. In particular, as discussed in Chapter 4 (Sections 4.7), the arterial input is particularly sensitive to partial voluming (i.e. limited spatial resolution), peak saturation (i.e. suboptimal sequence parameters for AIF measurement), and voxel misregistration (i.e. EPI image artefacts). Since a globally defined AIF will influence all the perfusion estimates, the accuracy of the AIF measurement is strategic in achieving improved perfusion quantification. Furthermore, the temporal-resolution is a significant limitation in the characterisation of ischaemic tissue in patients with abnormal flow. For example, in Chapter 5, a significant underestimation of the maximum of the impulse response function was illustrated in Figure 5.4, which was purely a consequence of the temporal sampling[15].

Although DSC-MRI acquisition strategies have not been investigated in this thesis, an understanding of the current limitations and recent advances in scanner technology and data acquisition are fundamental to the development of good analysis techniques. Exciting developments in scanner technology such as higher field (3T compared with 1.5T) and parallel imaging (PI), provide the potential to improve perfusion quantification (Newbould *et al.* 2006). PI enables the EPI readouts to be shortened, facilitating higher temporal resolution data, and thereby reducing temporal discretisation artefacts. In addition, using PI there is an increased bandwidth per pixel in the phase-encoding direction, resulting in a reduction in EPI related image artefacts, such as the spatial shift of arterial voxels during the bolus passage. This improvement is particularly relevant for higher field scanners, where these types of image artefacts are more prevalent. Furthermore, partial volume effects can be reduced because of the increase spatial resolution available at higher field and using

[15] The sampling related perfusion measurement errors are in fact minimised if the delay is removed, by for example, using a local or regional AIF.

PI. The minimisation of these artefacts will result in fewer sources of error in calculating the arterial and tissue signals used in the deconvolution analysis.

For high temporal resolution short TR data, there is a danger of introducing T_1 sensitivity. However, this may be circumvented using multiple echoes: T_1 enhancement is identical for all the TEs, and can therefore be removed (see Section 4.7.1). Multiple echoes provide the further advantage of enabling an optimum contrast-to-noise ratio, CNR (i.e. TE ~T_2^*) over the wide range of T_2^* values present in the tissue and arteries during the passage of the contrast. The shorter EPI readout in PI techniques can enable the acquisition of multiple echoes.

At higher field strengths, susceptibility effects are greater, and consequently T_2* is shorter. PI can enable the acquisition of images with the necessarily short TE required for optimum CNR using gradient echo (GE) at high field.

Although not as significant as the T_2* shortening at 3T compared with 1.5T, it has been shown that the Gd-DTPA promotes shorter T_2 at 3T compared with 1.5T (Rohrer *et al.* 2005), i.e. the relaxivity of Gd-DTPA is greater at 3T compared with 1.5T. Similarly, at 3T, the Gd-DTPA promotes a longer T_1 compared with at 1.5T (Rohrer *et al.* 2005). These shorter T_2 times at 3T suggest that the optimum CNR for spin-echo (SE) sequences is achieved using a shorter TE, which has the advantage of minimising undesirable signal loss caused for example by chemical shifts or susceptibility differences. SE imaging also has the inherent advantage of improved microvascular sensitivity (see Section 10.6). At 3T, in addition to short T_2/T_2* values, the higher T_1/T_2 ratios are also advantageous in T_2/T_2*-weighted imaging, since T_1 enhancement is reduced.

In DSC-MRI, SNR is often sacrificed to achieve the desired short TR (there is insufficient time available for signal averaging). However, at higher field, there is intrinsically higher SNR. Although PI usually sacrifices SNR for improved spatial resolution, non-random noise in the form of EPI related susceptibility artefacts is substantially reduced. It should be noted that although in principle PI enables

improved temporal and spatial resolution, reduced image artefacts, and improved brain coverage, simultaneous improvement is difficult, and consequently an optimum trade-off is sought.

As 3T scanners with PI technology are becoming more widespread in clinical centres, optimising the pulse sequence to make the most of these technological advances will facilitate the routine acquisition of higher quality DSC-MRI perfusion data. Consequently, the accuracy of the data analysis (using such methods as proposed in Chapters 6, 7 and 9) will improve. Since perfusion information is particularly influential in the outcome of predictor-models, minimisation of errors in the data acquisition will improve their specificity and sensitivity in identifying areas of future infarction.

10.6 VESSEL-SIZE SENSITIVITY OF GRADIENT-ECHO EPI

In this thesis, the proposed techniques have been applied to clinical data acquired using GE-EPI. This is the most common clinical acquisition because one can achieve greater brain coverage and greater SNR than when using SE-EPI. Because SE-EPI has predominantly T_2-weighted[16], there is a much smaller change in signal intensity in response to the bolus, but there is also the inherent advantage of being weighted towards the microvasculature (Section 4.4). A major concern using GE-EPI is that due to the uniform vessel-size sensitivity, it will lack sensitivity to microvascular transit of the bolus because of contrast arising from larger veins.

In a study comparing GE- and SE-EPI bolus tracking measurements, Simonsen *et al.* (Simonsen *et al.* 2000) found that GE-EPI detected the same (small) difference in *CBF* and *CBV* as SE-EPI. Furthermore, the GE- and SE-EPI *CBF* measurements differed only by a proportionality factor. Although this analysis was performed using the standard SVD algorithm (which itself is subject to error (Section 4.8.4)), in

[16] Because the SE has an EPI acquisition, it also has a small degree of T_2*-weighting.

general it appears that *MTT* values derived by GE-EPI are likely to be as sensitive as ones derived by SE-EPI.

Another, perhaps more important consideration in the current work, is the effect that the uniform vessel-size sensitivity of the GE-EPI sequence has on the shape of the response function $\tilde{r} = \left(CBF \cdot R_{eff}(t)\right)_{est}$, since this function is used to identify delay and dispersion (Chapters 6, 7 and 9) and in characterising the vascular transport function (VTF) (Chapter 8). Although *in vivo* it is not possible to validate the accuracy of the shape of each the extracted $\tilde{r}$ in each voxel, one can compare the shapes of the $\tilde{r}$ extracted in a hemisphere unaffected by bolus delay and dispersion, with those in a hemisphere affected by bolus delay and dispersion, and with those determined in computer simulations. It was found that the GE-EPI response functions extracted in the unaffected hemispheres closely match what one would expect for a single well-mixed compartment (Section 4.6.4).

It has also been reported that there are differences in the ICA decomposition of GE- and SE-EPI concentration time-course data (Calamante *et al.* 2004). The different arterial and tissue contributions are presumably related to the different vessel-size sensitivity of the MR sequences. This could be an important consideration for both defining the VTF, which relies on an ICA-defined local-AIF (Chapter 8) and correcting dispersion-related perfusion measurement errors, using an ICA-defined regional-AIF (Chapter 9).

In the regional-AIF analysis proposed Chapter 9, the shape of $\tilde{r}$ is used to determine the regions of delay and dispersion. It is therefore important that these shapes can be relied upon to identify delay and dispersion. Furthermore, subtle differences between the GE- and SE-EPI concentration time course data may have an effect on the ICA-based selection of a new regional-AIF chosen in the delay/dispersed region. Similarly, in Chapter 8, the shape of $\tilde{r}$ and the accuracy of the ICA-defined local-AIF are significant in defining a shape of the VTF. Inaccuracies associated with the uniform vessel-size sensitivity of GE-EPI may indeed contribute to the large

prediction intervals found for the relationships between vascular delay, dispersion and the lognormal parameters (first half of Chapter 9).

A comparison of GE- and SE-EPI *in vivo* data could potentially allow an investigation into vessel-size sensitivity effects on the shape of $\tilde{r}$. In addition one could investigate the extent to which vessel-size sensitivity affects the selection and shape of the ICA-defined local/regional-AIFs, and the consequent characterisation/correction of vascular transport. However, since the SNR in SE-EPI data is lower, the inaccuracies introduced in the regularised deconvolution of the concentration time-course data may over-power the improved microvascular sensitivity of the data. Therefore, it may not be impossible to discern whether any detected differences are real or an artefact of the regularised-deconvolution. Investigation into these effects is beyond the scope of this thesis, the main objective of which is to provide a methodology of improved perfusion quantification in standard acquisition clinical data.

10.7 FURTHER WORK

In order for the methodology presented in this thesis to impact on the everyday management of patients with stroke, further development is needed. Firstly, it is necessary to remove the need for human interaction. Fully automated methods that generate accurate perfusion maps, and if necessary, maps indicating where the perfusion estimates are less reliable, would allow the analysis to be performed by a non-expert and ensure consistency of results. If possible the regional AIF methodology presented in Chapter 9 should be developed for the automated delineation of delayed/dispersed regions and selection of the arterial components from within these regions. This would complement the already use-independent deconvolution methodology in Chapters 6 and 7. Automation would facilitate the routine incorporation of such methodologies in the assessment of at-risk tissue in stroke patients.

Optimisation of the algorithms would improve computational speed. This would enable the results of the analysis to be available minutes after the acquisition. The automated, convenient, and fast analysis of patient data would impact on the speed of diagnosis, and consequently assist in the appropriate treatment of patients within the projected therapeutic time-window. Exactly how much brain is lost per unit time in acute cerebral ischaemia is unknown. However, estimates suggest that each minute in which a large vessel ischaemic stroke is left untreated, the average patient loses 1.9 million neurons, 13.8 billion synapses and 12km of axonal fibres (Saver 2006). In light of this, computation speed is imperative. Currently, several minutes are required to process one slice of data using the methodology in Chapter 7. By optimising the C++ code, this time could be significantly reduced.

In addition, it is necessary for the techniques to be robust for use on data acquired from any of the MRI manufacturers. Such generalisation was sought in Chapter 7, and demonstrated in the analysis of patient data from various scanners in Chapter 9. Further refining and testing should be performed to ensure the method's robustness in all situations.

Future work is therefore required to refine the techniques proposed in this thesis so that they are completely automated, optimised, and generalised, together with the development of a user-friendly interface. Such time-saving, generalisation, and convenience would greatly enhance the clinical usefulness of the techniques and the resulting perfusion maps, in particular in application to predictor-models.

In addition to simulated data, predictor-models themselves offer a means of validation for novel analysis methods. If a GLM developed using the newly analysed data were found to give more accurate predictions of infarction, the new methodology would be beneficial in terms of patient management. Further work to compare the accuracy of predictions made from acute patient data analysed using the regional AIF (Chapters 7 and 9) with those from a standard analysis, would highlight whether or not the improvements observed by testing with the simulated data set (Chapter 5), actually

correspond to significant improvement in terms of assessing patients likely to benefit from reperfusion treatments.

10.8 CONCLUSION

A significant increase in the availability of MRI scanners has taken place in the last decade, and accordingly MR is increasingly used to image acute ischaemic stroke. In response, there has recently been a great deal of interest in combining multimodal MRI data to predict tissue outcome following stroke. Achieving accurate input data for these models is the focus of active research, and considerable progress is being made. Accordingly, there is a promising future for MRI methods to fulfil their full potential in providing accurate diagnosis and management of stroke patients.

11 REFERENCES

Abragam, A. Principles of Nuclear Magnetism. 1968. Oxford, Clarendon Press.

Adams HP, Jr., Brott TG, Furlan AJ, Gomez CR, Grotta J, Helgason CM, Kwiatkowski T, Lyden PD, Marler JR, Torner J, Feinberg W, Mayberg M, and Thies W (1996) Guidelines for Thrombolytic Therapy for Acute Stroke: a Supplement to the Guidelines for the Management of Patients with Acute Ischemic Stroke. A statement for healthcare professionals from a Special Writing Group of the Stroke Council, American Heart Association *Stroke* 27:1711-1718

Alsop DC and Detre JA (1996) Reduced transit-time sensitivity in noninvasive magnetic resonance imaging of human cerebral blood flow *J.Cereb.Blood Flow Metab* 16:1236-1249

Alsop DC and Detre JA (1998) Multisection cerebral blood flow MR imaging with continuous arterial spin labeling *Radiology* 208:410-416

Alsop DC, Wedmid A, and Schlaug G (2002) Defining a local input function for perfusion quantification with bolus contrast MRI *In: Proceedings of the 10th Annual Meeting of ISMRM, Honolulu, USA* 65

Andersen IK, Szymkowiak A, Rasmussen CE, Hanson LG, Marstrand JR, Larsson HB, and Hansen LK (2002) Perfusion quantification using Gaussian process deconvolution *Magn.Reson.Med.* 48:351-361

Astrup J, Siesjo BK, and Symon L (1981) Thresholds in cerebral ischemia - the ischemic penumbra *Stroke* 12:723-725

Awate SP and Whitaker RT (2005) Nonparametric neighborhood statistics for MRI denoising *Inf.Process Med.Imaging* 19:677-688

Baird AE, Benfield A, Schlaug G, Siewert B, Lovblad KO, Edelman RR, and Warach S (1997) Enlargement of human cerebral ischemic lesion volumes measured by diffusion-weighted magnetic resonance imaging *Ann.Neurol.* 41:581-589

Baird AE and Warach S (1998) Magnetic resonance imaging of acute stroke *J.Cereb.Blood Flow Metab* 18:583-609

Bammer R and Schoenberg SO (2004) Current concepts and advances in clinical parallel magnetic resonance imaging *Top.Magn.Reson.Imaging* 15:129-158

Bao P and Zhang L (2003) Noise reduction for magnetic resonance images via adaptive multiscale products thresholding *IEEE Trans.Med.Imaging* 22:1089-1099

Barbier EL, Silva AC, Kim SG, and Koretsky AP (2001) Perfusion imaging using dynamic arterial spin labeling (DASL) *Magn.Reson.Med.* 45:1021-1029

Bardutzky J, Shen Q, Henninger N, Schwab S, Duong TQ, and Fisher M (2007) Characterizing tissue fate after transient cerebral ischemia of varying duration using quantitative diffusion and perfusion imaging *Stroke* 38:1336-1344

Basser PJ, Mattiello J, and LeBihan D (1994) MR diffusion tensor spectroscopy and imaging *Biophys.J.* 66:259-267

Bassingthwaighte JB (1966) Plasma indicator dispersion in arteries of the human leg *Circ.Res.* 19:332-346

Biagi L, Abbruzzese A, Bianchi MC, Alsop DC, Del Guerra A, and Tosetti M (2007) Age dependence of cerebral perfusion assessed by magnetic resonance continuous arterial spin labeling *J.Magn Reson.Imaging* 25:696-702

Bleaney, B. I. and Bleaney, B. Electricity and Magnetism. 3[1]. 1989. Oxford, England, Oxford University Press.

Bloch F (1948) Nuclear Induction *Physics Review* 70:460-474

Bloembergen N, Purcell EM, and Pound RV (1948) Relaxation effects in nuclear magnetic resonance absorption *Physics Review* 73:679

Boxerman JL, Hamberg LM, Rosen BR, and Weisskoff RM (1995) MR contrast due to intravascular magnetic susceptibility perturbations *Magn.Reson.Med.* 34:555-566

Boxerman JL, Rosen BR, and Weisskoff RM (1997) Signal-to-noise analysis of cerebral blood volume maps from dynamic NMR imaging studies *J.Magn.Reson.Imaging* 7:528-537

Bracewell RN (1986) The Fourier Transform and its applications *McGraw-Hill* 2:

Busza AL, Allen KL, King MD, van Bruggen N, Williams SR, and Gadian DG (1992) Diffusion-weighted imaging studies of cerebral ischemia in gerbils. Potential relevance to energy failure *Stroke* 23:1602-1612

Butcher KS, Parsons M, MacGregor L, Barber PA, Chalk JB, Bladin CF, Levi C, Kimber T, Schultz D, Fink J, Tress B, Donnan GA, and Davis S (2005) Refining the perfusion-diffusion mismatch hypothesis *Stroke* 36:1153-1159

Bydder M and Du J (2006) Noise reduction in multiple-echo data sets using singular value decomposition *Magn.Reson.Imaging* 24:849-856

Calamante F, Gadian DG, and Connelly A (2000) Delay and dispersion effects in dynamic susceptibility contrast MRI: simulations using singular value decomposition *Magn.Reson.Med.* 44:466-473

Calamante F, Gadian DG, and Connelly A (2002) Quantification of perfusion using bolus tracking

magnetic resonance imaging in stroke: assumptions, limitations, and potential implications for clinical use *Stroke* 33:1146-1151

Calamante F, Gadian DG, and Connelly A (2003a) Quantification of bolus-tracking MRI: Improved characterization of the tissue residue function using Tikhonov regularization *Magn.Reson.Med.* 50:1237-1247

Calamante F, Lythgoe MF, Pell GS, Thomas DL, King MD, Busza AL, Sotak CH, Williams SR, Ordidge RJ, and Gadian DG (1999a) Early changes in water diffusion, perfusion, T1, and T2 during focal cerebral ischemia in the rat studied at 8.5 T *Magn.Reson.Med.* 41:479-485

Calamante F, Morup M, and Hansen LK (2004) Defining a local arterial input function for perfusion MRI using independent component analysis *Magn.Reson.Med.* 52:789-797

Calamante F, Thomas DL, Pell GS, Wiersma J, and Turner R (1999b) Measuring cerebral blood flow using magnetic resonance imaging techniques *J.Cereb.Blood Flow Metab* 19:701-735

Calamante F, Willats L, Gadian DG, and Connelly A (2006) Bolus delay and dispersion in perfusion MRI: implications for tissue predictor models in stroke *Magn.Reson.Med.* 55:1180-1185

Calamante F, Yim PJ, and Cebral JR (2003b) Estimation of bolus dispersion effects in perfusion MRI using image-based computational fluid dynamics *Neuroimage.* 19:341-353

Callaghan, P. T. Principles of imaging. Principles of nuclear magnetic resonance imaging. 1991. Oxford, UK, Oxford University Press.
Ref Type: Book Chapter

Carroll TJ, Haughton VM, Rowley HA, and Cordes D (2002) Confounding effect of large vessels on MR perfusion images analyzed with independent component analysis *AJNR Am.J.Neuroradiol.* 23:1007-1012

Carroll TJ, Rowley HA, and Haughton VM (2003) Automatic calculation of the arterial input function for cerebral perfusion imaging with MR imaging *Radiology* 227:593-600

Chen NK and Wyrwicz AM (2004) Removal of EPI Nyquist ghost artifacts with two-dimensional phase correction *Magn.Reson.Med.* 51:1247-1253

Chen Q, Siewert B, Bly BM, Warach S, and Edelman RR (1997) STAR-HASTE: perfusion imaging without magnetic susceptibility artifact *Magn.Reson.Med.* 38:404-408

Christensen S, Wu O, Hjort N, Mouridsen K, Gottrup C, Fiehler J, Rother J, and Østergaard L (2004) Local Arterial Input Functions based on Vascular Territories *In: Proceedings of the 12th Annual Meeting of ISMRM, Tokyo, Japan*363

Conturo TE, Akbudak E, Kotys MS, Chen ML, Chun SJ, Hsu RM, Sweeney CC, and Markham J (2005) Arterial input functions for dynamic susceptibility contrast MRI: requirements and signal options *J.Magn.Reson.Imaging* 22:697-703

Dempster AP, Laird NM, and Rubin DB (1977) Maximum likelihood from incomplete data via the EM algorithm *J R Stat Soc B* 39:1-38

Detre JA and Alsop DC (1999) Perfusion magnetic resonance imaging with continuous arterial spin labeling: methods and clinical applications in the central nervous system *Eur.J.Radiol.* 30:115-124

Detre JA, Leigh JS, Williams DS, and Koretsky AP (1992) Perfusion imaging *Magn.Reson.Med.* 23:37-45

Dohmen C, Bosche B, Graf R, Reithmeier T, Ernestus RI, Brinker G, Sobesky J, and Heiss WD (2007) Identification and clinical impact of impaired cerebrovascular autoregulation in patients with malignant middle cerebral artery infarction *Stroke* 38:56-61

Donoho DI and Johnstone IM (1994) Ideal spatial adaptation via wavelet shrinkage *Biometrika* 81:425-455

Drayer BP, Wolfson SK, Reinmuth OM, Dujovny M, Boehnke M, and Cook EE (1978) Xenon enhanced CT for analysis of cerebral integrity, perfusion, and blood flow *Stroke* 9:123-130

Du AT, Jahng GH, Hayasaka S, Kramer JH, Rosen HJ, Gorno-Tempini ML, Rankin KP, Miller BL, Weiner MW, and Schuff N (2006) Hypoperfusion in frontotemporal dementia and Alzheimer disease by arterial spin labeling MRI *Neurology* 67:1215-1220

Edelman RR, Siewert B, Darby DG, Thangaraj V, Nobre AC, Mesulam MM, and Warach S (1994) Qualitative mapping of cerebral blood flow and functional localization with echo-planar MR imaging and signal targeting with alternating radio frequency *Radiology* 192:513-520

Ellinger R, Kremser C, Schocke MF, Kolbitsch C, Griebel J, Felber SR, and Aichner FT (2000) The impact of peak saturation of the arterial input function on quantitative evaluation of dynamic susceptibility contrast-enhanced MR studies *J.Comput.Assist.Tomogr.* 24:942-948

Farrar TC and Becker ED (1971) Pulse and Fourier Transform NMR. Introduction to theory and methods. *Academic Press, NewYork, USA*46-65

Fiebach JB, Schellinger PD, Jansen O, Meyer M, Wilde P, Bender J, Schramm P, Juttler E, Oehler J, Hartmann M, Hahnel S, Knauth M, Hacke W, and Sartor K (2002) CT and diffusion-weighted MR imaging in randomized order: diffusion-weighted imaging results in higher accuracy and lower interrater variability in the diagnosis of hyperacute ischemic stroke *Stroke* 33:2206-2210

Fisel CR, Ackerman JL, Buxton RB, Garrido L, Belliveau JW, Rosen BR, and Brady TJ (1991) MR contrast due to microscopically heterogeneous magnetic susceptibility: numerical simulations and applications to cerebral physiology *Magn.Reson.Med.* 17:336-347

Fullerton, G. D. Physiological Basis of Magnetic Relaxation. Stark, D. D. and Bradley, W. G. Magnetic Resonance Imaging, Vol.1. 88-108. 1992. St Louis, Mosby Year Book.

Gadian, D. G. Instrument design and operation. NMR and its applications to living systems. 1995. Oxford, UK, Oxford University Press.

Gobbel GT and Fike JR (1994) A deconvolution method for evaluating indicator-dilution curves *Phys.Med.Biol.* 39:1833-1854

Golay X, Hendrikse J, and Lim TC (2004) Perfusion imaging using arterial spin labeling *Top.Magn.Reson.Imaging* 15:10-27

Golay X, Stuber M, Pruessmann KP, Meier D, and Boesiger P (1999) Transfer insensitive labeling technique (TILT): application to multislice functional perfusion imaging *J.Magn.Reson.Imaging* 9:454-461

Goldberg MP (2007) New approaches to clinical trials in neuroprotection: introduction *Stroke* 38:789-790

Gonzalez RG (2006) Imaging-guided acute ischemic stroke therapy: From "time is brain" to "physiology is brain" *AJNR Am.J.Neuroradiol.* 27:728-735

Gore JC (2003) Principles and practice of functional MRI of the human brain *J.Clin.Invest* 112:4-9

Gottrup C, Thomsen K, Locht P, Wu O, Sorensen AG, Koroshetz WJ, and Østergaard L (2005) Applying instance-based techniques to prediction of final outcome in acute stroke *Artif.Intell.Med.* 33:223-236

Grandin CB, Bol A, Smith AM, Michel C, and Cosnard G (2005) Absolute CBF and CBV measurements by MRI bolus tracking before and after acetazolamide challenge: repeatabilily and comparison with PET in humans *Neuroimage.* 26:525-535

Grandin CB, Duprez TP, Smith AM, Mataigne F, Peeters A, Oppenheim C, and Cosnard G (2001) Usefulness of magnetic resonance-derived quantitative measurements of cerebral blood flow and volume in prediction of infarct growth in hyperacute stroke *Stroke* 32:1147-1153

Grieve SM, Blamire AM, and Styles P (2002) Elimination of Nyquist ghosting caused by read-out to phase-encode gradient cross-terms in EPI *Magn.Reson.Med.* 47:337-343

Griswold MA, Jakob PM, Heidemann RM, Nittka M, Jellus V, Wang J, Kiefer B, and Haase A (2002) Generalized autocalibrating partially parallel acquisitions (GRAPPA) *Magn.Reson.Med.* 47:1202-1210

Hacke W, Albers GW, Al Rawi Y, Bogousslavsky J, Davalos A, Eliasziw M, Fischer M, Furlan AJ, Kaste M, Lees KR, Soehngen M, and Warach S (2005) The Desmoteplase in Acute Ischemic Stroke Trial (DIAS): a phase II MRI-based 9-hour window acute stroke thrombolysis trial with intravenous desmoteplase *Stroke* 36:66-73

Hacke W, Brott T, Caplan L, Meier D, Fieschi C, von Kummer R, Donnan GA, Heiss WD, Wahlgren NG, Spranger M, Boysen G, and Marler JR (1999) Thrombolysis in acute ischemic stroke: controlled trials and clinical experience *Neurology* 53:S3-14

Hansen PC (1992) Analysis of discrete ill-posed problems by means of the L-curve *SIAM Rev* 32:561-580

Hansen PC (1994) Ragularisation tools: a MATLAB package for analysis and solution of ill-posed problems *Numerical Algorithms* 6:1-35

Harris RK (1983) Nuclear magnetic resonance spectroscopy. A physiochemical view. *Pitman, London*pp85-pp91

Hatazawa J, Fujita H, Kanno I, Satoh T, Iida H, Miura S, Murakami M, Okudera T, Inugami A, Ogawa T, and . (1995) Regional cerebral blood flow, blood volume, oxygen extraction fraction, and oxygen utilization rate in normal volunteers measured by the autoradiographic technique and the single breath inhalation method *Ann.Nucl.Med.* 9:15-21

Heiss WD (2001) Imaging the ischemic penumbra and treatment effects by PET *Keio.J.Med.* 50:249-256

Helpern JA, Branch CA, Yongbi MN, and Huang NC (1997) Perfusion imaging by un-inverted flow-sensitive alternating inversion recovery (UNFAIR) *Magn.Reson.Imaging* 15:135-139

Herscovitch P (1989) Cerebral blood flow and metabolism measured with oxygen-15 radiotracers *J.Neuropsychiatry Clin.Neurosci.* 1:S19-S29

Herscovitch P, Markham J, and Raichle ME (1983) Brain blood flow measured with intravenous H2(15)O. I. Theory and error analysis *J.Nucl.Med.* 24:782-789

Herscovitch P and Raichle ME (1985) What is the correct value for the brain--blood partition

coefficient for water? *J.Cereb.Blood Flow Metab* 5:65-69

Hjort N, Butcher KS, Davis SM, Kidwell CS, Koroshetz WJ, Rother J, Schellinger PD, Warach S, and Østergaard L (2005) Magnetic resonance imaging criteria for thrombolysis in acute cerebral infarct *Stroke* 36:388-397

Hossmann KA (1994) Viability thresholds and the penumbra of focal ischemia *Ann.Neurol.* 36:557-565

Hou L, Yang Y, Mattay VS, Frank JA, and Duyn JH (1999) Optimization of fast acquisition methods for whole-brain relative cerebral blood volume (rCBV) mapping with susceptibility contrast agents *J.Magn.Reson.Imaging* 9:233-239

Hudetz AG, Feher G, and Kampine JP (1996) Heterogeneous autoregulation of cerebrocortical capillary flow: evidence for functional thoroughfare channels? *Microvasc.Res.* 51:131-136

Ibaraki M, Shimosegawa E, Toyoshima H, Takahashi K, Miura S, and Kanno I (2005) Tracer delay correction of cerebral blood flow with dynamic susceptibility contrast-enhanced MRI *J.Cereb.Blood Flow Metab* 25:378-390

Iida H, Kanno I, Miura S, Murakami M, Takahashi K, and Uemura K (1986) Error analysis of a quantitative cerebral blood flow measurement using H2(15)O autoradiography and positron emission tomography, with respect to the dispersion of the input function *J.Cereb.Blood Flow Metab* 6:536-545

Jehenson P, Westphal M, and Schuff N (1990) Analytical method fro compensation of eddy-current effects induced by pulsed magnetic field gradients in NMR systems *J.Magn.Reson.* 90:264-278

Jesmanowicz A, Bandettini PA, and Hyde JS (1998) Single-shot half k-space high-resolution gradient-recalled EPI for fMRI at 3 Tesla *Magn.Reson.Med.* 40:754-762

Jezzard P and Clare S (1999) Sources of distortion in functional MRI data *Hum.Brain Mapp.* 8:80-85

Johansson E, Olsson LE, Mansson S, Petersson JS, Golman K, Stahlberg F, and Wirestam R (2004) Perfusion assessment with bolus differentiation: a technique applicable to hyperpolarized tracers *Magn.Reson.Med.* 52:1043-1051

Johnson KM, Tao JZ, Kennan RP, and Gore JC (2000) Intravascular susceptibility agent effects on tissue transverse relaxation rates in vivo *Magn.Reson.Med.* 44:909-914

Jones TH, Morawetz RB, Crowell RM, Marcoux FW, FitzGibbon SJ, DeGirolami U, and Ojemann RG (1981) Thresholds of focal cerebral ischemia in awake monkeys *J.Neurosurg.* 54:773-782

Jung S and Swinney HL (2005) Velocity difference statistics in turbulence *Phys.Rev.E.Stat.Nonlin.Soft.Matter Phys.* 72:026304

Kadah YM (2004) Adaptive denoising of event-related functional magnetic resonance imaging data using spectral subtraction *IEEE Trans.Biomed.Eng* 51:1944-1953

Kaneko K, Kuwabara Y, Mihara F, Yoshiura T, Nakagawa M, Tanaka A, Sasaki M, Koga H, Hayashi K, and Honda H (2004) Validation of the CBF, CBV, and MTT values by perfusion MRI in chronic occlusive cerebrovascular disease: a comparison with 15O-PET
5 *Acad.Radiol.* 11:489-497

Kao YH, Wan X, and MacFall JR (1998) Simultaneous multislice acquisition with arterial-flow tagging (SMART) using echo planar imaging (EPI) *Magn.Reson.Med.* 39:662-665

Karch R, Neumann F, Podesser BK, Neumann M, Szawlowski P, and Schreiner W (2003) Fractal properties of perfusion heterogeneity in optimized arterial trees: a model study *J.Gen.Physiol* 122:307-321

Kennan RP, Zhong J, and Gore JC (1994) Intravascular susceptibility contrast mechanisms in tissues *Magn.Reson.Med.* 31:9-21

Kidwell CS, Alger JR, and Saver JL (2003) Beyond mismatch: evolving paradigms in imaging the ischemic penumbra with multimodal magnetic resonance imaging *Stroke* 34:2729-2735

Kidwell CS, Alger JR, and Saver JL (2004) Evolving paradigms in neuroimaging of the ischemic penumbra *Stroke* 35:2662-2665

King RB, Deussen A, Raymond GM, and Bassingthwaighte JB (1993) A vascular transport operator *Am.J.Physiol* 265:H2196-H2208

Kiselev VG (2001) On the theoretical basis of perfusion measurements by dynamic susceptibility contrast MRI *Magn.Reson.Med.* 46:1113-1122

Kiselev VG (2005) Transverse relaxation effect of MRI contrast agents: a crucial issue for quantitative measurements of cerebral perfusion *J.Magn.Reson.Imaging* 22:693-696

Knight RA, Dereski MO, Helpern JA, Ordidge RJ, and Chopp M (1994) Magnetic resonance imaging assessment of evolving focal cerebral ischemia. Comparison with histopathology in rats *Stroke* 25:1252-1261

Knutsson L, Larsson EM, Thilmann O, Stahlberg F, and Wirestam R (2006) Calculation of cerebral perfusion parameters using regional arterial input functions identified by factor analysis *J.Magn.Reson.Imaging* 23:444-453

Kontaxakis G and Strauss LG (1998) Maximum likelihood algorithms for image reconstruction in positron emission tomography *Radionuclides for Oncology*73-106

Kroll K, Wilke N, Jerosch-Herold M, Wang Y, Zhang Y, Bache RJ, and Bassingthwaighte JB (1996) Modeling regional myocardial flows from residue functions of an intravascular indicator *Am.J.Physiol* 271:H1643-H1655

Kuschinsky W and Paulson OB (1992) Capillary circulation in the brain *Cerebrovasc.Brain Metab Rev.* 4:261-286

Kwong KK, Chesler DA, Weisskoff RM, Donahue KM, Davis TL, Østergaard L, Campbell TA, and Rosen BR (1995) MR perfusion studies with T1-weighted echo planar imaging *Magn.Reson.Med.* 34:878-887

Lange K and Carson R (1984) EM reconstruction algorithms for emission and transmission tomography *J.Comput.Assist.Tomogr.* 8:306-316

Larsen OA and Larsen NA (1964) Cerebral Hematocrit in Normal Man *J.Appl.Physiol* 19:571-574

Levin JM, Kaufman MJ, Ross MH, Mendelson JH, Maas LC, Cohen BM, and Renshaw PF (1995) Sequential dynamic susceptibility contrast MR experiments in human brain: residual contrast agent effect, steady state, and hemodynamic perturbation *Magn.Reson.Med.* 34:655-663

Limpert E, Werner SA, and Abbt M (2001) Log-normal distributions across the sciences: keys and clues *BioScience* 51:341-352

Lin W, Celik A, Derdeyn C, An H, Lee Y, Videen T, Østergaard L, and Powers WJ (2001) Quantitative measurements of cerebral blood flow in patients with unilateral carotid artery occlusion: a PET and MR study *J.Magn.Reson.Imaging* 14:659-667

Liu HL, Pu Y, Liu Y, Nickerson L, Andrews T, Fox PT, and Gao JH (1999) Cerebral blood flow measurement by dynamic contrast MRI using singular value decomposition with an adaptive threshold *Magn.Reson.Med.* 42:167-172

Lorenz C, Benner T, Chen PJ, Lopez CJ, Ay H, Zhu MW, Menezes NM, Aronen H, Karonen J, Liu Y, Nuutinen J, and Sorensen AG (2006) Automated perfusion-weighted MRI using localized arterial input functions *J.Magn.Reson.Imaging*

Lythgoe DJ, Østergaard L, William SC, Cluckie A, Buxton-Thomas M, Simmons A, and Markus HS (2000) Quantitative perfusion imaging in carotid artery stenosis using dynamic susceptibility contrast-enhanced magnetic resonance imaging *Magn.Reson.Imaging* 18:1-11

Mallat SG (1989) A Theory of Multiresolution Signal Decomposition: The Wavelet Representation *IEEE Trans.Pat.Anal.Mach.Intel.* 11:674-693

Mansfield P and Maudsley AA (1977) Medical imaging by NMR *Br.J.Radiol.* 50:188-194

Marks MP, de Crespigny A, Lentz D, Enzmann DR, Albers GW, and Moseley ME (1996) Acute and chronic stroke: navigated spin-echo diffusion-weighted MR imaging *Radiology* 199:403-408

Martel AL, Fraser D, Delay GS, Morgan PS, and Moody AR (2003) Separating arterial and venous components from 3D dynamic contrast-enhanced MRI studies using factor analysis *Magn Reson.Med.* 49:928-933

Martin WR, Powers WJ, and Raichle ME (1987) Cerebral blood volume measured with inhaled C15O and positron emission tomography *J.Cereb.Blood Flow Metab* 7:421-426

McKeown MJ, Hansen LK, and Sejnowsk TJ (2003) Independent component analysis of functional MRI: what is signal and what is noise? *Curr.Opin.Neurobiol.* 13:620-629

Meier P and Zeirler KL (1954) On the theory of the indicator-dilution method for measurement of blood flow and volume *J.Appl.Physiol* 6:731-744

Meyer E (1989) Simultaneous correction for tracer arrival delay and dispersion in CBF measurements by the H215O autoradiographic method and dynamic PET *J.Nucl.Med.* 30:1069-1078

Mlynash M, Eyngorn I, Bammer R, Moseley M, and Tong DC (2005) Automated method for generating the arterial input function on perfusion-weighted MR imaging: validation in patients with stroke *AJNR Am.J.Neuroradiol.* 26:1479-1486

Moon TK (1996) The expectation maximisation algorithm *IEEE Signal Processing*47-60

Morgan PS, Bowtell RW, McIntyre DJ, and Worthington BS (2004) Correction of spatial distortion in EPI due to inhomogeneous static magnetic fields using the reversed gradient method *J.Magn Reson.Imaging* 19:499-507

Mori S and van Zijl PC (1995) Diffusion weighting by the trace of the diffusion tensor within a single scan *Magn.Reson.Med.* 33:41-52

Moseley ME, Cohen Y, Mintorovitch J, Chileuitt L, Shimizu H, Kucharczyk J, Wendland MF, and Weinstein PR (1990) Early detection of regional cerebral ischemia in cats: comparison of diffusion- and T2-weighted MRI and spectroscopy *Magn.Reson.Med.* 14:330-346

Mouridsen K, Christensen S, Gyldensted L, and Østergaard L (2006a) Automatic selection of arterial input function using cluster analysis *Magn.Reson.Med.* 55:524-531

Mouridsen K, Friston K, Hjort N, Gyldensted L, Østergaard L, and Kiebel S (2006b) Bayesian estimation of cerebral perfusion using a physiological model of microvasculature *Neuroimage.* 33:570-579

Murase K, Kikuchi K, Miki H, Shimizu T, and Ikezoe J (2001) Determination of arterial input function using fuzzy clustering for quantification of cerebral blood flow with dynamic susceptibility contrast-enhanced MR imaging *J.Magn.Reson.Imaging* 13:797-806

Newbould RD, Stare ST, Clayton DB, Alley MT, Albers GW, Lansberg M, and Brammer R (2006) PERMEATE: High temporal resolution multi-echo/multi-slice dynamic susceptibility contrast perfusion imaging using GRAPPA EPI *In: Proceedings of the 14th Annual Meeting of ISMRM, Seattle, USA* 14:673

Norris DG, Niendorf T, and Leibfritz D (1994) Health and infarcted brain tissues studied at short diffusion times: the origins of apparent restriction and the reduction in apparent diffusion coefficient *NMR Biomed.* 7:304-310

Ogawa S, Lee TM, Kay AR, and Tank DW (1990) Brain magnetic resonance imaging with contrast dependent on blood oxygenation *Proc.Natl.Acad.Sci.U.S.A* 87:9868-9872

Ordidge RJ, Wylezinska M, Hugg JW, Butterworth E, and Franconi F (1996) Frequency offset corrected inversion (FOCI) pulses for use in localized spectroscopy *Magn.Reson.Med.* 36:562-566

Østergaard L, Chesler DA, Weisskoff RM, Sorensen AG, and Rosen BR (1999) Modeling cerebral blood flow and flow heterogeneity from magnetic resonance residue data *J.Cereb.Blood Flow Metab* 19:690-699

Østergaard L, Johannsen P, Host-Poulsen P, Vestergaard-Poulsen P, Asboe H, Gee AD, Hansen SB, Cold GE, Gjedde A, and Gyldensted C (1998a) Cerebral blood flow measurements by magnetic resonance imaging bolus tracking: comparison with [(15)O]H2O positron emission tomography in humans *J.Cereb.Blood Flow Metab* 18:935-940

Østergaard L, Smith DF, Vestergaard-Poulsen P, Hansen SB, Gee AD, Gjedde A, and Gyldensted C (1998b) Absolute cerebral blood flow and blood volume measured by magnetic resonance imaging bolus tracking: comparison with positron emission tomography values *J.Cereb.Blood Flow Metab* 18:425-432

Østergaard L, Sorensen AG, Kwong KK, Weisskoff RM, Gyldensted C, and Rosen BR (1996a) High resolution measurement of cerebral blood flow using intravascular tracer bolus passages. Part II: Experimental comparison and preliminary results *Magn.Reson.Med.* 36:726-736

Østergaard L, Weisskoff RM, Chesler DA, Gyldensted C, and Rosen BR (1996b) High resolution measurement of cerebral blood flow using intravascular tracer bolus passages. Part I: Mathematical approach and statistical analysis *Magn.Reson.Med.* 36:715-725

Ostrem JL, Saver JL, Alger JR, Starkman S, Leary MC, Duckwiler G, Jahan R, Vespa P, Villablanca JP, Gobin YP, Vinuela F, and Kidwell CS (2004) Acute basilar artery occlusion: diffusion-perfusion MRI characterization of tissue salvage in patients receiving intra-arterial stroke therapies *Stroke* 35:e30-e34

Perthen JE (2003) Measurement of Cerebral Perfusion using Magnetic Resonance Techniques: Chapter 5 - Bolus tracking perfusion measurements in infants. *Doctor of Philosophy Thesis, University College London.*pp131-136

Perthen JE, Calamante F, Gadian DG, and Connelly A (2002) Is quantification of bolus tracking MRI reliable without deconvolution? *Magn.Reson.Med.* 47:61-67

Powers WJ (1991) Cerebral hemodynamics in ischemic cerebrovascular disease *Ann.Neurol.* 29:231-240

Pruessmann KP, Weiger M, Scheidegger MB, and Boesiger P (1999) SENSE: sensitivity encoding for fast MRI *Magn.Reson.Med.* 42:952-962

Qian H and Bassingthwaighte JB (2000) A class of flow bifurcation models with lognormal distribution and fractal dispersion *J.Theor.Biol.* 205:261-268

Raichle ME, Martin WR, Herscovitch P, Mintun MA, and Markham J (1983) Brain blood flow measured with intravenous H2(15)O. II. Implementation and validation *J.Nucl.Med.* 24:790-798

Read SJ, Hirano T, Abbott DF, Sachinidis JI, Tochon-Danguy HJ, Chan JG, Egan GF, Scott AM, Bladin CF, McKay WJ, and Donnan GA (1998) Identifying hypoxic tissue after acute ischemic stroke using PET and 18F-fluoromisonidazole *Neurology* 51:1617-1621

Rempp KA, Brix G, Wenz F, Becker CR, Guckel F, and Lorenz WJ (1994) Quantification of regional cerebral blood flow and volume with dynamic susceptibility contrast-enhanced MR imaging *Radiology* 193:637-641

Rohrer M, Bauer H, Mintorovitch J, Requardt M, and Weinmann HJ (2005) Comparison of magnetic properties of MRI contrast media solutions at different magnetic field strengths *Invest Radiol.* 40:715-724

Rose SE, Chalk JB, Griffin MP, Janke AL, Chen F, McLachlan GJ, Peel D, Zelaya FO, Markus HS, Jones DK, Simmons A, O'Sullivan M, Jarosz JM, Strugnell W, Doddrell DM, and Semple J (2001) MRI based diffusion and perfusion predictive model to estimate stroke evolution *Magn.Reson.Imaging* 19:1043-1053

Rose SE, Janke AL, Griffin MP, Strudwick MW, Finnigan S, Semple J, and Chalk JB (2004) Improving the prediction of final infarct size in acute stroke with bolus delay-corrected perfusion MRI measures *J.Magn.Reson.Imaging* 20:941-947

Rosen BR, Belliveau JW, Vevea JM, and Brady TJ (1990) Perfusion imaging with NMR contrast agents *Magn.Reson.Med.* 14:249-265

Roussel SA, van Bruggen N, King MD, Houseman J, Williams SR, and Gadian DG (1994) Monitoring the initial expansion of focal ischaemic changes by diffusion-weighted MRI using a remote controlled method of occlusion *NMR Biomed.* 7:21-28

Runge VM, Kirsch JE, Wells JW, Dunworth JN, Hilaire L, and Woolfolk CE (1994) Repeat cerebral blood volume assessment with first-pass MR imaging *J.Magn.Reson.Imaging* 4:457-461

Saver JL (2006) Time is brain--quantified *Stroke* 37:263-266

Schellinger PD, Jansen O, Fiebach JB, Heiland S, Steiner T, Schwab S, Pohlers O, Ryssel H, Sartor K, and Hacke W (2000) Monitoring intravenous recombinant tissue plasminogen activator thrombolysis for acute ischemic stroke with diffusion and perfusion MRI *Stroke* 31:1318-1328

Schmithorst VJ, Dardzinski BJ, and Holland SK (2001) Simultaneous correction of ghost and geometric distortion artifacts in EPI using a multiecho reference scan *IEEE Trans.Med.Imaging* 20:535-539

Schreiber WG, Guckel F, Stritzke P, Schmiedek P, Schwartz A, and Brix G (1998) Cerebral blood flow and cerebrovascular reserve capacity: estimation by dynamic magnetic resonance imaging *J.Cereb.Blood Flow Metab* 18:1143-1156

Shen Q, Ren H, Fisher M, Bouley J, and Duong TQ (2004) Dynamic tracking of acute ischemic tissue fates using improved unsupervised ISODATA analysis of high-resolution quantitative perfusion and diffusion data *J.Cereb.Blood Flow Metab* 24:887-897

Shen Q, Ren H, Fisher M, and Duong TQ (2005) Statistical prediction of tissue fate in acute ischemic brain injury *J.Cereb.Blood Flow Metab* 25:1336-1345

Silva AC, Zhang W, Williams DS, and Koretsky AP (1995) Multi-slice MRI of rat brain perfusion during amphetamine stimulation using arterial spin labeling *Magn.Reson.Med.* 33:209-214

Silva AC, Zhang W, Williams DS, and Koretsky AP (1997) Estimation of water extraction fractions in rat brain using magnetic resonance measurement of perfusion with arterial spin labeling *Magn.Reson.Med.* 37:58-68

Simonsen CZ, Ostergaard L, Smith DF, Vestergaard-Poulsen P, and Gyldensted C (2000) Comparison of gradient- and spin-echo imaging: CBF, CBV, and MTT measurements by bolus tracking *J.Magn Reson.Imaging* 12:411-416

Smith AM, Grandin CB, Duprez T, Mataigne F, and Cosnard G (2000) Whole brain quantitative CBF and CBV measurements using MRI bolus tracking: comparison of methodologies *Magn.Reson.Med.* 43:559-564

Smith MR, Lu H, and Frayne R (2003) Signal-to-noise ratio effects in quantitative cerebral perfusion using dynamic susceptibility contrast agents *Magn.Reson.Med.* 49:122-128

Smith MR, Lu H, Trochet S, and Frayne R (2004) Removing the effect of SVD algorithmic artifacts present in quantitative MR perfusion studies *Magn.Reson.Med.* 51:631-634

Sobesky J, Zaro WO, Lehnhardt FG, Hesselmann V, Neveling M, Jacobs A, and Heiss WD (2005) Does the mismatch match the penumbra? Magnetic resonance imaging and positron emission tomography in early ischemic stroke *Stroke* 36:980-985

Sodickson DK and Manning WJ (1997) Simultaneous acquisition of spatial harmonics (SMASH): fast imaging with radiofrequency coil arrays *Magn.Reson.Med.* 38:591-603

Sorensen AG, Buonanno FS, Gonzalez RG, Schwamm LH, Lev MH, Huang-Hellinger FR, Reese TG, Weisskoff RM, Davis TL, Suwanwela N, Can U, Moreira JA, Copen WA, Look RB, Finklestein SP, Rosen BR, and Koroshetz WJ (1996) Hyperacute stroke: evaluation with combined multisection diffusion-weighted and hemodynamically weighted echo-planar MR imaging *Radiology* 199:391-401

Sorensen AG, Tievsky AL, Østergaard L, Weisskoff RM, and Rosen BR (1997) Contrast agents in functional MR imaging *J.Magn.Reson.Imaging* 7:47-55

Sourbron S, Luypaert R, Van Schuerbeek P, Dujardin M, and Stadnik T (2004) Choice of the regularization parameter for perfusion quantification with MRI *Phys.Med.Biol.* 49:3307-3324

Stejskal EO and Tanner JE (1965) Spin diffusion measurements: spin-echoes in the presence of a time-dependent field gradient. *J.Chem.Phys.* 42:288-292

Thompson HK, Starmer C, Whalen R, M, ntocsh H, and Tarmer C (1964) Indicator Transit time considered as a Gamma Variate *Circ.Res.* 14:502-515

Tikhonov AN (1963) Solution of incorrectly formulated problems and the regularisation method *Soviet Math Dokl* 4:1035-1038

Tomandl BF, Klotz E, Handschu R, Stemper B, Reinhardt F, Huk WJ, Eberhardt KE, and Fateh-Moghadam S (2003) Comprehensive imaging of ischemic stroke with multisection CT *Radiographics* 23:565-592

Trouillas P and von Kummer R (2006) Classification and pathogenesis of cerebral hemorrhages after thrombolysis in ischemic stroke *Stroke* 37:556-561

van Osch MJ, Vonken EP, Bakker CJ, and Viergever MA (2001) Correcting partial volume artifacts of the arterial input function in quantitative cerebral perfusion MRI *Magn.Reson.Med.* 45:477-485

van Osch MJ, Vonken EP, Viergever MA, van der GJ, and Bakker CJ (2003) Measuring the arterial input function with gradient echo sequences *Magn.Reson.Med.* 49:1067-1076

Villringer A, Rosen BR, Belliveau JW, Ackerman JL, Lauffer RB, Buxton RB, Chao YS, Wedeen VJ, and Brady TJ (1988) Dynamic imaging with lanthanide chelates in normal brain: contrast due to magnetic susceptibility effects *Magn.Reson.Med.* 6:164-174

Vonken EP, Beekman FJ, Bakker CJ, and Viergever MA (1999a) Maximum likelihood estimation of cerebral blood flow in dynamic susceptibility contrast MRI *Magn.Reson.Med.* 41:343-350

Vonken EP, van Osch MJ, Bakker CJ, and Viergever MA (1999b) Measurement of cerebral perfusion with dual-echo multi-slice quantitative dynamic susceptibility contrast MRI *J.Magn.Reson.Imaging* 10:109-117

Vymazal J, Righini A, Brooks RA, Canesi M, Mariani C, Leonardi M, and Pezzoli G (1999) T1 and T2 in the brain of healthy subjects, patients with Parkinson disease, and patients with multiple system atrophy: relation to iron content *Radiology* 211:489-495

Wang J, Aguirre GK, Kimberg DY, Roc AC, Li L, and Detre JA (2003) Arterial spin labeling perfusion fMRI with very low task frequency *Magn.Reson.Med.* 49:796-802

Warwick JM (2004) Imaging of brain function using SPECT *Metab.Brain Dis.* 19:113-123

Weber MA, Thilmann C, Lichy MP, Gunther M, Delorme S, Zuna I, Bongers A, Schad LR, Debus J, Kauczor HU, Essig M, and Schlemmer HP (2004) Assessment of irradiated brain metastases by means of arterial spin-labeling and dynamic susceptibility-weighted contrast-enhanced perfusion MRI: initial results *Invest Radiol.* 39:277-287

Weisskoff RM, Zuo CS, Boxerman JL, and Rosen BR (1994) Microscopic susceptibility variation and transverse relaxation: theory and experiment *Magn.Reson.Med.* 31:601-610

Welch KM, Windham J, Knight RA, Nagesh V, Hugg JW, Jacobs M, Peck D, Booker P, Dereski MO, and Levine SR (1995) A model to predict the histopathology of human stroke using diffusion and T2-weighted magnetic resonance imaging *Stroke* 26:1983-1989

White SJ, Hajnal JV, Young IR, and Bydder GM (1992) Use of fluid-attenuated inversion-recovery pulse sequences for imaging the spinal cord *Magn.Reson.Med.* 28:153-162

Willats L, Connelly A, and Calamante F (2006) Improved deconvolution of perfusion MRI data in the presence of bolus delay and dispersion *Magn.Reson.Med.* 56:146-156

Williams DS, Detre JA, Leigh JS, and Koretsky AP (1992) Magnetic resonance imaging of perfusion using spin inversion of arterial water *Proc.Natl.Acad.Sci.U.S.A* 89:212-216

Wink AM and Roerdink JB (2004) Denoising functional MR images: a comparison of wavelet denoising and Gaussian smoothing *IEEE Trans.Med.Imaging* 23:374-387

Wintermark M (2005) Brain perfusion-CT in acute stroke patients *Eur.Radiol.* 15 Suppl 4:D28-D31

Wintermark M, Smith WS, Ko NU, Quist M, Schnyder P, and Dillon WP (2004) Dynamic perfusion CT: optimizing the temporal resolution and contrast volume for calculation of perfusion CT parameters in stroke patients *AJNR Am.J.Neuroradiol.* 25:720-729

Wirestam R, Bibic A, Latt J, Brockstedt S, and Stahlberg F (2006) Denoising of complex MRI data by wavelet-domain filtering: application to high-b-value diffusion-weighted imaging *Magn.Reson.Med.* 56:1114-1120

Wirestam R and Stahlberg F (2005) Wavelet-based noise reduction for improved deconvolution of time-series data in dynamic susceptibility-contrast MRI *MAGMA.* 18:113-118

Wolff SD and Balaban RS (1989) Magnetization transfer contrast (MTC) and tissue water proton relaxation in vivo *Magn.Reson.Med.* 10:135-144

Wong EC, Buxton RB, and Frank LR (1997) Implementation of quantitative perfusion imaging techniques for functional brain mapping using pulsed arterial spin labeling *NMR Biomed.* 10:237-249

Wong EC, Buxton RB, and Frank LR (1998) Quantitative imaging of perfusion using a single subtraction (QUIPSS and QUIPSS II) *Magn.Reson.Med.* 39:702-708

Wu O, Koroshetz WJ, Ay H, O'Donnell J, Benner T, Østergaard L, Lopez CJ, Zhu MW, Dijkhuizen RM, Rosen BR, and Sorensen AG (2004) Comparison of CBF deconvolution techniques using bolus tracking in the presence of delayed tracer arrival in acute stroke patients. *In: Proceedings of the 12th Annual Meeting of ISMRM, Tokyo, Japan*41

Wu O, Koroshetz WJ, Østergaard L, Buonanno FS, Copen WA, Gonzalez RG, Rordorf G, Rosen BR, Schwamm LH, Weisskoff RM, and Sorensen AG (2001) Predicting tissue outcome in acute human cerebral ischemia using combined diffusion- and perfusion-weighted MR imaging *Stroke* 32:933-942

Wu O, Østergaard L, Weisskoff RM, Benner T, Rosen BR, and Sorensen AG (2003) Tracer arrival timing-insensitive technique for estimating flow in MR perfusion-weighted imaging using singular value decomposition with a block-circulant deconvolution matrix *Magn.Reson.Med.* 50:164-174

Wu O, Sumii T, Asahi M, Sasamata M, Østergaard L, Rosen BR, Lo EH, and Dijkhuizen RM (2007) Infarct prediction and treatment assessment with MRI-based algorithms in experimental stroke models *J.Cereb.Blood Flow Metab* 27:196-204

Wu O, Sumii T, Sasamata M, Rosen BR, Lo EH, and Dijkhuizen RM (2005) Effect of occlusion duration on risk of infarction in a rat embolic stroke model studied with serial MRI-based predictive algorithms *In: Proceedings of the 13th Annual Meeting of ISMRM, Miami, USA*

Yang QX, Posse S, Le Bihan D, and Smith MB (1996) Double-sampled echo-planar imaging at 3 tesla 5 *J.Magn Reson.B* 113:145-150

Ye FQ, Mattay VS, Jezzard P, Frank JA, Weinberger DR, and McLaughlin AC (1997) Correction for vascular artifacts in cerebral blood flow values measured by using arterial spin tagging techniques *Magn.Reson.Med.* 37:226-235

Young AR, Sette G, Touzani O, Rioux P, Derlon JM, MacKenzie ET, and Baron JC (1996) Relationships between high oxygen extraction fraction in the acute stage and final infarction in reversible middle cerebral artery occlusion: an investigation in anesthetized baboons with positron

emission tomography *J.Cereb.Blood Flow Metab* 16:1176-1188

Zhang H, Maki JH, and Prince MR (2007) 3D contrast-enhanced MR angiography *J.Magn.Reson.Imaging* 25:13-25

Zhang W, Williams DS, Detre JA, and Koretsky AP (1992) Measurement of brain perfusion by volume-localized NMR spectroscopy using inversion of arterial water spins: accounting for transit time and cross-relaxation *Magn.Reson.Med.* 25:362-371

Zhou J, Mori S, and van Zijl PC (1998) FAIR excluding radiation damping (FAIRER) *Magn.Reson.Med.* 40:712-719

Zierler KL (1965) Tracer-dilution techniques in the study of microvascular behavior *Fed.Proc.* 24:1085-1091

UNIVERSITY OF LONDON

SENATE HOUSE. MALET STREET, LONDON, WCIE 7HU

REPRODUCTION OF THESES

A thesis which is accepted by the University for the award of a Research Degree is placed in the Library of the College and in the University of London Library. The copyright of the thesis is retained by the author.

As you are about to submit a thesis for a Research Degree, you are required to sign the declaration below. This declaration is separate from any which may be made under arrangements with the College at which you have *pursued* your course (for internal candidates only). The declaration will be destroyed if your thesis is not approved by the examiners, being either rejected or referred for revision.

Academic Registrar

To be completed by the candidate

NAME IN FULL (Block Capitals) LISA WILLATS

TITLE OF THESIS Improved Quantification of Perfusion in Patients with Cerebrovascular Disease

DEGREE FOR WHICH THESIS IS PRESENTED Ph. D

DATE OF AWARD OF DEGREE *(To be completed by the University)* 30 SEP 2007

DECLARATION

1. I authorise that the thesis presented by me in *[2007] for examination for the MPhil/PhD Degree of the University of London shall, if a degree is awarded, be deposited in the library of the appropriate College and in the University of London Library and that, subject to the conditions set out below, my thesis be made available for public reference, inter-library loan and copying.

2. I authorise the College or University authorities as appropriate to supply a copy of the abstract of my thesis for inclusion in any published list of theses offered for higher degrees in British universities or in any supplement thereto, or for consultation in any central file of abstracts of such theses.

3. I authorise the College and the University of London Libraries, or their designated agents, to make a microform or digital copy of my thesis for the purposes of inter-library loan and the supply of copies.

4. I understand that before my thesis is made available for public reference, inter-library loan and copying, the following statement will have been included at the beginning of my thesis: The copyright of this thesis rests with the author and no quotation from it or information derived from it may be published without the prior written consent of the author.

5. I authorise the College and/or the University of London to make a microform or digital copy of my thesis in due course as the archival copy for permanent retention in substitution for the original copy.

6. I warrant that this authorisation does not, to the best of my belief, infringe the rights of any third party.

7. I understand that in the event of my thesis being not approved by the examiners, this declaration would become void.

***Please state year.**

DATE 16th February 2007 SIGNATURE [redacted]

Note: The University's Ordinances make provision for restriction of access to an MPhil/PhD thesis and/or the abstract only in certain specified circumstances and for a maxiumum period of two years. If you wish to apply for such restriction, please enquire at your College about the conditions and procedures. External Students should enquire at the Research Degree Examinations Office, Room NBQ1 (North Block), Senate House.

THIS DECLARATION MUST BE COMPLETED AND RETURNED WITH THE MAIN EXAMINATION ENTRY FORM